UNIVERSITAT
POLITÈCNICA
DE VALÈNCIA

Understanding the microscopic mechanism for the industrially relevant ethylene/ethane separation by silver-containing molecular sieves

Author: Gabrielli Almeida

Directors: Dr. Mónica Jiménez-Ruiz
Dr. Teresa Blasco Lanzuela

September, 2024

Preamble

This thesis has received funding from the European Union's Horizon 2020 research and innovation programme under the Marie Skłodowska-Curie grant agreement No 847439 in the framework of the PhD doctoral training InnovaXN. This project was a partnership between the Institut Laue-Langevin (ILL) in Grenoble (France), the Instituto de Tecnología Química (ITQ) Universidad Politecnica de Valencia (Spain) and Cepsa SA industry in Madrid, (Spain). Dr. Mónica Jiménez-Ruiz worked as ILL local supervisor and Dr. Teresa Blasco Lanzuela at ITQ-UPV as academic supervisor.

I would like to thank my supervisors, Mónica and Teresa, for the completion of this thesis work. Without the massive help of our collaborators, it wouldn't be possible either: thank you Fernando Rey, Germán Sastre and Jacques Ollivier. Many, many thanks to my peer Alessandra.

This thesis investigates the microscopic mechanisms of the selective adsorption and diffusion of ethylene on silver containing zeolites by a combination of Inelastic Neutron Scattering (INS), Quasielastic Neutron Scattering (QENS) and Density Functional Theory (DFT). Zeolites has been successfully applied as adsorbents materials to several challenging separations due to their remarkable and tunable chemical physical properties. One particular use is related to the separation of alkenes from alkanes. Apart from working as molecular sieves, the selective interaction of the alkene with transition metal cations located in the cavities of the zeolites plays a crucial role enhancing the selective separation by a mechanism known as π complexation. The π complexation binding energy is intermediate between a strong physisorption and a weak chemisorption, which allows high selectivity and regenerability of the targeted molecules adsorbed on the transition metal site. Although several studies have been published regarding the adsorption of ethylene on Ag-zeolites, most are based on experimental techniques or on purely theoretical predictions that do not completely describe the system under investigation. Therefore, the interaction of ethylene with silver and the factors that determine this selective adsorption mechanism and the diffusion of the adsorbed ethylene on Ag-zeolites are not fully understood yet. The combination of theoretical (DFT) and experimental (INS and QENS) approaches to study ethylene π-complexation in silver small pore zeolites CHA, RHO and LTA allows to understand the influences of the local geometry of the framework and the neighboring chemical environment of the Ag^+ sites on the formation of π-complexes and diffusion of the molecule. Furthermore, this method may be extended to investigations in many alike materials (whether other zeolites or different microporous systems) as a tool to provide satisfactory qualitative and quantitative information.

Esta tesis investiga los mecanismos microscópicos de la adsorción selectiva y difusión de etileno en zeolitas que contienen plata mediante una combinación de dispersión inelástica de neutrones (INS), dispersión cuasielástica de neutrones (QENS) y teoría funcional de densidad (DFT). Las zeolitas se han aplicado con éxito como materiales adsorbentes en varias separaciones desafiantes debido a sus propiedades físicas químicas notables y ajustables. Un uso particular está relacionado con la separación de alquenos de alcanos. Además de funcionar como tamices moleculares, la interacción selectiva del alqueno con los cationes de metales de transición ubicados en las cavidades de las zeolitas juega un papel crucial al mejorar la separación selectiva mediante un mecanismo conocido como complejación π. La energía de unión de la complejación π es intermedia entre una fisisorción fuerte y una quimisorción débil, lo que permite una alta selectividad y regenerabilidad de las moléculas adsorbidas en el sitio del metal de transición. Aunque se han publicado varios estudios sobre la adsorción de etileno en zeolitas con Ag, la mayoría se basan en técnicas experimentales o en predicciones puramente teóricas que no describen completamente el sistema bajo investigación. Por lo tanto, la interacción del etileno con la plata y los factores que determinan este mecanismo de adsorción selectiva y la difusión del etileno adsorbido en zeolitas con Ag aún no se comprenden completamente. La combinación de enfoques teóricos (DFT) y experimentales (INS y QENS) para estudiar la complejación π de etileno en zeolitas de plata de poros pequeños CHA, RHO y LTA permite comprender las influencias de la geometría local de la estructura y entorno de los sitios Ag^+ en la formación de complejos π y difusión de la molecula. Además, este método puede extenderse a investigaciones en muchos materiales similares (sean otras zeolitas o diferentes sistemas microporosos) como una herramienta para proporcionar información cualitativa y cuantitativa satisfactoria.

Esta tesi investiga els mecanismes microscòpics de l'adsorció selectiva i difusió d'etilé en zeolites que contenen plata mitjançant una combinació de dispersió inelàstica de neutrons (INS), dispersió cuasielástica de neutrons (QENS) i teoria funcional de densitat (DFT). Les zeolites s'han aplicat amb èxit com a materials adsorbents en diverses separacions desafiadores a causa de les seues propietats físiques químiques notables i ajustables. Un ús particular està relacionat amb la separació d'alquens d'alcans. A més de funcionar com a tamisos moleculars, la interacció selectiva de l'alqué amb els cations de metalls de transició situats en les cavitats de les zeolites juga un paper crucial en millorar la separació selectiva mitjançant un mecanisme conegut com a complexació π. L'energia d'unió de la complexació π és intermèdia entre una fisisorción forta i una quimisorción feble, la qual cosa permet una alta selectivitat i regenerabilidad de les molècules objectiu adsorbidas en el lloc del metall de transició. Encara que s'han publicat diversos estudis sobre l'adsorció d'etilé en zeolites con Ag, la majoria es basen en tècniques experimentals o en prediccions purament teòriques que no descriuen completament el sistema sota investigació. Per tant, la interacció de l'etilé amb la plata i els factors que determinen este mecanisme d'adsorció selectiva i la difusió de l'etilé adsorbido en zeolites con Ag encara no es comprenen completament. La combinació d'enfocaments teòrics (DFT) i experimentals (INS i QENS) per a estudiar la complexació π d'etilé en zeolites de plata de porus xicotets CHA, RHO i LTA permet comprendre les influències de la geometria local de l'estructura i entorn dels llocs Ag^+ en la formació de complexos π i difusió. A més, este mètode pot estendre's a investigacions en molts materials similars (ja siguen altres zeolites o diferents sistemes microporosos) com una ferramenta per a proporcionar informació qualitativa i quantitativa satisfactòria.

Contents

Resumen **vii**

Contents **xiii**

1 Introduction **1**

1.1 Why for and how to separate olefins from paraffins? 1
1.2 Zeolites 5
  1.2.1 A brief story about zeolites 5
  1.2.2 Structure 6
  1.2.3 Classification 8
  1.2.4 Properties and applications 8
1.3 Separation Mechanisms and Diffusion in Zeolites 10
  1.3.1 Selective Adsorptive Separation in Zeolites 10
    1.3.1.1 Size Exclusion Effect 11
    1.3.1.2 Kinetic Effect 11
    1.3.1.3 Equilibrium Effect 12
  1.3.2 Diffusion in Zeolites: a few concepts 14
1.4 Objectives of this Thesis 16

2 Methods and Materials **17**

2.1 Neutron Scattering Spectroscopy 17
  2.1.1 Properties of neutrons 17
  2.1.2 Basics of Neutron Scattering 19
    2.1.2.1 The Scattering Cross-Section 20
    2.1.2.2 Scattering from a single fixed nucleus 21
    2.1.2.3 Fermi's Golden Rule 21
    2.1.2.4 Understanding the double differential cross-section 22
    2.1.2.5 Coherent and Incoherent scattering 23
    2.1.2.6 Correlation Functions 25
    2.1.2.7 Energy and Momentum conservation laws 26
  2.1.3 Inelastic Neutron Scattering 28
    2.1.3.1 Geometry and kinematic range of INS instruments 28
    2.1.3.2 IN1-Lagrange spectrometer 31
    2.1.3.3 Incoherent Approximation 32
    2.1.3.4 The Scattering Law 33
  2.1.4 Quasielastic Neutron Scattering 34
    2.1.4.1 Fickian Self-Diffusion Coefficients 36

2.1.4.2 Jump Diffusion Models . . . 37
2.1.4.3 IN5 Spectrometer . . . 38
2.2 Computational Methods . . . 40
2.2.1 Principles of DFT . . . 40
2.2.2 The Hohenberg-Kohn-Sham formulation of DFT . . . 41
2.2.3 DFT Functionals . . . 42
2.2.4 The Lattice Dynamics . . . 43
2.2.4.1 The harmonic approximation . . . 43
2.2.5 Population Analysis and Electron Density Difference . . . 46
2.2.6 Computational Protocol . . . 47
2.3 Samples Preparation . . . 48
2.3.1 Synthesis of zeolitic materials . . . 48
2.3.1.1 Obtaining Na-CHA . . . 48
2.3.1.2 Obtaining NaCs-RHO . . . 48
2.3.1.3 Obtaining HNa-LTA . . . 48
2.3.2 Cation Exchange: Na → Ag . . . 49
2.3.3 Ethylene loading . . . 49

3 Evidence, characterization and comparison of π-complex formation upon ethylene adsorption on different Ag-zeolites 51
3.1 Identification of silver species and interaction with ethylene in Ag-zeolites samples . . . 53
3.2 Evidence and characterization of π-complex in silver containing CHA type zeolite . . . 54
3.2.1 Conception of computational model . . . 54
3.2.1.1 C_2H_4 Ag^+-CHA configuration . . . 54
3.2.1.2 C_2H_4 Ag_3^+-CHA configuration . . . 57
3.2.2 Comparison between experimental INS and theoretical DFT results . . . 58
3.2.3 Frequency Analysis of the vibrational bands . . . 59
3.2.4 Characterization of π-complexation . . . 61
3.2.4.1 Electron Density Difference and ^{13}C NMR results . . . 62
3.2.4.2 C=C stretching shift calculation and Infrared Spectrum . . . 63
3.2.4.3 Adsorption energy and charge transfer . . . 64
3.3 Evidence and characterization of π-complex in silver containing RHO type zeolite . . . 65
3.3.1 Conception of computational models . . . 65
3.3.2 Comparison between experimental INS and theoretical DFT results . . . 67
3.3.3 Frequency analysis of the vibrational bands . . . 70
3.3.4 Characterization of π-complexation . . . 71
3.3.4.1 Electron Density Difference and ^{13}C NMR results . . . 71
3.3.4.2 C=C stretching shift calculation and Infrared Spectrum . . . 72
3.3.4.3 Adsorption energy and charge transfer . . . 72
3.4 Evidence and characterization of π-complex in silver containing LTA type zeolite . . . 73
3.4.1 Conception of computational models . . . 73
3.4.2 Comparison between experimental INS and theoretical DFT results . . . 75
3.4.3 Frequency analysis of the vibrational bands . . . 76
3.4.4 Characterization of π-complexation . . . 78
3.4.4.1 Electron Density Difference and ^{13}C NMR results . . . 78
3.4.4.2 C=C stretching shift calculation and Infrared Spectrum . . . 79
3.4.4.3 Adsorption energy and charge transfer . . . 79
3.5 Effects of cage topology on the formation of Ag-C_2H_4 π-complexes in silver containing zeolites 79
3.6 Partial Conclusion . . . 83

4 Diffusion of ethylene adsorbed on Ag-zeolites 85
4.1 Quasielastic Neutron Scattering Experiments . . . 85
4.1.1 General Description of QENS data . . . 85

4.1.1.1 HWHM fitting . . . 90
4.1.1.2 Activation Diffusion Barrier . . . 92
4.1.2 Discussion . . . 93
4.2 Partial Conclusion . . . 95

5 General Conclusions 97

APPENDIX 101
A.1 XRD patterns . . . 101
A.2 UV-vis and ^{13}C NMR spectra . . . 101
A.3 Structural details of DFT models . . . 103
A.3.1 Energy Calculation details for Ag-CHA model: framework configuration . 103
A.3.2 C_2H_4 $Ag_3{}^+$-CHA configuration . . . 104
A.3.3 AgRHO and NaAg-RHO: configuration details . . . 105
A.4 C=C stretching shift calculation . . . 105
A.5 Mulliken Charge Analysis . . . 106
A.6 Molecular Dynamics . . . 115
A.7 Supporting QENS and INS data . . . 118
A.7.1 QENS C_2H_4 Ag-CHA . . . 118
A.7.2 QENS C_2H_4 CsAg-RHO . . . 124
A.7.3 QENS C_2H_4 HAg-LTA . . . 130
A.7.4 S(Q) of C_2H_4 Ag-zeolites . . . 136
A.7.5 INS: heated sample at 300K . . . 137

Bibliography 139

List of Figures

1.1 Simplified block diagram for a generic steam cracking process. Taken from [5] . . . 2
1.2 Relevant Properties of Ethylene and Ethane molecules. Tm stands for melting temperature and Tb for boiling temperature. . . . 3
1.3 Different representations for the basic unit of zeolites, the TO_4 tetrahedron. . . . 5
1.4 Fig.(a) indicates SBUs that form 4-, 5- and 6-rings; Fig. (b) indicates CBUs that form double rings, such as *d4r* (double 4-rings) and *d6r* (double 6-rings) . . . 7
1.5 Representation of different zeolite frameworks (SOD, LTA, FAU) based on the same type of cage: sodalite. . . . 7
1.6 Pore size classification according to the number of T atoms of pore aperture. . . . 8
1.7 Classification of zeolites according to pore connectivity. . . . 8
1.8 Differences in the range of diffusivity calculated by different experimental and computational methods. Adapted from [67]. . . . 15

2.1 Comparison between the trend of X-ray and neutron cross-section from lighter to heavier atoms. While the intensity of a scattered X-Ray varies linearly with number of orbital electrons, the intensity of scattered neutron wave varies 'randomly' throughout the periodic table. . . . 18
2.2 Nuclear fission scheme: an uranium atom adsorbs a neutron after their collision. The unstable nucleus splits into two, realising neutrons along with thermal energy. . . . 19
2.3 Representation of the scattering process. The incident neutrons interacts with a sample and some neutrons are scattered in the direction ϕ, θ, reaching a detector of small area (dS). . . . 20
2.4 Interaction of a neutron plane wave of unit amplitude with a nucleus to produce a spherical scattered wave. Taken from [78]. . . . 21
2.5 Scattering triangles illustrating the scattering process and possible outcomes after interacting of a sample: elastic interaction or inelastic interaction (with gain or loss of energy by the neutron). 26
2.6 Different molecular motions accessible according to energy transfer, time and length ranges. Adapted from [85]. . . . 27
2.7 Time, length, energy and momentum transfer ranges available for different spectrometers at ILL: IN1-Lagrange, Time-of-Flight (TOF) based spectrometers, Backscattering (BS) based spectrometers and Neutron Spin Echo (NSE) based spectrometers. Adapted from [66]. . . . 28
2.8 Kinematic range of A. Direct spectrometer and B. indirect spectrometer. Taken from [80]. . . 29
2.9 Inelastic scattering triangle with the condition $\vec{k_i}$»$\vec{k_f}$. . . . 30
2.10 Kinematic range reached by the indirect geometry spectrometer (IN1-Lagrange) at final energy $E_f = 4.5$ meV. Scattering angles from 34-69°, that corresponds to the two extreme values of the scattering angles on IN1-Lagrange. . . . 30

2.11 Example of vibrational spectra of L-cysteine molecule, where: (a) INS spectrum (measured at hot source indirect spectrometer TOSCA), (b) Raman spectrum and (c) infrared spectrum. The area highlighted in yellow at high energy indicate the decrease in the intensity of INS spectrum compared to the other techniques. Taken from [86]. 31
2.12 Vertical cut layout of IN-1 Lagrange at ILL. Taken from [88]. 32
2.13 Representation of a quasielastic spectrum with components: instrument resolution, lorentzian and background. In black, the representation of a fitting. 35
2.14 Representation of quasielastic broadening as a function of Q: Half Width at Half Maximum (HWHM). Taken from [72]. 35
2.15 Broadenings as function of Q^2 for jump diffusion models: Chudley and Elliot model (CE), Hall and Ross (HR), Singwi and Sjölander (SS) and Fick models. Taken from [70] 37
2.16 Schematics of the cold-neutron multi-chopper spectrometer IN5 at the ILL. Taken from[94]. . 38
2.17 Kinematic Range of the direct geometry IN5 spectrometer, considering an initial energy fixed at 3.55 meV or $\lambda = 5$ Å. 39
2.18 Generic potential energy curve for two atoms, representing a minimum at a separation of r_0 that could correspond to the bond length, the steep rise for shorter distances that indicates the repulsion due to overlap of electron density of the two atoms, and the softer rise towards zero for larger separations indicating the attractive interaction. Taken from [98]. 44

3.1 Positions for compensating cations identified for CHA framework. 55
3.2 Potential Energy Surface plot indicates a deeper minimum energy for the system when ethylene is interacting with silver cation placed at position S_2. Moreover, from this calculations, we also observed that, in position S_2, the equilibrium distance estimated between the x-axis of C double bond from ethylene to Ag cation is 2.44Å. 56
3.3 Unit cell representing CHA framework with Ag^+ placements. Blue atoms represented by balls are Ag. Framework represented by lines, where yellow is Si atoms, red is O atoms and pink is Al. 57
3.4 Unit cell of CHA representing CHA framework with $Ag_3{}^+$ placements. Blue atoms represented by balls are Ag. Framework represented by lines, where yellow is Si atoms, red is O atoms and pink is Al. 57
3.5 Calculated INS for Ag^+-CHA and $Ag_3{}^+$ considering only fundamental frequencies. 58
3.6 Structural details of *cha* cage in the energy minimized C_2H_4 Ag- CHA model. The distances between Ag and the closest framework oxygen atoms, d_{Ag-Oz}, as well as Ag-C, d_{C-Ag} are also shown. C_2H_4 molecule is represented before and after the system energy minimization with its corresponding C-H distances, d_{C-H}. Al, Ag, C and H atoms are highlighted and identified in the figure. O atoms are highlighted in the 6-ring where Ag cation sits, O_z are the 6-ring Oxygen atoms closest to Ag. Si and O atoms of *cha* cage are represented by brownish lines to facilitate Ag-C_2H_4 complex visualization. The complex lies in a region called 8-ring pocket. 59
3.7 Comparison between experimental and calculated INS spectra, fundamental and total frequencies (considering first overtones), of C_2H_4 adsorbed on Ag-CHA with that of pure gas fore reference. 60
3.8 Illustration of the vibrational modes of ethylene. Modes g) (theoretical value at $\approx$ 1425 cm^{-1}) and h) (theoretical value at $\approx$ 1648 cm^{-1}) are not included in the range of the INS spectra represented in Fig. 3.7. 61
3.9 Isosurfaces created for -8.369eÅ^{-3}, representing the electron density difference between ethylene and Ag-CHA. The yellow shade represents areas of charge depletion while the blue one, of charge accumulation. This rearrangement is attributed to π-complexation interaction. The picture illustrates the full contribution of the Ag-CHA lattice atoms and the molecule. 63
3.10 IR spectrum for ethylene adsorbed on Ag-CHA. It shows a redshift of C=C stretching if compared to gas phase ethylene (1623 cm^{-1}), suggesting an effective interaction between Ag species and the molecule by π-complexation. 64
3.11 Possible positions for extra-framework cations in RHO zeolite. Cs^+ preferred site is S_5 and while Na^+ and Ag^+ prefer site $S_{2'}$. 66

3.12 Unit cells representing RHO framework with Ag$^+$, Cs$^+$ and Na$^+$ placements for CsAg-RHO and NaAg-RHO. Configuration Ag-RHO (not displayed in the picture) keep the same position of Ag species as for CsAg-RHO and NaAg-RHO. 67

3.13 INS and theoretical spectra obtained for different RHO models, considering only fundamental frequencies. The one that best fits the experimental data is CsAg-RHO. 68

3.14 Structural details of *lta* cage in A. before and in B. after geometry optimized C_2H_4 CsAg-RHO model. The distortion of *d8r* and *lta* cages are shown, indicating the structural phase change from Im3m (highly symmetric) to I43m (asymmetric). CsAg-RHO model, the conical narrowing of *lta* cage occurs in the region where Ag-C_2H_4 complex lies. The distances between Ag and the closest framework oxygen atoms, $\mathrm{d_{Ag-Oz}}$, as well as Ag-C, $\mathrm{d_{C-Ag}}$ are also shown. C_2H_4 molecule is represented before and after the system energy minimization with its corresponding C-H distances, $\mathrm{d_{C-H}}$. Al, Ag, C and H atoms are highlighted and identified in the figure. O atoms are highlighted in 6-rings where Ag cation sits. The other O atoms of the framework as well as Si atoms are represented by brownish (and dark blue lines in *d8r* details) to facilitate Ag-C_2H_4 complex visualization. The upper elliptical 8-rings in CsAg-RHO are highlighted in light blue (8-ring side pockets). 69

3.15 Comparison between experimental and calculated INS spectra, fundamental and total frequencies (considering first overtones), of C_2H_4 adsorbed on CsAg-RHO with that of pure gas fore reference. 70

3.16 Isosurfaces created for -8.369eÅ^{-3}, representing the electron density difference between ethylene and CsAg-RHO. The yellow shade represents areas of charge depletion while the blue one, of charge accumulation. This rearrangement is attributed to π-complexation interaction. The picture illustrates the full contribution of the CsAg-RHO lattice atoms and the molecule. . . . 72

3.17 Cages disposition in LTA framework. *lta* cage is highlighted in blue and *sodalite* cage, in orange. 73

3.18 Possible position of H in LTA framework, taken from [119]. O1-H and O3-H point to a 8-ring at the intersection between two *lta* cages while O2-H points to a 6-ring at the intersection between *lta* and *sodalite* cages. 74

3.19 Unit cells of LTA framework with Ag$^+$ and H$^+$ placements. Blue atom represented by ball is Ag while white one represents H. Framework represented by lines, where yellow is Si atoms, red is O atoms and pink is Al. Ag-LTA not represented, keeping the same Ag$^+$ placement as in HAg-LTA-(O2) and HAg-LTA-(O3). 74

3.20 Comparison of the experimental INS spectrum of HAg-LTA sample with the calculated neutron spectra for all configurations considered: C_2H_4 Ag-LTA, C_2H_4 HAg-LTA-(O2) and C_2H_4 HAg-LTA-(O3), with fundamental frequencies. 75

3.21 Structural details of *lta* cage in the energy minimized C_2H_4 HAg- LTA model. The distances between Ag and the closest framework oxygen atoms, $\mathrm{d_{Ag-Oz}}$, as well as Ag-C, $\mathrm{d_{C-Ag}}$ are shown. C_2H_4 molecule is represented before and after the system energy minimization with its corresponding C-H distances, $\mathrm{d_{C-H}}$. Al, Ag, C and H atoms are indicated in the figure. O atoms are highlighted in the 6-ring where Ag cation is placed, O_z are the 6-ring Oxygen atoms closest to Ag. Si and O atoms of *lta* cage are represented by brownish lines to facilitate Ag-C_2H_4 complex visualization. The complex lies in a region called 8-ring pocket. 76

3.22 Comparison between experimental and calculated INS spectra of C_2H_4 adsorbed in HAg-LTA. Green full line spectra are related to total contribution, while the dashed line represent only first overtones. Experimental ethylene gas phase spectrum is represented in grey. 77

3.23 Isosurfaces created for -8.369eÅ^{-3}, representing the electron density difference between ethylene and HAg-LTA. The yellow shade represents areas of charge depletion while the blue one, of charge accumulation. This rearrangement is attributed to π-complexation interaction. The picture illustrates the full contribution of the HAg-LTA lattice atoms and the molecule. . . . 78

3.24 Comparison between experimental and calculated INS spectra of C_2H_4 adsorbed in Ag-CHA, CsAg-RHO and HAg-LTA. Full line spectra represent total contribution (fundamental and first overtone) while the dashed line represent only fundamentals. 80

3.25 Comparison between 8-ring side pockets of Ag-CHA, CsAg-RHO and HAg-LTA with the distances between the centroids of the 8-rings. 81

3.26 Isosurfaces created for -8.369eÅ^{-3}, corresponding to the electron density difference between ethylene and frameworks. The yellow regions represents areas of charge depletion while the blue one, of charge accumulation. This rearrangement is attributed to π-complexation interaction. The details on the right side of the picture schematize the contributions of the Oxygen atoms from the 8-ring pockets. 82

4.1 As-measured QENS spectra for ethylene adsorbed on Ag-CHA, CsAg-RHO and HAg-LTA at different temperatures compared to loaded zeolite sample measured at 50K as reference. . . . 87
4.2 QENS spectra obtained for ethylene adsorbed on Ag-CHA, CsAg-RHO and H-LTA at 100K at Q = 1.00 Å. Red is the total fit while Black, Green and Yellow are used to represent the instrument resolution, Lorentzian and flat background functions. 89
4.3 Q dependencies of the HWHM of the quasielastic components of the QENS spectra at 100, 175 and 235 K for ethylene diffusing in Ag-CHA, CsAg-RHO and HAg-LTA. Each can be fitted with a Hall-Ross jump diffusion model. Herein, the errors displayed by the experimental HWHM curves are only related to neutron point data, i.e. related to the instrument statistics, not taking into account corrections due to the zeolite framework contribution by other theoretical methods. 91
4.4 Arrhenius plots for diffusion of ethylene adsorbed on Ag-CHA, CsAg-RHO and HAg-LTA. The activation energies obtained are listed in Table 4.1. 93
4.5 Summary chart correlating cage dimensions and maximum jump length (at 235K) and activation diffusion barrier values. The motion observed in QENS data must correspond to a small fraction of non-adsorbed molecules or to short diffusion motions of ethylene associated with silver, both happening within the instrument time window. 94

A.1 XRD patterns of zeolites Ag-CHA, CsAg-RHO and HAg-LTA, consistent with database of IZA[45] for each corresponding zeolite type. 101
A.2 UV-Visible spectra of silver exchanged and degassed (at 400 °C overnight) for Ag-CHA, CsAg-RHO and HAg-LTA (only degassed spectrum). 102
A.3 ^{13}C MAS NMR spectra of free-ethylene gas compared to ethylene adsorbed on Ag-CHA, CsAg-RHO and HAg-LTA zeolites. Spinning rotation bands are indicated by asteriks (*). 103
A.4 ^{13}C NMR spectra of ethylene adsorbed on Ag-CHA, H-CHA and Na-CHA in comparison with C_2H_4. Spinning rotation bands are signed by asterisk. 103
A.5 C_2H_4 Ag_3^+ configuration after geometry optimization. Details of atom distances and atoms also shown. 104
A.6 Ag-RHO and NaAg-RHO are represented in the figure. For these configurations, after geometry optimization, the framework also undergoes symmetry change, as explained for CsAg-RHO. In CsAg-RHO model, the major axis (d1) of the deformed upper 8-rings are in direction x-x'. For Ag-RHO and NaAg-RHO, d1 is in the direction y-y'. As a result, in Ag-RHO and NaAg-RHO the

$$cagenarrowingoccursintheregionoppositetowheretheAg-C$$

$_2H_4$ is located. 105
A.7 C=C streching calculation by comparing calculated C=C stretching frequency of C_2H_4 with the calculated C_2H_4 adsorbed on each Ag-zeolite. These values are ≈ 46 cm^{-1} for Ag-CHA, 56 cm^{-1} for CsAg-RHO and 42 to HAg-LTA. 105
A.8 Server atom index generated by Materials Studio for C_2H_4 Ag-CHA model. 108
A.9 Server atom index generated by Materials Studio for C_2H_4 CsAg-RHO model. 112
A.10 Server atom index generated by Materials Studio for C_2H_4 HAg-LTA model. 114
A.11 Experimental, DFT and MD results. 116
A.12 QENS spectra obtained for ethylene adsorbed on Ag-CHA at 100K at different Q values. Red is the total fit while Black, Green and Yellow are used to represent the instrument resolution, Lorentzian and flat background functions. 118
A.13 QENS spectra obtained for ethylene adsorbed on Ag-CHA at 100K at different Q values. Red is the total fit while Black, Green and Yellow are used to represent the instrument resolution, Lorentzian and flat background functions. 119

A.14 QENS spectra obtained for ethylene adsorbed on Ag-CHA at 175K at different Q values. Red is the total fit while Black, Green and Yellow are used to represent the instrument resolution, Lorentzian and flat background functions. 120
A.15 QENS spectra obtained for ethylene adsorbed on Ag-CHA at 175K at different Q values. Red is the total fit while Black, Green and Yellow are used to represent the instrument resolution, Lorentzian and flat background functions. 121
A.16 QENS spectra obtained for ethylene adsorbed on Ag-CHA at 235K at different Q values. Red is the total fit while Black, Green and Yellow are used to represent the instrument resolution, Lorentzian and flat background functions. 122
A.17 QENS spectra obtained for ethylene adsorbed on Ag-CHA at 235K at different Q values. Red is the total fit while Black, Green and Yellow are used to represent the instrument resolution, Lorentzian and flat background functions. 123
A.18 QENS spectra obtained for ethylene adsorbed on CsAg-RHO at 100K, 175K and 235K at different Q values. Red is the total fit while Black, Green and Yellow are used to represent the instrument resolution, Lorentzian and flat background functions. 124
A.19 QENS spectra obtained for ethylene adsorbed on CsAg-RHO at 100K, 175K and 235K at different Q values. Red is the total fit while Black, Green and Yellow are used to represent the instrument resolution, Lorentzian and flat background functions. 125
A.20 QENS spectra obtained for ethylene adsorbed on CsAg-RHO at 175K, 175K and 235K at different Q values. Red is the total fit while Black, Green and Yellow are used to represent the instrument resolution, Lorentzian and flat background functions. 126
A.21 QENS spectra obtained for ethylene adsorbed on CsAg-RHO at 175K, 175K and 235K at different Q values. Red is the total fit while Black, Green and Yellow are used to represent the instrument resolution, Lorentzian and flat background functions. 127
A.22 QENS spectra obtained for ethylene adsorbed on CsAg-RHO at 235K, 175K and 235K at different Q values. Red is the total fit while Black, Green and Yellow are used to represent the instrument resolution, Lorentzian and flat background functions. 128
A.23 QENS spectra obtained for ethylene adsorbed on CsAg-RHO at 235K, 175K and 235K at different Q values. Red is the total fit while Black, Green and Yellow are used to represent the instrument resolution, Lorentzian and flat background functions. 129
A.24 QENS spectra obtained for ethylene adsorbed on HAg-LTA at 100K at different Q values. Red is the total fit while Black, Green and Yellow are used to represent the instrument resolution, Lorentzian and flat background functions. 130
A.25 QENS spectra obtained for ethylene adsorbed on HAg-LTA at 100K at different Q values. Red is the total fit while Black, Green and Yellow are used to represent the instrument resolution, Lorentzian and flat background functions. 131
A.26 QENS spectra obtained for ethylene adsorbed on HAg-LTA at 175K at different Q values. Red is the total fit while Black, Green and Yellow are used to represent the instrument resolution, Lorentzian and flat background functions. 132
A.27 QENS spectra obtained for ethylene adsorbed on HAg-LTA at 175K at different Q values. Red is the total fit while Black, Green and Yellow are used to represent the instrument resolution, Lorentzian and flat background functions. 133
A.28 QENS spectra obtained for ethylene adsorbed on HAg-LTA at 235K at different Q values. Red is the total fit while Black, Green and Yellow are used to represent the instrument resolution, Lorentzian and flat background functions. 134
A.29 QENS spectra obtained for ethylene adsorbed on HAg-LTA at 235K at different Q values. Red is the total fit while Black, Green and Yellow are used to represent the instrument resolution, Lorentzian and flat background functions. 135
A.30 The Q-ω space of C_2H_4 Ag-zeolites measured in IN5. 136
A.31 Cuts of S(Q,ω) along |Q| from 0 to 2.5 Å^{-1} over energy values from -0.2 to 0.2 meV, representing S(Q). 137
A.32 INS comparison between C_2H_4 Ag-CHA sample before and after heating at 300K. 138

Chapter 1

Introduction

1.1 Why for and how to separate olefins from paraffins?

Olefins (or alkenes) are fundamental components in the chemical industry. With an annual global production at the scale of several million metric tons, ethylene and propylene are among the most valuable feedstocks for manufacturing numerous commodities, such as polyethylene and polypropylene [1–4]. Nowadays, there are many methods to obtain light olefins, employing diverse kinds of feedstocks (crude oil, natural gas, coal, biomass) [5]. If natural gas is used as raw material, it can go through different transformation processes: separation of methane, ethane, and propane; oxidative coupling of methane (OCM) via ethane; methanol production via steam reforming of natural gas to give a few examples. The substances resulting from these processes, then, may undergo further reactions as a mean to produce light olefins (i.e. ethylene, propylene, butenes) as final products.

Among the technologies that can be applied to obtain light olefins, Fluid Catalytic Cracking (FCC) and Steam Cracking (SC) are the ones that stand out [6–8].

FCC is a process mainly adopted in petroleum refining to convert heavy hydrocarbons, in general from crude oil distillation, into lighter and more valuable products such as gasoline and diesel. Although its objective is not the production of olefins, it results in the production of some light olefins as by-products. Steam cracking, by the other hand, is specifically designed for the production of light olefins, including ethylene and propylene. The final goal of steam cracking is to break down larger hydrocarbon molecules, which are mainly derived from natural gas or naphtha, into smaller olefin molecules.

Zhao et al.[9] carried out an analysis of twenty different processes for the production of light olefins. In their study, they concluded that Steam Cracking, a process developed during the 1960s, in fact, is still the leading technology for olefin production and a benchmark for all others. The conventional method (steam cracking of ethane) is the most energy-efficient process, as 40% of the hydrocarbons are converted into olefins requiring about 60 GJ per tons of high-value chemicals (HVCs), while the total energy required in methane-based pathways is approximately 30% higher. Going further, coal and biomass based alternative methods consume about 60–150% more energy.

Figure 1.1 shows a simplified and generic steam cracking process flowchart for the production of ethylene, the molecule of interest in this work. Basically, saturated hydrocarbons are broken into smaller unsaturated hydrocarbons by means of a reaction with steam. The feed of the cracker furnace can be composed by liquefied petroleum gas (LPG), naphta or ethane and butane. Naphtha feedstocks leads to a wider spectrum of products in opposition to the gases, which, on the other hand, result in a higher conversion of ethylene and propylene.

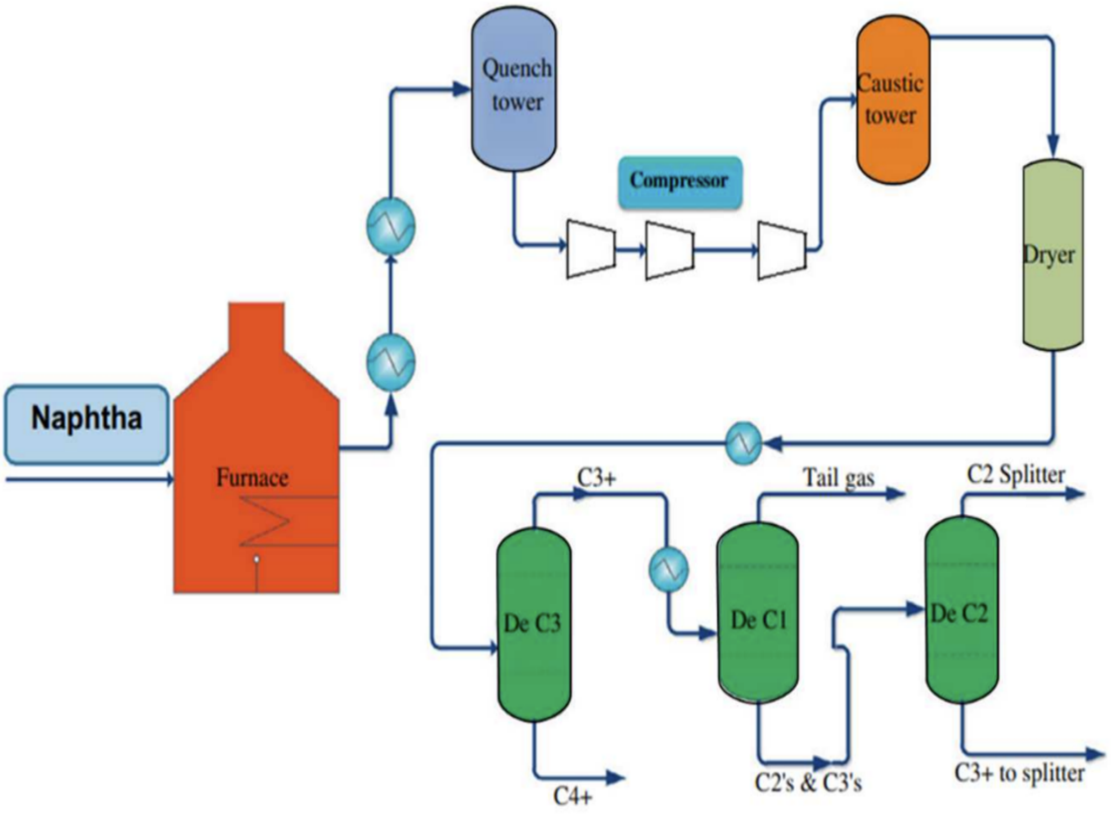

Figure 1.1: Simplified block diagram for a generic steam cracking process. Taken from [5]

After the cracking of the larger molecules, the hydrogenation of methane, ethylene, propylene, C4-gases and minor products happens in the cracker. The heavier liquid components are removed first and the cracked gas is, then, cooled by quench water. The next steps are compression and washing with caustic soda in order to eliminate remaining acidic gases such as H_2S and CO_2. In the dryer, the water from the gas is removed and it proceeds to the deethaniser, where the split of the C3 fraction occurs.

Following the deethaniser, a selective hydrogenation separates undesired acetylene from the shorter hydrocarbons (at C2 fraction). The C2 fraction is cooled and distilled to remove hydrogen and methane. Ethylene is, then, obtained in the C2-splitter in an ethane/ethylene mixture. The C3 fraction is linked to a depropaniser to generate a propane/propylene mixture. C4 olefins are produced in the debutanizer.

A separation and purification of ethane/ethylene mixture must be carried out as a polymer-grade ethylene of >99.5 % is required for most industrial application (i.e. production of polyethylene) [10]. The separation and purification processes transform a certain mixture into single products by relying on selective mechanisms that take advantage of the different properties displayed by each of the mixture components, such as boiling point, sizes, polarity and affinity (Fig. 1.2).

The current industrial process available and effective enough to separate ethylene from ethane is called cryogenic distillation, in a setup with distillation columns containing over one hundred trays[11, 12]. Such process relies on combining high pressure and very low temperatures to separate the chemicals through boiling-point-based separation technology. It means that it requires a significant input of energy to achieve and maintain the low temperatures necessary for effective separation, specially due the fact that ethylene and ethane have similar boiling points. This is an expensive process which accounts for the most of the production costs in fine chemical and petrochemical industries and represents 10–15% of the world's energy consumption [13, 14].

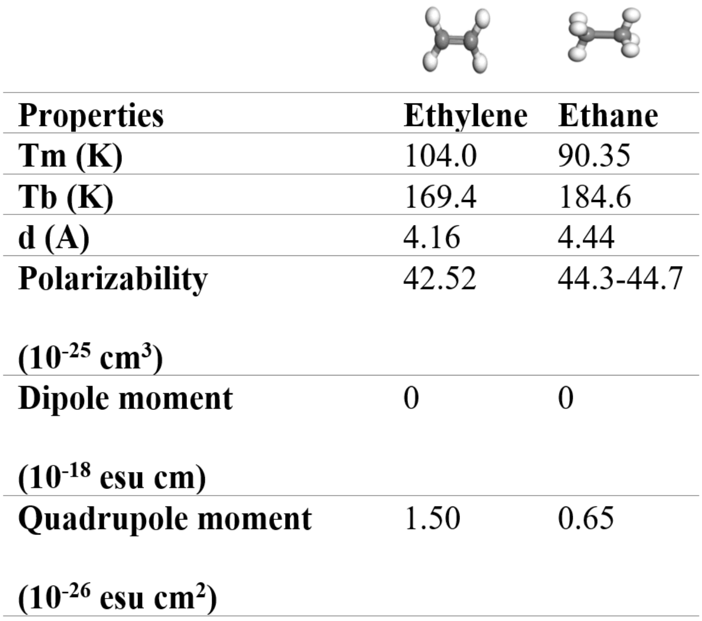

Properties	**Ethylene**	**Ethane**
Tm (K)	104.0	90.35
Tb (K)	169.4	184.6
d (A)	4.16	4.44
Polarizability (10^{-25} cm^3)	42.52	44.3-44.7
Dipole moment (10^{-18} esu cm)	0	0
Quadrupole moment (10^{-26} esu cm^2)	1.50	0.65

Figure 1.2: Relevant Properties of Ethylene and Ethane molecules. Tm stands for melting temperature and Tb for boiling temperature.

In this context, the development of alternative technologies with enhanced energy efficiency for ethylene/ethane and alike separations is highly encouraged. This replacement would represent such a positive step towards a more sustainable production that it is considered one of the seven chemical separation solutions to "change the world"[15]. Most of these alternative technologies consist on **adsorbent materials and selective adsorption-based separation methods**.

A variety of studies have demonstrated that C_2H_4/C_2H_6 separation by means of membranes or porous adsorbents, such as Metal-Organic Frameworks (MOFs), Porous Aromatic Framework (PAFs), carbon based adsorbents and zeolites, is a highly promising approach [4, 11, 14, 16–19]. Due to the nearly identical sizes of alkenes/alkanes, these alternative materials should rely on other interaction mechanisms on top of steric effects, as, for instance, specific selectivity towards only one of the molecules in terms of polarity and affinity. In this sense, the adsorbent's surface properties play a crucial role. They can be engineered to favor the adsorption of specific molecules or types of molecules.

It is known that the unsaturated bonds of alkenes are able to donate electrons, assuming a role of Lewis bases. These electrons can interact with Lewis acids, such as transition metal cations, through the so called π-complexation. In this case, the molecule is adsorbed on the metal, allowing the recovery of the molecule upon heat treatments. This pathway was employed for selective adsorption of ethylene in a mixture with ethane by liquid membranes doped with Cu^+[20] or Ag^+[21, 22], for instance, leading to improved permeability and separation of olefins. Nevertheless, the long-term operational stability of these membranes still needs further improvements.

Another recent example is the report of a microporous tailored MOF effectively presenting an optimal pore window size and containing chelated Cu(I) ions to form a selective adsorption site for C_2H_4 molecules [23]. However, only a few MOFs and PAFs with very high selectivity can be used industrially, since most of the organic linkers present in their composition will experience levels of instability under diverse temperature and pressure conditions [24, 25] and carbon-based adorbents surface has limited functional groups [17].

Zeolites, on the other hand, are microporous crystalline materials known for their physico-chemical stability, which have been largely used as adsorbents for industrial separation and purification since the 1950s [26]. Recent studies have shown remarkable selectivities of these materials towards ethylene/ethane separations at ambient temperature. One example is ITQ-55 [27], a pure-silica small-pore zeolite which can successfully separate ethylene from ethane relying on its high framework flexibility and unique pore topology with heart-shaped cages. The selectivity reaches almost 100%, however it is achieved at the expense of reduced adsorption capacity as a result of pores contraction. Considering aluminum rich aluminosilicates, the selectivity for ethylene adsorption can be enhanced through exchange with several transition metal cations (Co(II), Ni(II), Zn(II), Fe(III), Cu(II), Ag(I) to mention few examples) [19, 28, 29] that provide an appropriate selective binding with ethylene by taking advantage of π-complexes formation. Indeed, Min et al. [30] reported the excellent separation performance of Ag-ZK-5 zeolite (framework code KFI) towards C_2H_4/C_2H_6 with fast adsorption kinetics thanks to the combination of preferential adsorption of the olefin over the paraffin due to Ag^+ sites and the steric size exclusion of ethane.

Although some research articles has been published regarding the adsorption of ethylene on Ag-zeolites, most studies are based on experimental techniques or on purely theoretical predictions that do not completely describe the system under investigation [31–35]. Therefore, the interaction of ethylene with silver and the factors that determine the adsorption process on Ag-zeolites are not fully understood yet. In a broadly way, this thesis proposes an investigation on how the local geometry of small-pore zeolites and the neighboring chemical composition of the Ag^+ sites influence the formation and characteristics of π-complexes in these materials and, consequently, the adsorption and diffusion process of ethylene on Ag-zeolites.

In the next sections of this chapter the concepts of zeolite materials are clarified, as well as the adsorptive separation processes in such materials, highlighting the mechanisms behind the adsorption through π-complexation scheme. A brief discussion about diffusion in adsorption is also drawn. The specific objectives to be achieved throughout our study are detailed, clarifying the choices of methods employed for our purposes. Finally, the thesis outline describes how the next chapters are organized and what to expect from each of them.

1.2 Zeolites

In this section, a brief definition and development of zeolites over history is given, followed by a description of how the zeolitic structures are organized and classified. Finally, the fundamental properties of these materials are correlated to their main application nowadays. This section follows the references [36–44], that can be consulted for further information.

1.2.1 *A brief story about zeolites*

Etymologically the term zeolite means “boiling stone”. It was first used in 1756 when the Swedish mineralogist Cronstedt observed the behavior of a natural mineral solid (*stilbite*) during its heating process. It was known years later that this phenomenon was due to the presence of hydration water inside the pores of the solid, which is eliminated upon heating.

Zeolites are defined as microporous and crystalline materials composed of TO_4 tetrahedra sharing their vertices (Oxygen atoms) with other four TO_4 tetrahedra (Fig. 1.3), forming a three-dimensional network with channels and cavities of molecular dimensions. Classically, tetrahedral T atoms (tri and tetravalent cations) referred only to Al and Si atoms, resulting in aluminosilicates. However, elements such as B, Ge, Ti, among others, can integrate the network through isomorphic substitutions. These materials with substituting atoms, or heteroatoms, are also called zeotypes. Depending on the oxidation state of the tetrahedral T atom, the zeolitic structure may be electronically charged. If Si atoms, tetravalent, are replaced by trivalent heteroatoms, for example Al, the framework will become negatively charged. In this case, it is compensated by cations placed within the channels and cavities. Currently, zeolites can be found in the form of natural minerals or synthesized.

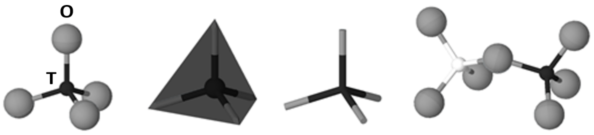

Figure 1.3: Different representations for the basic unit of zeolites, the TO_4 tetrahedron.

It was only 100 years after being "discovered" by Cronstedt that zeolites regained some attention from chemists. It was demonstrated that these materials had a reversible hydration and dehydration, concluding that water molecules were simply included and not chemically bonded to the zeolite. Shortly after, in 1858, the cation-exchange properties of zeolites were explored for the first time, which allowed the first industrial application of zeolites: as water softener. Further investigations have shown that dehydrated zeolites like *chabazite*, for example, could absorb gaseous ammonia, carbon dioxide, hydrogen sulfide, alcohol, chloroform and benzene. Such property of zeolites was studied in detail by J. W. McBain, who came up with the term "molecular sieve". This effect could not be fully explained until the structural porosity of zeolites was described after the first structural elucidations of these materials.

Inspired by the work of McBain, another scientist, Barrer, focused on studying the separation of mixtures of various molecules using zeolites. He was responsible of introducing these materials as potential adsorbents for separation processes. Barrer also achieved a method to successfully synthesize zeolites by mimicking the crystallization conditions of natural zeolites (hydrothermal conditions, i.e., alkaline media and temperatures above 200°C), initiating the modern era of zeolites in the 1940’s. Not only the synthesis of analogs of natural zeolites were possible, but of new ones with no natural counterpart as well. These discoveries attracted the interest of the industry towards the material, promoting the development of commercial zeolites production and their applications. In this scenario, Union Carbide, an industry in the USA, played a very important role lauching a research program in association with Barrer and Robert M. Milton, in 1949, that led to the development of an adsorption method to separate nitrogen from oxygen. Inspired by the previous works of McBain and Barrer, Milton designed this separation, which was only possible before with traditional cryogenic distillation, using chabazite as adsorbent. Therefore, this event marked the introduction of zeolites as adsorbents in industrial gas separations. Furthermore, Milton also found a new and more gentle route for the synthesis by lowering the crystallization temperature and using more reactive silica sources and alkaline media in the precursor gel.

Although nowadays zeolites can be synthesized using a series of techniques, such as solvothermal route, the hydrothermal one developed by Milton is the most common and presents great efficiency. With this method, the synthesis is carried out at temperatures between 100 - 200°C, in high-pressure autoclaves, using a precursor gel containing water as solvent, T atoms, organic or inorganic cations and mineralizing agents. In the precursor gel, the T atoms come from sources of silicon, aluminum or various heteroatoms, the cations can act as structure drivers and the mineralizing agents, OH^- or F^-, are responsible for breaking and reformulating T-O-T bonds.

The synthesis conditions introduced by Milton allowed the scaling up of the syntheses, enabling the commercialization of zeolites A and X for adsorption applications in 1954. Since then, the interest for zeolites for adsorption, ion-exchange and catalysis is still ongoing, alongside with the fundamental research in order to find new structures, modifying synthesis methods for already known structures and much more.

1.2.2 Structure

As mentioned before, TO_4 tetrahedra act as the primary units of the zeolitic structure, being referred to in the literature as BBUs (Basic Building Unit). The bonding of BBUs, in turn, results in the formation of secondary units, known as SBUs (Secondary Basic Unit). Consequently, CBUs (Compositional Building Unit) are formed from the union of a finite number of SBUs. Each structure can have more than one type of CBUs. Thus, the resulting combination of SBUs and CBUs defines and describes the zeolitic framework they form. That is, the rings (pores), channels, cavities and cages created from the connection of tetrahedral units are responsible for the development of the zeolitic structure as a whole, making each one of them unique. Figure 1.4 shows examples of: (a) SBUs that form 4-, 5- and 6-rings; a (b) CBUs that create double rings, such as *d4r* (double 4-rings) and *d6r* (double 6-rings).

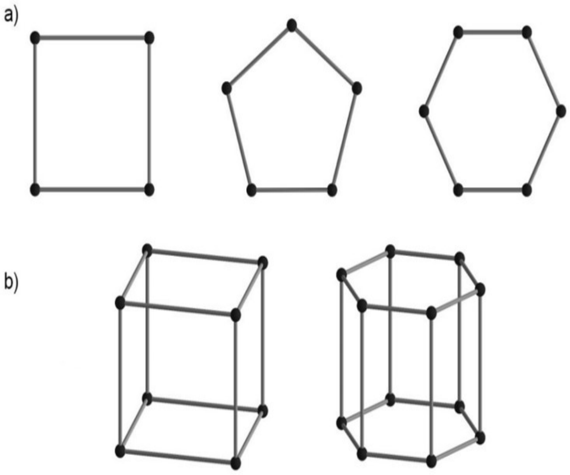

Figure 1.4: Fig.(a) indicates SBUs that form 4-, 5- and 6-rings; Fig. (b) indicates CBUs that form double rings, such as *d4r* (double 4-rings) and *d6r* (double 6-rings)

Finally, Figure 1.5 represents the formation of CBUs and of zeolitic structures. In the example, the same type of cage, the sodalite, associated (or not) with distinct units gives rise to three different structures. According to IZA (International Zeolite Association) [45], so far there are 256 distinct zeolitic frameworks, each one indicated by a 3-letter code (i.e. SOD, LTA, FAU, etc).

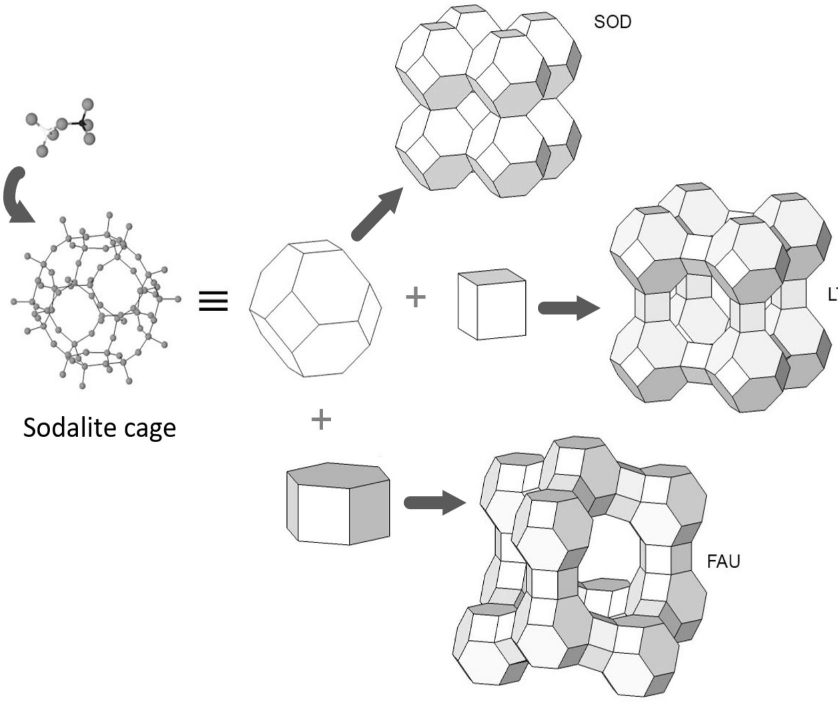

Figure 1.5: Representation of different zeolite frameworks (SOD, LTA, FAU) based on the same type of cage: sodalite.

1.2.3 Classification

Taking into account structural factors, zeolites can be classified according to the size and connectivity of their pores.

The pore size classification is based on the number of T atoms that circumscribe the smallest ring in a channel, the pore aperture. Thus, the pores are labeled as small (8-ring; d ≈ 4 Å), medium (10-ring; d ≈ 5.5 Å), large (12-ring; d ≈ 7 Å) and extra-large (≥ 14-ring ; d ≥ 7 Å), as shown in Figure 1.6.

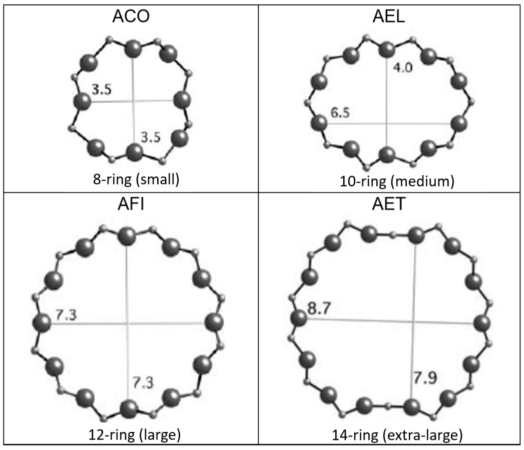

Figure 1.6: Pore size classification according to the number of T atoms of pore aperture.

The pore connectivity classifies a structure in mono (1D), bi (2D) or three-dimensional (3D) depending on the number of directions that a molecule can follow in its diffusional flow while inside a channel. This classification is represented, in a generic way, in Figure 1.7.

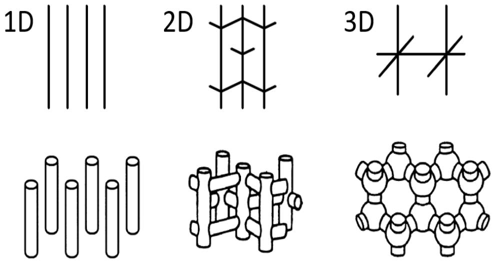

Figure 1.7: Classification of zeolites according to pore connectivity.

1.2.4 Properties and applications

Zeolites present high thermal and moderate to high chemical stabilities, so that traditional aluminosilicates are usually thermally stable up to 700 °C and resistant to dissolution in both acids and bases under normal conditions. Apart from their stability, the main applications of zeolites derive from three fundamental properties they have, which are related to their structure and chemical composition.

- **Notable ion exchange capacity**: resulting from the presence of mobile compensating cations inside the pores and cavities of the material. The ion exchange capacity of zeolites increases as the number of compensating cations grows, which depends on the composition of the material. For aluminosilicates, this number increases with the content of Al. Based on this property, zeolites are widely used as ion exchangers in processes for softening hard water and removal of toxic metal ions. The use of zeolites as ion exchangers for various industrial applications has been extensively reviewed by several authors. Zeolite 4A, for example, has been used as a component in laundry detergents since the 1970's, replacing phosphates as water softeners, which helps to mitigate the environmental hazard associated with phosphates. In 1994, a synthetic zeolite with a GIS structure showing improved performance over zeolite 4A was commercialized for the same application. The natural zeolite clinoptilolite has been intensively applied to remove heavy metal cations from water. Moreover, zeolites have been utilized in the removal of radioactive ions from waste streams. The same clinoptilolite and chabazite, alongside with synthetic zeolites with CHA, FAU, and LTA structures, have been employed to mitigate the effects of nuclear accidents or the presence of radioactive waste, especially in the removal of Cs-137. One famous example is their use as part of the remediation efforts during the aftermath of Chernobyl nuclear accident in 1986.

- **Catalytic properties**: these properties are originated by the presence of active sites (most frequently associated to the introduction of trivalent heteroatoms) besides the shape and polarity selectivities of the zeolitic framework that, together, play an important role on the product selectivities, making these materials a true catalytic reactor. Zeolites have been used as catalysts in a wide range of industrial processes, particularly in oil refining, petrochemistry, and related processes. An example is their application in the Methanol to Olefins (MTO) processes, which converts methanol into light olefins (i.e. ethylene and propene). Zeolite catalysts like SAPO-34 and ZSM-5 have been commercialized for this application. Another one is in the Catalytic Cracking for Propene Production, where ZSM-5 [46] catalysts are mostly employed, favoring the formation of light C2-C4 olefins when heavier hydrocarbons are cracked.

- **High internal surface area and adsorption capacity**: these properties favor the steric separation of molecules according to the pore size of the zeolites. Besides the pore size, also the composition of the material influences its adsorption capacity in such a way that zeolites can selectively adsorb molecules of a specific size and polarity, depending on the characteristics of the zeolitic framework. Some of the uses of zeolites as adsorbents are in gas separation and purification processes in chemical and petrochemical industry. An ideal adsorbent for separation is selective towards one or more components of the mixture, presents a large (working) adsorption capacity, it is easily regenerable, durable and stable at relevant conditions. Moreover, adsorbents must be cheap and prone to be shaped in order to achieve optimal mechanical and dynamical properties. The thermal stability of zeolites along with their structural and compositional variety make them an excellent option for tailoring their properties for specific applications. The selectivity in adsorptive separations, as to be better explained later, can be based on differences in the interactions of the components of the mixture, depending mostly on the chemical composition of the adsorbent. Alternatively, the adsorption selectivity can be originated by differences between the rate at which the components are adsorbed, relying on the adsorbent's structure and pore dimensions. It is worth to mention that apart from pore dimensions, framework flexibility can greatly affect the selectivity in adsorption and diffusion processes. In fact, some adsorption and diffusion results in zeolites could only be completely understood after the framework flexibility are considered. This flexibility can be guest-induced, as exemplified by the adsorption of ethylene on the molecular sieve ITQ-55 (explained in details in the next section) [47–50]. In other cases, as it occurs on CO_2 adsorption on RHO and

> related zeolites due to trapdoor mechanism. In this case, the flexibility of RHO zeolite is due to the ability of the Cs^+ cation to displace out from and into the *d8r* window sites [51], controlling the adsorption capacity.

Overall, zeolitic materials present solid properties and applicability for separation processes in many process and consist in a topic under ongoing development.

1.3 Separation Mechanisms and Diffusion in Zeolites

In this section, the separation mechanisms in zeolites are introduced, followed by a brief discussion on diffusion in microporous materials. References [17, 44, 52, 53] are recommended for deeper review.

1.3.1 Selective Adsorptive Separation in Zeolites

Adsorption is a phenomenon that leads to transfer of molecules, atoms or ions from a fluid phase to the vicinity of an interface. If the system in question is a gas-solid or liquid-solid, this interface is therefore the solid surface.

According to the strength of the interaction between the adsorbate and the adsorbent surface, adsorption is classified into physical (physisorption) or chemical (chemisorption) phenomenon. The intermolecular forces that play a role in a physisorption account for interactions mechanisms between induced or permanent dipoles and/or quadrupoles. Chemisorption processes, on the other hand, are based on mechanisms with changes in the electronic structure of the adsorbent and the adsorbate, leading to the formation of a chemical bond. Thus, it is expected the absolute value of physisorption enthalpy to be lower ($\leq$ 40 kJ/mol) than that of chemisorption ($\geq$ 80 kJ/mol).

A selective adsorption mechanism refers to the process by which certain substances or molecules are preferentially adsorbed onto a solid surface, while others are excluded or adsorbed to a lesser extent. These selectivity mechanisms can be based on various factors such as molecular size, shape, polarity, and specific interactions between the adsorbate and the adsorbent.

Therefore, the first step is to differentiate each molecule in terms of physical and chemical properties. As seen in Figure 1.2 for ethylene/ethane, olefins, in general, possess slightly smaller kinetic diameters and a larger dipolar or quadrupolar moments if compared to paraffins and can establish chemical bonds (π interactions) with a transition metal center through the C=C double bonds. Considering these aspects, we can highlight three possible types of selective adsorptive separation mechanisms based on: size exclusion (molecular sieving), kinetics and equilibrium (thermodynamics) effects.

1.3.1.1 Size Exclusion Effect

The size exclusion or sieving effect relies on the fact that only small enough and compatible shaped molecules can access a given zeolite through its window-pores while all others are excluded, allowing high selectivity levels. In order to achieve the separation of a two components mixture, for example, the key idea is to select a zeolite whose maximum window size (or pore aperture) is between the molecular sizes of the two components in question.

This requirement is so precise that is limiting and difficult to select a zeolite that perfectly and naturally fulfil such a need. For this reason, in most cases, a zeolite that roughly satisfies the requirement can be tuned in order to enhance its molecular sieving properties. Some of the strategies applied to precisely tune the pore aperture of a zeolite are:

- Modifying the window accessible area by changing the type of compensating cation in the framework;

- Changing the pore shape by relocating guest species or adding water molecules;

- Expanding or shrinking the pore aperture by changing the T–O bond length (by adjusting the Si/Al ratio for aluminosilicate zeolites, for example).

Zeolite A (framework code LTA) is one of the most common examples in which the pore aperture size can be finely tuned by modifying the type of compensating cations. In terms of olefin/paraffin separation, Aguado et al. [33], use the strategy of partial ion-exchange of Ca^{2+}/Ag^{+} with a 92% content of Ag, achieving absolute molecular sieving. Using a similar approach, Xiao and co-workers [54] tuned the aperture size of pores in zeolite A between $\approx$ 3.8 and 4.2 Å in 0.2 Å increments by a partial ion exchange of Ca^{2+} by Ag^{+}. The resultant AgCa-A achieved a nearly absolute molecular sieving of C_2H_4/C_2H_6. Pore-size measurement and molecular modeling corroborate that the pore size of AgCa-A was tuned to be in between the molecular sizes of C_2H_4 and C_2H_6. Although effective, these adsorbents required very specific designing, representing quite a challenge and demanding a lot of resources.

1.3.1.2 Kinetic Effect

Kinetic separation principle is based on the differences in the diffusion rates of different molecules, which can also be considered as a partial molecular sieve effect, which can be used to separate the components. Also, the pore size of the adsorbent needs to be precisely tailored to measure between the kinetic diameters of the two molecules that require separation. One example of kinetic separation by zeolites is that of ethylene and ethane by a flexible pure silica zeolite (ITQ-55) [27], as mentioned previously. The large heart-shaped cages of ITQ-55 allows the kinetic separation of ethylene from ethane with selectivity of $\approx$100%. When ethylene molecules enter the center of the 8 ring window, the window size of ITQ-55 will expand from 2.38 Å to 3.08 Å due to the remarkable framework flexibility. Ethylene molecule, slightly smaller than ethane, holds the pore opening during molecular diffusion being selectively adsorbed in the zeolite. Nevertheless, the successful case of pure silica ITQ-55 for the molecular sieving separation of ethane and ethylene is very particular and suffers from limited adsorption capacity for industrial application.

1.3.1.3 Equilibrium Effect

Equilibrium separation relies on an interaction between the adsorbate and the adsorbent; specifically, the targeted molecules of the adsorbate (the ones that will be recovered) interact with the adsorption sites. In a mixture, molecules having stronger interaction with the adsorbent will preferentially be adsorbed over the others with weaker interaction, leading to their separation.

In highly cationic zeolites, that is high Al content aluminosilicate zeolites, compensating cations are uniformly dispersed on the negatively charged oxides in the material framework. Cations with high valences (i.e. charges) and small ionic radii (that is, high charge density) would strongly polarize the zeolite. Due to its greater quadrupole and dipole moments compared to ethane, ethylene presents a polar nature. This means that, when in contact with highly polarized cationic zeolites, the alkene is preferentially adsorbed into their pores and, as a consequence, most cationic zeolites are olefin-selective, as shown by other studies with zeolites, as in Na, K, Ca -FAU, Na-LTA, Na-MOR and Na-CHA to name a few[55–57].

The interaction strength of ethylene with the adsorbent can be enhanced through cation exchange with several transition metal cations. In fact, this conclusion resulted from the study of Carter et al.[58], almost 60 years ago, while investigating the adsorption of ethylene on a series of faujasite zeolites (i.e. Na-X, K-X, Ca-X, Cd-X, Ag-X) by infrared spectroscopy and microcalorimetry. They reported that the nature of the adsorption of ethylene is dependent on the nature of the exchangeable cations. It was observed that for all cases, except for Cd-X and Ag-X zeolites, the ethylene molecule can be readily removed by evacuation indicating that is weakly attached to the zeolites. While the heat of adsorbtion for ethylene on Na-X was 36kJ/-mol, the one for ethylene on Ag-X and Cd-X were 75.7 kJ/mol and 62.3 kJ/mol, respectively. The stronger interaction between ethylene and Ag-X and Cd-X is possible because, besides the physical interaction (i.e. nonbonding interaction) provided by dipoles of adsorbent-adsorbant, there is also a chemical interaction such as *π-complexation* between ethylene and the adsorption site, which enhances the separation selectivity and adsorption capacity of these adsorbents.

As mentioned previously in section 1.1, the presence of a π electron cloud and higher quadrupole moment is what enables olefins to form π-complexes with a few specific metals. Several transition metal cations such as Co(II), Ni(II), Zn(II), Fe(III), Cu(II), Cd(II), Ag(I), Pd(I) to mention some examples have been proposed as good candidates to provide an adequate selective binding with ethylene, being Ag-zeolites among the most efficient.

Despite the outstanding results reported up until now, there is not a material appropriate for industrial applications. The development of a suitable adsorbent for ethylene is still an industrial challenge that requires further investigation, being π-complexation method key.

Defining and characterizing the π-complexation

The formation and mechanisms of π-complexation itself is well-known. Basically, in this process, a σ bond is formed by the electron charge transfer from the p orbitals of ethylene (or an alkene) to the empty (5)s orbital of the Ag cation (or another transition metal). Simultaneously, there is backdonation of charges from the filled (4)d^{10} orbital of Ag^{+} to the antibonding π^* orbital of ethylene. This results in the formation of a π-complex. Both carbon atoms of ethylene binds symmetrically to transition metal cations, forming metalcarbon bonds. The π complexation binding energy is intermediate between a strong physisorption and a weak chemisorption. In other words, unlike the strong chemical interaction through covalent bonds, the π complexation interaction has the potential to afford both high selectivity and regenerability by selectively binding with moderate strength targeted molecules to the adsorption site.

A further observation made by Carter et al. [58] during the study of ethylene on faujasites describes the fact that changes in the vibrational properties upon gas adsorption are bound to the nature of the adsorption mechanism. In fact, a correlation between the shift of the ethylene C=C stretching and the heat of adsorption of ethylene on silver-zeolite was reported: C=C stretching vibrational modes of adsorbed ethylene were featured at lower frequencies than in the gas phase, showing redshifts from 30 - 70 cm^{-1}. Therefore, a way to confirm the formation of π-complexes after the adsorption is by analyzing the changes in the internal mode frequencies of the adsorbate with respect to the free molecule, especially the C=C stretching.

The C=C stretching vibration frequency of gas phase ethylene at 1623 cm^{-1} is only Raman-active. However, upon adsorption on transition metal cation centers, the ethylene molecule may lose its symmetry as all vibrational modes of ethylene become IR-active. The change in the geometry of adsorbed ethylene involves not only the C=C bond, that will tend to lengthen with the redshift of C=C stretching, but also the hydrogen atoms suffer the effect of metal-to-alkene charge transfer and the strong electrostatic field in the zeolite cavity around the complex. Therefore, IR spectroscopy has been extensively used for studying ethylene adsorption on zeolites.

The ethylene's librational modes (below 1000 cm^{-1}), however, cannot be observed by infrared, requiring an aid of other techniques such as Raman spectroscopy. The analysis of the librational modes is important since they provide information about the local environment surrounding the confined molecule. Once ethylene is adsorbed and "trapped" within the zeolite, the Raman spectra are difficult or impossible to analyze due to the high fluorescence levels that many zeolites present: the signals of the molecule would be engulfed by the ones coming from the zeolite lattice. Neither of these difficulties apply to inelastic neutron-scattering (INS) spectroscopy whatsoever, for which there are also no electromagnetic selection rules and all vibrational modes of hydrogenated molecules can be visualized[32, 59]. This technique has been used to investigate adsorbed molecules in zeolites since the 1980's, with remarkable success. More information about the benefits of INS and its application as a probing method in this work will be given in Chapter 2.

In previous studies, the redistribution of charges upon adsorption with a net transfer from the π (ethylene) to the 5s (Ag^+) orbitals [60, 61] have been identified by a high field shift of the ^{13}C NMR signal of ethylene adsorbed on Ag-zeolites or Ag-supported catalyst [62–65]. This way, ^{13}C NMR is a tool to confirm if ethylene molecule is preferentially interacting with silver species in a framework that could possibly contain other adsorption sites.

Moreover, the adsorption on zeolites can be studied not only experimentally but also by means of computational methods. Screening of real or theoretical adsorbents for separation of alkenes from alkanes can be approached with computational tools [44]. These methods allow researchers to simulate the vibrational frequencies of a model, for example, and understand the underlying molecular interactions by a further comparison with experimental data. This can give valuable insights into the fundamental mechanisms of adsorption on zeolites, as geometries and energies of the systems can also be evaluated.

Uzunova et al.[60], for instance, adopted an approach to interpret the adsorption and activation of ethylene in transition metal exchanged clinoptolite by means of Density Functional Theory calculations. They related deformation density maps with the role of the framework during the charge transfer from metal species to ethylene molecule during π-complexation. It was reported that the framework oxygen atoms that are the nearest from the metal sites, referred to as O_z, act as an electron reservoir as they provide electrons from the negatively charged framework to the metallic species in π-complexation. Based on this information, theory about the role of the framework in the charge transfer from the metal cations to the ethylene molecule in the system investigated was proposed. It was proved that there are more elements involved in π-complexation than a single exchange between metal and molecule: the electrostatic field around the complex, provided by the zeolitic framework, also affects the formation, characteristics and behaviour of the π-complexes.

1.3.2 Diffusion in Zeolites: a few concepts

As mentioned previously, adsorption separation processes rely on the selective adsorption of hydrocarbon molecules or impurities onto adsorbent materials, being zeolites largely applied for this matter. The effectiveness of these materials depends on both their thermodynamic and transport properties [66]. It is essential to know and control transport properties to ensure rapid diffusion thus minimizing the required amount of adsorbent used. Additionally, some separation mechanisms are based on differences in the diffusion rates of the various components. This way, it is important to control the intracrystalline diffusion of hydrocarbon molecules within zeolites.

Moreover, the study of diffusion of a molecule in zeolite *per se* is interesting because the interactions between molecules and the different zeolite type frameworks can result in diverse and unexpected behavior [67].

Molecular diffusion through the pores of a zeolite crystal is considerably different from gaseous diffusion. In gases, diffusion is governed by interactions or collisions between molecules driven by their thermal motion. Many properties of these gaseous system, which is an isotropic medium, can be derived and calculated from Brownian motion theory. Considering a macroporous lattice (pore diameters of greater than 50 nm), the molecule-molecule collisions are still more often than molecule-wall. However, as the pore dimension decreases going to microporous scale (pore diameters of less than 2 nm), molecule-wall collisions dominate and the diffusion becomes more dependent on the adsorbent characteristics, such as pore diameter, pore wall structure and channels [67, 68].

Due to the great importance of determining the diffusion rates of molecules inside of zeolites, a number of different experimental techniques have been applied to this study. These techniques can be divided into two types: macroscopic and microscopic ones[66]. Macroscopic techniques measure the transport diffusivity of a gas, in a bed of zeolite crystals or membrane, caused by a change of the adsorbate concentration. Microscopic techniques, on the other hand, measure the motion of adsorbates (self-diffusion) through a zeolite crystal in a time and length scales much shorter than the ones of macroscopic techniques, giving crucial information about the microscopic mechanisms of diffusion in a system.

The diffusivities acquired with each of these techniques vary significantly among each other, which is expected since each technique is based on different principles and has different time and length scales. As a result, a direct comparison between techniques is, in most of the cases, a hard task. Some of these techniques and the differences in the diffusivity range can be found in Figure 1.8.

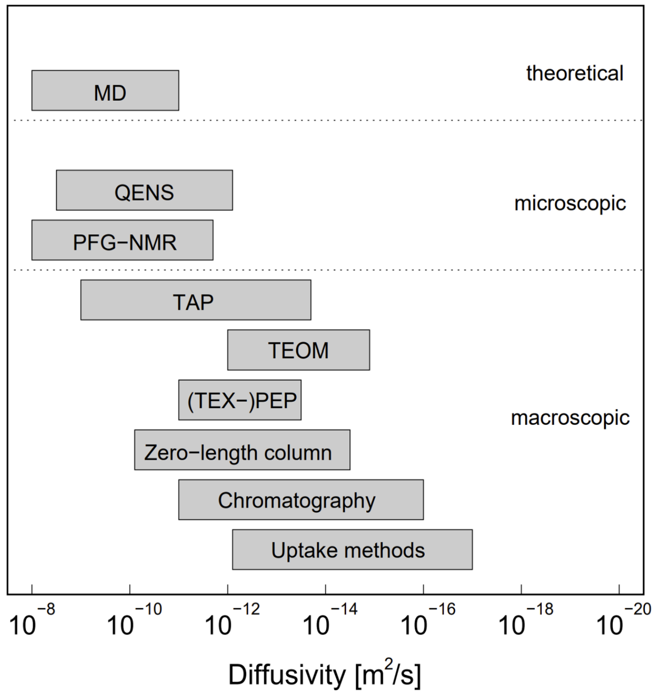

Figure 1.8: Differences in the range of diffusivity calculated by different experimental and computational methods. Adapted from [67].

As depicted in Figure 1.8, the techniques currently available for studying microscopic diffusion include Quasielastic Neutron Scattering (QENS) and Pulse Field Gradient (PFG) NMR. PFG NMR, for instance, was the first microscopic advanced method for the measurement of diffusion in zeolites. Even though this technique is capable of describing the dynamics of an adsorbed molecule, it achieves molecular displacements down to 0.1–1 µm for times on the order of 1 ms, in contrast to QENS (0.1–100 nm and 10^{-3}–100 ns). Jobic [66, 69–72] observed that diffusion motions in zeolites, i.e. jumps from one favourable site to another corresponding favourable site, within the same supercage and intercage diffusion, could fall within the time scale accessible on QENS instruments. Later, the enhancement of Molecular Dynamics (MD) simulations has allowed a further interpretation of QENS data, assisting the identification of the kind of motion(s) that thrive in a specific system, as both QENS and MD techniques reach similar time and length scales of investigation (0.1–100 nm and 10^{-3} –100 ns) therefore leading to comparable and more detailed results.

In a QENS experiment, the propagation of a molecule within a zeolite can be described as successive jumps of the adsorbate between adsorption sites [66]. The adsorption sites are recurring in every unit cell of the zeolite, and thus the elementary adsorption steps may be characterized for a certain adsorbate-adsorbent pair [44].

The elementary adsorption steps found in microporous diffusion is a level of the kinetics of adsorption that follow different mechanisms, depending on the specific characteristics of the sorbate-sorbent system (e.g. molecular structure, adsorbent structure, sorbate-sorbent interactions, and sorbate-sorbate interactions). The distances involved in these steps (from several Å to nm) are short compared to the length scales required to define the overall diffusion process. However, a large number of elementary steps leads to diffusion.

Different elementary adsorption steps have been observed for a variety of zeolites. They can be described as intracage jumps or cage-to-cage-jumps. In intracage jumps, the adsorbate jumps from one adsorption site to another considering the same cavity. This type of motion is more likely to occur if the molecule's critical diameter is comparable to the window size and the cavity has many adsorption sites. In cage-to-cage jumps, the adsorbate jumps from an adsorption site in one cavity to another in a neighboring cavity. The activation energy required for cage-to-cage jump tends to be higher than the one required for intracage jumps [44].

Hedin et al.[73] performed PFG NMR experiments to investigate the intracrystalline self-diffusion coefficients of small hydrocarbons (methane, ethane, ethylene and propylene) on all-Si-CHA and Si-LTA (ITQ-29) structures at 301 K and 101.3 kPa, describing a correlation between the size of the 8-ring windows of the cages and the size of the molecules on the measured self-diffusivities.

Several works of Jobic and O'Malley [66, 72, 74–76], for example, have successfully used QENS and Molecular Dynamics calculations to investigate the diffusion of different range of molecules (e.g. benzene, *n*-alkanes, amonia, phenol) in zeolites, microscopically detailing their molecular diffusion.

However, QENS data related to diffusion of ethylene on the systems under study on this work have not been reported yet.

1.4 Objectives of this Thesis

The general goal of this thesis is to investigate the microscopic mechanisms of the selective adsorption and diffusion of ethylene on silver containing zeolites.

Specifically, it aims to understand the influences of the local geometry of small-pore zeolites (CHA, RHO, LTA) and the neighboring chemical environment of the Ag^+ sites on the formation of π-complexes in each of these materials and, consequently, on the adsorption and diffusion process of ethylene on Ag-zeolites. A combination of Inelastic and Quasielastic Neutron Scattering and Density Functional Theory was used. The specific choice of CHA, RHO and LTA zeolites due to their consolidated role as adsorbents in the industry, similar small pore sizes, but different cavity shapes and flexibilities, which are key parameters in this study.

Chapter 2

Methods and Materials

This chapter will introduce the methods approached in this thesis work. The study is based on a combination of Neutron Scattering techniques and Density Functional Theory (DFT), with secondary aid of Nuclear Magnetic Resonance (NMR), Ultraviolet-visible (UV-vis) and Infared (IR) spectroscopies. As neutron scattering techniques (Inelastic and Quasielastic) and DFT are the core methods employed, the basic concepts of their theory is presented in the next sections. The synthesis process of the materials used is also included at the end of the chapter.

2.1 Neutron Scattering Spectroscopy

There are currently a wide variety of experimental techniques that use neutron as probe to investigate the structure (diffraction) and dynamics (spectroscopy) of many classes of materials in an extraordinary range of length and time scales. In this Chapter, however, we will only focus on the two major techniques relevant to this work: Inelastic Neutron Scattering (INS) and Quasielastic Neutron Scatering (QENS).

2.1.1 Properties of neutrons

In 1932, James Chadwick observed that an unknown particle was emitted when beryllium was bombarded with He nuclei. This elementary particle, known as neutron ($^1_0$n), has no charge, rest mass similar to that of the proton (1.675 x 10^{-27} kg) and a magnetic moment (spin 1/2).

The energy of a neutron, indicated by E, is correlated to its velocity v according to the expression $E = \frac{1}{2}mv^2$. E can also be represented as a function of neutron's temperature T, $E = \frac{3}{2}k_BT$, where k$_B$ is the Boltzmann constant. Due to the wave-particle duality, neutrons are described as a plane wave of wavelenght λ and a wave vector **k**, which is collinear to the direction of propagation. The modulus of the wave vector is linked to the wavelength through the formula $|\mathbf{k}|= \frac{2\pi}{\lambda}$ in a way that E is equally expressed as follows:

$$E = \frac{\hbar^2 k^2}{2m} = \frac{h^2}{2m\lambda^2} \tag{2.1}$$

where h represents the Planck constant and $\hbar$ is its reduced form.

Some very particular and interesting properties of neutrons consolidate their role as a powerful characterization tool, such as:

- **Neutron wavelengths**: which are similar to atomic distances and its energies are equivalent to those of several elementary excitations in solids and liquids. These fundamental properties allow neutrons to be an important probe, informing atoms positions and how they are moving.

- **Neutrons sensitivity and selectivity**: in opposition to what happens to X-Rays, neutrons are scattered by nuclear rather than electric forces. The intensity of the scattered neutron wave depends only on the internal structure of the probed nuclei instead of mass or electric charge of the atoms (Fig. 1.1). As a consequence, neutrons can be sensitive to both heavy and light atoms.

- **Neutron sensitivity to H**: in neutron scattering, the uniquely high cross section of Hydrogen renders this atom's information about ten times more visible than that of any other atoms.

- **Neutron's charge neutrality**: being neutral, neutrons are unimpeded by the electron cloud and are thus able to penetrate deep into matter. It means it is a non destructive probe. As a result, complex sample environment apparatus (i.e. furnaces or high-pressure systems which require thick-walled containment vessels) can be used without significant neutron flux attenuation.

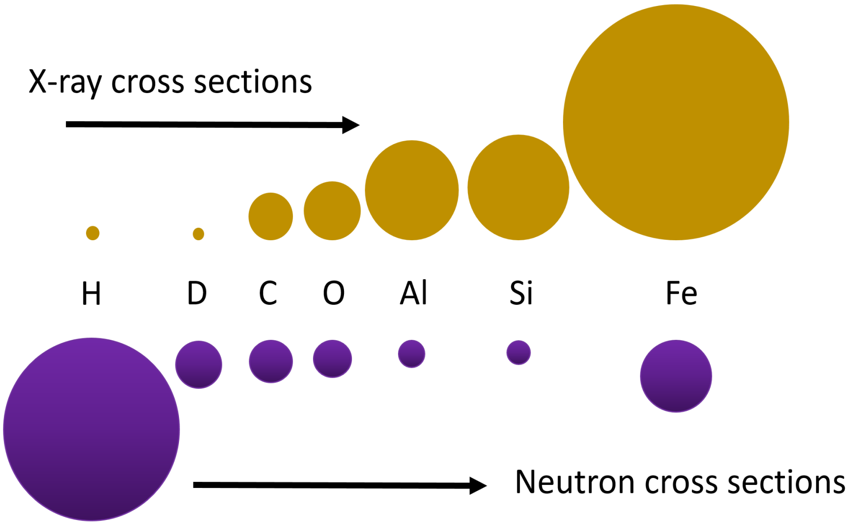

Figure 2.1: Comparison between the trend of X-ray and neutron cross-section from lighter to heavier atoms. While the intensity of a scattered X-Ray varies linearly with number of orbital electrons, the intensity of scattered neutron wave varies 'randomly' throughout the periodic table.

Free neutrons can be produced by spallation sources and nuclear reactors. At spallation sources, neutrons are generated by striking high energy proton beams against a heavy target. At a nuclear reactor, neutrons are produced by means of nuclear fission (Fig. 2.2). At ILL, enriched uranium, ^{235}U, is used as fuel element. In a such nuclear process, an uranium atom adsorbs a neutron after their collision. The nucleus produced is unstable and splits into two. Additionally, neutrons are produced along with thermal energy. These neutrons created during fission, however, have energies of a few MeV. In order to feed the chain reaction process of the reactor and to be useful experimentally, these neutrons are cooled down by a moderator. In the case of ILL, the moderator arranged around the primary source is deuterated water (D_2O), which produces thermal neutron (≈ 25 meV). However, many experiments need higher (≈ 100 meV, "hot neutron") or lower (≈5 meV, "cold neutron") neutron energies, obtained from secondary moderators (respectively, graphite at 2000K and liquid hydrogen at 30K), which are located within the principal moderator. The new local conditions created by the introduction of secondary moderators alter the average energy. The moderated neutrons are collected from the tank using neutron guides to experimental set up.

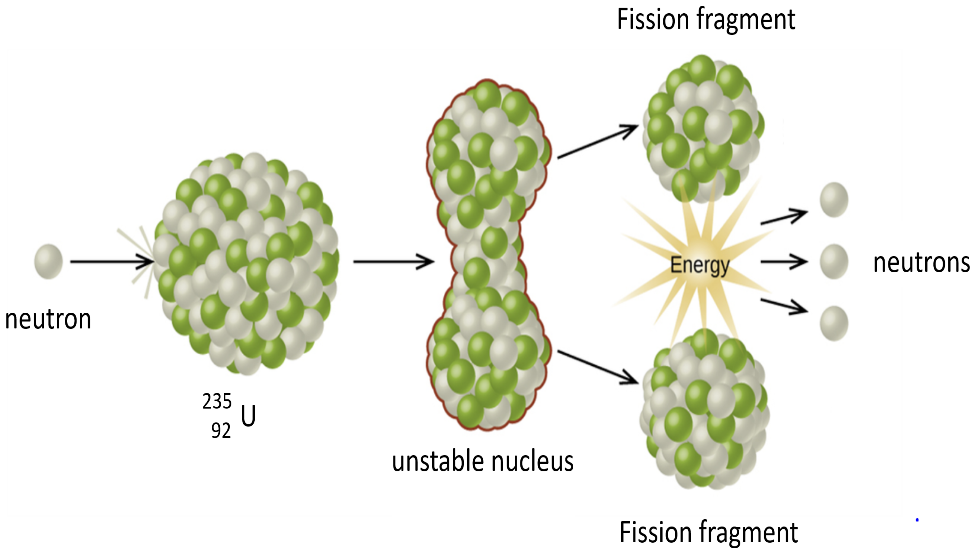

Figure 2.2: Nuclear fission scheme: an uranium atom adsorbs a neutron after their collision. The unstable nucleus splits into two, realising neutrons along with thermal energy.

To properly explain how neutrons interact with matter during a scattering experiment, the fundamental concepts of neutron scattering theory should be presented first.

2.1.2 Basics of Neutron Scattering

In this section, the most important concepts of neutron scattering are approached as a tool to understand this study. The basis of the theoretical discussion on neutron scattering and neutron vibrational spectroscopy are references [59, 77–83].

2.1.2.1 The Scattering Cross-Section

Considering a generic scattering experiment where a monochromatized neutron beam of initial energy E_i reaches a sample. After interacting with the sample, the neutron beam has a final energy E_f. Figure 2.3 represents a single neutron scattering event. The quantity measured during this interaction is known as cross-section.

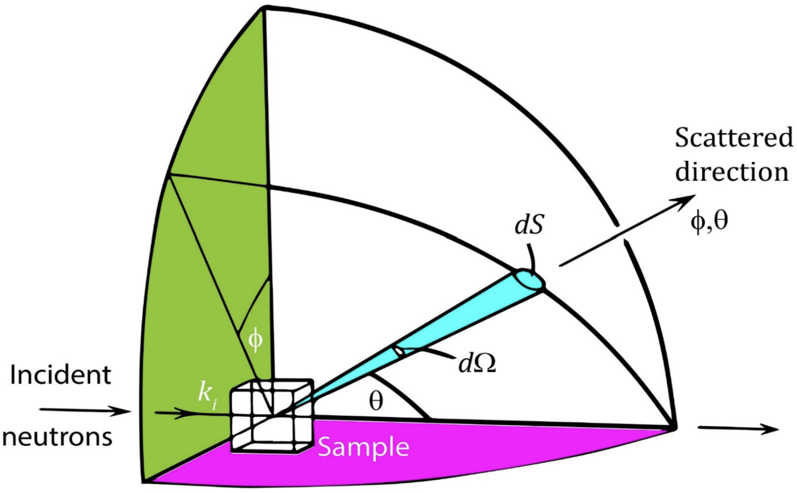

Figure 2.3: Representation of the scattering process. The incident neutrons interacts with a sample and some neutrons are scattered in the direction ϕ, θ, reaching a detector of small area (dS).

In scheme of Figure 2.3, a neutron counter of small surface area dS measures the number of neutrons scattered in the direction θ, ϕ as a function of their energy E_f. The intensity measured by the counter is equal to the partial differential scattering cross-section, given by:

$$I_{counter} = \frac{N}{\phi d\Omega E_f} = \frac{d^2\sigma}{d\Omega dE_f} \tag{2.2}$$

Being N the number of neutrons scattered per second covered by the small solid angle dΩ with final energy between E$_f$ and E$_f$ + dE$_f$ and ϕ is the flux of the incident neutrons.

The partial differential scattering cross-section $\frac{d^2\sigma}{d\Omega dE_f}$ is the flux of neutrons per small solid angle dΩ that interact with a certain energy transfer $\hbar\Omega$ and momentum transfer $\hbar\vec{Q}$. This was, the partial differential cross-sections are the quantities that are measured in the scattering experiment.

2.1.2.2 Scattering from a single fixed nucleus

The topic above, referring to the differential cross-section, focus on the description of scattering data. Now, it is important to understand how the structure of the sample relates to the measured deflections at the atomic level.

Considering a nuclear scattering by a single nucleus fixed in a certain position, the origin is set to be at the position of the nucleus. The wavevector of incident neutrons, k_i, which can be described by the complex plane wave $\Psi_{inc} = \exp(\mathrm{i}k_\mathrm{i}\mathrm{z})$, is travelling in the z direction. After interacting with the atom, the neutrons move radially outwards (Fig. 2.4).

The wave function of the neutrons at the point r can be indicated as: $\Psi_{SC}=\frac{-b}{r}\exp(\mathrm{i}k_\mathrm{i}\mathrm{z})$, where b is a constant known as the scattering length.

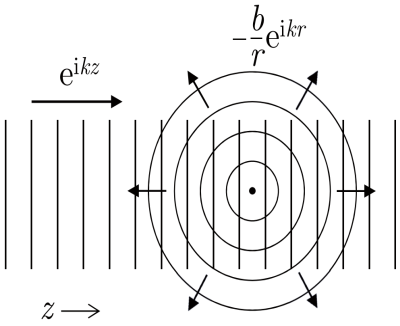

Figure 2.4: Interaction of a neutron plane wave of unit amplitude with a nucleus to produce a spherical scattered wave. Taken from [78].

The magnitude of the scattering length b establishes the strength of the scattering. As mentioned before, b is a characteristic of the nucleus, and varies throughout the periodic table and among isotopes of elements. Its values also depend on the spin state of the neutron–nucleus system.

The total cross-section σ_{tot} (which corresponds to the cross section of the neutrons scattered in all directions and for all energies) is expressed as follows:

$$\sigma_{tot} = \int_0^\infty \int_{alldirections} \left(\frac{d^2\sigma}{d\Omega dE_f}\right) d\Omega dE_f = 4\pi b^2 \tag{2.3}$$

2.1.2.3 Fermi's Golden Rule

The scattering process itself can be described by the Fermi's Golden Rule. In general words, it is a quantum mechanics concept that gives the rate of change between the neutron in the single incoming state and a final state.

The differential cross-section, $\left(\frac{d\sigma}{d\Omega dE_f}\right)_{k_i \rightarrow \lambda_f}$ can be regarded as the sum of all processes in which the state of a scattering system changes from λ_i to λ_f, and the state of the neutron changes from k_i to k_f, as given by the equation:

$$\left(\frac{d\sigma}{d\Omega dE_f}\right)_{\lambda_i \to \lambda_f} = \frac{1}{\phi}\frac{1}{\Omega}\sum_{k_f} W_{k_i,\lambda_i \to k_f,\lambda_f} \tag{2.4}$$

$W_{k_{i},i \to k_f,\lambda_f}$ is the number of transitions per second from the state k_i,λ_i to the state k_f,λ_f, while ϕ indicates the flux of incident neutrons. The fundamental concept of quantum mechanics, known as Fermi's Golden Rule, then plays a role in the equation:

$$\sum_{k_f} W_{k_i,\lambda_i \to k_f,\lambda_f} = \frac{2\pi}{\hbar}\rho_{k_f} |\, \langle k_f \lambda_f | V | k_i \lambda_i \rangle \,|^2 \tag{2.5}$$

Wherein ρ_{k_f} is the number of momentum states in dΩ per unit energy range for neutrons in the state k$_f$. The term between brackets is the probability of a transition from the eigenstate $|k_i\lambda_i\rangle$ to $|k_f\lambda_f\rangle$ submitted to a perturbation. V is understood as the interaction potential and represents the interaction between the neutron and the sample, calculated by the sum over all atoms in the sample.

2.1.2.4 Understanding the double differential cross-section

The double differential cross section $\left(\frac{d^2\sigma}{d\Omega dE_f}\right)$ can be expressed as a function of the exchange of energy and momentum, considering a situation where all the scattered neutrons have the same final energy, as follows:

$$\left(\frac{d^2\sigma}{d\Omega dE_f}\right)_{\lambda_i \to \lambda_f} = \frac{k_f}{k_i}\left(\frac{m}{2\pi\hbar^2}\right) |\langle k_f \lambda_f | V | k_i \lambda_i \rangle|^2 \, \delta\left(E_{\lambda_i} - E_{\lambda_f} + E_i - E_f\right) \tag{2.6}$$

In this expression, E$_{\lambda_i}$ and E$_{\lambda_f}$ are the initial and final energies of the scattering system while the δ-function is a mathematical term Erelated to the energy distribution of the scattered neutrons.

The interaction potential V can now be represented in the form of a function. The nucleus-neutron interaction is a short range force described by the *Fermi pseudopotential.* It is indicated by the equation:

$$V_j(\vec{Q}) = \frac{2\pi\hbar^2}{m} b_j \tag{2.7}$$

$V_j(\vec{Q})$ is the Fourier transform of the Fermi pseudopotential function $V_j(\vec{x_j})$ of the j^{th} nucleus, and b_j is its scattering length.

The Born Approximation implies that the interaction with a scatterer point is independent of the scattering from other scatterers in a system. Applying this assumption and the definition of the pseudopotential $V(\vec{Q})$, the probability of a neutron with a wavevector $\vec{k_i}$ being scattered by a potential $V(\vec{r})$ is represented by:

$$\left| \int e^{i\vec{k_i}\cdot\vec{r}} V(\vec{r}) e^{i\vec{k_f}\cdot\vec{r}} d\vec{r} \right|^2 = \left| \int e^{i\vec{Q}\cdot\vec{r}} V(\vec{r}) d\vec{r} \right|^2 \tag{2.8}$$

This leads to the generalization of equation 2.6 for all the processes and not only for those limited to an initial state λ to another λ'. This way, it is given as:

$$\frac{d^2\sigma}{d\Omega dE_f} = \frac{k_f}{k_i} \frac{1}{2\pi\hbar} \sum_{jj'} b_{j'} b_j \int_{-\infty}^{\infty} \left\langle e^{-iQ\cdot\overrightarrow{R_{j'}}(0)} e^{iQ\cdot\overrightarrow{R_j}(t)} \right\rangle \times e^{-i\omega t} dt \tag{2.9}$$

Here, the nucleus labelled j is at position $\vec{R_j}(t)$ at time t and nucleus labelled j' is at position $\vec{R_{j'}}(0)$ at time 0. $\vec{R_j}$ is a time-dependent Heisenberg operator containing H, the Hamiltonian of the scattering system. It is this very equation (eq.2.9) that links the measurements and the information on the studied system. In other words, there is a correlation between the measured cross-section $\left(\frac{d^2\sigma}{d\Omega dE_f}\right)$ to the Heisenberg operators that contain Hamiltonians, which finally hold the properties of the scattering system as function of $\vec{Q}$ and ω. $\vec{Q}$ and ω are known quantities derived from the conservation laws (to be better explained later), i.e. $\hbar\omega = E_i - E_f$ and $\vec{Q} = \vec{k_i} - \vec{k_f}$.

2.1.2.5 Coherent and Incoherent scattering

In neutron scattering it is important to address the distinction between two concepts: coherent and incoherent scattering. Taking a scattering system consisting of a single element where the scattering length b varies from one nucleus to another due to the presence of nuclear isotope or spin, the coherent scattering can be defined as a type of scattering which would be given by the same system if all the scattering lengths were equal to their mean value. By contrast, the incoherent scattering comes from the deviations of the scattering lengths of the actual system from their mean value.

Assuming that the scattering system contains a large number of scattering centers and every possible nuclear isotope and spin orientation exists with the random distribution, we define f_i as the relative frequency with which a value b_i occurs. Thus, the average value of b for such system is $\overline{b} = \sum{}_i f_i b_i$ and the average value of b^2 is $\overline{b^2} = \sum{}_i f_i b_i^2$. The equation 2.9 can, then, be rewritten as:

$$\frac{d^2\sigma}{d\Omega dE_f} = \frac{k_f}{k_i} \frac{1}{2\pi\hbar} \sum_{jj'} \overline{b_{j'} b_j} \int \langle j', j \rangle \, e^{-i\omega t} dt \tag{2.10}$$

being

$$\langle j', j \rangle = \left\langle e^{-i\vec{Q}\cdot\overrightarrow{R_{j'}}(0)} e^{i\vec{Q}\cdot\overrightarrow{R_j}(t)} \right\rangle \tag{2.11}$$

Assuming there is no correlation between the b values of the different nuclei, it follows:

$$\overline{b_{j'}b_j} = (\bar{b})^2 \quad \text{for} \quad j' \neq j$$

$$\overline{b_{j'}b_j} = \overline{b^2} \quad \text{for} \quad j' = j$$

And, therefore:

$$\frac{d^2\sigma}{d\Omega dE_f} = \frac{k_f}{k_i}\frac{1}{2\pi\hbar}(\bar{b})^2 \sum_{j,j'}^{N} \int \langle j', j\rangle \, e^{-i\omega t} dt$$

$$+\frac{k_f}{k_i}\frac{1}{2\pi\hbar}\left\{\overline{b^2} - (\bar{b})^2\right\} \sum_{j}^{N} \int \langle j, j\rangle e^{-i\omega t} dt = \tag{2.12}$$

$$\left(\frac{d^2\sigma}{d\Omega dE_f}\right)_{coh} + \left(\frac{d^2\sigma}{d\Omega dE_f}\right)_{inc} \tag{2.13}$$

It confirms that the cross-section is composed by both coherent and incoherent scattering, where each one of them can be indicated as follows:

$$\left(\frac{d^2\sigma}{d\Omega dE_f}\right)_{coh} = \frac{\sigma_{coh}}{4\pi}\frac{k_f}{k_i}\frac{1}{2\pi\hbar} \sum_{j,j'(j\neq j')}^{N} \int_{-\infty}^{\infty} \left\langle e^{-i\vec{Q}\cdot\overrightarrow{R_{j'}}(0)} e^{i\vec{Q}\cdot\overrightarrow{R_j}(t)} \right\rangle \times e^{-i\omega t} dt \tag{2.14}$$

$$\left(\frac{d^2\sigma}{d\Omega dE_f}\right)_{inc} = \frac{\sigma_{inc}}{4\pi}\frac{k_f}{k_i}\frac{1}{2\pi\hbar} \sum_{j,j'(j=j')}^{N} \int_{-\infty}^{\infty} \left\langle e^{-i\vec{Q}\cdot\overrightarrow{R_j}(0)} e^{i\vec{Q}\cdot\overrightarrow{R_j}(t)} \right\rangle \times e^{-i\omega t} dt \tag{2.15}$$

In these expressions, $\sigma_{coh} = 4\pi(\bar{b})^2$ and $\sigma_{inc} = 4\pi(\overline{b^2} - (\bar{b})^2)$.

Equation 2.14 reveals that the coherent scattering involves correlations between the position of the same atom at different times and, mainly, between different atoms at different times. The scattered waves from the different atoms interfere with each other, providing information about diffraction and coherent movements.

Equation 2.15 indicates that the incoherent scattering only involves the correlation between the positions of the same atom at different times. The scattered waves from different atoms does not interfere. This type of scattering provides information about self-correlation processes, e.g. diffusion.

Table 2.1 displays a few values of σ_{coh} and σ_{inc} for nuclei present in the materials analysed in this thesis. Hydrogen nucleus displays the largest scattering cross-section of the periodic table, with 82 barns. It is mainly an incoherent scattered (σ_{inc} H = 80.2 barns compared to σ_{coh} H = 1.8 barns), justifying the high sensitivity of this nucleus to neutron techniques.

Element	σ_{coh}	σ_{inc}	σ_{tot}
H	1.756	80.260	82.020
C	5.551	0.001	5.552
Si	2.163	0.004	2.167
Al	1.495	0.008	1.503
O	4.232	0.000	4.232
Ag	2.181	0.325	2.505

Table 2.1: Scattering cross sections of a few elements. Taken from [84]). Values given in barns.

2.1.2.6 Correlation Functions

Correlation functions play a significant role in neutron scattering, serving as essential tools for computing diverse properties within the scattering system. Additionally, they offer a deeper understanding of the physical implications associated with terms present in the scattering cross-section. The following formulas are expressed only for incoherent scattering for simplification (although the same process can be applied for coherent scattering as well).

From the correlation function in the real space, several neutron scattering functions can be derived. They are all linked by Fourier transforms and reverse Fourier transforms. In this context, the intermediate function, $I_{inc}(\vec{Q},t)$, should be acknowledged. It is the Fourier transform in space of the Van Hove function $G(\vec{r},t)$, which is the probability of a particle at the initial time t = 0 to find another particle at the position $\vec{r}$ at the time t, knowing the initial position $\vec{r}$. The intermediate function is expressed as:

$$I_{\text{inc}}\,(\vec{Q},t) = \frac{1}{N}\sum_j \left\langle e^{-i\vec{Q}\cdot\vec{R_j}(0)} e^{i\vec{Q}\cdot\vec{R_j}(t)} \right\rangle \tag{2.16}$$

By taking the Fourier transform in space and time of $G(\vec{r},t)$, the **incoherent scattering function** $S_{inc}(\vec{Q},\omega)$ is defined:

$$S_{inc}(\vec{Q},\omega) = \frac{1}{2\pi\hbar}\int_{-\infty}^{\infty} I_{inc}(\vec{Q},t)e^{-i\omega t}dt \tag{2.17}$$

Placing the scattering function in Equations 2.14 and 2.15 gives:

$$\left(\frac{d^2\sigma}{d\Omega dE_f}\right)_{coh} = \frac{\sigma_{coh}}{4\pi}\frac{k_f}{k_i}NS_{coh}(\vec{Q},\omega) \tag{2.18}$$

$$\left(\frac{d^2\sigma}{d\Omega dE_f}\right)_{inc} = \frac{\sigma_{inc}}{4\pi}\frac{k_f}{k_i}NS_{inc}(\vec{Q},\omega) \tag{2.19}$$

The total dynamical structure factor comprehends the coherent and incoherent scattering functions, being expressed by:

$$S_{\text{tot}}\,(\vec{Q},\omega) = S_{coh}(\vec{Q},\omega) + S_{inc}(\vec{Q},\omega) \tag{2.20}$$

2.1.2.7 Energy and Momentum conservation laws

Figure 2.5) illustrates the scattering triangles, representing a scattering process. The magnitude and direction of momentum transfer vector $\vec{Q}$ is defined by the magnitudes of the incident and scattered neutron wave vectors and the angle 2θ (or scattering angle) by which the incident neutron is scattered throughout the scattering event. In other words, $\vec{Q}$ is the vector difference between the scattered vector $\vec{k_f}$ and the initial one $\vec{k_i}$: $\vec{Q} = \vec{k_f} - \vec{k_i}$. The energy gain or loss is given by $\Delta E = \hbar\omega = E_f - E_i$. In a scattering process between particles, the total momentum and energy are conserved.

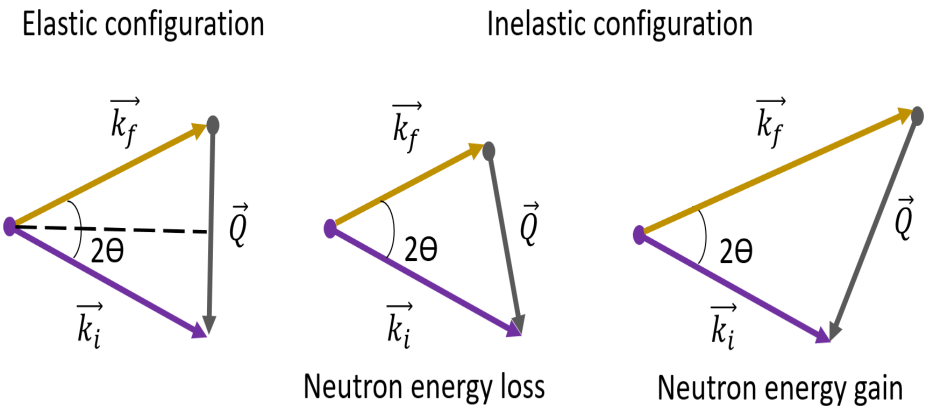

Figure 2.5: Scattering triangles illustrating the scattering process and possible outcomes after interacting of a sample: elastic interaction or inelastic interaction (with gain or loss of energy by the neutron).

The modulus of $\vec{Q}$ can be calculated by cosine rule:

$$|\vec{Q}|^2 = |\vec{k_i}|^2 + |\vec{k_f}|^2 - 2cos|\vec{k_i}||\vec{k_f}| \tag{2.21}$$

After the collision of particles, a few different outcomes can be observed.

- $E_f = E_i$ and $|\vec{k_f}| = |\vec{k_i}|$: there is no change in the neutron energy; the scattering is **elastic**.
- $E_f \neq E_i$ and $|\vec{k_f}| \neq |\vec{k_i}|$: there is loss or gain in the neutron energy; the scattering is **inelastic**.
- $E_f \approx E_i$ and $|\vec{k_f}| \approx |\vec{k_i}|$: there is a broadening of the elastic line; the scattering is **quasielastic**.

The different scattering regimes with exchange of energy (inelastic and quasielastic) do not probe the same molecular phenomena, as each one can only be accessible within a specific framework of energy, time and length (Fig. 2.6), i.e. within a specific $S(\vec{Q},\omega)$ space. Therefore, the objective of neutron scattering measurements is to obtain the scattering function $S(\vec{Q},\omega)$.

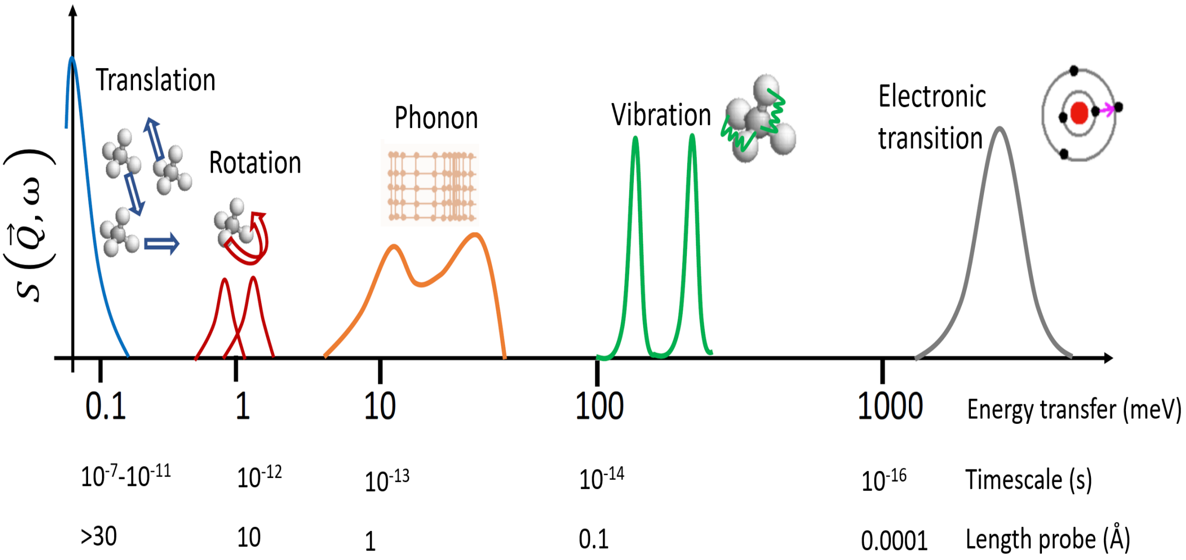
$S(\vec{Q},\omega)$
Translation
Rotation
Phonon
Vibration
Electronic transition
0.1
1
10
100
1000
Energy transfer (meV)
10^{-7}-10^{-11}
10^{-12}
10^{-13}
10^{-14}
10^{-16}
Timescale (s)
>30
10
1
0.1
0.0001
Length probe (Å)

Figure 2.6: Different molecular motions accessible according to energy transfer, time and length ranges. Adapted from [85].

In neutron scattering, the kinematic range refers to the range of momentum and energy transfers that can be probed in an experiment setup. **This setup includes the energy of the incident neutron beam (if it is hot, thermal or cold neutrons), the geometry of the instrument (direct or indirect, to be explained in section 2.1.3.1), the scattering angles allowed by the instrument geometry and the angular coverage of the detectors**. A suitable instrument should have a kinematic range that matches the $S(\vec{Q}, \omega)$ space of a phenomenon to be investigated.

Figure 2.7 illustrates the typical energy, time and $\vec{Q}$ ranges associated with instruments installed at ILL guides according to the spectrometer technique. For example, it shows that the indirect geometry spectrometer IN1-Lagrange probes energy transfer in the order of 0 meV to 1 eV, compatible with the energy scale of vibrational motions. On the other hand, direct geometry Time-of-Flight (ToF) based spectrometers may probe time scales on the order of 10 femtoseconds to hundreds of picoseconds, a window that allows the observation of the elastic peak broadening caused by molecules diffusing over a time scale ranging from 10 ns to 1 ps.

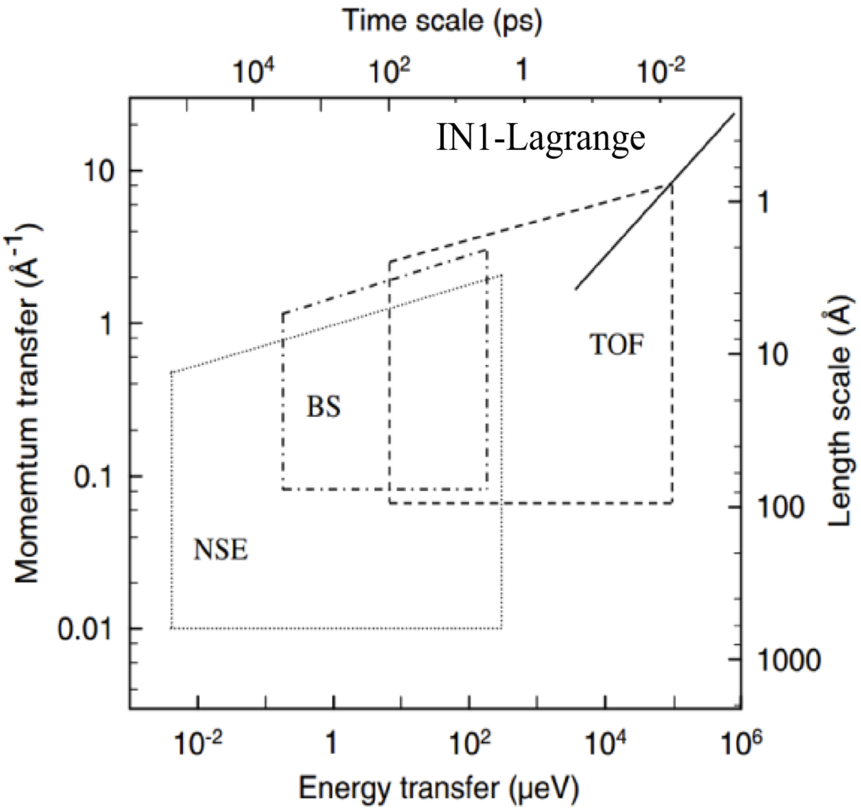

Figure 2.7: Time, length, energy and momentum transfer ranges available for different spectrometers at ILL: IN1-Lagrange, Time-of-Flight (TOF) based spectrometers, Backscattering (BS) based spectrometers and Neutron Spin Echo (NSE) based spectrometers. Adapted from [66].

The kinematic range of the Inelastic and Quasielastic Neutron Scattering instruments used in this thesis will be explained in the following sections, as well as how to interpret $S(\vec{Q},\omega)$ information obtained from each.

2.1.3 *Inelastic Neutron Scattering*

2.1.3.1 *Geometry and kinematic range of INS instruments*

In Inelastic neutron scattering (INS) we investigate the atomic dynamics of a system, that is of a sample. As explained in subsection 2.1.2.6, this information is contained in the scattering function $S(\vec{Q},\omega)$, which should be measured during the experiment. To achieve this, the kinematic range (the range of momentum and energy transfer) reached by the instrument used in such experiment has to be compatible.

The relationship between $\vec{Q}$ and ω is drawn from the conservation laws for the momentum and energy transfer and is represented by the scattering triangle for an inelastic configuration (seen in Fig. 2.5). From equations 2.1 and 2.21, the equation of kinematic range is obtained:

$$\frac{\hbar^2\vec{Q}^2}{2m} = E_i + E_f - 2(E_iE_f)^{1/2}cos(2\theta) \tag{2.22}$$

INS spectrometers may be divided into two classes: direct geometry spectrometers and Indirect (or inverted) geometry spectrometers.

In direct geometry spectrometers, the incident energy, $\mathrm{E_i}$, is fixed. This way, the energy transfer is computed by changing the final energy, $\mathrm{E_f}$. $\mathrm{E_f}$ can be eliminated from equation 2.22, giving:

$$\frac{\hbar^2\vec{Q}^2}{2m} = 2E_i - \hbar\omega - 2[E_i(E_i - \hbar\omega)]^{1/2}cos(2\theta) \tag{2.23}$$

Generically, if the incident energy is kept fixed while the scattering angle varies, different values for the pair $\vec{Q}$, ω are obtained, creating a defined $S(\vec{Q},\omega)$ space, as shown in Figure 2.8A.

In indirect geometry spectrometers, the final energy, $\mathrm{E_f}$, is fixed. The energy transfer is computed by changing the incident energy, $\mathrm{E_i}$. $\mathrm{E_i}$ can be eliminated from equation 2.22, giving:

$$\frac{\hbar^2\vec{Q}^2}{2m} = 2E_f + \hbar\omega + 2[E_f(E_f + \hbar\omega)]^{1/2}cos(2\theta) \tag{2.24}$$

For different set of scattering angles, a generic $S(\vec{Q},\omega)$ space is generated, as shown in Figure 2.8B.

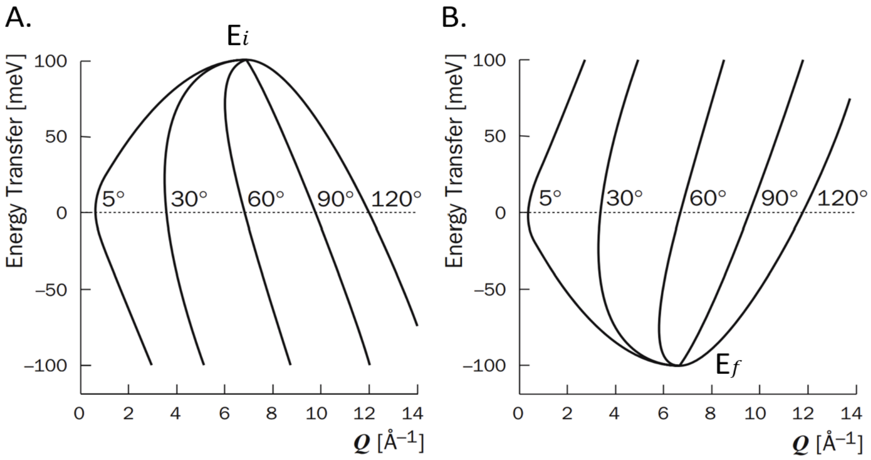

Figure 2.8: Kinematic range of A. Direct spectrometer and B. indirect spectrometer. Taken from [80].

For this thesis, the interest in INS is centered on vibrational spectroscopy. As seen in Figure 2.6, the access to vibrational modes requires hot neutrons (neutron energy of 100 meV– 1eV). Most studies have used indirect geometry instruments for this end. The main reason lies in their easy design, operation, output and good energy resolution at these energies[86]. As it is going to be detailed in the next subsection, this kind of instrument is composed by an incident beam tube, a sample position, a bandpass filter and detectors. As its fixed final energy is small, $\vec{k_f}$ is also small, meaning that for most situations $\vec{k_i} \gg \vec{k_f}$ and consequently $\vec{Q} \approx \vec{k_i}$ (Fig. 2.9). In this case, there is a correlation between energy transfer ($\mathrm{E_T}$) where $E_T \approx 16Q^2$.

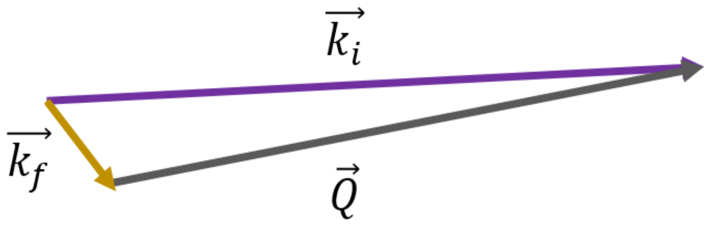

Figure 2.9: Inelastic scattering triangle with the condition $\vec{k_i}$»$\vec{k_f}$.

The peculiar configuration of this hot source indirect spectrometer results in a kinematic range with no Q-dependence (as illustrated in Fig. 2.10). Additionally, considering this geometry, the instrument works at relatively high values of $\vec{Q}$. In practice, this means that the resulting INS spectrum covers the same energy range (0-4000cm $^{-1}$ or 0-500 meV) that Infrared and Raman spectroscopies (Fig 2.11). The hot source indirect spectrometer available at ILL is IN1-Lagrange, which is going to be detailed next, as well as the main advantages in comparison to the other spectroscopic techniques Infrared and Raman.

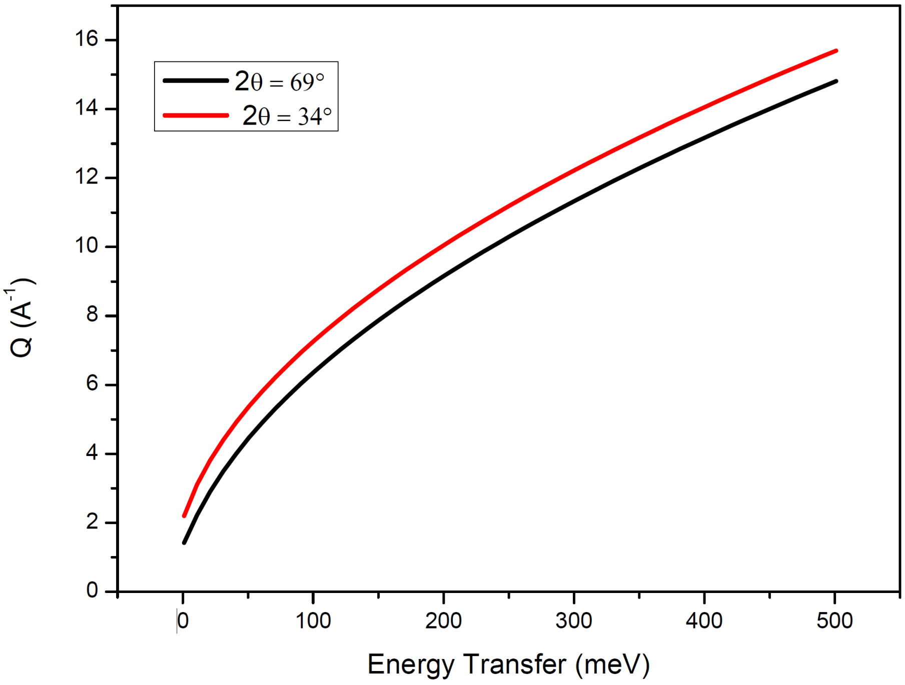

Figure 2.10: Kinematic range reached by the indirect geometry spectrometer (IN1-Lagrange) at final energy E$_f$ = 4.5 meV. Scattering angles from 34-69°, that corresponds to the two extreme values of the scattering angles on IN1-Lagrange.

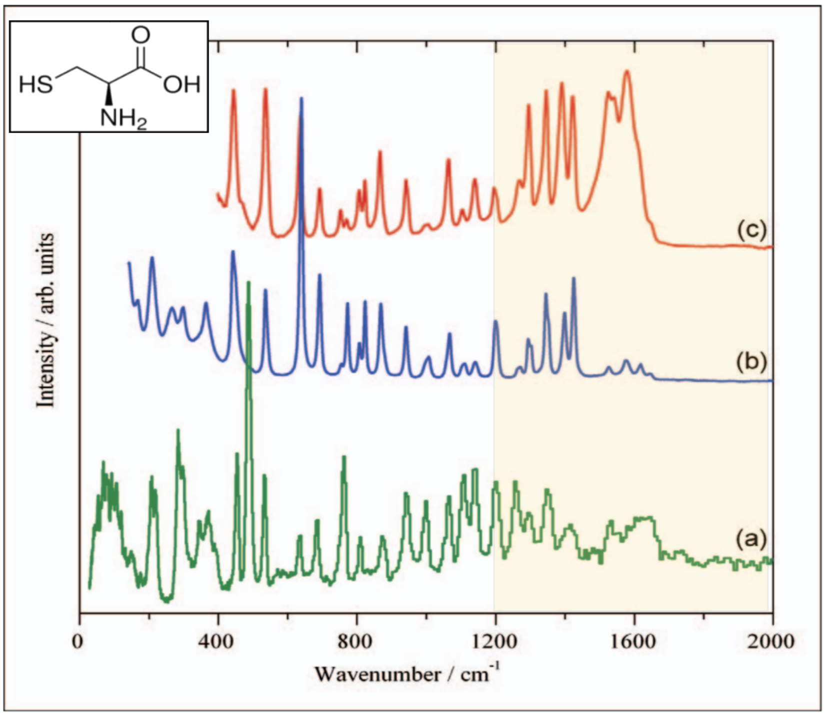

Figure 2.11: Example of vibrational spectra of L-cysteine molecule, where: (a) INS spectrum (measured at hot source indirect spectrometer TOSCA), (b) Raman spectrum and (c) infrared spectrum. The area highlighted in yellow at high energy indicate the decrease in the intensity of INS spectrum compared to the other techniques. Taken from [86].

2.1.3.2 IN1-Lagrange spectrometer

IN1-Lagrange (Large Area Graphite Analyzer for Genuine Excitations)[87, 88], depicted in Fig. 2.12, is an indirect neutron vibrational spectrometer located at the hot source of the Institut Laue-Langevin (ILL), in Grenoble. It covers a broad energy range (0-4000cm $^{-1}$ or 0-500 meV), within which the internal modes of H atoms can be found, and it can be employed in a wide range of different systems, such as zeolites and metallic catalysts, hydrides of metals and intermetallic compounds, nano-crystalline materials and geochemistry matters, to mention a few examples.

Initially, the incident neutron beam is monocromatized by one of the multi-face crystal monochomators (Cu220, Cu331, Si111 and Si311) installed in IN1-Lagrange. The instrument operates in a scanning mode, where both the monochromator and the secondary spectrometer move at each energy step (different values for Ei) on $\theta - 2\theta$ scans. This way, it covers the entire energy range provided by the hot source. After interacting with the sample, the scattered neutrons reach a secondary spectrometer equipped with a beryllium filter that removes scattered neutrons with energies higher than 5.2 meV aiming to avoid high-order harmonics reflections in the analyzer. The analyzer, by its turn, has a fixed final energy of 4.5 meV, which defines that only neutrons with the same final energy are recorded by small single counter (3He detector), with an energy resolution of $\approx 2\%$ E$_i$.

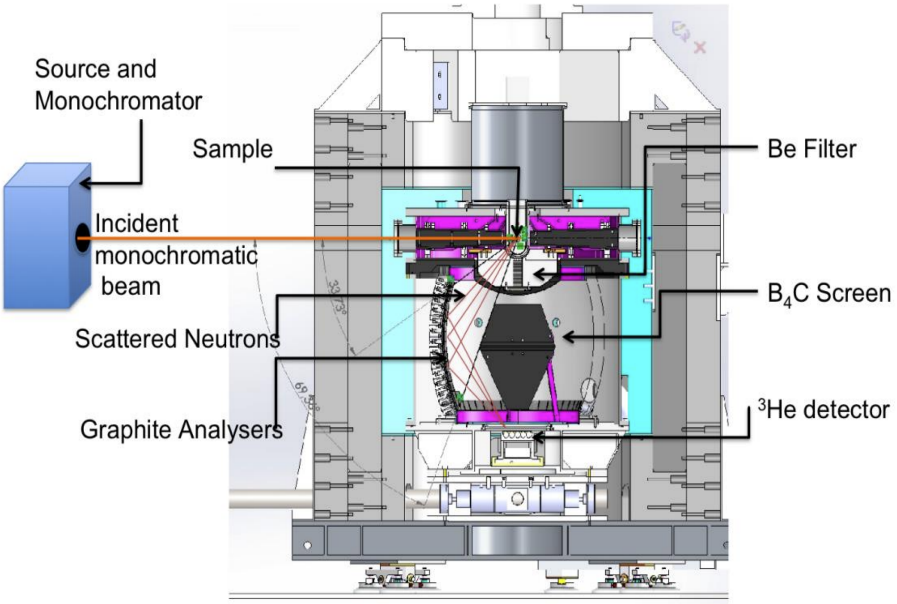

Figure 2.12: Vertical cut layout of IN-1 Lagrange at ILL. Taken from [88].

For this thesis, INS spectra were measured at 10 K in order to decrease the Debye-Waller factor. For all experiments, the incident energy of neutron beam was defined by a Cu(220) monochromator, providing a range of energy transfer from 200 to 1400 cm^{-1} (24-200 meV) with a resolution of $\Delta E/E \approx 2\%$.

The powdered samples containing ethylene were measured in quartz cells (Ag-CHA: 4 C_2H_4/u.c. and mass 235mg / AgCs-RHO: 1 C_2H_4/u.c. and mass 638mg/ HAg-LTA: 1 C_2H_4/u.c. and mass 534.2 mg). Blank Ag-CHA and CsAg-RHO samples as well as empty quartz cells were measured in order to subtract background and scattering from the zeolite framework for data reduction. The data reduction was performed using a code on LAMP.

2.1.3.3 Incoherent Approximation

As detailed previously, IN1-Lagrange is a hot source indirect spectrometer of low fixed final energy. It means that for most cases $\vec{k_i} \gg \vec{k_f}$ and consequently $\vec{Q} \approx \vec{k_i}$ and equally high (as shown by the scattering triangle in Fig. 2.9).

When atoms are static in their equilibrium position, the neutron waves suffer interference phenomena and provide coherent information about a system. However, due to the internal thermal energy of the system, these atoms positions are in fact oscillating nearby their equilibrium point.

With the increasing magnitude of momentum transfer vector $\vec{Q}$, as seen in Figure 2.10, the scattering processes with exchange of energy inevitably also increases at the expense of elastic scattering decreasing. Finally, when the wavelength of the incoming neutron is not larger than the intermolecular distances in the scattering system (i.e. Q >> 2π/d, being d interatomic distances), elastic information is no longer accessible. Therefore, the dynamic response of the scattering system can be calculated simply by treating the scattering as **inelastic and inco-**

herent. This simplifying approach is known as **incoherent approximation** and is taken into account when interpreting IN1-Lagrange measurements, as discussed in the next subsection.

2.1.3.4 The Scattering Law

The INS measurement data is represented by the scattering law, which characterizes all the molecular vibrations taking place in a system under investigation. The scattering law provides the expression for the intensity of an INS mode of vibrating molecules:

$$S\left(Q, n\omega_i\right) \propto \frac{\left(QU_i\right)^{2n}}{n!} \exp\left(-\left(QU_{\mathrm{Tot}}\right)^2\right) \sigma_i \tag{2.25}$$

As already explained, the scattering function $S(\vec{Q}, \omega)$ is the measured intensity and focus on the dynamics of each individual atom in the sample. It depends on two variables: the momentum and energy transfer. U_i stands for an atomic displacement for whichever atom i, while U_{Tot} represents the sum of atomic displacements of all the atoms within the system; σ_i is the incoherent scattering cross-section of atom i.

In general terms, the scattering law describes the relative intensities of each $\mathrm{j^{th}}$ mode established at a momentum transfer Q and energy transfer ω_i for each atom i with corresponding cross section σ_i, being n the excitation state (n=1 for fundamental, n=2 for overtone...).

It is worth to recall that the incoherent scattering cross section of the elements σ_i is both element and isotope dependent. As mentioned in subsection 2.1.1, for H atom this value is 80.2 barns (whereas for most elements it is < 5 barns). Therefore, for this kind of experiment, it is highly probable and expected that the observed modes are those involving motion of hydrogen, which makes INS particularly interesting for probing hydrogenated samples.

Moreover, further information can be extracted from equation 2.25 by analysing the an important term: $(QU_{\mathrm{Tot}})^2$ (exponential).

This exponential term is known as Debye–Waller Factor (DWF). An increase of the DW factor turns the measuring of vibrational spectra quite challenging, therefore it should be avoided by controlling one of its dependable variables, Q or U_{Tot}. U_{Tot} represents the thermal motion of the atoms in the system, thus experiments must occur under temperatures below 30K to scale down this parameter. On the other hand, the momentum transfer value is always high in IN1-Lagrange (Fig. 2.10). It causes a decreasing in the intensities of vibrational bands at high energies, requiring the aid of supporting experimental techniques such as Infrared and Raman or theoretical calculations to overcome this drawback in the interpretation of results. The comparison of the different kind of spectra in Figure 2.11 (subsection 2.1.3.1) well illustrates the effects of DW factor on the high energy range of INS spectrum.

As the Scattering law provides the information about all the vibrational motion of the atoms in the system investigated by neutron experiments, it can as well be explained as a representation of the generalized density of states: $S\left(Q, n\omega_i\right) \propto GDOS$. The GDOS, is defined as the probability of finding an atom in a particular position at a given moment of time. This relation is what allows the comparison between experimental and theoretical data, as further explained in section 2.2.4.1.

In resume, some advantages of using Inelastic Neutron Scattering as a probe for vibrational spectroscopy are:

- **Neutron scattering techniques are not subject to the rules of optical selection**: it means that all vibrations are active and, in principle, measurable. During the scattering process, the neutron transfers momentum to the atom therefore the INS measurements are not limited at the Brillouin zone centre, as are photon techniques, such as Raman and Infrared. Additionally, the measured INS intensities are proportional to both the concentration and the atomic displacement of the scattering atoms in the sample, being specially sensitive to H atoms.

- **Neutron scattering spectra are easily and accurately modelled by computers**: due to the fact that neutron interaction with matter is nuclear, the theoretical spectrum can be easily obtained with the calculated normal modes and expression 2.25.

2.1.4 Quasielastic Neutron Scattering

As mentioned previously in section 2.1.2.7, different kinds of motions can be distinguished when neutrons are used to probe molecular dynamics. Figure 2.5 shows the representation of the scattering function and the molecular motions associated to each range of energy required. At high energies, from $\approx$ 100 meV to 500 meV, it is possible to identify vibrational motions, as seen by Inelastic Neutron Scattering. At $E = 0$, there is no exchange of energy between the incident neutron and molecules, which means that the nuclei are motionless and it is represented by a dirac function centred at $E = 0$. When stochastic (non-periodic) motions consistent with particles moving on the timescales of pico- to nanoseconds are observed, there is a broadening of the elastic line and the regime is called quasielastic scattering.

This subsection, heavily based on references [66, 69–72, 89] focus on the quasielastic scattering, clarifying the relation between the quasielastic broadening and molecular motion. In this technique, the procedure to understand the information acquired is based on the fitting of theoretical diffusion models to the broadenings obtained experimentally. A discussion about how these observables are interpreted by models of diffusion is drawn next.

Recalling equation 2.17, which shows that the $S_{inc}(\vec{Q}, \omega)$ is the Fourrier Transform in time and space of the van Hove correlation function $G(r, t)$, it results that $\vec{Q}$ and ω are, then, Fourrier transformed variables of r and t, where $\vec{Q}$ has the dimension of reciprocal distance and ω, the dimension of angular frequency $(2\pi/t_{seconds})$. Therefore, small $\vec{Q}$ values indicates average values over long distances while slow motions happening throughout long times correspond to small $\Delta\omega$.

The accessible windows to observe a certain type of motion depends on the kinematic range of an instrument (cold,thermal or hot neutrons with different energy range associated), as mentioned previously, but it also depends on the resolution of the chosen spectrometer. If the characteristic time of motion is shorter than the inverse of the instrumental resolution, then a broadening of the scattering function can be observed. When the timescale of the motion is larger than the inverse of the instrumental resolution (i.e. it is slower than the instrument can detect), the shape of the peak is given by the instrumental resolution function. If the observed motion is faster than the instrument can detect, the signal is lost in the background. The representation of quasielastic signal is shown in Figure 2.13.

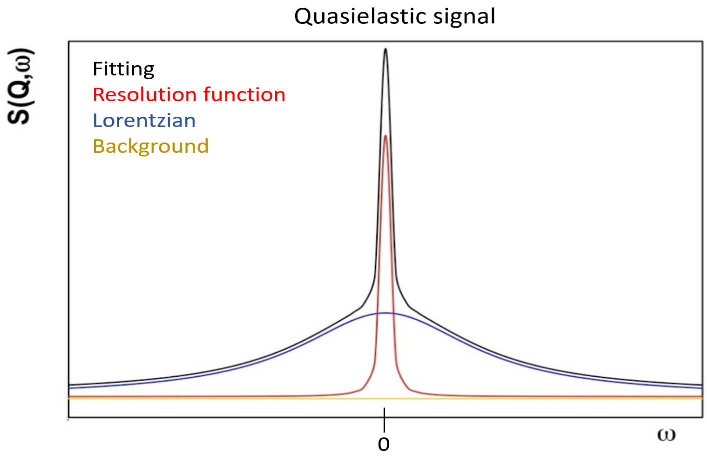

Figure 2.13: Representation of a quasielastic spectrum with components: instrument resolution, lorentzian and background. In black, the representation of a fitting.

The scattering function, therefore, can be represented by the following equation:

$$S(Q,\omega) = \exp\left(-\left(QU_{\mathrm{Tot}}\right)^2\right)\left[A_0(Q)\delta(\omega) + (1 - A_0(Q)\mathcal{L}(Q,\omega)) \circledast R(\omega)\right] + B(Q) \tag{2.26}$$

where, the exponential term is the Debye-Waller Factor; the term $A_0(Q)$ represents the ratio between the elastic and the total intensity from the elastic and quasielastic signal and it is known as Elastic Incoherent Structural Factor (EISF), used to identify the geometry of a motion. $\delta(\omega)$ is a delta function describing the particles that are immobile in the time window probed by the instrument. The term $\mathcal{L}(Q,\omega)$ is the broadening of the elastic line represented by a Lorentzian function. In order to be correctly quantified, the broadening of the scattering function has to be convoluted with the instrumental resolution function $R(\omega)$. $B(Q)$ is the background term including the motions that are too fast for the instrument resolution.

The Lorentzian features will vary as a function of Q (Fig. 2.14). The dependence of the Lorentzian broadening as a function of Q is important because such parameter, known as Half Width at Half Maximum **(HWHM)**, can be fitted to theoretical models in order to provide information about the diffusion behaviour of a molecule.

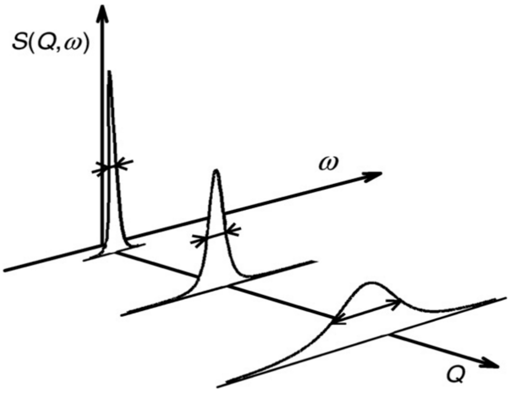

Figure 2.14: Representation of quasielastic broadening as a function of Q: Half Width at Half Maximum (HWHM). Taken from [72].

Such models can refer to free diffusion process similar to liquid systems (the case described by Fickian diffusion) or can also refer to a motion character described as a molecule remaining stationary for a given period on a site before translating very quickly to the next site (jump diffusion), as explained in the following subsections.

2.1.4.1 Fickian Self-Diffusion Coefficients

Fick's second law can describe the motion of a molecule over long enough distances and time. It is indicated by:

$$\frac{\partial p(\vec{r},t)}{\partial t} = D_s \nabla^2 p(\vec{r},t) \tag{2.27}$$

Where $p(\vec{r},t)$ is the probability of finding an atom at position $\vec{r}$ at time t. This equation has as solution the self-part of the van Hove correlation function $G(\vec{r},t)$. Applying a spacial Fourier transform on equation the incoherent scattering function, $S_{inc}(\vec{Q},\omega)$ (2.17), we obtain the following intermediate self-scattering function:

$$I_S(Q,t) = \exp\left(-D_s Q^2 t\right) \tag{2.28}$$

Then, the incoherent scattering $S(\vec{Q},\omega)$ can be obtained by the time Fourier transform of eq. 2.28, showing the incoherent scattering function changes with mobility (self diffusion coefficient D_s) according to:

$$S(Q,\omega) = \frac{1}{\pi}\frac{D_S Q^2}{\omega^2 + (D_S Q^2)} \tag{2.29}$$

which corresponds to a Lorentzian energy profile for isotropic diffusion. As previously mentioned, the scattering functions are measured at different values of Q, revealing the parameter referred to as HWHM. For Fick diffusion, the HWHM of this Lorentzian profile is related to Q according to the expression:

$$\Delta\omega(Q) = D_s Q^2 \tag{2.30}$$

This way, the plot of the HWHM as a function of Q^2 indicates a linear dependance and its gradient is the self-diffusion coeficient D_s (Fig. 2.15).

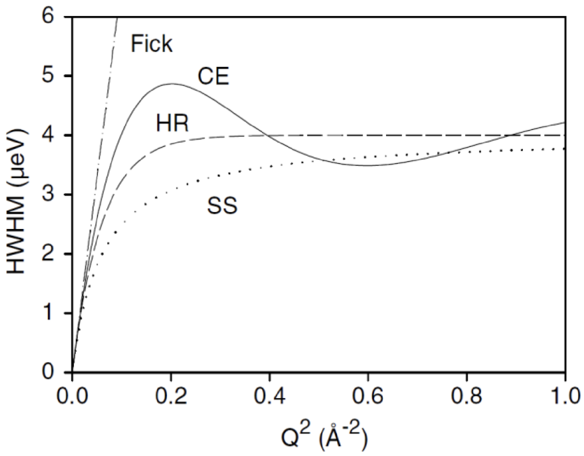

Figure 2.15: Broadenings as function of Q^2 for jump diffusion models: Chudley and Elliot model (CE), Hall and Ross (HR), Singwi and Sjölander (SS) and Fick models. Taken from [70]

2.1.4.2 Jump Diffusion Models

In confined systems, at large Q, the dependance of HWHM with $\vec{Q}$ leaves linear behavior tending towards an asymptotic curve (Fig. 2.15). In this case, the scattering function will be Lorentzian in form, however the width of the energy spectrum will differ from the DQ^2 dependence when higher Q are reached.

In jump diffusion models, it is assumed that between two events leading to diffusion, the particle remains on a given site for a time τ_0, called residence time, which is very long if compared to the jump duration τ. Several jump diffusion models that consider deviations from the continuous diffusion response at large Q are found in literature. Some of the most applied methods are Chudley-Elliot, Hall and Ross and Singwi and Sjölander.

The model of Chudley and Elliot [90] was firstly used to describe liquid systems with local order being now largely applied for systems such as ion diffusion in lattices through to diffusion of sorbates in microporous solids. This model assumes a constant jump length d, with the HWHM dependence on Q ($\Delta\omega$(Q)) represented by:

$$\Delta\omega(Q) = \frac{1}{\tau}\left(1 - \frac{\sin(Qd)}{(Qd)}\right) \tag{2.31}$$

Hall and Ross model [91] (equation 2.32) was originally developed for random jump diffusion with a Gaussian distribution of jump lengths. Singwi and Sjölander model [92] (equation 2.33) was firstly formulated for liquid water with the hypothesis that each molecule oscillates for a mean time before going through continuous linear motion. Both models assume a jump length distribution around a mean square jump length $\langle l^2 \rangle$ and have also been used to describe diffusion of sorbates in zeolites, as the example of acetylene [93].

$$\Delta\omega(Q) = \frac{1}{\tau}\left[1 - \exp\left(-\frac{Q^2\left\langle l^2\right\rangle}{6}\right)\right] \tag{2.32}$$

$$\Delta\omega(Q) = \frac{1}{\tau}\left[1 - \left(\frac{\exp(-2W)}{1 + DQ^2\tau}\right)\right] \tag{2.33}$$

Where $2W = DQ^2\tau\frac{\langle R^2\rangle}{\langle l^2\rangle}$, $\langle R^2\rangle$ is the mean square radius of the thermal cloud developed during oscillatory motion.

The Q dependencies of the broadenings associated with these models are illustrated in Figure 2.15, including the Q^2 dependence related to Fickian diffusion for a given diffusion coefficient. It is shown that at small Q values, the Q dependence is compatible with that of Fickian diffusion behaviour for all jump models.

2.1.4.3 IN5 Spectrometer

IN5 (Fig. 2.16) is a cold neutron direct Time-of-flight spectrometer largely used for measurements in the small energy and momentum transfer region with values of approximately 1 % E_i for the energy resolution. For instance, it can measure: quasi-elastic scattering in solids, liquids, molecular crystals and inelastic scattering with small energy transfers in the range 10 µeV - 100 meV.

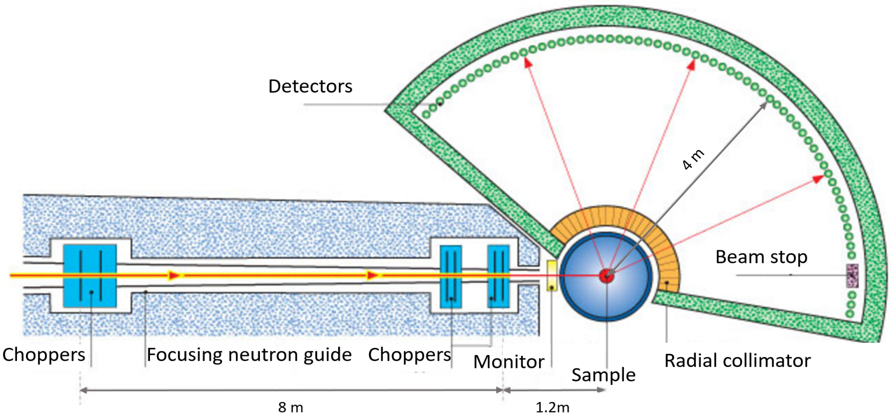

Figure 2.16: Schematics of the cold-neutron multi-chopper spectrometer IN5 at the ILL. Taken from[94].

This Time-of-flight spectrometer allow the simultaneous recording of scattered neutrons over a large $\vec{Q}$ and ω range. Its kinematic range, calculated from equation 2.23, is represented in Figure 2.17 for an initial energy E_i set at 3.55 meV ($\lambda = 5$ Å), as an example.

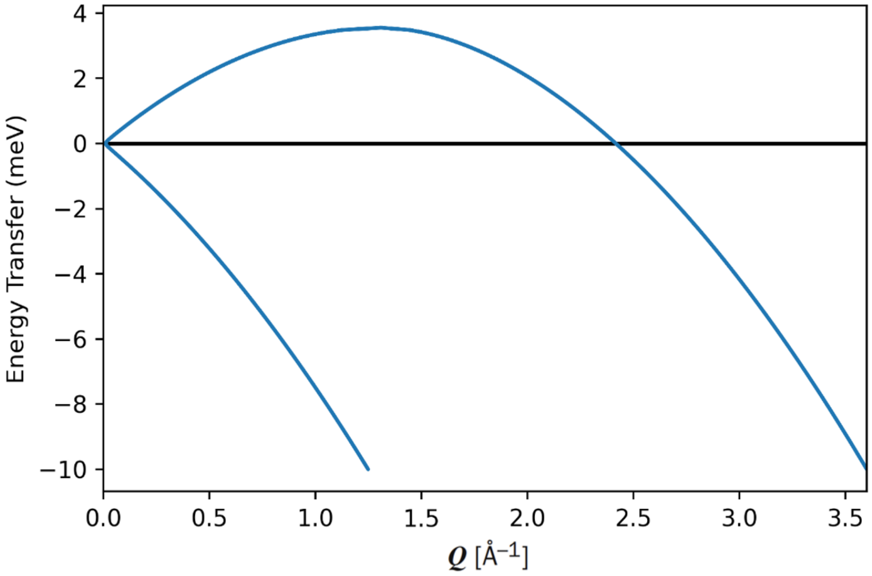

Figure 2.17: Kinematic Range of the direct geometry IN5 spectrometer, considering an initial energy fixed at 3.55 meV or λ = 5 Å.

First, the continuous white neutron flux from the neutron is turned into a pulsed monochromatic beam by a set of 6 choppers. Then, the monochromatic neutron bursts are scattered by the sample. The scattered neutrons are collected by detectors array of 30 m^2. The time-of-flight analysis of incoming neutrons from each monochromatic burst gives a three dimensional spectrum of x, y (detector position), t (time). The final energy is considered in terms of kinetic energy: it is based on the time it takes for the neutron to reach the detectors after interacting with the sample. These parameters, then, allows to access the dynamic structure factor, $S(\vec{Q},\omega)$.

Neglecting other geometrical effects, the energy, time and wavelength resolutions of IN5 are correlated as follows:

$$\frac{\Delta E}{E} = \frac{2\Delta\tau}{\tau} = \frac{2\Delta\lambda}{\lambda}$$

where $\Delta\tau$ is the time resolution of the detector, and τ is the TOF of the neutron.

In order to get a better resolution in time and energy, the usual way is to reduce the uncertainty on λ by narrowing the slits of the choppers at the expense of neutron flux.

For the experiments described in this thesis, all samples were measured at IN5 using an incident neutron wavelength of 5 Å, resulting in an elastic energy resolution of $\approx$ 100 μeV. With this setting, the accessible momentum transfer range was from of 0.4-2 Å^{-1}., and the energy transfer range was +3.0 to -10 meV, covering motions in the order of $\approx$ 1 ps (same kinematic range represented in Fig. 2.16). Samples in 8 mm diameter quartz cell containing $\approx$ 500 mg and 98mbar of ethylene were measured at different temperatures (100, 175 and 235K). The sample transmission of over 90% was calculated with the Beer-Lambert form in a way multiple scattering effects are deemed negligible. Data reduction was performed on Mantid software package.

2.2 Computational Methods

As mentioned previously, one of the many advantages of using neutron scattering as a tool in vibrational spectroscopy is that it can be easily modeled by and compared with computer simulations.

In this work, the aim of the theoretical approach is to calculate the vibration frequencies of the atoms in zeolite samples, based on models that would represent them at the best way possible. A good agreement between experimental and theoretical experimental vibrational spectra validates the theoretical model, allowing a further understanding of systems in microscopic detail and providing information about the host-guest interaction between adsorbed molecule and zeolitic framework.

To determine these vibrational frequencies, a computational technique based on Density Functional Theory was employed. With this method, it is possible to compute the vibrations of a specific atomic arrangement and it is referred to as Lattice Dynamics. In order to further analyse the nature of the biding mechanisms observed in our materials, other two methods based on DFT were carried out: Population Analysis by Mulliken Charges and Electron Density Difference.

The sections related to DFT are based on references [95–97]. While Lattice Dynamics topic and Mulliken Charge Analysis are mostly based on references [98] and references [99–101], respectively.

2.2.1 Principles of DFT

From quantum mechanics theory, it is known that the Ψ wavefunction contains all the information about the quantum state of a system, e.g. energy levels, momentum, and other observable properties. In order to understand the behaviour of quantum particles, it is necessary to determine the corresponding many-body wavefunction Ψ, by solving the Schrödinger equation. If the discussion is restricted to stationary electronic states, only the time-independent version of the Schrödinger equation is considered, $\hat{H}\Psi(\vec{r},t) = E\Psi$, where E represents the total energy of the system in the quantum state specified by the many-body wavefunction Ψ.

Hartree-Fock (HF), a traditional electronic structure calculation method, attempt to obtain approximate solutions to the Schrödinger equation of N interacting electrons moving in an external, electrostatic potential. The main drawback of such method is to consider a proper treatment of electron-electron interactions in species that contain two or more electrons, which leads to inaccuracies in most cases.

The Density Functional Theory rises as a different and largely successful approach. Rather than the many body wave-function, the fundamental variable in DFT is the one-body density, which is intuitively defined as the probability of finding any electron at a position $\vec{r}$. As the density, $\rho = \rho(\vec{r})$, is a function of only three spatial coordinates (instead of the 3N coordinates of the wave-function), DFT can be performed even for large systems. Despite the simplicity of the method, DFT calculations yield most often very accurate results.

The next subsections are dedicated to the Hohenberg-Kohn-Sham formulation, which is the foundation of DFT, followed by a description of the exchange correlation functions.

2.2.2 The Hohenberg-Kohn-Sham formulation of DFT

The first “density functional theory” for electronic systems was given by Thomas (1927) and Fermi (1927, 1928), who described a model for calculating atomic properties based purely on the electron density $\rho(\vec{r})$ and set the general shape of the key ideas of DFT. However, it is the equations of Hohenberg-Kohn theorem (1964) and Kohn-Sham formulation (1965) that are considered as the backbone of the method.

The core concept of density functional theory is the observation that, if E_0 is the lowest possible energy of the system (the energy of the ground state), then E_0 is a functional of the electron density only, $E_0 = E(\rho)$, which reduces the initial problem of the quantum state energy of 3N variables to a three variables one. Therefore, the consequence is that all that is needed for calculating the total energy in the ground state is the electron density. This statement is called Hohenberg-Kohn theorem.

However, the Hohenberg-Kohn theorem does not clarify how to construct the functional of the electron density. Although the exact form of this functional is still unknown, many useful approximations have been developed since the original work of Hohenberg and Kohn.

In the Kohn-Sham (KS) method, there is a replacement of the fully interacting many-body system by an ensemble of virtual particles in a modified potential $V(\vec{r})$ that has the same density ρ as the real electronic system, in a way that the total energy functional $E[\rho]$ is represented by:

$$E[\rho] = T_s[\rho] + V_{ext}[\rho] + E_H[\rho] + E_{xc}[\rho] \tag{2.34}$$

$T_s[\rho]$ is the non-interacting kinetic energy, $V_{ext}[\rho]$ is the external potential, $E_H[\rho]$ is the Hartree energy (representing the classical Coulomb interaction of an interacting charge density $\rho(r)$), and $E_{xc}[\rho]$ is the exchange correlation functional, which holds the correlation part that is not considered in the HF methods. With this decomposition, $T_s[\rho]$ and $E_H[\rho]$ are given by exact expressions, which is very advantageous. The idea is to break down the unknown function of density into the sum of known contributions taken from external potential, kinetic energy and Hartree energy and an unknown contribution, the exchange and correlation energy. If the $E_{xc}[\rho]$ is known, the total energy of the system in its ground state could be calculated using the electron density.

The electron density, by its turn, is obtained calculating the exact ground-state and energy by finding $\rho(vecr)$ in a way that:

$$\frac{\delta E[\rho]}{\delta \rho} = 0 \tag{2.35}$$

considering the condition where:

$$\int \rho(r)dr = N \tag{2.36}$$

Going back to $E_{xc}[\rho]$ term, it is important to mention that it is often divided into two contributions, an exchange term and a correlation term:

$$E_{xc}[\rho] = E_x[\rho] + E_c[\rho] \tag{2.37}$$

Herein, the exchange energy $E_x[\rho]$ of a system of electrons is associated with the Pauli exclusion principle and the correlation energy $E_c[\rho]$ is taking into account the correlated motion of each electron with every other.

However, the functional $E_{xc}[\rho]$ is not known, the problem is to find useful and sufficiently accurate approximations to $E_{xc}[\rho]$. Currently, several approximate functional are available. In the next subsection we are going to approach two classes of these functionals: the local density approximations (LDA) and the generalized gradient approximations (GGA).

2.2.3 DFT Functionals

The Local Density Approximation (LDA) is considered the most basic functional. The principle of this approximation is the assumption that electrons are evenly distributed along a system, i.e. electron distribution is homogeneous. This way, the value of the electron density is constant throughout any point of the considered system. The expression of the exchange correlation energy, then, is written as:

$$E_{xc}^{LDA}[\rho(r)] = \int \varepsilon_{xc}[\rho(r)]\rho(r)dr \tag{2.38}$$

where $\varepsilon_{xc}[\rho(r)] = \varepsilon_x[\rho(r)] + \varepsilon_c[\rho(r)]$.

The values for $\varepsilon_x[\rho(r)]$ and $\varepsilon_c[\rho(r)]$ can be obtained from quantum Monte Carlo calculations. Several simple parameterizations are available for the resultant exchange correlations energy. Due to its basis, LDA is a good approximation for systems with spatially slowly varying densities.

However, as most of the systems investigated nowadays are heterogeneous, the electron density cannot be considered evenly distributed. LDA would not be the best solution in terms of accuracy in these cases. Besides, LDA does not consider van der Waals interactions in a molecular system and poorly represents hydrogen bonding structures. Therefore, functionals considering a different approach for the electron density are necessary.

The Generalized Density Approximation (GGA) emerges as a breakthrough, taking into account the non-homogeneity of real electron density. The exchange correlation energy in GGA is written as:

$$E_{xc}^{GGA}[\rho(r)] = \int f_{GGA}\{\rho(r), \nabla\rho(r)\}dr \tag{2.39}$$

Here, the difference between LDA and GGA is that the function f in GGA gives information about the gradient of the electron density in opposition to the term $\rho(\vec{r})$ of LDA, which is constant.

As in LDA, GGA functionals are also based on a set of fitting parameters. The challenge is to choose an appropriate functional depending on the investigated system. This choice, in general, relies on trial and error and previous experience. One example of exchange-correlation functional is the Perdew, Burke and Erzenhof (PBE)[102]; it is an evolution of the PW91 functional and it is recognized for its general applicability giving accurate results for a wide range of systems in terms of optimized geometries and ground state energies, among other properties. It is the common choice for zeolite materials, for instance.

Along with the PBE functional, dispersion corrections can be used. It is the case of the TS-corrections (Tkatchenko and Scheffer)[103], implemented in 2010, which takes into account van der Waals dispersion interactions. These interactions, by their turn, are essential for accurate predictions of some molecular and materials properties, such as binding energies.

2.2.4 The Lattice Dynamics

Lattice dynamics (LD) consists in the study of the vibrations of the atoms in crystals, with applications in many types of materials. In this thesis, it is used as a method to simulate the vibrational modes of adsorbed ethylene inside of different zeolites containing Ag as acid site. Important information can be extracted by analyzing the vibrational modes of the adsorbed molecule and, therefore, about the interaction between ethylene and the metal transition species itself.

In this subsection, the basic notions about the lattice dynamics for a crystalline system will be given, in order to understand how the LD method allow to obtain vibrational information from a virtual atomic model.

2.2.4.1 The harmonic approximation

In the classic approach of Lattice Dynamics to calculate normal modes of a crystal, one of the most important concepts is the harmonic approximation. Figure 2.18 represents the potential energy curve for two atoms, where the minimum potential energy is reached at the minimum distance between them, r_0, possibly corresponding to their bond length. The normal mode would correspond to a vibrational state in which atoms move in a simple harmonic motion around their equilibrium position.

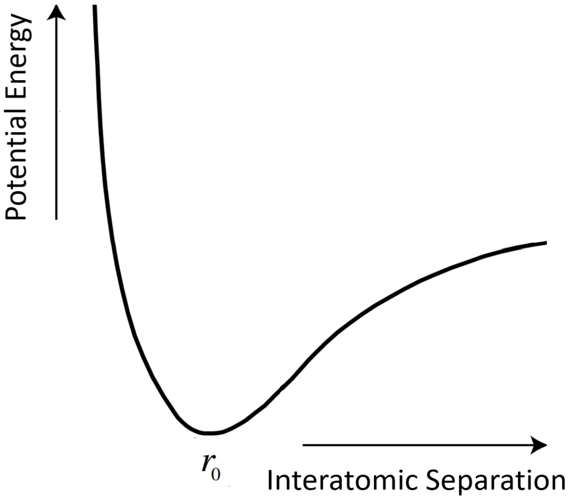

Figure 2.18: Generic potential energy curve for two atoms, representing a minimum at a separation of r_0 that could correspond to the bond length, the steep rise for shorter distances that indicates the repulsion due to overlap of electron density of the two atoms, and the softer rise towards zero for larger separations indicating the attractive interaction. Taken from [98].

The potential energy, then, is represented by a Taylor expansion around the minimum point r_0, as follows:

$$E(r) = E_0 + \frac{1}{2}\frac{\delta^2 E}{\delta r^2}\bigg|_{r_0}(r-r_0)^2 + \frac{1}{3!}\frac{\delta^3 E}{\delta r^3}\bigg|_{r_0}(r-r_0)^3 + \frac{1}{4!}\frac{\delta^4 E}{\delta r^4}\bigg|_{r_0}(r-r_0)^4 + \ldots \tag{2.40}$$

The harmonic approximation itself is the suppression of all the terms whose power is higher than 2.

In a crystalline arrangement of atoms, the total energy E of a lattice is expressed by:

$$E = \frac{1}{4}\sum_{n,n'}\sum_{j,j'}\phi^{j,j'}_{n,n'}\left(u_{j,n} - u_{j'n'}\right)^2 = \frac{1}{2}\sum_{n,n'}\sum_{j,j'} u_{j,n}\Phi^{j,j'}_{n,n'}u_{j'n'} \tag{2.41}$$

Where n and n' represent unit cells and j and j' stand for the atoms in the unit cell; $\phi^{j,j}_{n,n'}$ is the differential of an individual bond energy related to the displacements of the atoms within the bond, while $\Phi^{j,j'}_{n,n'}$ is the differential of the overall energy related to the atomic displacement.

The atomic displacement in the unit cell is expressed in the formula:

$$u_{j,n}(t) = \tilde{u}_j \exp(i(kna - \omega t)) \tag{2.42}$$

Then, the use of Newton's Second Law *(force = mass × acceleration)* , allows to obtain a generalised equation of motion for the system:

$$\omega^2 e_j = \sum_{j',n'}\frac{1}{\sqrt{m_j m_{j'}}}\Phi^{j,j'}_{n,n'}e^{ik(n'-n)a}e_j \tag{2.43}$$

This expression comes from the force acting on each atom, which is given by the derivative of the energy with respect to displacement, and acceleration, given as the second time derivative of the atomic displacement. It can also be expressed in matrix form:

$$\omega^2 \vec{e} = D(\vec{k}) \cdot \vec{e} \Longrightarrow \omega^2 = \vec{e}^T \cdot D(\vec{k}) \cdot \vec{e} \tag{2.44}$$

Being

$$\vec{e} = \begin{pmatrix} \vdots \\ e_j \\ \vdots \end{pmatrix} \tag{2.45}$$

and

$$D_{j,j'}(\vec{k}) = \frac{1}{\sqrt{m_j m_{j'}}} \sum_{n'} \Phi^{j,j'}_{0,n'} e^{i\vec{k}\cdot\left(\vec{r}_{j,0} - \vec{r}_{j',n'}\right)} \tag{2.46}$$

where $D(\vec{k})$ is defined as the dynamical matrix of the system.

The equation of motion, 2.44, is recognized as an eigenvalue/ eigenvector equation. In this case, the values of ω^2 are the eigenvalues of the dynamical matrix $D(\vec{k})$. These eigenvalues are obtained by means of the diagonalisation of the matrix $D(\vec{k})$. The eigenvectors are found to be the elements of matrix e.

This way, the frequencies of the normal modes can be calculated. Gathering the information of energy or frequencies as a sum over all vibrational modes for many possible wavevectors, a histogram can be created where the x-axis represents energy or frequency bins, and the y-axis represents the number of states (or modes) within each bin. Such histogram is named as density of states $g(\omega)$, which is actually the sum of the individual atomic contributions to the vibrational density of states (VDOS), i.e. VDOS=$\sum_i g_i(\omega)$ being i the atomic element.

The theoretical generalized density of states, GDOS$_{th}$, comes from the VDOS, and is represented by: $GDOS_{th} \propto \sum_i \frac{\sigma_i}{m_i} g_i(\omega) e^{-2\Omega_i(Q)}$, where σ_i indicate the experimental individual cross section, m_i is the mass and $\Omega_i(Q)$ is the Debye-Waller factor for the atom i.

As the hydrogen scattering cross section is very large compared to the other atoms of our samples (or models), the individual contributions of any atoms are often considered negligible compared to those of hydrogen in the case of INS measurements, thus the $GDOS_{th}$ can be approximated as $GDOS_{th} \propto g_H(\omega)$, where $g_H(\omega)$ is the hydrogen partial density of states. The GDOS$_{th}$, therefore the $g_H(\omega)$, is extracted from the VDOS via Abins code[104] implemented on Mantid software [105] and can be directly compared to the experimental intensity of the INS spectrum $S(Q, n\omega_i)$ (equation 2.25).

2.2.5 Population Analysis and Electron Density Difference

The analysis of the electron population of each atom of an assembly of atoms is called population analysis. The Mulliken analysis is the most used population analysis method, since it is one of the oldest and simplest.

Assuming a double occupancy of orbitals φ_i, the electronic density ρ can be written as:

$$\rho(\boldsymbol{r}) = 2\left[|\varphi_1(\boldsymbol{r})|^2 + |\varphi_2(\boldsymbol{r})|^2 + \dots \left|\varphi_{\frac{N}{2}}(\boldsymbol{r})\right|^2\right] \tag{2.47}$$

The density distribution ρ is represented by a cloud carrying a charge - Ne. The equation 2.47 means that this cloud is composed by the individual clouds of the molecular orbitals, each one carrying two electrons.

The principle of Linear Combination of Atomic Orbitals (LCAO) approximation assumes that any molecular orbital can be represented by a sum of atomic orbitals. If this assumption is applied in ρ, then ρ becomes a sum of the contributions, each being a product of two atomic orbitals. Going further, ρ can be divided into contributions of particular atoms. The charge corresponding to such contribution could be calculated and the nucleus point charge could be located.

From Eq. 2.47, after using the LCAO expansion $\varphi_i = \sum_r c_{ri}\chi_r$, it follows:

$$N = \int \rho(\boldsymbol{r})\mathrm{d}V = 2\sum_{i=1}^{N/2}\int |\varphi_i(\boldsymbol{r})|^2 \ \mathrm{d}V = \sum_i \sum_{rs} 2c_{ri}^* c_{si} S_{rs} = \sum_{rs} P_{rs}S_{rs} = \mathrm{Tr}(\boldsymbol{PS}) \tag{2.48}$$

Where S_{rs} stand for the overlap integrals between the atomic orbitals r and s, c are the corresponding LCAO coefficients and **P** is known as the charge and bond-order matrix.

$$P_{sr} = \sum_i 2c_{ri}^* c_{si} \tag{2.49}$$

The summation r and s may be carried out with highlighting from which atom A the particular atomic orbital comes (here it is assumed that the atomic orbital are centered on the nuclei). This gives an equivalent formula (A and B denote atoms):

$$N = \sum_A \sum_{r\in A} \sum_B \sum_{s\in B} P_{rs}S_{rs} \tag{2.50}$$

Then, the atomic partitioning can be described as:

$$\begin{gathered} N = \sum_A q_A \\ q_A = \sum_{r\in A}\left(\sum_B \sum_{s\in B} P_{rs}S_{rs}\right) \end{gathered} \tag{2.51}$$

where q is known as Mulliken charge. These charges are often calculated in practical applications and are useful to provide information on how much of the electronic density ρ is concentrated on atom A. Knowing this quantity is valuable because it can be used to analyze intermolecular interactions, such as hydrogen bonding or van der Waals interactions, by examining the distribution of partial charges on atoms involved in the interactions. This helps in understanding the stability and binding energies of molecular complexes or aggregates.

However, the application of partial charges as the only method to describe the spatial distribution of electron density in a molecule is not always a good choice. As such method does not provide information about the topography associated with the charge distribution. In most cases, this distribution can be non-symmetrical. For instance, an atom can carry an overall positive charge while also having considerable areas of negative charge concentration. It would cause attractive interactions with other positively charged atoms even though the partial charge would theoretically predict repulsion.

Therefore, methods based on the electron density for visualising its distribution in three dimensions are quite necessary. Electron Density Difference (EDD) is defined as the difference between an assumed standard or model electron density and the actual observed or DFT computed electron density. In the study of catalysis, electron density difference analysis helps in designing and optimizing catalyst materials. By comparing electron density distributions at the catalyst surface before and after adsorption of reactant molecules, active sites can be identified. The analysis also gives hints about the nature of the bonding between adsorbate and adsorbant.

2.2.6 Computational Protocol

For this thesis, the theoretical Vibrational Density of States, VDOS(ω), was computed based on the direct method of first-principles calculations. All models proposed here (and shown in Chapter 3) were based on 1x1x1 unit cells keeping the same cell parameters of the crystallographic information file (cif) available at the International Zeolite Association website[45].

The calculations were performed on the relaxed structure, at the Γ point, using DMol3 *ab-initio* simulation package in Materials Studio software [106]. The dynamical matrix eigen modes were calculated taking into account the TS (Tkatchenko-Scheffler) method for DFT-D correction. Perdew-Burke-Ernzerhof parametrization of the Generalized Gradient Approximation (PBE-GGA) [102] and double numerical plus-d-function (DND) all atoms basis set were applied for all calculations. Orbital cutoff parameters were set as global, providing a value based on the quality of the output and composition of system. For the calculations described here, these values are 6.1 Å (for RHO structure) and 4.8 Å (for CHA and LTA), consistent with fine geometry optimization calculations. Fine quality convergence tolerances values were set as default for energy, maximum force and displacement ($1.0e^{-5}$ Ha, 0.002 Ha/Å and 0.005 Å, respectively).

The calculated neutron scattering spectra, which is the partial density of states related to hydrogen $g_H()$ in a hydrogenated system, were, then, extracted from the eigenmodes with AbINS software [104] implemented by Mantid [105].

Population analysis generated by Mulliken atomic charges calculation was performed in the energy minimized models, in order to investigate the charge transfer between Ag-zeolites and ethylene molecule. For this calculation, CASTEP package on Materials Studio was required.

Electron density difference (EDD) calculations were performed aiming to understand the binding nature of adsorption in these systems. Molecule and framework were separately defined as two different sets. Norm conserving pseudopotential was used. EDDs were also calculated with CASTEP package.

2.3 Samples Preparation

The samples studied in this thesis have been synthesized at Instituto de Tecnología Química U.P.V.-C.S.I.C. Universidad Politecnica de Valencia (Spain). Here we describe the synthesis of zeolites CHA, RHO and LTA and post synthesis treatments: cation exchange (Na → Ag) and ethylene loading.

2.3.1 *Synthesis of zeolitic materials*

Firstly, the materials are obtained by standard hydrothermal zeolite synthesis. The three zeolites obtained at this stage contained mostly Na as compensating cations. Remaining Cs and H were also found in the case of RHO and LTA zeolites, respectively.

2.3.1.1 Obtaining Na-CHA

Zeolite Na-CHA was synthesized according to the following procedure: 11.5 g of sodium silicate (32.9% SiO_2, 12.21% Na_2O: 54.9 H_2O, Merck), 0.9 g of CBV500 (56% SiO_2: 20% Al_2O_3: 0.15% Na_2O: 23.85% H_2O, Zeolyst), 1.89 g of N,N,N-trimethyl-1-adamantammonium iodide (Structure Directing Agent, SDA) and 0.124 g of NaOH were dissolved in 22.9 g of deionized water, staying under stirring for 2 hours. The final gel, with molar composition SiO_2 : 0.04 Al_2O_3 : 0.09 SDA : 0.34 Na_2O : 25 H_2O, was placed in teflon lined stainless steel autoclaves to crystallize at 135 °C for 7 days without rotation. The solid was recovered by filtration and drying at 100 °C.

2.3.1.2 Obtaining NaCs-RHO

For NaCs-RHO zeolite synthesis, 0.86 g of crown ether 18-C-6 (99% purity, Merck), 0.67 g of $CsOH{\cdot}H_2O$ and 0.29 g of NaOH (ACS reagent, 97.0%, pellets, Merck) were dissolved in 5.76 g of distilled water. Then, 1.43 g of sodium aluminate (58.4% Al_2O_3, 38.7% Na_2O, Carlo Erba) and 11.0 g of colloidal silica (Ludox AS-40, Merck) were added and the resulting mixture was stirred at room temperature for 24 h. The final gel composition was: 1.8 Na_2O : 0.3 Cs_2O : Al_2O_3 : 10 SiO_2 : 0.5 18-Crown-6 : 100 H_2O. Zeolite crystallization was carried out in teflon-lined stainless-steel autoclaves at 125 °C under rotation for 3 days. The solid was recovered by filtration and drying at 100 °C.

2.3.1.3 Obtaining HNa-LTA

The reagents used in the synthesis of LTA zeolite were tetraethylammonium hydroxide (TEA-OH, 35% wt.), diethyl dimethylammonium hydroxide (DEDMA-OH, 20% wt.), aluminium isopropoxide (IPA, 98% wt.), Ludox AS-40 colloidal silica solution (40% wt.), tetramethylammonium chloride (TMA-Cl, 97% wt.) and sodium chloride (NaCl, 99% wt). All of them were provided by Aldrich, excluding sodium chloride from Scharlab.

LTA zeolite with Si/Al ratio of 5 was obtained by hydrothermal synthesis, using Ludox AS-40 as silica source, IPA as aluminium source and TEA-OH, DEDMA-OH and TMA-Cl as organic structure directing agents. 12 g of TEA-OH, 11.4 g of EMA-OH and 1.96 g of IPA. After stirring for 30 minutes at room temperature, 14.20 g of Ludox AS-40 was added and left to go for one hour. This performed solution was ageing for one day at 100 °C in a polypropylene pot. Then, 0.56 g of TMA-Cl, 0.30 g of NaCl and 4 g of distilled water was added under stirring until a homogeneous mixture was obtained.

The final gel, with a molar relation of SiO_2: 0.05 Al_2O_3: 0.30 TEA-OH: 0.20 EMA-OH: 0.05 TMA-Cl: 0.05 NaCl: 17 H_2O, was transferred into a stainless steel autoclave and crystallised at 100 °C for 22 days. The solid obtained was filtered, washed with distilled water, and dried at 100 °C.

2.3.2 Cation Exchange: Na → Ag

Ag-CHA and CsAg-RHO zeolites were obtained by silver exchange of Na-CHA and NaCs-RHO. The occluded organic template was removed upon calcination at 580 °C in both zeolites. Then, an ionic exchange is carried out under stirring conditions during 24h, using a 0.3 M $AgNO_3$ solution, in such a way that the sodium present in the zeolite is exchanged for silver, obtaining Ag-CHA and CsAg-RHO zeolites. The silver exchange was carried out mixing 2.3 g of zeolite a 0.3 M $AgNO_3$ solution (0.64 g $AgNO_3$ dissolve in 11.45 mg of distilled water) under stirring for 24 hours at 25 °C. Then, the zeolites were filtered, washed with distilled water and dried at 100 °C.

For HAg-LTA, the material was calcined in air at 600 °C for 3 hours to eliminate the organic templates. Hence, it was submitted to ion exchange treatment with an $AgNO_3$ solution at room temperature for 24 hours and followed by calcination at 600 °C, in order to obtain about 30% silver exchange.

The XRD patterns of Ag-CHA, CsAg-RHO and HAg-LTA are compatible of the CHA, RHO and LTA-type structures (section A.1 of the Appendix, Fig.A.1). Chemical compositions were determined by scanning electron microscopy with energy dispersive X-ray spectroscopy (EDX-SEM) on a JEOL JSM-6300 scanning electron microscope using a back-scattered electrons (BSE) detector and a beam power of 10 KV. Ag-CHA has Si/Al = 4.9, Na/Al = 0.1 and Ag/Al = 0.54 molar ratios; CsAg-RHO has Si/Al = 4.6, Na/Al = 0.1, Cs/Al = 0.29 and Ag/Al = 0.57; HAg-LTA has Si/Al = 4.9 and Ag/Al = 0.26 molar ratios.

2.3.3 Ethylene loading

The zeolites were degassed at 400 °C overnight under high vacuum conditions ($\approx 10^{-5}$ mbar). Then, $\approx$ 4 molecules of ethylene per unit cell were adsorbed on Ag-CHA ($T_{36}O_{72}$), and $\approx$ 1 molecule of ethylene per unit cell on CsAg-RHO ($T_{48}O_{96}$) and HAg-LTA ($T_{24}O_{48}$) to carry out INS and QENS experiments.

Table 2.2 summarizes the chemical composition of each loaded Ag-zeolite.

Table 2.2: Summarizing table with chemical composition of loaded Ag-zeolites.

Sample	Si/Al	Na/Al	Ag/Al	Cs/Al	H/Al	C2H4/u.c.
C2H4 Ag-CHA	4.9	0.1	0.54	0	≈ 0	≈ 4
C2H4 CsAg-RHO	4.6	0.1	0.57	0.29	0	≈ 1
C2H4 HAg-LTA	4.9	0	0.26	0	0.75	≈ 1

Chapter 3

Evidence, characterization and comparison of π-complex formation upon ethylene adsorption on different Ag-zeolites

This chapter aims to characterize the interaction between ethylene and Ag^+ exchanged zeolites and to prove the development of a mechanism called π-complexation. Herein a multidisciplinary approach was employed, combining Inelastic Neutron Scattering (INS), Infrared (IR) spectroscopy, Nuclear Magnetic Resonance (NMR), UV-vis and Density Functional Theory (DFT) calculations. CHA, RHO and LTA type zeolites were chosen due to their similar small pore sizes and pore volume, but different cavity shapes and framework flexibility. Furthermore, the interpretation of derived DFT Electron Density Difference along with the detailed analysis of a band in INS spectra within the librational region enabled the evaluation of the effects of the different frameworks cages on the aforementioned interaction, in terms of cage geometry and electrostatic field.

As explained previously in section 1.3.1.3, during the π-complexation between ethylene and a metal transition cation, the molecule symmetrically binds to the metal species through metal-carbon bonds with both carbon atoms.

In the π-complexation mechanism of ethylene and silver, the electron charge transfer from the p orbitals of ethylene to the empty 5s orbital of the Ag cation forms a σ bond while simultaneously there is backdonation of charges from the filled $4d^{10}$ orbital of Ag^+ to the antibonding π^* orbital of the adsorbate. The electron charge backdonation from silver to ethylene, $d(Ag^+) \longrightarrow \pi^*$ (C_2H_4) dominates the adsorption mechanism, producing a lengthening of the C=C bonds, a redshift of the stretching vibrations and a high field shift of the ^{13}C NMR signal of ethylene adsorbed on Ag-zeolites or Ag-supported catalyst [62–65]. Theoretical calculations on the adsorption of ethylene on Ag^+ -zeolites points out to a redistribution of charges upon adsorption with a net transfer from the π (ethylene) to the 5s (Ag^+) orbitals [60, 61].

In this work, the identification, characterization and comparison of π-complex formation upon ethylene adsorption on different Ag-zeolites are carried out by a combination of experimental and theoretical techniques. Inelastic Neutron Scattering is employed as the main vibrational spectroscopy technique. It is interpreted with the aid of Density Functional Theory calculations, which also provides microscopic and electronic details of the system.

The correct choice of atomic positions when generating a model along with calculation parameters are crucial in order to satisfactorily describe the properties of such system, e.g. adsorption energies, fundamental frequency vibrations and electronic distribution. **In this work, we considered 4 main steps to conceive each zeolite model as follows**:

- **Identification of silver species and interaction with ethylene in Ag-zeolites samples**

  During the post synthesis thermal treatment of Ag-zeolites samples, the silver species Ag^+ may undergo a process of reduction resulting in the possible formation of silver clusters or nanoparticles. Therefore, before conceiving a model, the state of silver was experimentally identified by means of UV-vis. ^{13} C NMR was carried out in order to provide a better picture of adsorbed ethylene surroundings and confirm its interaction specifically with the silver species instead of with other possible adsorption sites (counter cations) contained in Ag-zeolites samples.

- **Configuration design**

  In this step, simplified configurations for the Ag-zeolites are elaborated. Although the models here described are generated based on UV-Vis results (state of Ag species) and samples composition (type and proportion of compensating cations and sample loading, Table 2.2), their conception should hold a maximum of simplicity in order to facilitate the interpretation of INS results.

- **Placement of compensating cations and adsorbed ethylene**

  The most probable positions for each compensating cation and the relative position between Ag $^+$ and the ethylene molecule in CHA, RHO and LTA frameworks are identified. They are mostly based on information found in literature.

- **Chosen model**

  The best simplified configuration (therefore the adopted model) for each Ag-zeolite in this work is the one that features the best match between theoretical and experimental INS spectra. From this model, it is possible to extract all microscopic information needed in order to deeply understand the π-complex mechanism formation in all systems under investigation.

The next section will cover the identification of silver species in each sample. The following sections are related to the characterization of π-complex in each zeolite, including the conception of the models for the DFT calculations and INS results, culminating with the analysis of the effects of cage topology on the characteristics of the π-complex.

3.1 Identification of silver species and interaction with ethylene in Ag-zeolites samples

The UV-Vis spectra of the hydrated and evacuated (at 400 °C) Ag-CHA, CsAg-RHO and HAg-LTA samples were measured and compared. These results were provided by the ITQ group and are part of another thesis in collaboration with this present work. The UV-vis spectra is found in section A.2, Figures A.2.

The hydrated sample of Ag-CHA and CsAg-RHO display only the presence of dispersed Ag^+ (signals from 190 to 250 nm relative to a transition of Ag^+ from $4d^{10}$ state to $4d^9 5s^1$) coordinated to water molecules and oxygen atoms from the lattice[107, 108].

Upon degassing at 400 °C, small Ag clusters are also formed on Ag-CHA (broad bands centred at about 400 nm), co-existing with Ag^+ species. Based on previous works[109], the peaks referring to the Ag clusters were assigned to Ag_3^+ clusters.

The hydrated and evacuated (at 400 °C) CsAg-RHO samples do not significantly change after evacuation at 400 °C, indicating that silver species remain as dispersed Ag^+.

For HAg-LTA zeolite, the UV-vis spectrum indicate signals between 190 and 225 nm after the degassing treatment at 400 °C and high vacuum conditions, also corresponding to the presence of silver dispersed ions.

^{13}C NMR of ^{13}C-ethylene free (gas phase) and adsorbed on Ag-zeolites were also provided and analysed by the ITQ group in order to confirm that ethylene is in fact interacting with the silver species instead of interacting with other active sites in the samples. All spectra can be found in section A.2, Figure A.3.

The spectrum of ^{13}C-ethylene presents a very narrow signal at $\delta\ ^{13}C = 123$ ppm, which broadens and shifts to high field when it is adsorbed on the Ag-CHA sample. In order to prove that the ethylene molecule is in fact interacting with the silver species in Ag-CHA sample (that contains residual quantities of Na^+ and even minor of H^+), ^{13}C NMR of ethylene adsorbed on H-CHA containing only H^+ and Na-CHA zeolites with only Na^+ as compensating cations were recorded as well (Fig. A.4). It was observed that the ^{13}C NMR signal of ethylene adsorbed on NaCHA is nearly the same than in the gas phase and it is just slightly low field shifted on H-CHA sample. On the other hand, the ^{13}C NMR spectrum of the ^{13}C-ethylene adsorbed on the Ag-CHA sample give a high field signal at $\delta\ ^{13}C = 110$ ppm, similar to previous results found in literature, describing the adsorption of ethylene on Ag/SiO_2 and Ag/Al_2O_3 catalysts.

Therefore, the chemical shift corresponding to $CH_2{=}CH_2$ adsorbed on Ag-CHA sample strongly suggests that ethylene is, in fact, adsorbed on Ag^+ sites even though this sample presents small quantities of Na^+ and H^+. From NRM results, however, more information about a possible adsorption on silver clusters cannot be drawn.

For CsAg-RHO, the spectrum of ^{13}C-ethylene presents a very narrow signal at $\delta\ ^{13}C = 123$ ppm that broadens and shifts to high field (110 pm) when it is adsorbed, as happens to Ag-CHA sample, confirming an interaction with Ag^+ sites. However, the spectrum of ethylene adsorbed on CsAg-RHO displays a second signal at $\delta\ ^{13}C = 115$ ppm, suggesting that ethylene is adsorbed on Ag^+ sites on which the $d \longrightarrow \pi^*$ backdonation from Ag^+ to ethylene occurs to lesser extent.

The ^{13}C-ethylene adsorbed on the HAg-LTA zeolite signal appears at a higher field at $\delta\ ^{13}C = 116$ ppm, also poiting to the interaction between ethylene and Ag^+ cations and the formation of Ag^+-alkene complex where backdonation from Ag^+ to ethylene occurs to lesser extent.

3.2 Evidence and characterization of π-complex in silver containing CHA type zeolite

In this section the formation of the π-complex on silver containing CHA is evidenced and characterized by a combination of INS experiment and DFT calculations, supported by ^{13} C NMR, UV-vis and Infrared spectroscopies results.

3.2.1 Conception of computational model

As seen on section 3.1, upon degassing at 400 °C, C_2H_4 Ag-CHA sample presents two kinds of silver species: Ag^+ and Ag clusters.

This means that the configurations proposed for CHA model should include both types of silver species. However, a model that fully describes the co-existence of two different charged silver species, Ag^+ and Ag_3^+, would require the use of several unit cells, being too large for DFT calculations since it would demand excessive computing resources. This way, two configurations for CHA were generated separately: one simulating the interaction of ethylene with Ag^+ species and with Ag_3^+ clusters on the other.

CHA unit cell can be defined as a hexagonal lattice containing 36 tetrahedral (T) sites and consists of double 6-rings (*d6r*) and *cha* cavities (9.1 x 10.8 ^{2}) interconnected by a three-dimensional pore system with 8-ring windows[110]. Its chemical formula is represented by:

$$M_x^+ Si_{(36-x)} Al_x O_{72}$$

where M^+ is the compensating cation. The cell composition for C_2H_4 Ag^+-CHA configuration (framework) is $3Ag^+Si_{33}Al_3O_{72}$ and for C_2H_4 Ag_3^+-CHA configuration (framework) is $Ag_3^+Si_{35}AlO_{72}$. Each of them is going to be described separately in the following subsections.

3.2.1.1 C_2H_4 Ag^+-CHA configuration

For C_2H_4 Ag^+-CHA configuration, 3 Al atoms and 3 Ag^+ cations was considered (according to the sample chemical composition described in section 2.3, with ≈ 1 C_2H_4/Ag^+. Three extra-framework locations are described for CHA: center of 6-rings (S_2), center of 8-rings (S_3) and center of *d6r*s (S_1)[111, 112], as can be seen on Figure 3.1.

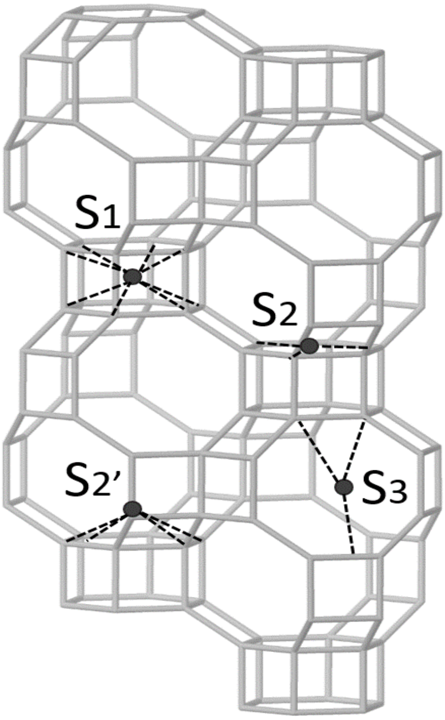

Figure 3.1: Positions for compensating cations identified for CHA framework.

Site S_1 was not considered in the calculations as the fitting of silver species and ethylene both together would not be feasible within this very small cage. As Ag^+ cations in CHA framework can be placed both at S_2 and S_3, quick energy calculations were performed placing a cation in each site and comparing the final values. It was observed that the most stable distribution of 3 Ag^+ was achieved by placing Ag cations at S_2 and S_3 sites, each one in a different *cha* cage (details in section A.3.1). Therefore, Al atoms were arranged in such a way that two are located in 6-rings and one in a 8-ring, all of them far from each other. The unit cell representation for this scheme is found in figure 3.3.

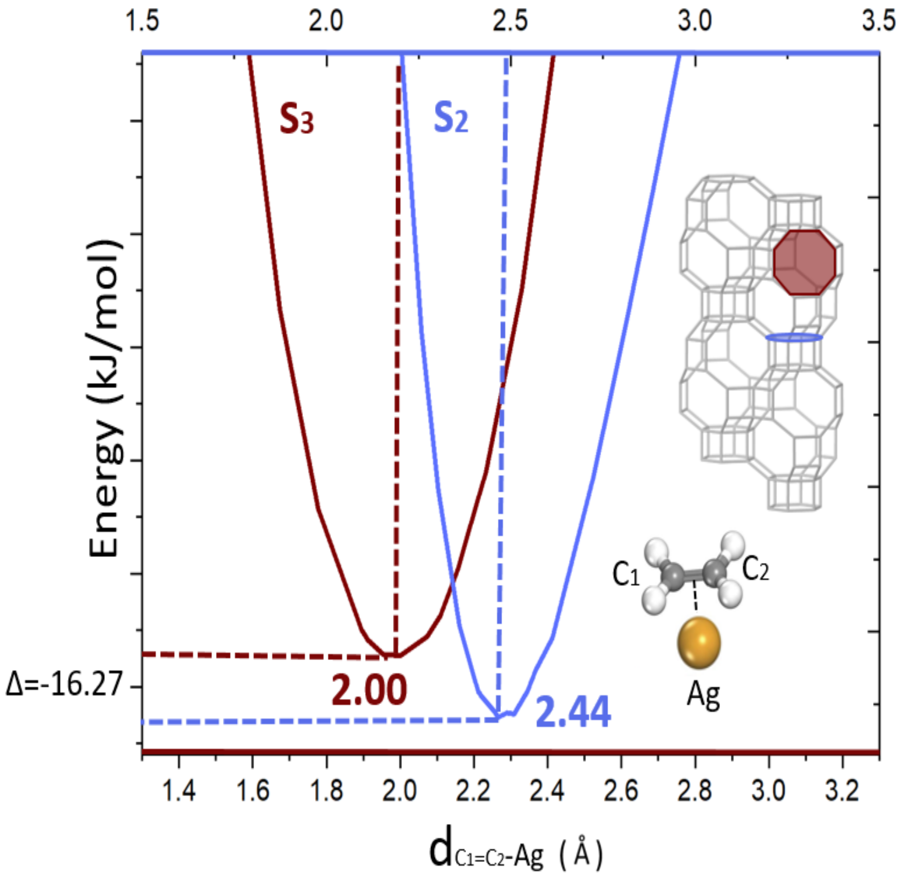

Figure 3.2: Potential Energy Surface plot indicates a deeper minimum energy for the system when ethylene is interacting with silver cation placed at position S_2. Moreover, from this calculations, we also observed that, in position S_2, the equilibrium distance estimated between the x-axis of C double bond from ethylene to Ag cation is 2.44Å.

Then, ethylene molecule was introduced inside the *cha* cage, close to a silver atom at the 6-ring (position S_2), as it presented a stronger C_2H_4 - Ag^+ interaction at this site, as shown by its Potential Energy Surface, PES, in figure 3.2. The hydrocarbon C=C bond axis of ethylene was placed in a way it is oriented parallel to this same 6-ring plane and above Ag (so the distance C-Ag could grow vertically inside the cage), following previous studies [34, 35].

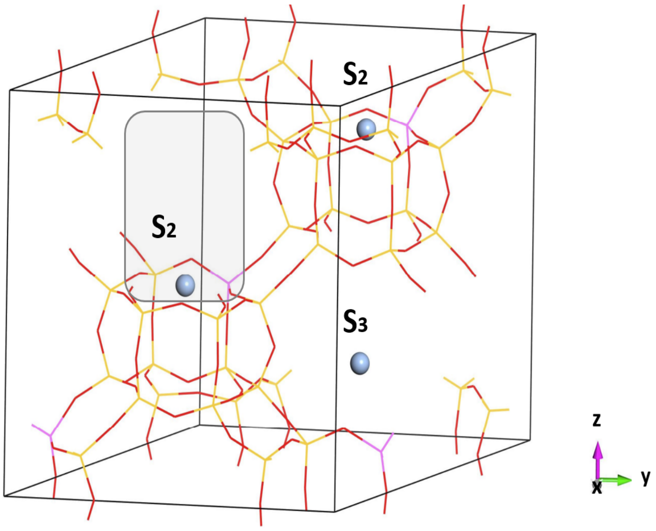

Figure 3.3: Unit cell representing CHA framework with Ag^+ placements. Blue atoms represented by balls are Ag. Framework represented by lines, where yellow is Si atoms, red is O atoms and pink is Al.

3.2.1.2 C_2H_4 Ag_3^+-CHA configuration

A single Ag_3^+ cluster was placed inside the CHA cavity at position S_2, indicated in Figure 3.2. It also contains 1 ethylene/u.c., which is placed in the same distance from Ag species as found for Ag^+-CHA model, as a starting point. Only 1 Al atom is needed in the CHA unit cell to compensate the charge coming from the cluster. A scheme of this configuration is shown in Figure 3.4. This initial position was also based on previous Molecular Dynamics simulations described in the Appendix (Figure A.11).

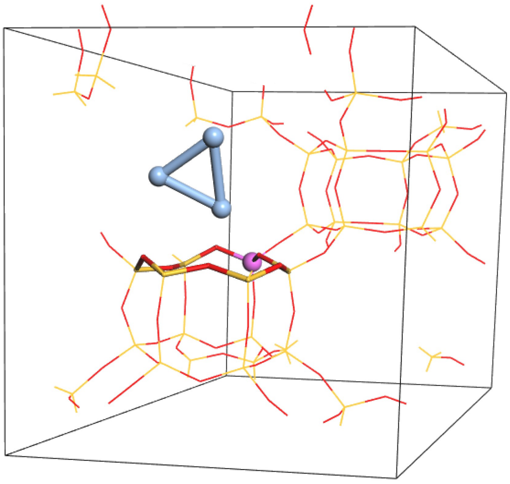

Figure 3.4: Unit cell of CHA representing CHA framework with $Ag_3{}^+$ placements. Blue atoms represented by balls are Ag. Framework represented by lines, where yellow is Si atoms, red is O atoms and pink is Al.

Periodic DFT calculations were performed for each configuration, according to the parameters described in section 2.2.6. After the geometry optimization of the system, its dynamical matrix was defined. As explained in subsection 2.2.4.1, the diagonalisation of the matrix provides the eigenvalues or frequencies of the normal modes and, therefore, the VDOS of the system. Using

Abins code [104] on Mantid software[105], the hydrogen partial density of states, $g_H(\omega)$, is extracted from the VDOS. Then, the calculated spectrum could be compared to the experimental intensity of the INS spectrum $S(Q,\omega)$ of the sample C_2H_4 Ag-CHA.

3.2.2 Comparison between experimental INS and theoretical DFT results

Figure 3.5 shows the comparison of the experimental INS spectrum of Ag-CHA with the calculated neutron spectra for Ag_3^+-CHA and Ag^+-CHA configuration, displaying only fundamental frequencies.

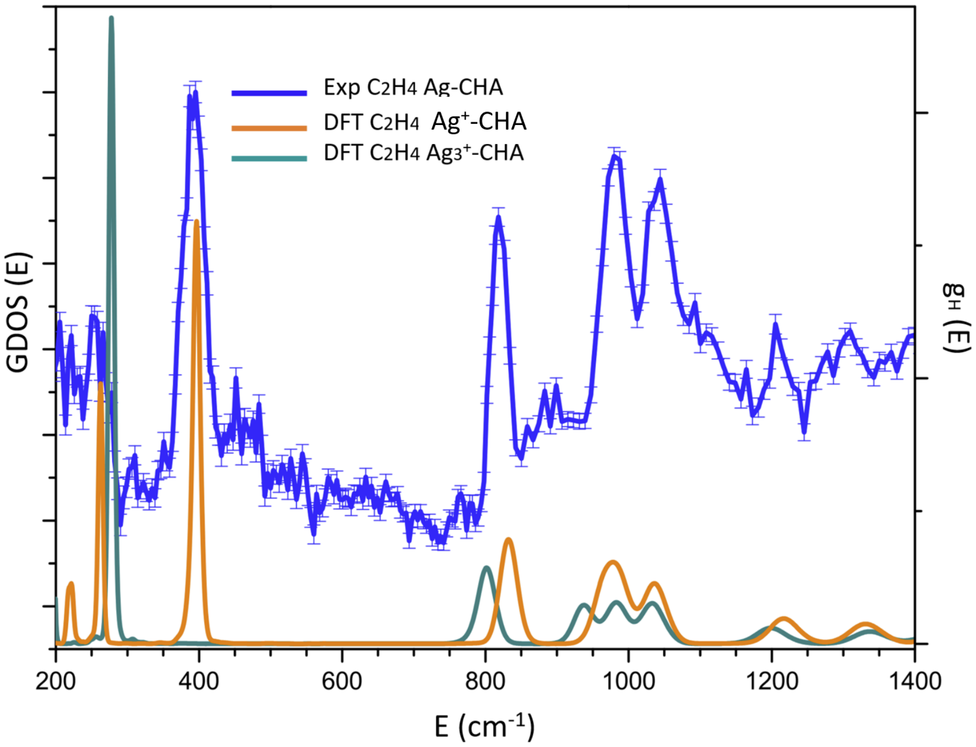

Figure 3.5: Calculated INS for Ag^+-CHA and $Ag_3{}^+$ considering only fundamental frequencies.

A very poor fitting is observed from the comparison between experimental INS spectrum of C_2H_4 Ag-CHA sample and C_2H_4 Ag_3^+-CHA while the calculated spectrum obtained for Ag^+-CHA is in excellent agreement with experimental one. It validates C_2H_4 Ag^+-CHA configuration as it fully describes the system. It means that the information provided by DFT calculations parting from C_2H_4 Ag^+-CHA are reliable. Therefore, the C_2H_4 Ag^+-CHA configuration is referred from now on as **C_2H_4 Ag-CHA**, the final model. This result reinforces the fact that despite the presence of other minor cations in the sample, ethylene interacts with silver species and that the preferred state of this silver species is Ag^+, as no contribution from the clusters in the interaction with ethylene could be clearly identified from INS spectrum.

After the geometry optimization of C_2H_4 Ag-CHA model, the position of Ag^+ cation slightly moves away from its initial position at the center of 6-ring (position S_2), as described in figure 3.3, protruding into the *cha* cage, in the position described as $S_{2'}$, keeping the orientation of hydrocarbon C=C bond axis of ethylene parallel to this same 6-ring plane, in agreement with previous studies [34, 35]. Figure 3.6 describes in detail the resulting C_2H_4 Ag-CHA model, highlighting the *cha* cage containing the ethylene molecule. The complex is located in between two 8-rings and a 6-ring, in a region called 8-ring pocket, which behaves as a reactive center due to the favored energy barrier conferred by the confined environment (to be detailed in section 3.5). Details of the "failed" C_2H_4 Ag_3^+-CHA configuration can be found in section A.3.2.

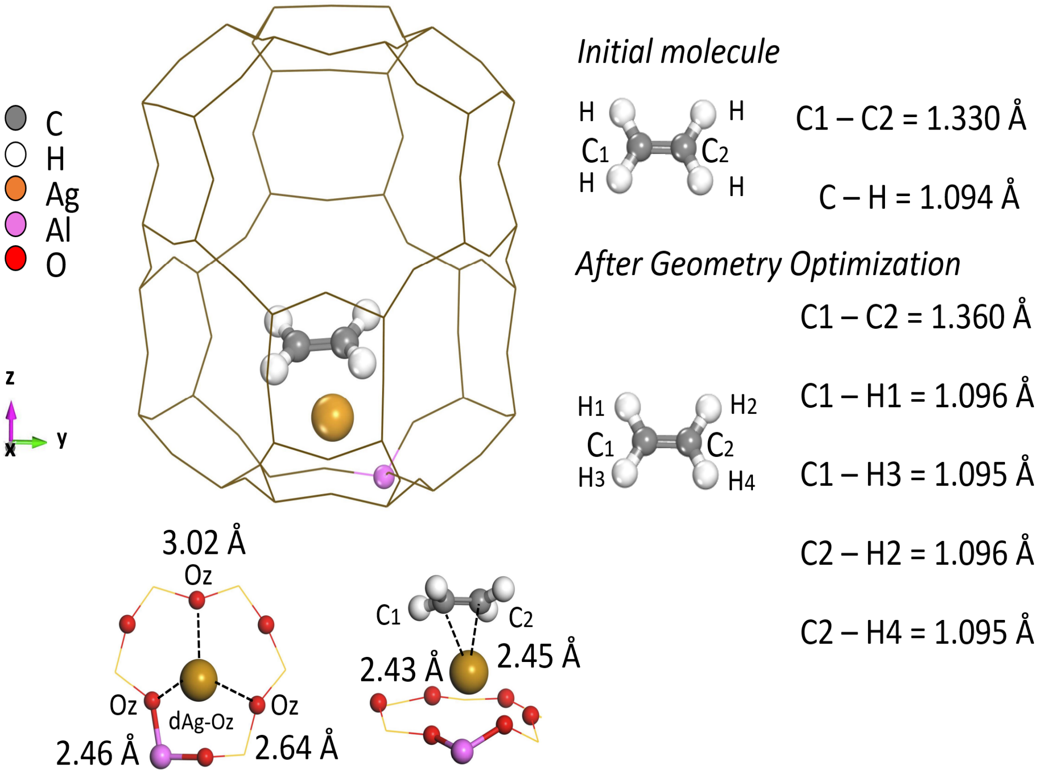
C
H
Ag
Al
O
z
y
x
Initial molecule
H
H
C1
C2
H
H
C1 – C2 = 1.330 Å
C – H = 1.094 Å
After Geometry Optimization
C1 – C2 = 1.360 Å
H1
H2
C1
C2
H3
H4
C1 – H1 = 1.096 Å
C1 – H3 = 1.095 Å
C2 – H2 = 1.096 Å
C2 – H4 = 1.095 Å
3.02 Å
Oz
Oz
Oz
dAg-Oz
2.46 Å
2.64 Å
C1
C2
2.43 Å
2.45 Å

Figure 3.6: Structural details of *cha* cage in the energy minimized C_2H_4 Ag- CHA model. The distances between Ag and the closest framework oxygen atoms, d_{Ag-Oz}, as well as Ag-C, d_{C-Ag} are also shown. C_2H_4 molecule is represented before and after the system energy minimization with its corresponding C-H distances, d_{C-H}. Al, Ag, C and H atoms are highlighted and identified in the figure. O atoms are highlighted in the 6-ring where Ag cation sits, O_z are the 6-ring Oxygen atoms closest to Ag. Si and O atoms of *cha* cage are represented by brownish lines to facilitate Ag-C_2H_4 complex visualization. The complex lies in a region called 8-ring pocket.

Once the C_2H_4 Ag-CHA model was validated, the frequency analysis of the vibrational bands calculated for Ag-CHA model allows us to identify the corresponding vibrational modes, as follows in the next subsection.

3.2.3 Frequency Analysis of the vibrational bands

Figure 3.7 compares the experimental and calculated INS spectra, fundamental and total (fundamental and overtones) frequencies, of C_2H_4 adsorbed on Ag-CHA with that of pure gas. The mode assignments and calculated frequencies for Ag-CHA are presented in Table 3.1. The calculated values described in the table correspond to the fundamental peaks of C_2H_4 Ag-CHA model. Each ethylene vibrational mode is illustrated on Figure 3.8. For reference, assignment of peaks for pure ethylene is in section A.4.

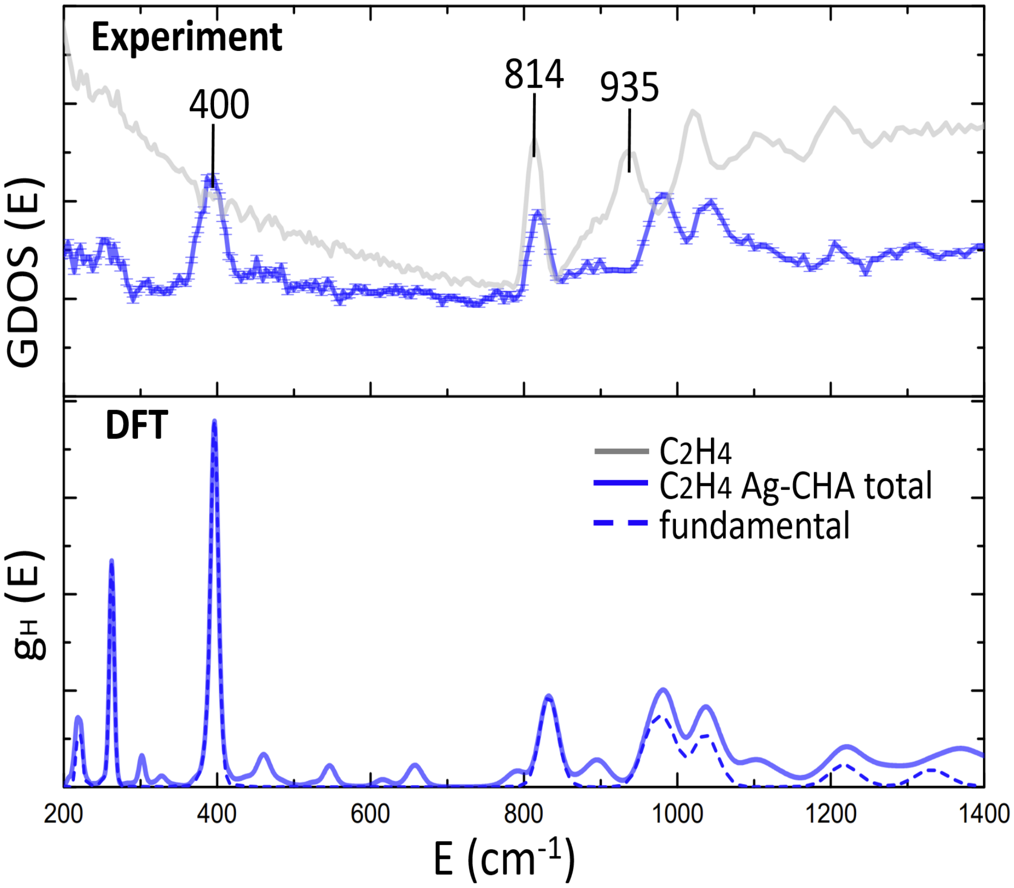

Figure 3.7: Comparison between experimental and calculated INS spectra, fundamental and total frequencies (considering first overtones), of C_2H_4 adsorbed on Ag-CHA with that of pure gas fore reference.

Comparing the INS spectra of pure ethylene with ethylene adsorbed in Ag-CHA, we observe that the well defined bands at the bending region, from 700 to 1400 cm^{-1}, corresponding to the internal modes of ethylene, are almost not altered upon adsorption. An exception is the one around 935 cm^{-1} (CH_2 wagging), which are blueshifted ($\approx$ 980 cm^{-1} and 977 cm^{-1} in experimental and calculated spectra respectively). In the adsorbed molecule, this band is attributed to the vibrations of CH_2 wagging in an asymmetric form. Ethylene molecules interacting with silver centers in zeolites are subjected to a force that induces them to be adsorbed in such a way that the angle formed between the C=C bond and the line connecting the center of it with the silver atom deviates from the perpendicularity. Thus, it suggests that the shift is a consequence of the disturbance provoked by the interaction with silver species [58].

The most significant difference in the spectra of pure ethylene and adsorbed ethylene on Ag-CHA, however, is the appearance of a significant vibrational band at $\approx$ 400 cm^{-1}. Bands at this region, between 200 until approximately 600 cm^{-1}, are correlated to the hampered rotations of ethylene, in consonance with earlier publications[31, 32, 113], and confirms the adsorption of the molecule inside the zeolite.

Table 3.1: Vibrational analysis of experimental and calculated frequencies (fundamental vibrations) of ethylene interacting with silver species in Ag-CHA

Model	Experimental freq. (cm^{-1})	Calculated freq. (cm^{-1})	Vibrational modes
Ag-CHA	220	220	Hindered rotations
	260	260	
	395	396	
	818	832	CH_2 in plane rocking (ν_{10})
	980	977	CH_2 wagging (ν_8) asymmetric
	1044	1024, 1037	CH_2 wagging (ν_7) asymmetric and CH_2 torsion (ν_4) asymmetric
	1205	1216	CH_2 in plane rocking (ν_6)
	1309	1326	CH_2 scissoring (ν_3)

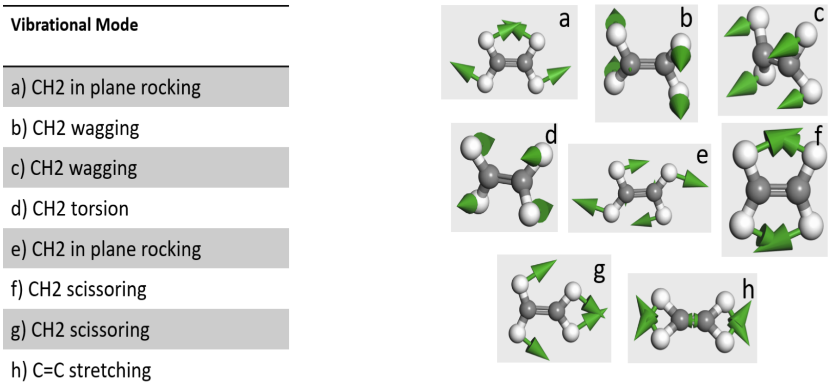

Vibrational Mode
a) CH2 in plane rocking
b) CH2 wagging
c) CH2 wagging
d) CH2 torsion
e) CH2 in plane rocking
f) CH2 scissoring
g) CH2 scissoring
h) C=C stretching

Figure 3.8: Illustration of the vibrational modes of ethylene. Modes g) (theoretical value at ≈ 1425 cm^{-1}) and h) (theoretical value at ≈ 1648 cm^{-1}) are not included in the range of the INS spectra represented in Fig. 3.7.

3.2.4 Characterization of π-complexation

The shifts in the vibrational bands of ethylene on Ag-CHA in comparison to that of pure ethylene, as evidenced by experimental INS spectra, proved this gas is in fact adsorbed on the zeolite. Based on UV-vis and ^{13}C NMR results, it was confirmed that ethylene interacts with the adsorption site created by Ag^+ species upon adsorption. This is endorsed by the validation of a DFT model that simulates the interaction of ethylene only with Ag^+ species in CHA framework.

It is known that the adsorption of an alkene on transition metal sites occurs through the π-complexation mechanism that involves the σ bonding by the electron charge transfer from the p orbitals of ethylene to the empty s orbital of the cation (5s orbital, in the case of Ag^+). Simultaneously, there is backdonation of charges from the filled $4d^{10}$ orbital of Ag^+ to the antibonding π^* orbital of the adsorbate. The electron charge backdonation from silver to ethylene, $d(Ag^+) \longrightarrow \pi^*$ (C_2H_4) dominates the adsorption mechanism [60–65].

The electronic nature of π-complexation in a system can be identified and proved by the analysis of the rearrangement of the electronic density between the elements involved by means of DFT calculation and further confirmed experimentally with a high field shift of the ^{13}C NMR signal of ethylene adsorbed on Ag-zeolite. Furthermore, as a consequence of this electronic interaction, a lengthening of the C=C bonds must occur leading to the redshift of the stretching vibrations, which can be observed by DFT calculations and well as by IR spectrum.

After proving experimentally and theoretically that the binding mechanism of ethylene on Ag-zeolites is based on the π-complexation mechanism, the extension of such interaction can also be estimated. In terms of strength, the adsorption by π-complexation is intermediate between a strong physisorption and a weak chemisorption. The values of adsorption energies as well as the estimation of the amount of charge transfer in a system can be obtained through DFT calculations.

Therefore, in this work, a combination of Electron Density Difference (EDD) analysis and ^{13}C NMR were used to evidence and characterize the nature of ethylene binding on Ag-zeolites as by π-complexation. The analysis of stretching vibration shifts were also carried out to confirm the formation of π-complex considering DFT calculated INS spectra and also experimental Infrared spectrum. Finally, the extension of the interaction is evaluated by DFT adsorption energy values and charge transfer analysis, this last one obtained through DFT Mulliken Charge Analysis method.

3.2.4.1 Electron Density Difference and ^{13}C NMR results

The visual representation (isosurfaces) of the electron density rearrangement of the system's components after their interaction are depicted in Figure 3.9.

In these Electron Density Difference (EDD) plots, the different colors indicate zones of depletion (yellow) and accumulation (blue) of electron density. For C_2H_4 Ag-CHA model, the EDD decreases nearby ethylene and increases in the region between ethylene and silver, implicating that the π-electron cloud of the olefins overlaps with the vacant outermost s -orbital forming a σ bond. Simultaneously, there is a decrease of the electron density at the metal and an increase along the C=C bond, corresponding to an electron π-backdonation from the d-orbital of the metal cation to the vacant π^* anti-bonding orbitals of the alkene. This back and forth movement of electrons responds to the mechanism broadly referred to as π-complexation. On the other hand, the high field shift of the ^{13}C NMR signal of ethylene adsorbed on Ag-CHA from $\delta\ ^{13}\mathrm{C} = 123$ ppm (pure ethylene) to $\delta\ ^{13}\mathrm{C} = 110$ ppm, as already explained in subsection 3.1, confirms the electron charge backdonation from silver to ethylene, $\mathrm{d(Ag^+)} \longrightarrow \pi^*\ (C_2H_4)$.

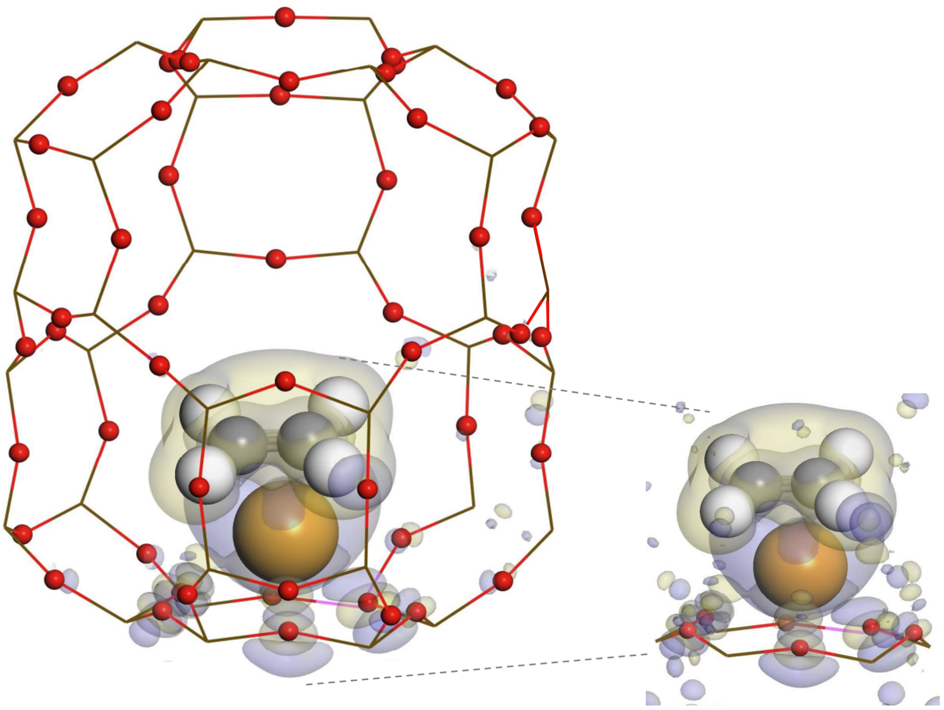

Figure 3.9: Isosurfaces created for -8.369eÅ^{-3}, representing the electron density difference between ethylene and Ag-CHA. The yellow shade represents areas of charge depletion while the blue one, of charge accumulation. This rearrangement is attributed to π-complexation interaction. The picture illustrates the full contribution of the Ag-CHA lattice atoms and the molecule.

3.2.4.2 C=C stretching shift calculation and Infrared Spectrum

The charge transfer dynamic between ethylene and silver weakens and lengthens the molecule's C=C double bond, causing the redshift of C=C frequency. Upon adsorption at transition metal cation site, the ethylene molecule loses its symmetry. Not only the C=C bond is affected by the π-complexation and by the electrostatic field of the zeolite framework, but also the C-H bonds experience minor lengthening or shortening varying among the bonds. As seen in Figure 3.6, C=C bond underwent lengthening of 0.03Å, whereas C-H bonds passed from equally distanced 1.094Å to varied lengths between 1.095 and 1.096Å.

Since INS spectroscopy is mainly sensitive to vibrations involving hydrogen atoms, C=C stretching is measured as a riding mode with a low intensity at 1500 cm^{-1}, and could probably be not visible as the resolution of INS bands at high energy tends to be reduced, as explained in section 2.1.3.4. This way, the information could not be extracted using **experimental** INS, although it was possible to calculate it from **theoretical** INS spectrum. The calculated value for C=C stretching shift ($\Delta_{C=C}$) can be compared then to experimental results obtained by a technique different than INS. In this case, IR spectroscopy is a complementary technique that allows the observation of adsorbed ethylene C=C stretching band within the interval 1600–1650 cm^{-1}. This band is not visible in the pure gas phase, however, as a result of ethylene's asymmetry after adsorption, all of its vibrational modes become IR-active.

Fig. 3.10 shows the IR spectrum of ethylene adsorbed on Ag-CHA. In this work, the experimental C=C stretching frequencies of ethylene adsorbed on Ag-CHA is red shifted 48cm^{-1} respect to the gas phase (pure gas C=C stretching frequency reference is 1623cm^{-1}), in excellent agreement with the $\approx$ 46 cm^{-1} found by DFT predictions (details about this calculation are in section A.4). These values are in accordance with previous studies reporting a correlation between the shift of the ethylene C=C stretching and the formation of π-complex between ethylene on silver-zeolite [58], in which C=C stretching vibrational modes of adsorbed ethylene featured redshifts from 30 - 70 cm^{-1}.

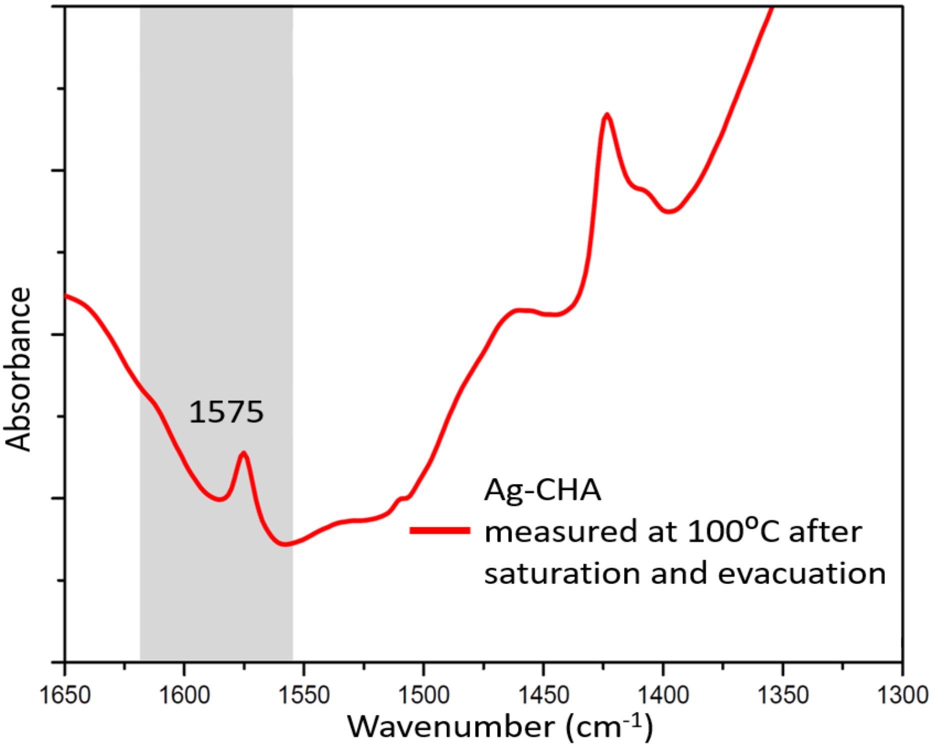

Figure 3.10: IR spectrum for ethylene adsorbed on Ag-CHA. It shows a redshift of C=C stretching if compared to gas phase ethylene (1623 cm^{-1}), suggesting an effective interaction between Ag species and the molecule by π-complexation.

Although they are correlated, the redshift experienced by C=C stretching frequency is not directly proportional to the C=C bond lengthening once the C-H bonds also suffer the effects of backdonation during π-complexation and of the electrostatic framework [60].

3.2.4.3 Adsorption energy and charge transfer

The adsorption energy of a system is calculated by subtracting the energy of the isolated adsorbed element (ethylene) and the isolated framework from the energy of full system (framework + adsorbed molecule), $\Delta_{E_{ads}} = E_{system} - E_{framework} - E_{C_2H_4}$. The adsorption energy value computed for ethylene adsorbed on Ag-CHA was -112.89 kJ/mol. This value is within the range characterized as between strong physisorption and weak chemisorption, as expected for π-complexation binding.

The total charge transfer between inorganic-organic elements was generated by Mulliken Charge Analysis calculations on Materials Studio software. For ethylene adsorbed on Ag-CHA, this transfer counts for 0.177e^{-}. In this DFT based calculation, the charge analysis provides numerical values for partial charges of all the elements in a system. To calculate the total charge transfer in each system, we sum up the charges of ethylene's elements after adsorption[114]. The partial charges for all the elements of Ag-CHA model are found in section A.5.

Table 3.2 summarizes the features used in the characterization of π-complex for C_2H_4 Ag-CHA, CsAg-RHO (section3.3) and HAg-LTA (section3.4),to be referred to along this Chapter.

Table 3.2: Summarizing table adressing structural details such as cage diameter (D_{cage}), distances between Ag-O_z, Ag-C and C-H), charge transfer (Δe^-), C=C stretching redshift, C=C bond lengthening ($\Delta_{C=C}$) and adsorption energies for C_2H_4 Ag-CHA, CsAg-RHO and HAg-LTA.

Model	d_{Ag-Oz} (Å)	$d_{C1,2-Ag}$ (Å)	d_{C-H} (Å)	Δe^-	C=C stretc.	$\Delta_{C=C}$ (Å)	Ads. Energy (kJ/-mol)
C_2H_4 Ag-CHA	2.46, 2.64, 3.02	2.43, 2.45	1.095-1.096 (1.094 before ads)	0.177	48 (exp), 46 (calc)	0.03	-112.89
C_2H_4 CsAg-RHO	2.49, 2.51, 2.84	2.44, 2.45	1.094-1.096 (1.091 before ads)	0.200	56 (calc)	0.03	-97.20
C_2H_4 HAg-LTA	2.33, 2.60, 2.64	2.42, 2.43	1.095-1.096 (1.095 before ads)	0.170	42 (calc)	0.03	-98.71

3.3 Evidence and characterization of π-complex in silver containing RHO type zeolite

In this section the formation of π-complexes on silver containing RHO type zeolite is evidenced and characterized by a combination of INS experiment and DFT calculations, supported by ^{13} C NMR.

3.3.1 Conception of computational models

RHO structure contains 48 T atoms/u.c.. Its chemical formula is given by:

$$M_xM'_ySi_{(48-(x+y))}Al_{x+y}O_{96}$$

where M and M' are compensating cations. The T atoms create large *lta* cages (11.4 x 11.4 Å^2) linked through double eight rings (*d8r*) units to six other neighbouring *lta* cages, forming a body-centered arrangement of interpenetrating yet not interconnected pore systems [115].

The RHO framework type is known for exhibiting one of the highest flexibilities among zeolite structures. It has been experimentally and theoretically observed in previous studies[47, 51] that, upon dehydration, a structural distortion can be observed, leading the framework to change from a high symmetry form (Im$\bar{3}$m) to a lower one (I$\bar{4}$3m). Such distortion occurs in a way to facilitate the coordination of compensating cations to oxygen atoms from the framework. As one of the consequences of this relaxation, the originally circular shape of the

8-rings becomes elliptical. Another consequence is the *lta* cage transformation, which switches from a nearly spherical to conical shape. The extent of 8-rings distortion on RHO type zeolite varies accordingly to which extra framework cations occupy its cavities [48]. For this reason, the presence of other compensating cations have been considered in our calculations.

As seen in section 2.3, incomplete Ag^+ cation exchange is achieved in the RHO sample. There are three different compensating cations: Na^+, Cs^+ and Ag^+. Therefore, three simple theoretical configurations were conceived: the first one containing only Ag^+ as compensating cation (**C_2H_4 Ag-RHO configuration**), the second one with Ag^+ and Na^+ (**C_2H_4 NaAg-RHO configuration**) and a third considering Ag^+ and Cs^+ (**C_2H_4 CsAg-RHO configuration**). All models keep a very simple proportion of 1 Ag^+: 1 (Na^+ or Cs^+): 1 C_2H_4 per unit cell, in an attempt to understand how these cations would contribute to the structural changes in RHO and, therefore, on ethylene-silver interaction.

Extra-framework cations on zeolite RHO can be distributed as displayed in Figure 3.11, where $S_1{}^1$ and $S_1{}^2$ correspond to sites within an octagonal prism displaced from a 4-ring site [49]. S_2 is placed at the center of a six-ring while $S_{2'}$ and S_3 are placed within the *lta* cage displaced from the 6- and 4- rings, respectively. Site S_5 lies at the center of a *d8r*. According to previous studies, Cs^+ preferably occupies site is S_5 within the *d8r* while Na^+ and Ag^+ are placed at site $S_{2'}$. This cationic arrangement was the one considered in the configurations described in this present work. Figure 3.12 depicts the unit cells for each of the framework configurations proposed. Despite the presence of other possible adsorption sites, only the interaction of ethylene with Ag^+ was simulated, as it was proven by the ^{13}C NMR spectra discussed above. Therefore, in all configurations, the ethylene molecule was placed near Ag^+, inside the *lta* cage with the same direction as described for C_2H_4 Ag-CHA model: with hydrocarbon C=C bond axis of ethylene was oriented parallel to the 6-ring plane where the Ag is placed and above Ag (so the distance C-Ag could grow vertically inside the cage).

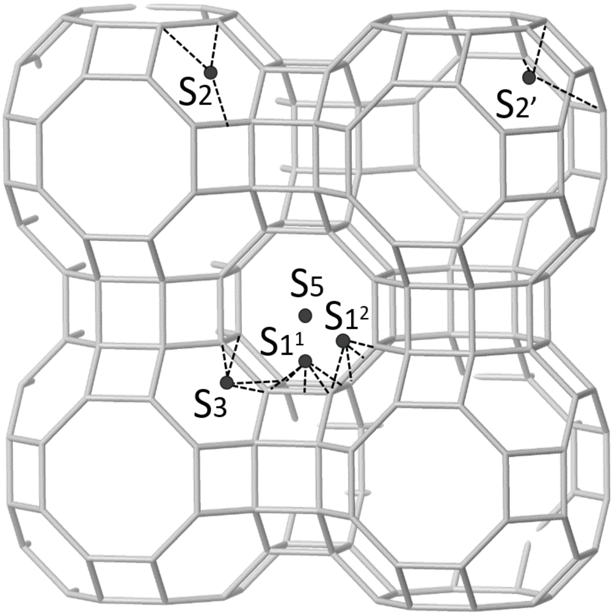

Figure 3.11: Possible positions for extra-framework cations in RHO zeolite. Cs^+ preferred site is S_5 and while Na^+ and Ag^+ prefer site $S_{2'}$.

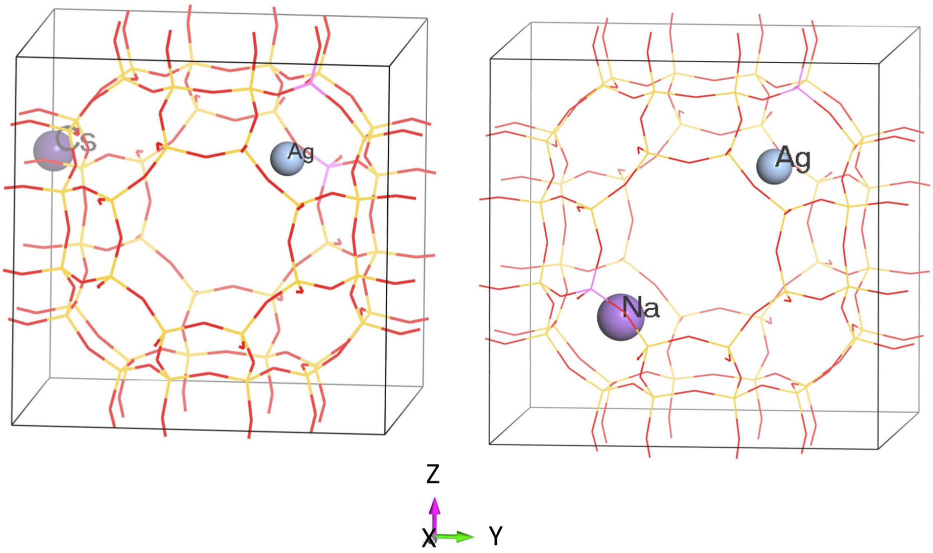

Figure 3.12: Unit cells representing RHO framework with Ag^+, Cs^+ and Na^+ placements for CsAg-RHO and NaAg-RHO. Configuration Ag-RHO (not displayed in the picture) keep the same position of Ag species as for CsAg-RHO and NaAg-RHO.

3.3.2 Comparison between experimental INS and theoretical DFT results

Figure 3.13 shows the comparison of the experimental INS spectrum of ethylene adsorbed on CsAg-RHO sample with the calculated neutron spectra for C_2H_4 Ag-RHO, NaAg-RHO and CsAg-RHO configurations, considering only fundamental frequencies.

The C_2H_4 CsAg-RHO configuration shows the best match with experimental INS data when compared to C_2H_4 Ag-RHO and C_2H_4 NaAg-RHO configurations, thus it is the one selected as our definitive model (from now on called C_2H_4 CsAg-RHO **model**). The major difference between the spectra of the different configurations lies on the librational region, indicating that depending on the cation used for each configuration, a more or lesser constricted environment is provided around the ethylene molecule. In order to fully comprehend the influence of the cation types on the flexibility of the RHO type zeolite framework and its direct effect on INS spectra of the adsorbed ethylene (and therefore ethylene binding), an analysis of the final structure after geometry optimization for all configurations was necessary and carried out.

After the geometry optimization of Ag-RHO, NaAg-RHO and CsAg-RHO configurations, the *d8r* and *lta* cages are distorted in all of them indicating the structural change from $Im\bar{3}m$ symmetry to $I\bar{4}3m$ symmetry. The degree of elliptical distortion of the *d8r* can be quantified by a parameter $\bar{\Delta}$, which is the average of the difference Δ[48, 116] between the longest (d1) and the shortest (d2) O-O distances within the cross-section of the *d8r* windows and can be represented by the formula:

$$\bar{\Delta} = \sum_{i=1}^{6} \Delta i$$

where i is each 8-ring in a *lta* cage per unit cell.

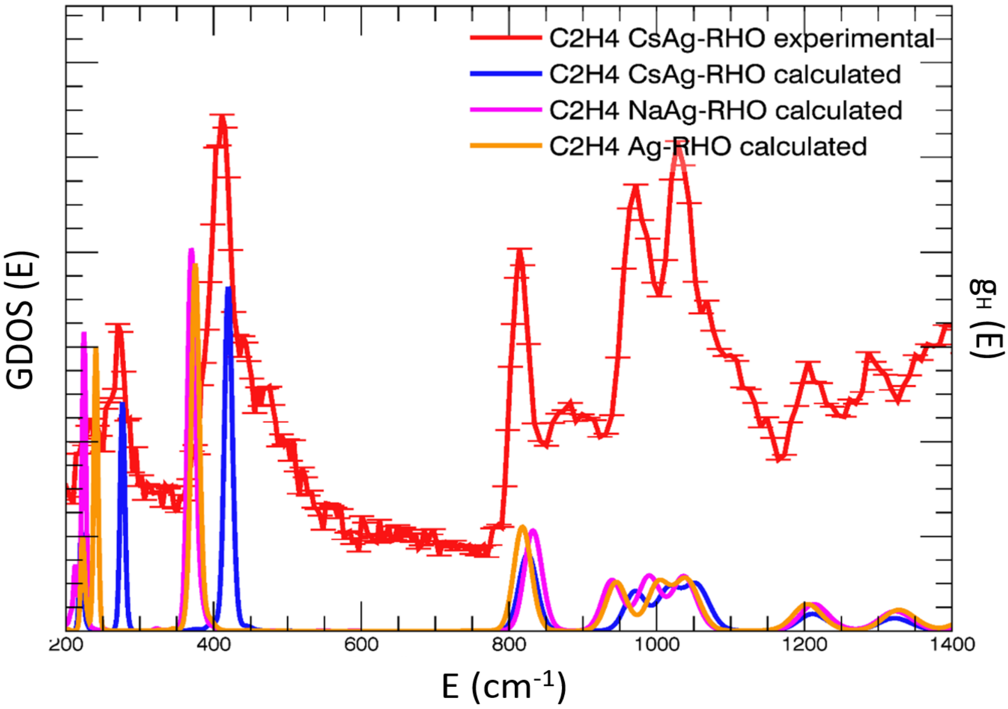

Figure 3.13: INS and theoretical spectra obtained for different RHO models, considering only fundamental frequencies. The one that best fits the experimental data is CsAg-RHO.

The values found for the elliptical distortion of C_2H_4 Ag-RHO, C_2H_4 NaAg-RHO and C_2H_4 CsAg-RHO configurations are 2.10, 2.37 and 2.17Å, respectively. These $\bar{\Delta}$ values are comparable to the ones reported by Grand and collaborators [48]. It was shown that the flexibility of RHO framework cages and the distortion of the *d8r* units upon water and CO_2 adsorption/desorption by temperature dependant in situ XRD and Rietveld refinements. For Na-RHO and NaCs-RHO samples, a $\bar{\Delta}$ of 2.10 Å and 2.16 Å, respectively, were found. Moreover, they also described the deformation of *lta* cages, which adopts a conical shape in the area of the 8-ring side pockets.

Herein, figure 3.14 illustrates the differences between the two symmetries on CsAg-RHO model (Im$\bar{3}$m, i.e. before model geometry optimization and I$\bar{4}$3m, after geometry optimization), picturing the deformations of 8-rings, the *d8r* and the overall structure in the region of the 8-ring pocket. The 8-ring side pockets are highlighted in blue.

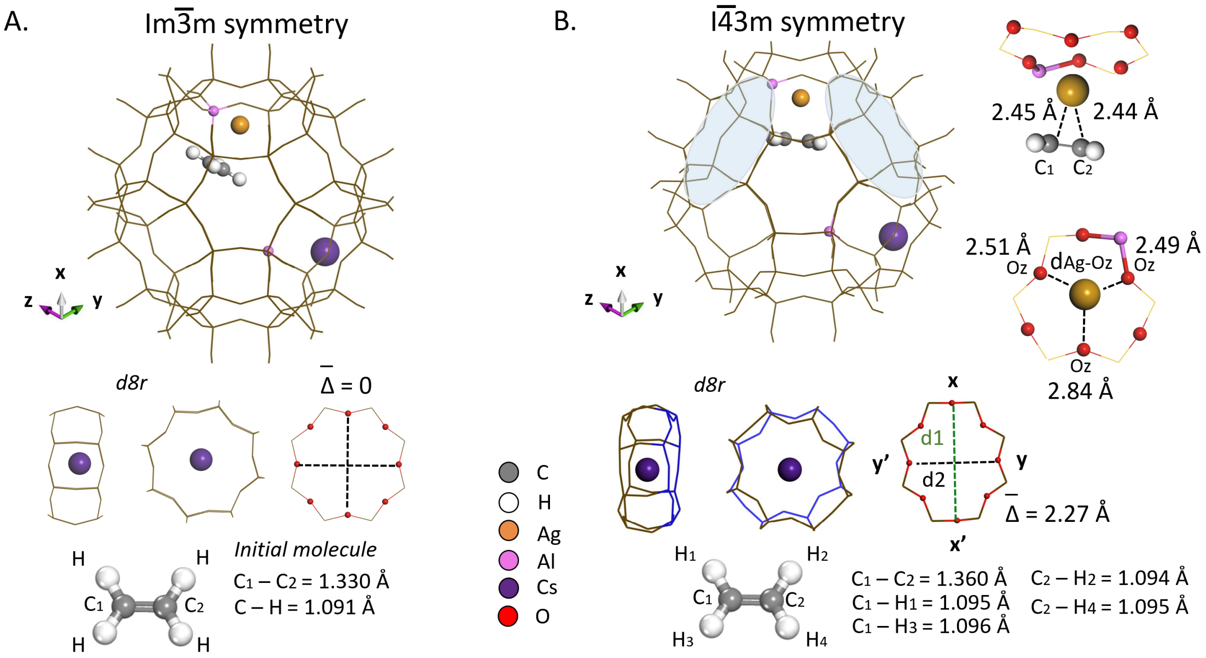

Figure 3.14: Structural details of *lta* cage in A. before and in B. after geometry optimized C_2H_4 CsAg-RHO model. The distortion of *d8r* and *lta* cages are shown, indicating the structural phase change from Im$\bar{3}$m (highly symmetric) to I$\bar{4}$3m (asymmetric). CsAg-RHO model, the conical narrowing of *lta* cage occurs in the region where Ag-C_2H_4 complex lies. The distances between Ag and the closest framework oxygen atoms, d_{Ag-Oz}, as well as Ag-C, d_{C-Ag} are also shown. C_2H_4 molecule is represented before and after the system energy minimization with its corresponding C-H distances, d_{C-H}. Al, Ag, C and H atoms are highlighted and identified in the figure. O atoms are highlighted in 6-rings where Ag cation sits. The other O atoms of the framework as well as Si atoms are represented by brownish (and dark blue lines in *d8r* details) to facilitate Ag-C_2H_4 complex visualization. The upper elliptical 8-rings in CsAg-RHO are highlighted in light blue (8-ring side pockets).

The same representation for C_2H_4 Ag-RHO and C_2H_4 NaAg-RHO configurations can be found in the Appendix, Figure A.6. The C_2H_4 Ag-RHO, C_2H_4 NaAg-RHO and C_2H_4 CsAg-RHO models also display structural distortions. Nevertheless, these distortions are not exactly the same: in C_2H_4 CsAg-RHO model, the conical narrowing of *lta* cage is located in the region where the C_2H_4 - Ag^+ complex lies, while for the others the narrowing is located in the opposite side of the cavity. In terms of 8-ring axis, the major axis (d1) of the upper elliptical 8-rings in C_2H_4 CsAg-RHO (indicated in light blue in Figure 3.14) is in x-x' direction while for C_2H_4 NaAg-RHO and C_2H_4 Ag-RHO configurations it is in y-y' direction. Ultimately, it means that in C_2H_4 CsAg-RHO model ethylene molecule is undergoing a higher constriction in its environment, which leads to the blueshift of the bands of INS spectra in the librational region (specially the one around 400 cm^{-1}). It evidences the fact that the very specific deformation arrangement found for C_2H_4 CsAg-RHO model, i.e. the shape of 8-ring side pockets in this system, is key to interpret Ag-C_2H_4 interactions in Ag-zeolites, as explained in detail in section 3.5.

Once the C_2H_4 CsAg-RHO model was validated, the frequency analysis of the vibrational bands calculated for this model allows us to identify the corresponding vibrational modes, as follows in the next subsection.

3.3.3 Frequency analysis of the vibrational bands

Figure 3.15 compares the experimental and calculated INS spectra, fundamental and total frequencies (considering first overtones), of C_2H_4 adsorbed on CsAg-RHO with that of pure gas. The mode assignments and calculated frequencies for ethylene adsorbed on CsAg-RHO are shown in Table 3.3. The calculated values described in the table correspond to the fundamental frequencies of C_2H_4 CsAg-RHO model.

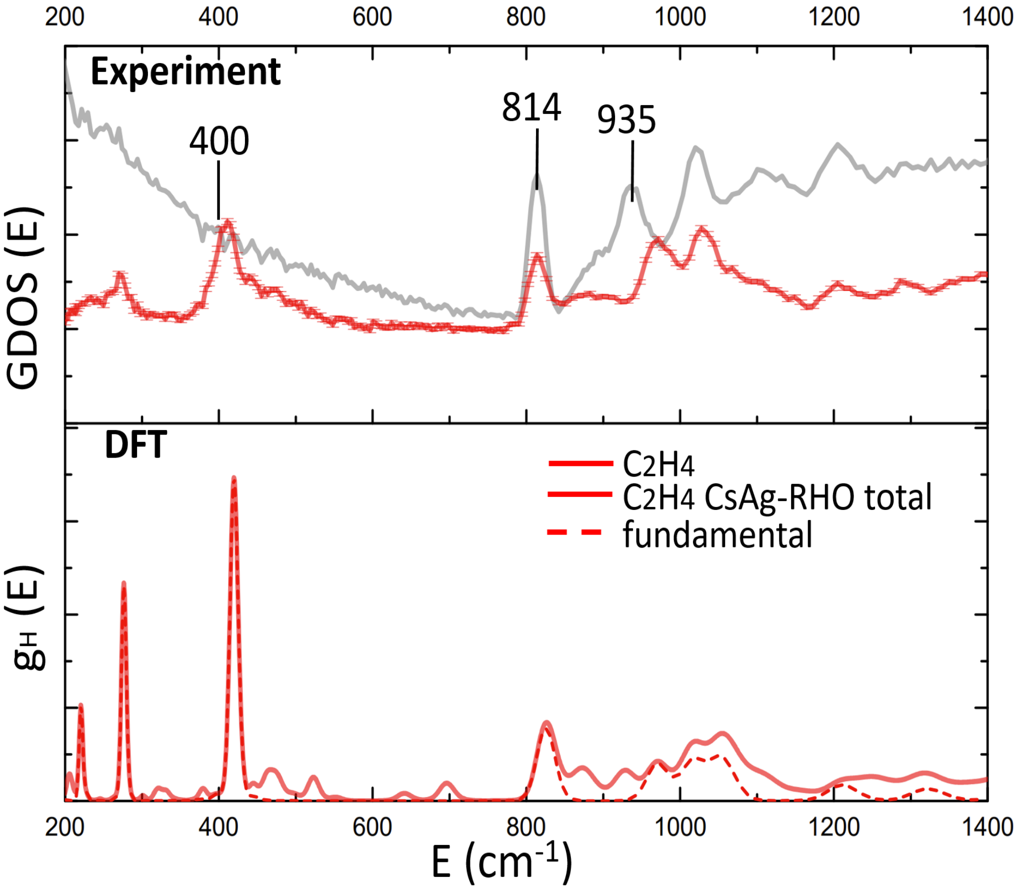

Figure 3.15: Comparison between experimental and calculated INS spectra, fundamental and total frequencies (considering first overtones), of C_2H_4 adsorbed on CsAg-RHO with that of pure gas fore reference.

Comparing the INS spectra of pure ethylene with ethylene adsorbed in CsAg-RHO, the presence of bands at ≈ 400 cm^{-1} in the librational region confirms the adsorption of ethylene on the zeolite.

As observed for C_2H_4 Ag-CHA model in subsection 3.2.3, in C_2H_4 CsAg-RHO,the bands corresponding to the internal modes of ethylene do not change. An exception being CH_2 wagging mode, around 935 cm^{-1} (CH_2 wagging), which is blueshifted (≈ 971 cm^{-1} and 970 cm^{-1} in experimental and calculated spectra respectively).

Table 3.3: Vibrational analyses of experimental and calculated frequencies of ethylene interacting with silver species in CsAg-RHO

Model	Experimental freq. (cm^{-1})	Calculated freq. (cm^{-1})	Vibrational modes
CsAg-RHO	230	221	Hindered rotations
	270	275	
	411	419	
	814	825	CH_2 in plane rocking (ν_{10})
	971	970	CH_2 wagging (ν_8) asymmetric
	1027	1020, 1052	CH_2 wagging (ν_7) asymmetric and CH_2 torsion (ν_4) asymmetric
	1205	1216	CH_2 in plane rocking (ν_6)
	1294	1323	CH_2 scissoring (ν_3)

3.3.4 Characterization of π-complexation

3.3.4.1 Electron Density Difference and ^{13}C NMR results

The EDD plot for C_2H_4 CsAg-RHO is shown in Figure 3.16. As reported for C_2H_4 Ag-CHA in subsection 3.2.4.1, the EDD decreases nearby ethylene and increases in the region between ethylene and silver, with a pattern of redistribution of charges compatible of that of π-complexation scheme.

As reported for C_2H_4 Ag-CHA in subsection 3.2.4.1, the EDD decreases nearby ethylene and increases in the region between ethylene and silver, with a pattern of redistribution of charges compatible of that of π-complexation scheme. The high field shift of the ^{13}C NMR signal of ethylene adsorbed on CsAg-RHO from 123 ppm (pure ethylene) to 115 ppm, adressed in subsection 3.1, confirms the electron charge backdonation from silver to ethylene, $d(Ag^+) \longrightarrow \pi^*$ (C_2H_4).

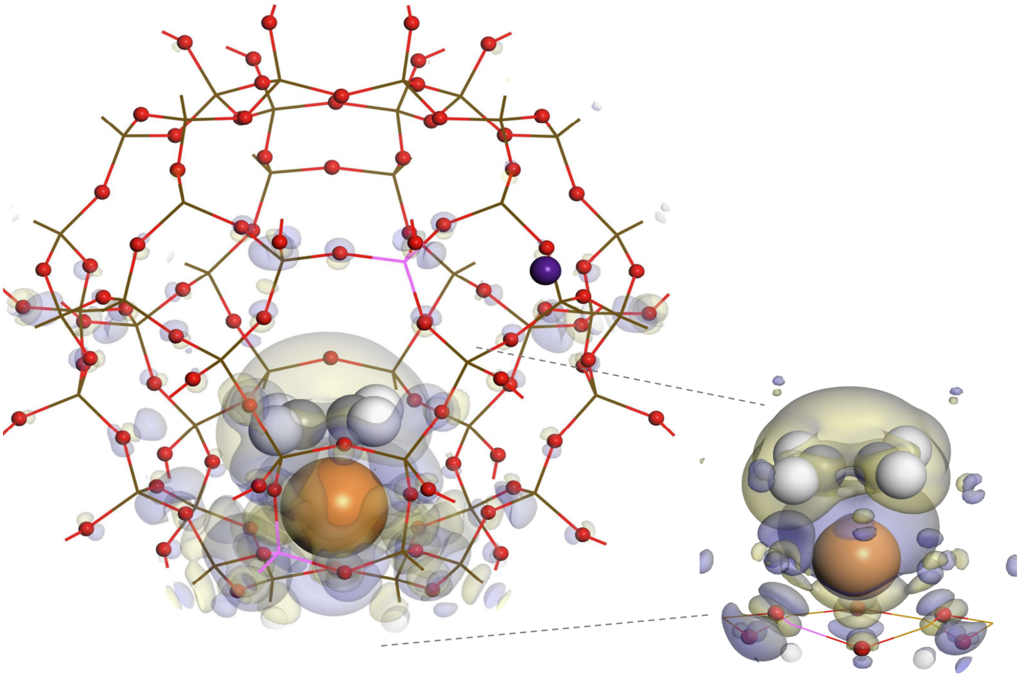

Figure 3.16: Isosurfaces created for -8.369eÅ^{-3}, representing the electron density difference between ethylene and CsAg-RHO. The yellow shade represents areas of charge depletion while the blue one, of charge accumulation. This rearrangement is attributed to π-complexation interaction. The picture illustrates the full contribution of the CsAg-RHO lattice atoms and the molecule.

3.3.4.2 C=C stretching shift calculation and Infrared Spectrum

The C=C stretching frequencies of ethylene adsorbed in CsAg-RHO was calculated by DFT and compared to pure ethylene's (pure gas C=C stretching frequency reference is 1623cm^{-1}). The details of this calculation is in section A.4. The Infrared spectrum for the sample could not be obtained due to problems related to its in-situ loading of ethylene (one hypothesis would be that the pellets were too dense to allow the diffusion of the gas). However, the DFT calculated value of 56 cm^{-1} for C=C stretching shift is in accordance with the range expected and related to π-complexation formation, from 30 - 70 cm^{-1}.

3.3.4.3 Adsorption energy and charge transfer

The adsorption energy and total charge transfer values are calculated as explained in 3.2.4.3.

The adsorption energy value computed for C_2H_4 CsAg-RHO model was -97.20 kJ/mol. This value is within the expected range between strong physisorption and weak chemisorption, characteristic of π-complexation binding.

The total charge transfer between inorganic-organic elements generated by Mulliken Charge Analysis counts for 0.200e$^-$. All the partial charges generated for C_2H_4 CsAg-RHO model are found in section A.5.

All the parameters of the π-complexation of ethylene adsorbed on CsAg-RHO are listed in Table 2.2.

3.4 Evidence and characterization of π-complex in silver containing LTA type zeolite

In this section the formation of π-complexes on silver containing LTA type zeolite is evidenced and characterized by INS experiment and DFT calculations, supported by ^{13} C NMR.

3.4.1 Conception of computational models

The unit cell of LTA type zeolite contains 24 T sites, being represented by the chemical formula:

$$M_xM'_ySi_{(24-(x+y))}Al_{x+y}O_{96}$$

where M and M' are compensating cations. LTA type has a three dimensional pore structure with a main cage composed by 4-6- and 8-rings (α or *lta* cage) at the center of the unit cell connected with eight secondary smaller cages (β or *sodalite* cages) interconnected via 4 double rings (*4dr*), as indicated in Figure 3.17. The accessibility of *lta* cages is controlled by the 8-rings (4.2Å) and can host different extra-framework cations [117].

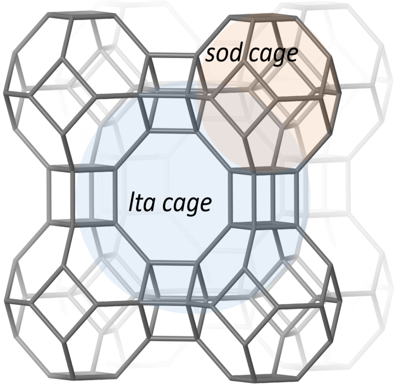

Figure 3.17: Cages disposition in LTA framework. *lta* cage is highlighted in blue and *sodalite* cage, in orange.

Following the chemical composition of the sample described in section 2.3, the LTA zeolite described here not only presents Ag^+ but also Brönsted Acid Sites (H^+). Previous studies [118] have confirmed the preference of Ag^+ to locate close to 6-ring windows of *lta* cages.

There are three possible placements for acid sites in LTA. The difference between these placements is related to which type of crystallographic oxygen (O1, O2, O3) the proton is attached to, as indicated in Figure 3.18. O1-H and O3-H point to a 8-ring at the intersection between two *lta* cages. O2-H points to a 6-ring at the intersection between *lta* and *sodalite* cages. It was reported by INS and DFT studies that, in high silica LTA-40 (Si/Al=40) [119], the large majority of the protons in the sample are of type O2-H. Minor quantities of O3-H were found and even less of O1-H.

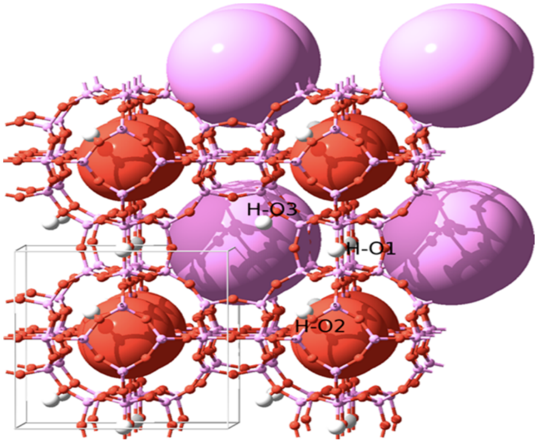

Figure 3.18: Possible position of H in LTA framework, taken from [119]. O1-H and O3-H point to a 8-ring at the intersection between two *lta* cages while O2-H points to a 6-ring at the intersection between *lta* and *sodalite* cages.

Three different configurations were conceived in order to evaluate the influence of these cations on the interaction with ethylene: **C_2H_4 Ag-LTA**, considering only Ag^+ species and **C_2H_4 HAg-LTA** (divided into C_2H_4 HAg-LTA-(O2) and C_2H_4 HAg-LTA-(O3)) changing the H between O2-H and O3-H, considering both Ag^+ and H^+ in a 1:1 proportion. Position O1-H was not considered due to the small probability of occurence, based on reference [119]. The composition was kept as simple as possible in order to evaluate the influence of H^+ and Ag^+ in the calculated INS spectra. Therefore, in these configurations, Ag^+ is placed at 6-ring for Ag^+ (the same $S_{2'}$ position as indicated in the *lta* cages of RHO in Fig. 3.11) and O2-H and O3-H for H^+.

The unit cells for each configuration can be found in Figure 3.19.

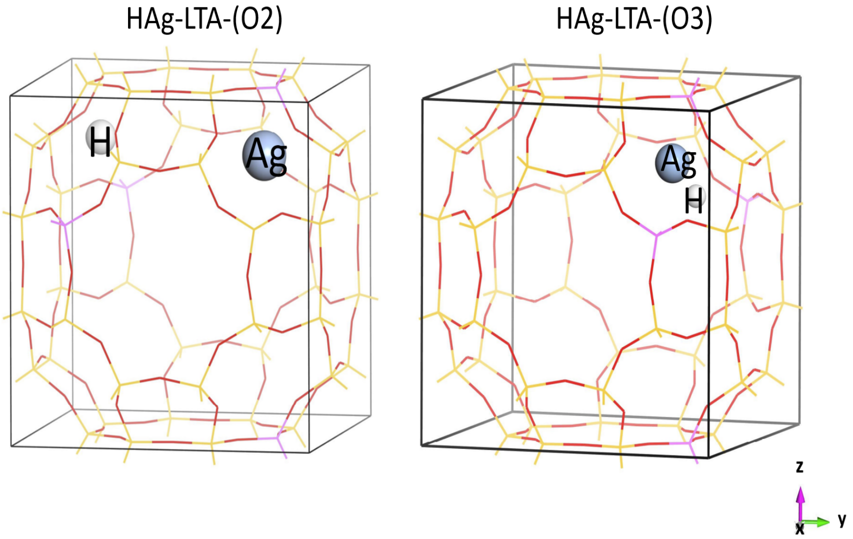

Figure 3.19: Unit cells of LTA framework with Ag^+ and H^+ placements. Blue atom represented by ball is Ag while white one represents H. Framework represented by lines, where yellow is Si atoms, red is O atoms and pink is Al. Ag-LTA not represented, keeping the same Ag^+ placement as in HAg-LTA-(O2) and HAg-LTA-(O3).

Despite the presence of other possible adsorption sites, only the interaction of ethylene with Ag^+ was simulated, as it was proven by the ^{13}C NMR results discussed above in section 3.1. Therefore, in all configurations, the ethylene molecule was placed near Ag^+ with hydrocarbon C=C bond axis of ethylene oriented parallel to the same 6-ring plane where the Ag is placed and above Ag in the same way as for the Ag-CHA and CsAg-RHO.

3.4.2 Comparison between experimental INS and theoretical DFT results

Figure 3.20 shows the comparison of the experimental INS spectrum of C_2H_4 HAg-LTA sample with the calculated neutron spectra for all configurations considered: C_2H_4 Ag-LTA, C_2H_4 HAg-LTA-(O2) and C_2H_4 HAg-LTA(O3), considering fundamental frequencies.

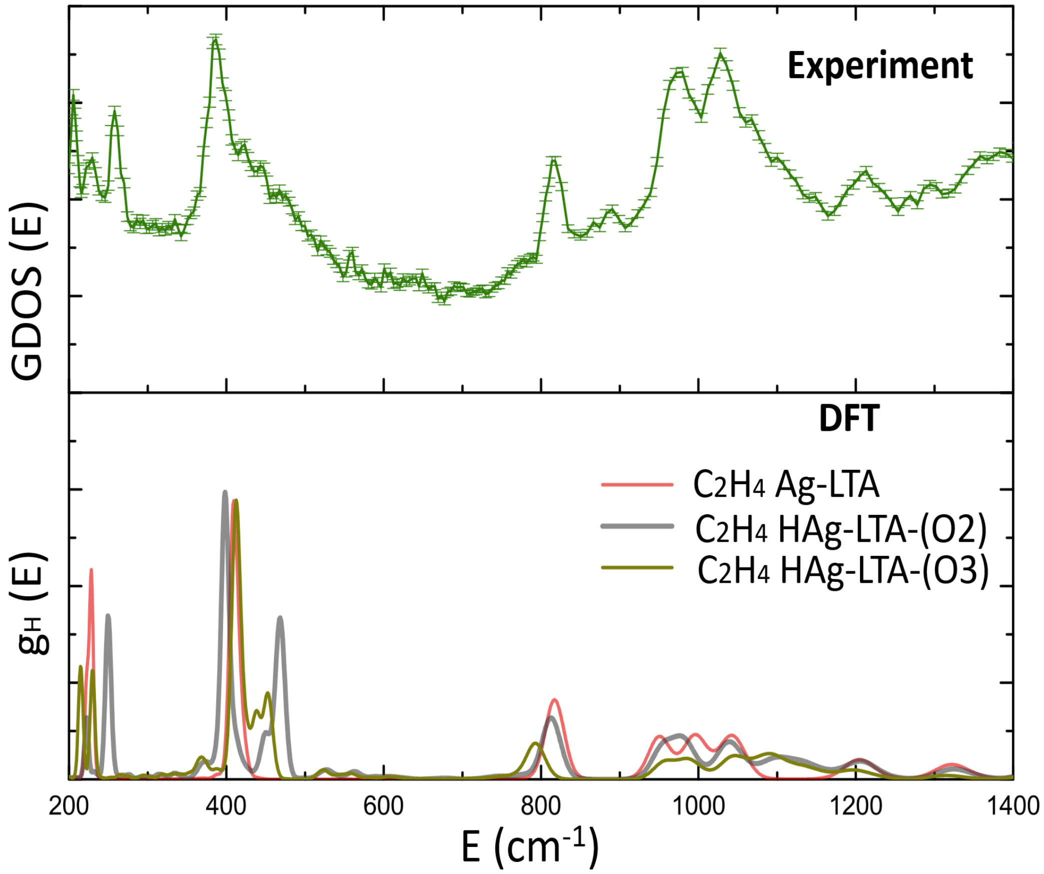

Figure 3.20: Comparison of the experimental INS spectrum of HAg-LTA sample with the calculated neutron spectra for all configurations considered: C_2H_4 Ag-LTA, C_2H_4 HAg-LTA-(O2) and C_2H_4 HAg-LTA-(O3), with fundamental frequencies.

The INS spectrum of C_2H_4 Ag-LTA configuration does not fully represent the experimental data, suggesting that the presence of H species, in fact, should not be neglected. Further, the comparison of experimental and calculated spectra confirms that there is probably a distribution of H positions (O3-H and O2-H at least, as O1-H was not calculated) in the sample. However, the large majority of the protons in the sample must be of type O2-H, which is the configuration that better reproduces the experimental INS results of HAg-LTA (C_2H_4 Ag-LTA HAg-LTA (O2)), as expected based on reference [119]. From now on this configuration is simply mentioned as C_2H_4 HAg-LTA model.

Figure 3.21 describes in detail the resulting model after geometry optimization, highlighting the *lta* cage containing the ethylene molecule.

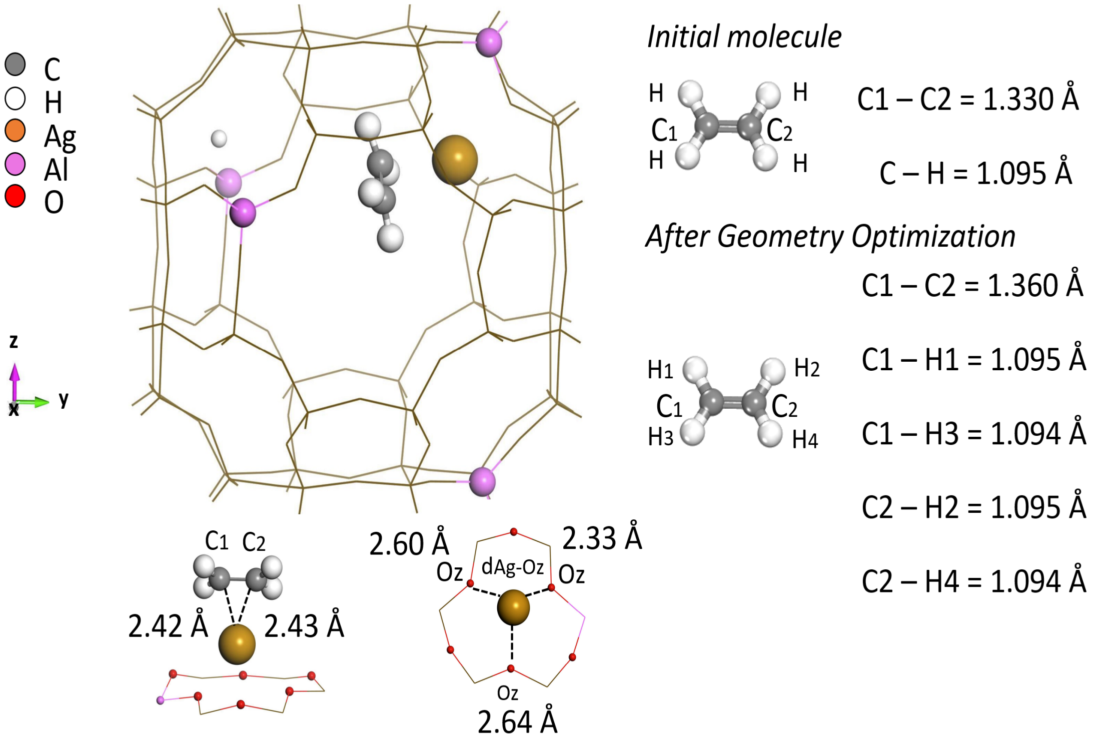
C
H
Ag
Al
O
z
x
y
Initial molecule
H
H
C1
C2
H
H
C1 – C2 = 1.330 Å
C – H = 1.095 Å
After Geometry Optimization
C1 – C2 = 1.360 Å
H1
H2
C1
C2
H3
H4
C1 – H1 = 1.095 Å
C1 – H3 = 1.094 Å
C2 – H2 = 1.095 Å
C2 – H4 = 1.094 Å
C1 C2
2.42 Å
2.43 Å
2.60 Å
2.33 Å
Oz
dAg-Oz
Oz
Oz
2.64 Å

Figure 3.21: Structural details of *lta* cage in the energy minimized C_2H_4 HAg- LTA model. The distances between Ag and the closest framework oxygen atoms, d_{Ag-Oz}, as well as Ag-C, d_{C-Ag} are shown. C_2H_4 molecule is represented before and after the system energy minimization with its corresponding C-H distances, d_{C-H}. Al, Ag, C and H atoms are indicated in the figure. O atoms are highlighted in the 6-ring where Ag cation is placed, O_z are the 6-ring Oxygen atoms closest to Ag. Si and O atoms of *lta* cage are represented by brownish lines to facilitate Ag-C_2H_4 complex visualization. The complex lies in a region called 8-ring pocket.

It shows that the Ag-C_2H_4 complex is located above a 6-ring and between two 8-rings, in a zone of the cavity addressed as 8-ring side pocket (to be detailed in section 3.5).

Once C_2H_4 HAg-LTA model was validated, the frequency analysis of the vibrational bands calculated for this model allows us to identify the corresponding vibrational modes, as follows in the next subsection.

3.4.3 Frequency analysis of the vibrational bands

Figure 3.22 compares the experimental and calculated INS spectra, fundamental and total frequencies (considering first overtones), of C_2H_4 adsorbed on HAg-LTA with that of pure gas. The mode assignments and calculated frequencies for C_2H_4 HAg-LTA are presented in Table 3.4. The calculated values described in the table correspond to the fundamental frequencies of C_2H_4 HAg-LTA model.

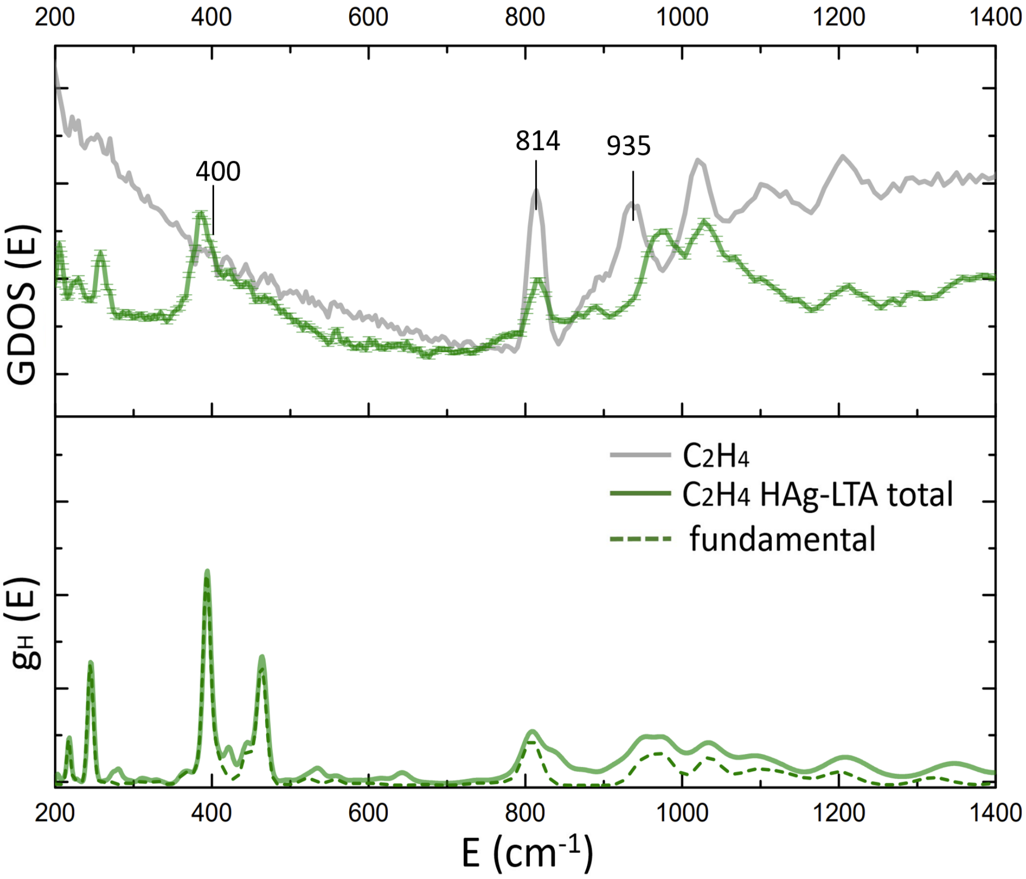

Figure 3.22: Comparison between experimental and calculated INS spectra of C_2H_4 adsorbed in HAg-LTA. Green full line spectra are related to total contribution, while the dashed line represent only first overtones. Experimental ethylene gas phase spectrum is represented in grey.

Table 3.4: Vibrational analyses of experimental and calculated frequencies of ethylene adsorbed on HAg-LTA

Model	Experimental freq. (cm^{-1})	Calculated freq. (cm^{-1})	Vibrational modes
HAg-LTA	229	218	Hindered rotations
	253	243	
	387	394	
	443-600	464-565	H lattice
	818	808	CH_2 in plane rocking (ν_{10})
	971	972	CH_2 wagging (ν_8) asymmetric
	1027	1029, 1039	CH_2 wagging (ν_7) asymmetric and CH_2 torsion (ν_4) asymmetric
	1100	1095	H lattice
	1213	1200	CH_2 in plane rocking (ν_6)
	1304	1324	CH_2 scissoring (ν_3)

The appearance of bands at ≈ 400 cm^{-1} in the librational region confirms the adsorption of ethylene on the HAg-LTA.

The internal modes of ethylene do not show any significant change, except the CH_2 wagging mode (935 cm^{-1}), that becomes assymetric after adsorption and is blueshifted ($\approx$ 971 cm^{-1} and 970 cm^{-1} in experimental and calculated spectra respectively).

3.4.4 Characterization of π-complexation

3.4.4.1 Electron Density Difference and ^{13}C NMR results

The of the electron density rearrangement of the system's components after their interaction are depicted in Figure 3.23.

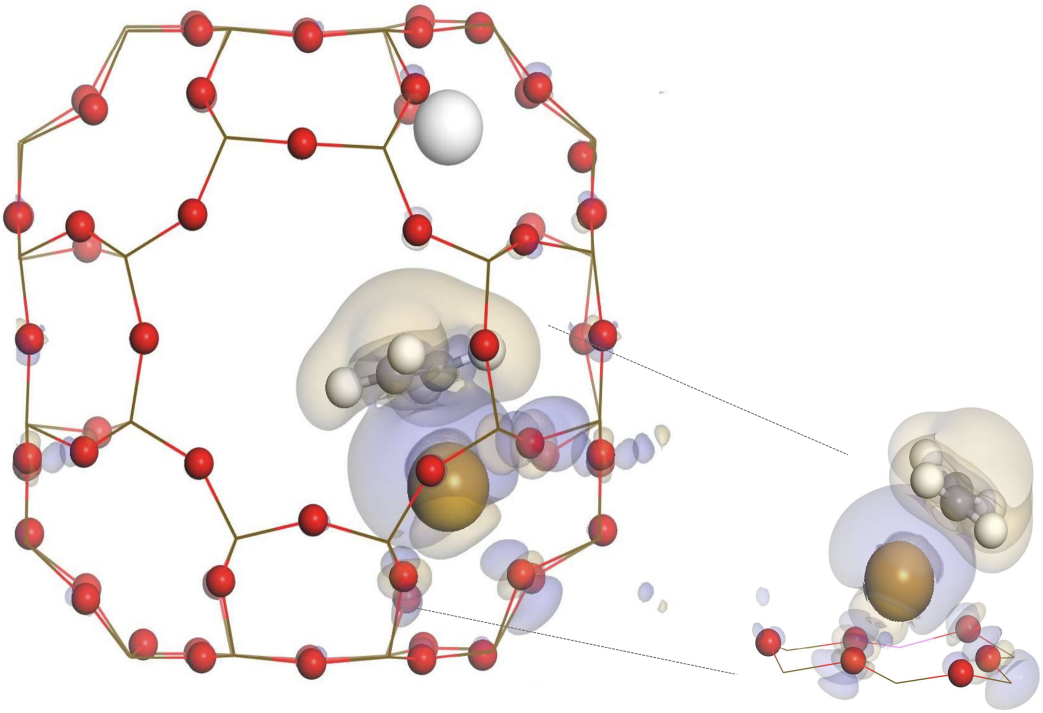

Figure 3.23: Isosurfaces created for -8.369eÅ^{-3}, representing the electron density difference between ethylene and HAg-LTA. The yellow shade represents areas of charge depletion while the blue one, of charge accumulation. This rearrangement is attributed to π-complexation interaction. The picture illustrates the full contribution of the HAg-LTA lattice atoms and the molecule.

The increase of electron density between ethylene molecule and silver and the decrease surround ethylene indicates the formation of π-complexation. The high field shift of the ^{13}C NMR signal of ethylene adsorbed on HAg-LTA from 123 ppm (pure ethylene) to 116 ppm, described in subsection 3.1, confirms the electron charge backdonation from silver to ethylene, $d(Ag^+) \longrightarrow \pi^* \ (C_2H_4)$.

3.4.4.2 C=C stretching shift calculation and Infrared Spectrum

The C=C stretching frequencies of ethylene adsorbed in HAg-LTA was calculated by DFT and compared to pure ethylene's (pure gas C=C stretching frequency reference is 1623cm^{-1}). The Infrared spectrum for the LTA sample could not be obtained due to problems related to its in-situ loading, most probably the same problem as related to RHO sample (probably related to diffusivity problems due to pellets thickness). The value found for C=C stretching shift related to π-complexation formation, 42 cm^{-1}, is in accordance with the range expected (30 - 70 cm^{-1}). Details of this calculation is in section A.4.

3.4.4.3 Adsorption energy and charge transfer

The adsorption energy and total charge transfer values are calculated as explained in 3.2.4.3.

The adsorption energy value computed for HAg-LTA model was -98.71 kJ/mol. This value is within the expected range between strong physisorption and weak chemisorption, characteristic of π-complexation binding.

The total charge transfer between inorganic-organic elements generated by Mulliken Charge Analysis counts for 0.170e^{-}. All the partial charges generated for HAg-LTA model are found in section A.5.

All the parameters of the π-complexation of ethylene adsorbed on HAg-LTA are listed in Table 2.2.

3.5 Effects of cage topology on the formation of Ag-C_2H_4 π-complexes in silver containing zeolites

The results on the interaction between ethylene and silver-containing zeolites were described in the sections 3.2, 3.3 and 3.4, referring to CHA, RHO and LTA frameworks respectively. Such results show differences, pointing to the influence of different types of cages (in terms of shape, dimension and flexibility) on the formation and strength of this interaction. The effects of the cage topology are reported in this section.

Firstly, the UV-vis spectra of degassed samples show the occurrence of different silver species depending on the zeolite structure. Highly dispersed Ag^{+} are the only species in CsAg-RHO and HAg-LTA, while Ag^{+} coexists with Ag$_3$$^{+}$ in the Ag-CHA zeolite, indicating that silver has partially agglomerated in this zeolite. Nevertheless, ^{13}C NMR spectrum indicates that the resonance at a chemical shift characteristic of the C_2H_4-Ag^{+} complex (δ^{13}C = 110 ppm) in all samples, proving that there is, in fact, an interaction taking place between ethylene and Ag^{+} adsorption sites (despite of other adsorption sites found in the zeolites according to their composition). The model of the proposed ethylene-Ag^{+} complex for each framework are confirmed by comparing the calculated and experimental INS data.

The comparison of the INS spectra of ethylene adsorbed on the Ag-CHA, CsAg-RHO and HAg-LTA zeolites (Fig. 3.24) shows that the major difference among them is the shift of characteristic band at 400 cm^{-1}, related to the molecule's librational mode. This band is blue-shifted for the RHO type structure and redshifted for LTA when compared to CHA and therefore means that it is sensitive the molecule's surroundings, i.e. to the geometry and electrostatic field provided by each cage. The higher the steric hindrance of adsorbed ethylene within a cage the more significant the shift of this band towards a higher wavenumber (cm^{-1}) in INS spectra. While there is a band centered at 395 cm^{-1} for Ag-CHA, it moves to 386 cm^{-1} for HAg-LTA and to 411 cm^{-1} for CsAg-RHO (experimental spectra).

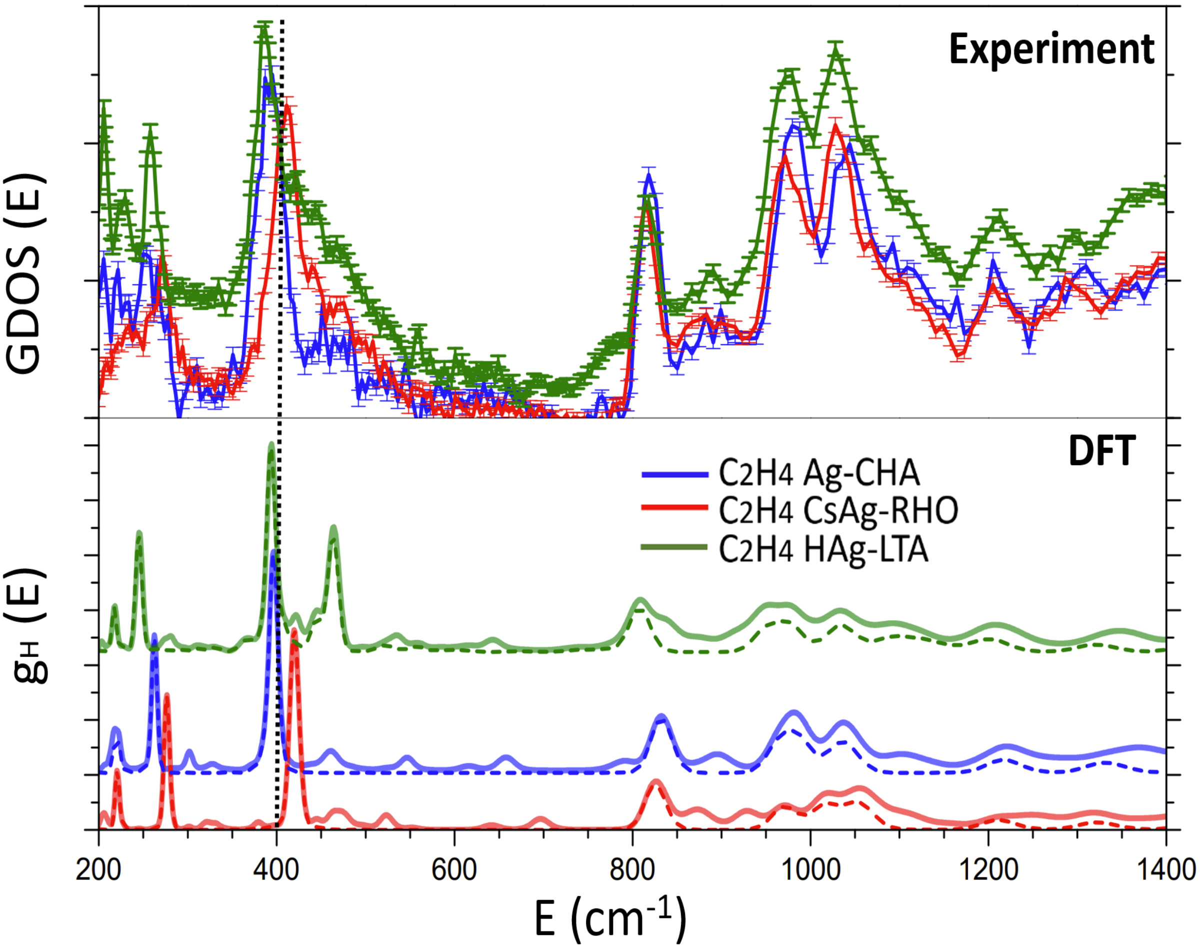

Figure 3.24: Comparison between experimental and calculated INS spectra of C_2H_4 adsorbed in Ag-CHA, CsAg-RHO and HAg-LTA. Full line spectra represent total contribution (fundamental and first overtone) while the dashed line represent only fundamentals.

The 8-ring side pocket, a region within the zeolites cages that accomodates the complex, works as a critical reactive center due to the favored energy barrier conferred by the constrained environment. From DFT, we observed that the 8-ring side pocket has a rectangular shape in C_2H_4 Ag-CHA model. C_2H_4 CsAg-RHO model confirmed the widely known ellipsoid deformation of RHO's 8-rings and consequently of the *lta* cages due to the presence of Cs^+ cations. In this case, *lta* cages undergo a narrowing in the 8-rings side pocket, which assumes a conic shape. Finally, C_2H_4 HAg-LTA model has a concave shape, giving more freedom to the complex. The geometry of the 8-ring side pockets for each zeolite is shown in Figure 3.25 with the distances between the centroids of the 8-rings. It confirms the relation between the shifts on the band around 400 cm^{-1} and the degree of hindrance of the adsorbed molecule inside each zeolite cage. However, there are more factors affecting the interaction of ethylene adsorbed on silver species than the geometry of the cage, requiring a deeper analysis also considering electronic factors.

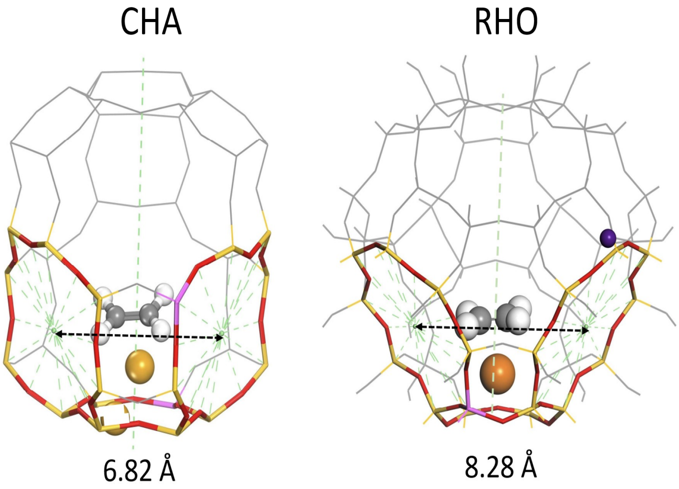

Figure 3.25: Comparison between 8-ring side pockets of Ag-CHA, CsAg-RHO and HAg-LTA with the distances between the centroids of the 8-rings.

In previous studies [60], it was possible to understand the role of the framework in the charge transfer from metal species to ethylene molecule by analysing the deformation density maps of the system. It was observed that the framework oxygen atoms that are the nearest from the metal sites, referred to as O_z, act as an electron reservoir as they provide electrons from the negatively charged framework to the metallic species in π-complexation.

As mentioned previously, in CHA, RHO and LTA structures, Ag^+ cations are placed at 6-rings, slightly displaced towards the interior of *cha* and *lta* cages. In this configuration, the metal form three shorter and three longer bonds to the lattice oxygen atoms of this ring (detailed in Figs. 3.9, 3.16 and 3.23 for C_2H_4 Ag-CHA, C_2H_4 Ag-RHO and C_2H_4 HAg-LTA models respectively). However, in the C_2H_4 CsAg-RHO model, besides the nearest O_z of the 6-ring where the Ag^+ is placed, also the nearest oxygens of adjacent 8-rings contribute to the electron transfer to the metal cation, due to the deformation of 8-rings in the region where the adsorption complex lies or, in other words, due to the conic shape of 8-ring side pockets. The coordination of Ag to oxygen atoms in C_2H_4 CsAg-RHO increases upon its structural distortion, i.e. Ag atom is surrounded by O coming from the 6-ring and also from ellipsoid shape 8-rings.

The coordination of Ag^+ to O atoms from the framework, therefore, define the total charge transfer between the inorganic-organic elements of the models. The total electron transfer of Ag^+-C_2H_4 CsAg-RHO is 0.200 e^-, a value higher than the ones found for Ag^+-C_2H_4 Ag-CHA (0.177 e^-) and HAg-LTA (0.170 e^-) (as calculated by Mulliken Charge Analysis). It also reflects on the C=C stretching of ethylene: the higher the total electron transfer, the higher the redshift (Table 3.2).

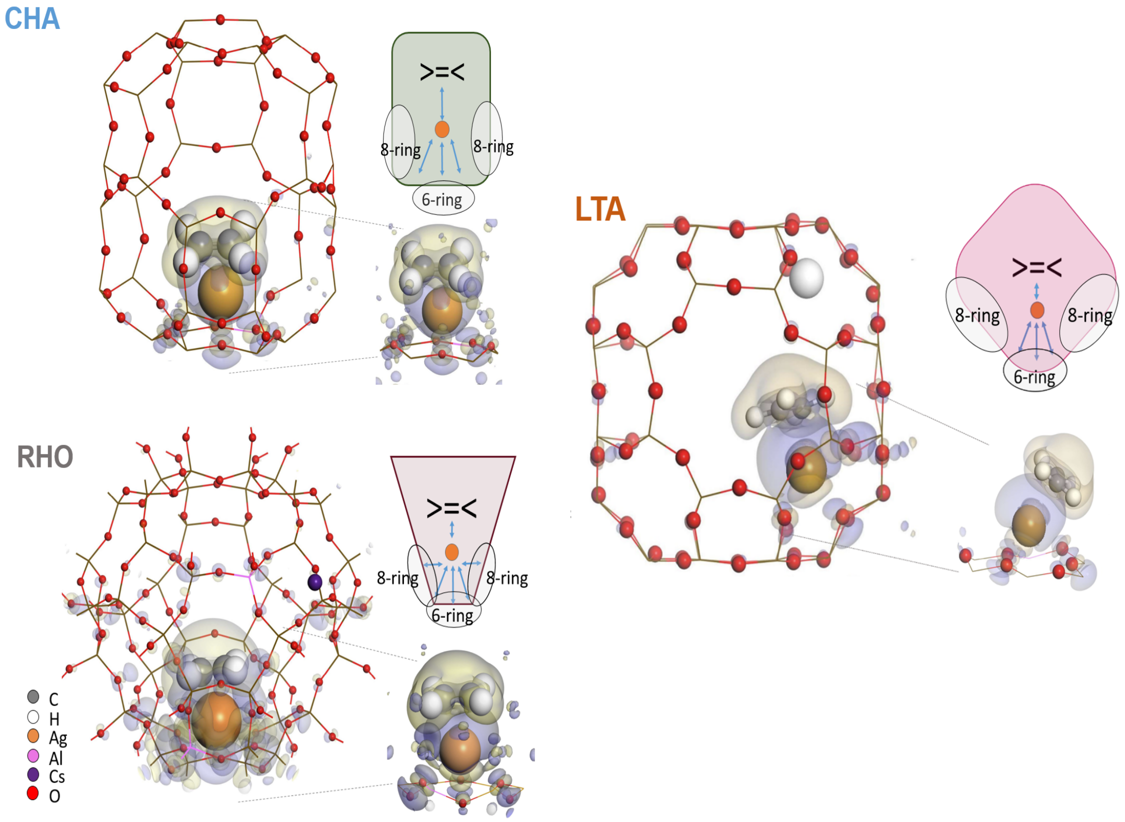

Figure 3.26: Isosurfaces created for -8.369eÅ^{-3}, corresponding to the electron density difference between ethylene and frameworks. The yellow regions represents areas of charge depletion while the blue one, of charge accumulation. This rearrangement is attributed to π-complexation interaction. The details on the right side of the picture schematize the contributions of the Oxygen atoms from the 8-ring pockets.

It was observed that the more constricted the 8-ring side pocket region, the denser the cloud of electrons from O framework around the silver species and the stronger the electrostatic field of the zeolite framework, as seen by EDD plots and schemes in Figure 3.26. The envelopment of silver species by a heavier electron cloud reduces its exposition as an active site, weakening the adsorption energy in a system. On the contrary, a more open and accessible pocket region means greater distances from framework O atoms (composing the 8-rings) to silver, possibly reducing electron transfer between framework and ethylene and making π-complexation formation more difficult. It suggests that there must be an ideal arrangement between 8-ring side pocket shape, Ag^+ coordination to O from the framework or electron transfer between framework and molecule (i.e. electrostatic field) as these aspects affect the adsorption strength. In fact, this is what was observed as C_2H_4 Ag-CHA features the most favorable adsorption energy (-112.89 kJ/mol) among the other 2 systems: C_2H_4 HAg-LTA with -98.71 kJ/mol and C_2H_4 CsAg-RHO with -97.20 kJ/mol, as its retangular 8-ring side pocket geometry is found to be a compromise between the larger pockets of LTA and the highly constricted pocket of RHO.

3.6 Partial Conclusion

This chapter summarized the characterization of the interaction between ethylene and Ag^+ exchanged zeolites, proving the development of a mechanism called π-complexation. Herein a multidisciplinary approach was employed, combining Inelastic Neutron Scattering (INS), Infrared (IR) spectroscopy, Nuclear Magnetic Resonance (NMR), UV-vis and Density Functional Theory (DFT) calculations.

DFT models for each system were created based on samples composition, UV-vis and ^{13}C NMR results, keeping the maximum of simplicity. The UV-vis spectra of degassed samples indicate the presence of different silver species depending on the zeolite structure. Ag^+ coexists with $Ag_3{}^+$ in the Ag-CHA zeolite, while it mostly remains as dispersed Ag^+ in CsAg-RHO and HAg-LTA. ^{13}C NMR spectrum results showed that despite the presence of other active sites in the zeolites (such as H^+, Na^+ and Cs^+), the ethylene interacts with Ag^+ species. The presence of $Ag_3{}^+$ cluster in Ag-CHA does not have an impact of the interaction with ethylene.

The models proposed in this thesis were validated by comparing the calculated and experimental INS data. DFT calculations confirmed the ellipsoid deformation of the 8-rings of RHO framework, provoked by Cs^+ species, causing a narrowing in the *lta* cage region containing the metal-adsorbate complex. This region is known as 8-ring side pocket, which functions as a critical reactive center as a result of the favored energy barrier conferred by the constrained environment. In CsAg-RHO, this region assumes a conic shape, while In Ag-CHA the 8-ring side pocket has a rectangular shape and a concave shape in HAg-LTA.

The INS characteristic band at 400 cm^{-1} within the librational region, which is sensitive to ethylene's surroundings, is blueshifted for the RHO type structure and redshifted for LTA, in comparison to CHA spectra. It suggest a higher steric hindrance within the *lta* cage of RHO structure and a lower one within the *lta* cage of LTA structure.

Electron Density Difference calculations, supported by ^{13}C NMR, confirms the adsorption mechanism of ethylene on Ag^+ based on π-complexation binding. The total electron transfer between organic and inorganic elements of Ag^+-C_2H_4 HAg-LTA is 0.170 e^-, which is smaller than the values found for Ag^+-C_2H_4 Ag-CHA (0.177 e^-) and CsAg-RHO (0.200 e^-) as calculated by Mulliken Charge Analysis. These values are correlated to the coordination of Ag^+ to O atoms from the framework. The higher charge transfer in CsAg-RHO is a consequence of the increase coordination of silver to O atoms from the framework created by the conical shape of 8-ring side pocket in this framework, while the opposite happens to LTA, with a larger 8-ring side pocket.

Considering this panorama, the Ag^+ adsorption center in CsAg-RHO is partially "blocked" by the extra electron cloud and the denser electrostatic field of the zeolite framework, which weakens the adsorption energy of C_2H_4-Ag^+ complex in CsAg-RHO comparing to Ag-CHA. On the other hand, the effects of the rarer electrostatic field within the larger 8-ring side pockets of LTA is also to weaken the adsorption energy of C_2H_4-Ag^+ complex in HAg-LTA comparing to Ag-CHA. These observations suggest that there must be an ideal arrangement between 8-ring side pocket shape, Ag^+ coordination to O from the framework or electron transfer between framework and molecule (i.e. electrostatic field) as these aspects have an impact on the adsorption strength achieved by a zeolitic system.

Chapter 4

Diffusion of ethylene adsorbed on Ag-zeolites

In this chapter, quasielastic data of ethylene adsorbed on Ag-zeolites are analysed and compared, as a first attempt to understand these systems. QENS spectra were fitted with a model for the scattering function considering only one Lorentzian function. HWHM curves were fitted using Hall-Ross jump diffusion model in order to obtain the diffusion parameters such as jump lengths, residence time and diffusivity coefficients. The trends observed for these parameters provided a qualitative comparison of the diffusion of ethylene adsorbed on different zeolites (Ag-CHA, CsAg-RHO and HAg-LTA) through a correlation with each zeolite cage geometry.

4.1 Quasielastic Neutron Scattering Experiments

In this section we present the results of QENS experiments and data treatment used to calculate the diffusion parameters for ethylene adsorbed on the Ag-zeolites studied in this thesis. The first subsection refers to the QENS results, describing the as-measured data, the HWHM fittings results and the obtention of diffusion parameters (residence time, jump lengths, self-diffusion coefficients and activation diffusion barrier) calculated with Hall-Ross jump diffusion model. The second subsection brings the discussion of the results, as an attempt to understand the correlation between the diffusion parameters found by QENS and the main features of the different structures investigated, detailed by DFT models and calculations already described in Chapter 3. Finally, a partial conclusion is drawn.

4.1.1 General Description of QENS data

The as-measured QENS spectra for ethylene adsorbed on Ag-zeolites at temperatures 100, 175 and 235K (at Q = 1.20 Å $^{-1}$) are shown and compared in Figure 4.1. C_2H_2 Ag-CHA at 50K was used as reference as no quasielastic signal is observed. The degassed zeolites samples were not measured and their signal could not be subtracted from the signal of the loaded zeolites.

The following observations can be made from these spectra:

- At 100K, the wider quasielastic broadening displayed by ethylene adsorbed on Ag-CHA in comparison to HAg-LTA and CsAg-RHO indicates a higher motion of the molecule in this zeolite.

- At 175K, the quasielastic signals broaden in all systems, indicating an increase on the mobility of ethylene. This increase is more significant for ethylene adsorbed on HAg-LTA, which almost overlaps the signal displayed by ethylene on Ag-CHA.

- At 235K, the quasielastic broadening of ethylene adsorbed on HAg-LTA finally overlaps the one displayed by ethylene on Ag-CHA.

Based on these observations, it is expected that:

- The activation diffusion barrier of ethylene adsorbed on HAg-LTA must be the higher.

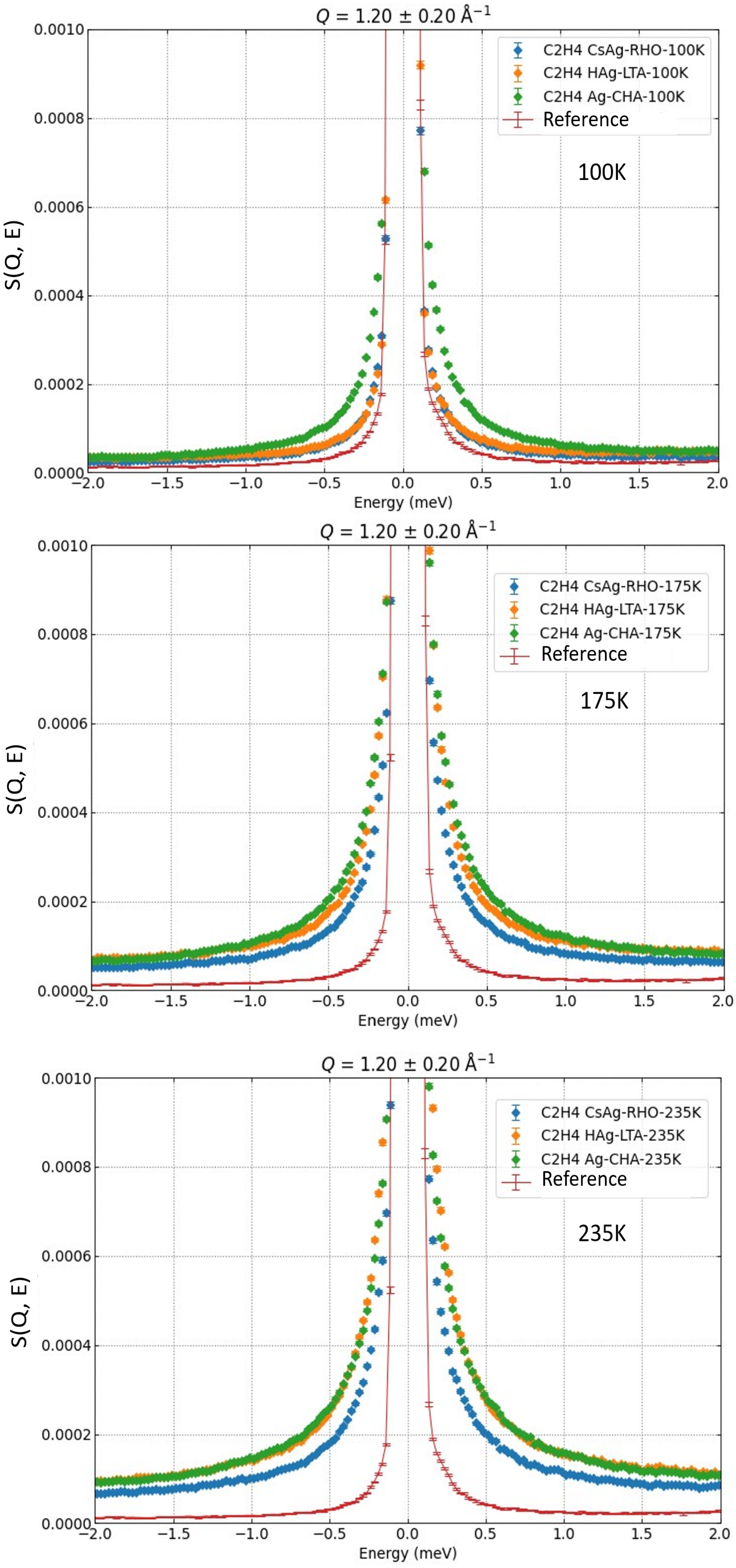

Figure 4.1: As-measured QENS spectra for ethylene adsorbed on Ag-CHA, CsAg-RHO and HAg-LTA at different temperatures compared to loaded zeolite sample measured at 50K as reference.

The QENS spectra were fitted with a model for the scattering function expressed by equation 2.26:

$$S(Q,\omega) = \exp\left(-\left(QU_{\mathrm{Tot}}\right)^2\right)\left[A_0(Q)\delta(\omega) + (1 - A_0(Q)\mathcal{L}(Q,\omega)) \circledast R(\omega)\right] + B(Q)$$

The quasielastic broadening term takes into account only one Lorentzian function ($\mathcal{L}(Q,\omega)$).

The fitted quasielastic spectra at 100 K and Q = 1.0 Å^{-1} for adsorbed ethylene on zeolites Ag-CHA, CsAg-RHO and HAg-LTA are depicted in Figures 4.2 (spectra related to other values of Q and different temperatures can be found in the section A.7 of the Appendix). The dots in grey are the as-measured QENS data; the red line is the total fit of components in equation ; the black and yellow lines are the instrument resolution and flat background functions, respectively; the green line is the Lorentzian function.

The EISF parameter for these systems are not discussed in this work due to the low mobile fraction of ethylene on the samples, which would not allow significant conclusions.

As mentioned in section 2.1.4, the dependence of the quasielastic broadening as a function of Q is represented by a parameter known as Half Width at Half Maximum **(HWHM)**. The HWHM curves can be fitted with theoretical diffusion models giving parameters related to the diffusion of an adsorbed molecule, such as jump lengths (L) and residence time (τ_0). The HWHM obtained for ethylene adsorbed on each Ag-zeolite and its derived parameters are described in the next subsection.

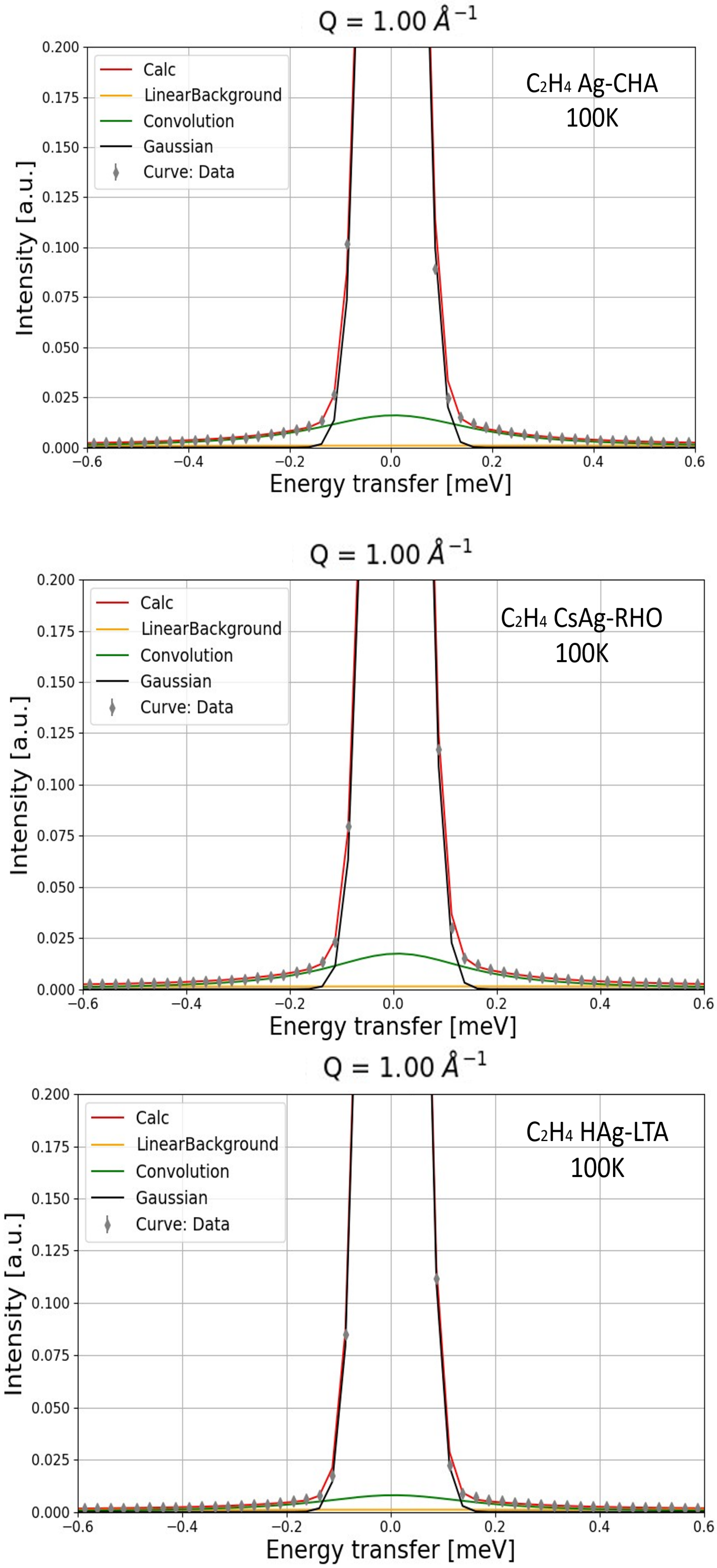

Figure 4.2: QENS spectra obtained for ethylene adsorbed on Ag-CHA, CsAg-RHO and H-LTA at 100K at Q = 1.00 Å. Red is the total fit while Black, Green and Yellow are used to represent the instrument resolution, Lorentzian and flat background functions.

4.1.1.1 HWHM fitting

The half-width half maxima (HWHM) of the Lorentzian components of the QENS spectra as a function of Q^2 at 100, 175 and 235K for the zeolites in this work are shown in Figure 4.3.

As mentioned above, the variation of the HWHM curve with Q^2 can be fitted with theoretical models, revealing valuable information about the diffusion behaviour of a molecule. These models can describe a type of motion characterized by jump diffusion, where a molecule remains stationary at a certain site for a given period of time before translating in a very fast interval to the next site. Different jump diffusion models found for molecules diffusing in zeolite materials were already discussed in session 2.1.4.2.

The HWHM curves represented in Figure 4.3 of ethylene adsorbed on Ag-CHA, CsAg-RHO and HAg-LTA could only be fitted with Hall-Ross jump diffusion model. Although, there are still significant deviations from experimental results.

The experimental HWHM curves present a significant peak at Q^2 between 0 and ≈ 1.0 $Å^{-2}$, reaching a minimum around 1.5 $Å^{-2}$ and then increasing again at higher Q^2.

A second Lorentzian function was, then, introduced to the equation 2.26 in order to represent another possible motion present in the same time window, however it could not fit the experimental QENS data. As mentioned previously, it was observed that the calculated QENS spectrum fits the experimental data very well considering just one Lorentzian.

These deviations, remarkably at the values ranging from 0 to ≈ 1.0 $Å^{-2}$, result from a phonon contribution due to very strong Bragg peaks found for the systems at corresponding Q values, coming from the zeolite framework. The S(Q,E) space and S(Q) for each sample are shown in the Appendix (Figs. A.30 and A.31).

On the other hand, it should be considered that, at the temperatures selected for the QENS experiments in this thesis, ethylene molecule most probably is still linked to Ag^+, as the energy provided is not enough to provoke the decomposition of the π-complex pair (proved by INS experiments, detailed in section A.7.5, fig. A.32). This could increase the complexity of the adsorbed molecule motion and its environment, also resulting in deviations on HWHM curves at mid and higher Q values, as reported in previous studies [120].

Further corrections to clarify and attenuate the framework contribution could not be completely carried out until the submission of this thesis.

However, despite the poor quality of the fitting, the parameters obtained with Hall-Ross model (residence time (τ_0), jump lengths (L) and self-diffusion coefficients (Ds)) were analyzed **as a first attempt to qualitatively understand such systems**.

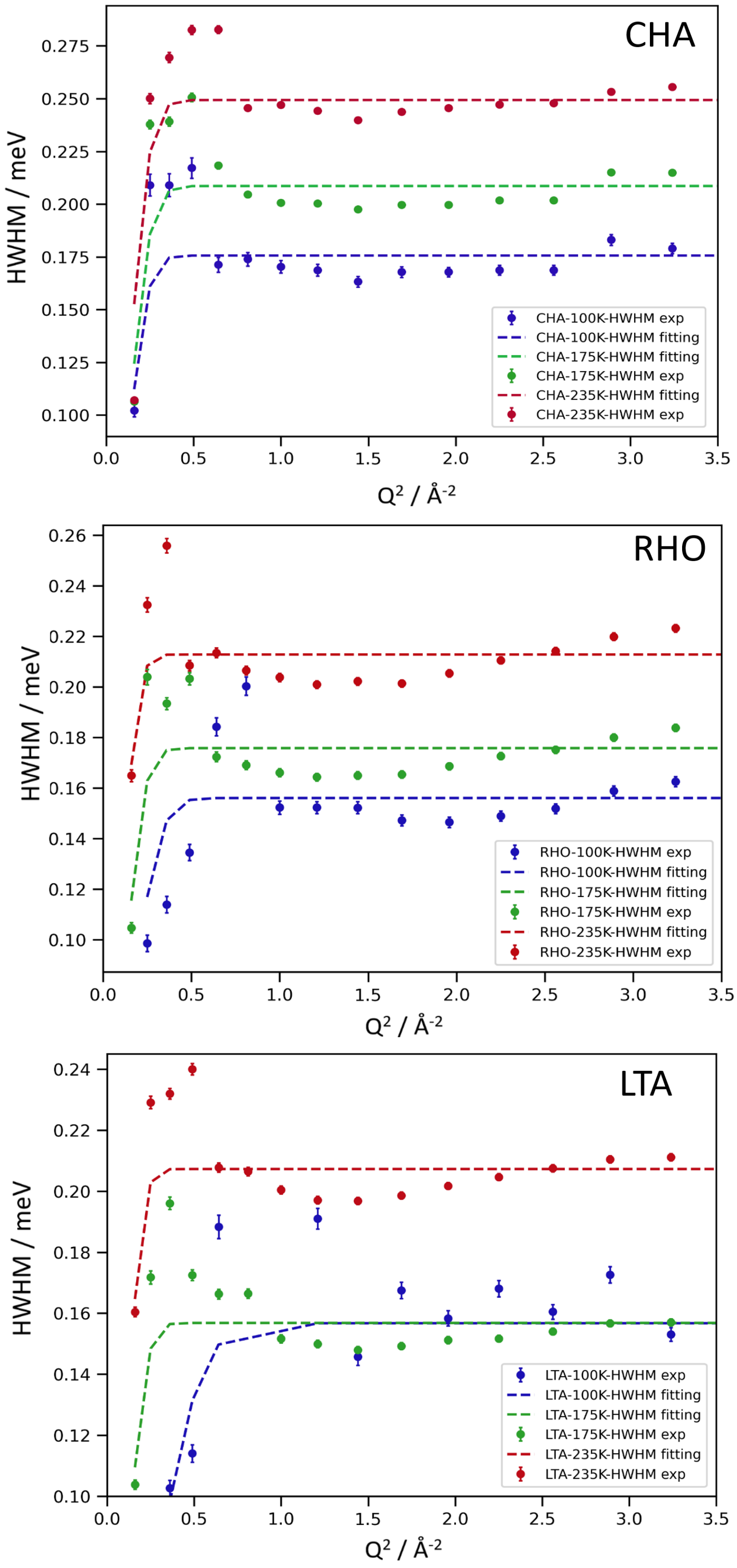

Figure 4.3: Q dependencies of the HWHM of the quasielastic components of the QENS spectra at 100, 175 and 235 K for ethylene diffusing in Ag-CHA, CsAg-RHO and HAg-LTA. Each can be fitted with a Hall-Ross jump diffusion model. Herein, the errors displayed by the experimental HWHM curves are only related to neutron point data, i.e. related to the instrument statistics, not taking into account corrections due to the zeolite framework contribution by other theoretical methods.

Table 4.1: Summarizing table addressing temperatures (K), L (Å), τ_0(ps), diffusivities (D_S) and apparent activation barrier (E_a, kJ/mol) as calculated based on Hall-Ross model.

	Temp. (K)	L (Å)	err	tau (ps)	err	D_S ($\times 10^{-8}$ m^2/s)	Ea (kJ/mol)
C_2H_4 Ag-CHA	100	8.40	± 1.17	3.74	± 0.01	9.43	0.57
	175	8.40	± 0.38	3.15	± 0.00	11.21	
	235	8.60	± 0.00	2.63	± 0.00	14.00	
C_2H_4 CsAg-RHO	100	6.65	± 0.00	5.24	± 0.00	5.24	1.90
	175	9.13	± 0.00	3.74	± 0.00	11.14	
	235	11.00	± 0.00	3.09	± 0.00	20.00	
C_2H_4 HAg-LTA	100	3.89	± 0.18	4.19	± 0.00	4.30	3.20
	175	9.67	± 0.79	3.87	± 0.01	11.14	
	235	11.11	± 0.96	3.17	± 0.00	19.46	

From the information described in Table 4.1, it can be observed that:

- The jump residence time (τ_0) decreases as the temperature increases from 100K to 235K.
- The jump lengths (L) values calculated for ethylene adsorbed on Ag-CHA are nearly constant for all temperatures while jump lengths found for ethylene on CsAg-RHO and HAg-LTA have a considerable increase as the temperature rises.

4.1.1.2 Activation Diffusion Barrier

The increase of ethylene diffusivity coefficients with temperature indicates that the diffusion is a thermally activated process. Therefore, the apparent activation barrier, which corresponds to the energy barrier that the molecule needs to overcome to initiate motion, was derived from the Arrhenius plot (Fig. 4.4). The calculated energy is indicated in Table 4.1 for each zeolite. The activation barrier for ethylene diffusion in the systems exhibit a maximum (3.20 kJ/mol) for LTA and a minimum (0.57 kJ/mol) for CHA, being that of RHO in between with 1.9 kJ/mol.

In the next subsection, the Ag-zeolite systems are analysed in terms of geometry as an attempt to correlate these features to the trends found for diffusion and activation diffusion barrier for each one of them.

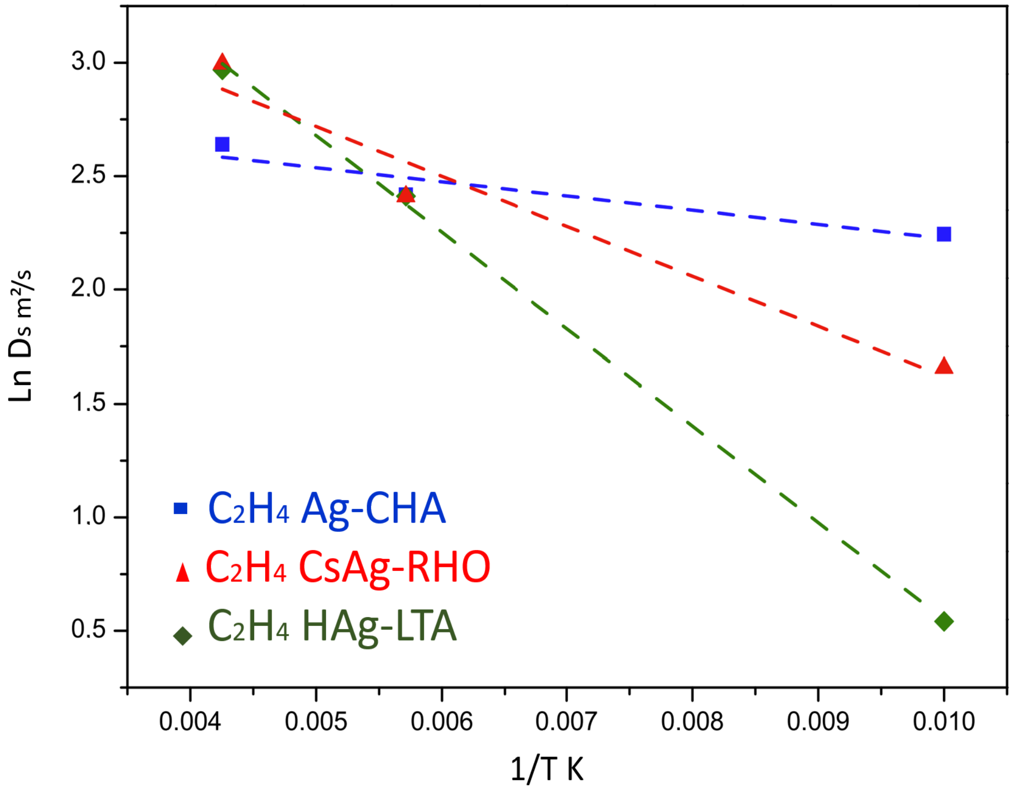

Figure 4.4: Arrhenius plots for diffusion of ethylene adsorbed on Ag-CHA, CsAg-RHO and HAg-LTA. The activation energies obtained are listed in Table 4.1.

4.1.2 Discussion

As explained in Chapter 1, when molecules diffuse freely in an isotropic medium (as in the case of a gas), the diffusion is described by the interactions or collisions that happen among the assemble of molecules as a function of their thermal motion. The diffusion in an intracrystalline medium, however, involves different aspects, especially in porous materials. Along with the inter molecular interactions, collisions between the molecules and the walls of the material in which they are confined should be considered while investigating the diffusion parameters. These molecule-walls interactions will become more and more relevant and characteristic defining for the diffusion process as the material passes from macro to microporous.

In recent studies involving Molecular Dynamics, the diffusion of small hydrocarbon molecules (such as methane, ethane and propane) in CHA, RHO and LEV zeolites was described [121]. Based on the MD trajectory analysis of adsorbed methane at temperatures ranging from 298K to 673K, the jump length (L) values of the adsorbed molecule diffusion path were extracted. It was confirmed that the length of each jump between the adjacent sites in adjacent cavities is closely related to the cavity dimension. The cavity dimensions reported by the same authors are found to be LEV (8.1 x 9.4 $Å^2$) $<$ CHA (9.1 x 10.8 $Å^{2}$) $<$ RHO (11.4 x 11.4 $Å^2$) and the inter-cavity jump length (L) follows the order of LEV (8.0 Å) $<$ CHA (9.1 Å) $<$ RHO (14.8 Å). The calculated diffusion trends for each zeolite have been reported to follow the order of RHO $>$ CHA $>$ LEV. Therefore, it suggests that larger cavities provides larger L and higher diffusion rates.

Herein, as expected, the calculated jump lengths L for ethylene adsorbed on Ag-CHA, CsAg-RHO and HAg-LTA at temperatures 100, 175 and 235 K increases with the increase of cage dimension. The maximum L values found are close enough to the theoretical cage dimensions (used in DFT calculations described in section 3, represented in Figure 4.5). For ethylene adsorbed on Ag-CHA (9.1 x 10.8 Å ^{2}), the maximum L value (at 235K) is 8.6 Å; for CsAg-RHO (11.4 x 11.4 Å^{2}), the maximum L value is 11 Å, slightly shorter than the L reached by ethylene on HAg-LTA (13 x 13 Å^{2}), 11.11 Å. Without further details from Molecular Dynamics simulations, it is not possible to define if the diffusion observed is intra or intercage.

Also the diffusion rate trend (observed in Figure 4.4) in Table 4.1 follows the increase in cage dimensions (LTA > RHO > CHA). Looking back at Figure 4.4, the diffusion of ethylene on HAg-LTA is the lowest one at 100K. But at 235K it already surpasses all others. The maximum L calculated for the cage (at 235K) is the longest, due to LTA dimensions (it is the largest cage among CHA and RHO). It means that the distances between the active sites where the molecule would preferably go to are also more distant from each other. In order to achieve this longer jump, this cage would require more energy. Thus, it explains why the activation barrier for diffusion of ethylene on HAg-LTA is the highest while for Ag-CHA (the smallest one) is the lowest.

Therefore, the features displayed by Ag-CHA justify why this zeolite has a smaller activation diffusion barrier (HAg-LTA > CsAg-RHO > Ag-CHA), as seen in Table 4.1.

The chart in Figure 4.5 summarizes the correlation between cage dimensions, jump lengths and activation diffusion barrier.

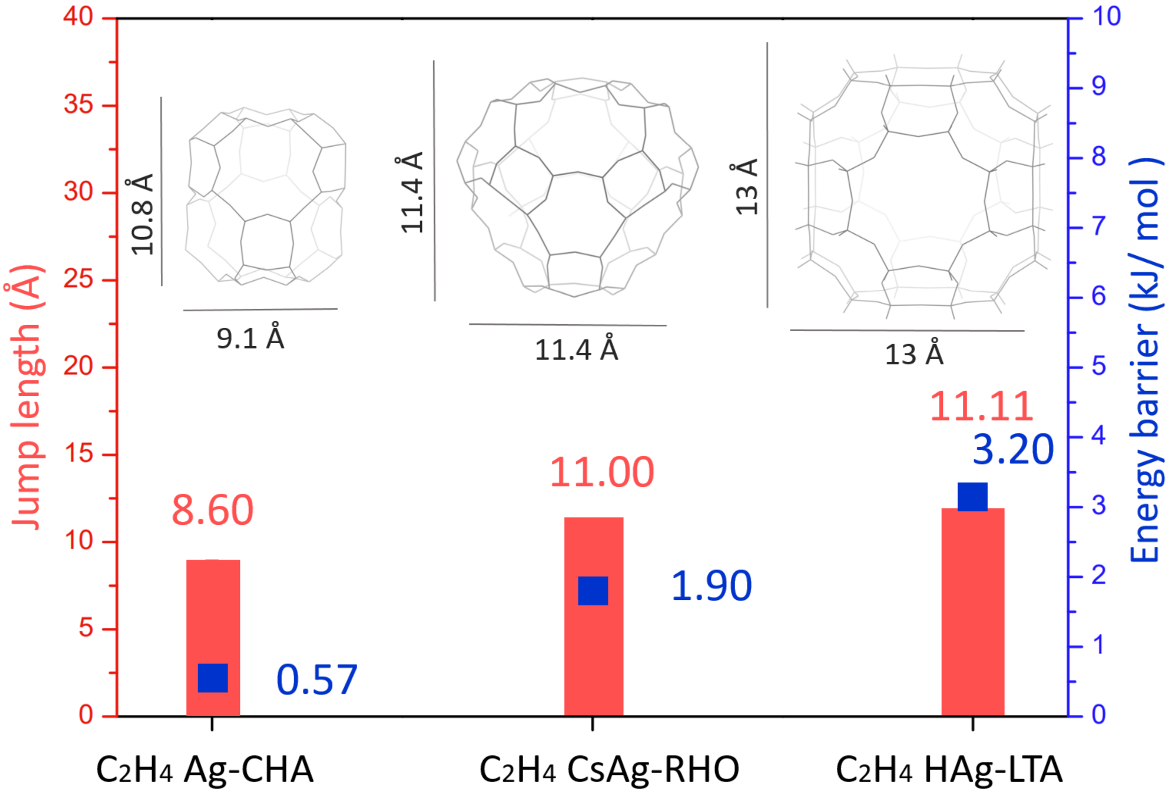

Figure 4.5: Summary chart correlating cage dimensions and maximum jump length (at 235K) and activation diffusion barrier values. The motion observed in QENS data must correspond to a small fraction of non-adsorbed molecules or to short diffusion motions of ethylene associated with silver, both happening within the instrument time window.

4.2 Partial Conclusion

QENS experiments were performed in Ag-CHA, CsAg-RHO and HAg-LTA zeolites loaded with ethylene at temperatures 100, 175 and 235K. The spectra were fitted with a model for the scattering function considering only one Lorentzian function for the quasielastic broadening term, i.e. considering only one type of motion to describe the system.

The fitting of HWHM curves was carried out even with some deviations from experimental data, as a first attempt to assess the systems qualitatively. The Hall-Ross jump diffusion model was used in order to obtain diffusion parameters (jump lengths, residency time, diffusivity coefficients) and, from them, calculate the activation diffusion barrier for the systems. It was confirmed the higher diffusion rate and activation diffusion barrier for ethylene adsorbed on HAg-LTA and the lowest diffusion rate and activation diffusion barrier for ethylene adsorbed on Ag-CHA, as a consequence of cage dimensions, being CsAg-RHO in between.

As the dimensions of LTA typology cage are the largest, the values found for jump lengths in these systems are also the longest.

The smallest cage size of CHA type zeolite explains the smallest activation diffusion barrier for ethylene adsorbed on Ag-CHA in comparison to HAg-LTA and CsAg-RHO (HAg-LTA > CsAg-RHO > Ag-CHA).

Chapter 5

General Conclusions

Selective adsorption based separation methods performed by adsorbent materials stand out as the most promising alternatives for chemically challenging separations, such as the case of ethylene/ethane.

One of the selective mechanisms applied to adsorbents is the equilibrium separation, based on the principle of preferentially allow the adsorption of certain molecules on the solid surface while excluding the others due to a stronger affinity towards one of them.

The well-known π-complexation is one effective way of achieving this targeted adsorption. In a π-complex, a transition metal donates electron to the antibonding orbitals of an unsaturated organic molecule while simultaneously accepting electron from the bonding orbitals of the molecule. Adsorbent materials can be functionalized with metal cations in order to enhance selectivity towards a desired component. Zeolites is a very suitable material for this purpose due to their remarkable physical and chemical properties.

It is possible to identify the formation of π-complexation by analysing the vibrational properties of a system upon adsorption as specific changes in the vibrational frequencies give hints about the nature of the adsorption mechanism. Although Infrared and Raman may be applied for this purpose, Inelastic Neutron Scattering present exceptional advantages such as: nuclear interaction with matter and sensitivity to hydrogen atoms. Apart from that, neutron scattering spectra are easily and accurately modelled, which allows the extraction of microscopic details related to the binding.

On the other hand, if the final aim of the selective adsorption is to recover the adsorbed component of interest, it is then necessary to evaluate the transport properties of the adsorbent. An efficient adsorbent has a fast diffusion and, therefore, can be used in smaller amounts. The microscopic study of diffusion is well established via Quasielastic Neutron Scattering technique, which describes microscopic diffusion in zeolites in terms of jumps.

This present thesis described the identification, characterization and comparison of π-complex formation on Ag-zeolites, aiming to understand how the local geometry of small-pore zeolites and the neighboring chemical composition of the Ag^+ sites influence the characteristics of π-complexes in these materials and, consequently, the adsorption and diffusion of ethylene on Ag-zeolites by a combination of Inelastic and Quasielastic Neutron Scattering and Density Functional Theory. CHA, RHO and LTA zeolites are largely applied in gas separation processes. They were chosen in this study due to their similar small pore sizes, but different cavity shapes and flexibilities.

The models proposed in this thesis were validated by comparing the calculated and experimental INS data. DFT calculations confirmed an ellipsoid deformation of the 8-rings of the flexible RHO framework. This deformation is caused by an attempt of the framework to coordinate Cs^+ species located inside *d8r*, which leads to a narrowing in the *lta* cage region where the metal-adsorbate complex lies. This region is known as 8-ring side pocket. The constrained environment of the 8-ring side pockets creates a favored energy barrier that works as a critical reactive center within zeolite cages. In CsAg-RHO, this region assumes a conic shape, while In Ag-CHA and HAg-LTA the 8-ring side pocket has a rectangular and concave shape, respectively.

The INS spectra of ethylene adsorbed on the Ag-CHA, CsAg-RHO and HAg-LTA shows that the characteristic band at 400 cm^{-1}, related to the molecule's librational mode, is blue-shifted for the RHO type structure and redshifted for LTA respect to CHA. This observation points to a higher steric hindrance of ethylene within RHO topology and a lower one for LTA.

Electron Density Difference calculations, supported by ^{13}C NMR, suggests that the adsorption mechanism of ethylene on Ag^+ relies on the π-complexation scheme (also proved by the C=C stretching of adsorbed ethylene). The ethylene donates electrons from its π-orbital to the outermost empty orbital of the cation, forming a σ bond. However, there is also a contributing transfer of electrons from the network oxygen atoms to Ag^+ and then to the π^* orbital of the adsorbed ethylene. These oxygen atoms are the closest ones from Ag species, O_z, that are located in the 6-ring of the pocket zone.

Mulliken Charge Analysis indicates a higher charge transfer in CsAg-RHO model than in Ag-CHA and HAg-LTA. This higher charge transfer is a result of the increased coordination of silver to O atoms from the framework created by the conical shape of 8-ring side pocket in RHO. The Ag^+ adsorption center in CsAg-RHO is enveloped by the extra electron cloud provided by O atoms of the deformed 8-rings. This blockage reduces the exposure of Ag species as an active site, leading to a weaker adsorption energy of C_2H_4-Ag^+ complex in CsAg-RHO respect to that of Ag-CHA. Meanwhile, the same effect of weaker adsorption energy happens to LTA, however due to the opposite reason: the weaker adsorption energy achieved by HAg-LTA if compared to Ag-CHA is due to the wider 8-ring side pockets of LTA, leading to a decreased coordination of O from the framework to Ag species.

The analysis of QENS results describes a higher diffusion rate and activation diffusion barrier for ethylene adsorbed on HAg-LTA and the lowest ones on Ag-CHA.

The dimensions of LTA typology cage are the largest, in a way that the values found for jump lengths in these systems are also the longest. It requires more energy to initiate a diffusion from one active site to the other.

Therefore, the arrangement between 8-ring side pocket shape, Ag^+ coordination to O from the framework and electron transfer between framework and molecule (i.e. electrostatic field) are key factors to be considered when aiming to achieve a certain range of adsorption energy in a system based on π-complexation. At the same time, the cage size also affects the diffusion rate and activation diffusion barrier for ethylene adsorbed on Ag-zeolites.

It leads to the question: among the three zeolites considered, which one would be more adequate from the industrial point of view, where the aim is to employ less energy as possible to recover the ethylene? In this case, the weaker interaction of ethylene-silver in the flexible CsAg-RHO zeolite would be a more interesting option. However, the mandatory presence of cesium in RHO framework may limit the accessibility to its pores and cages, becoming less efficient than the other two. On the other hand, HAg-LTA, which has an adsorption energy value very similar to the one of CsAg-RHO (-98.71 and -97.20 kJ/mol, respectively) providing higher diffusion rates, could be more efficient. Therefore, an optimized adsorbent must reach a compromise between separation efficiency, energy demand and diffusion rates.

The combination of theoretical and experimental approaches for ethylene π-complexation studies in silver zeolites may be extended to investigations in many alike materials (whether other zeolites or different microporous systems, e.g. Metal-Organic Frameworks) as a tool to provide satisfactory qualitative and quantitative information. This would allow the fine tuning of the synthesis conditions, facilitating the process of obtaining zeolites with target properties for separation processes.

As future work, it is expected to advance in the QENS studies of the systems (both in experimental and computational aspects with Molecular Dynamics simulations). Firstly, corrections must be carried out in order to attenuate the possible influence of framework Bragg peaks in HMHW data, providing a better fitting with diffusion models. Another aspect to be considered is to conduce experiments with increased loading of ethylene on Ag-zeolites in order to mimic real conditions. These studies would be supported by Molecular Dynamics simulations.

APPENDIX

A.1 XRD patterns

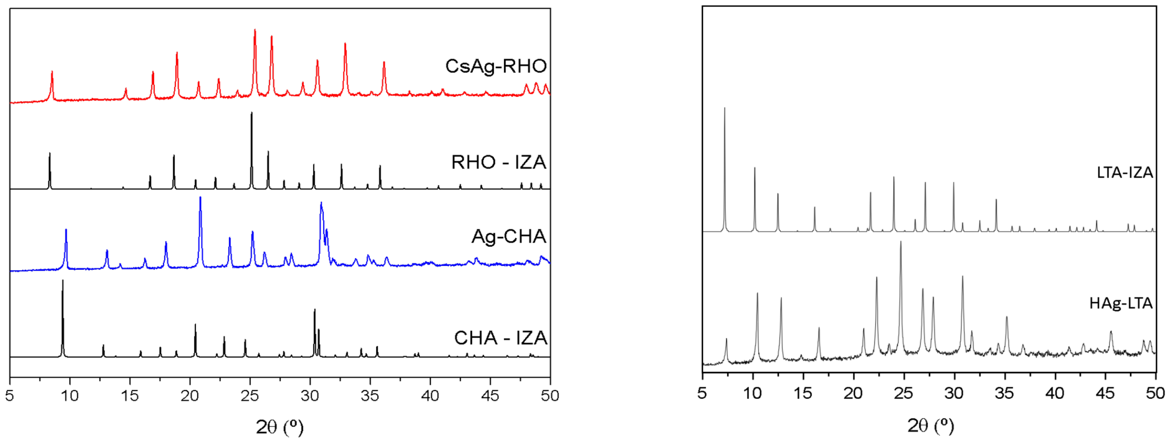

Figure A.1: XRD patterns of zeolites Ag-CHA, CsAg-RHO and HAg-LTA, consistent with database of IZA[45] for each corresponding zeolite type.

A.2 UV-vis and ^{13}C NMR spectra

The UV-Vis Cary 7000 spectrometer with a diffuse reflectance accessory (Praying Mantis Harrick) was used to carry out UV-Vis experiments. The spectra were measured using $BaSO_4$ as internal standard. Interpretation of spectra can be found in Chapter 3.

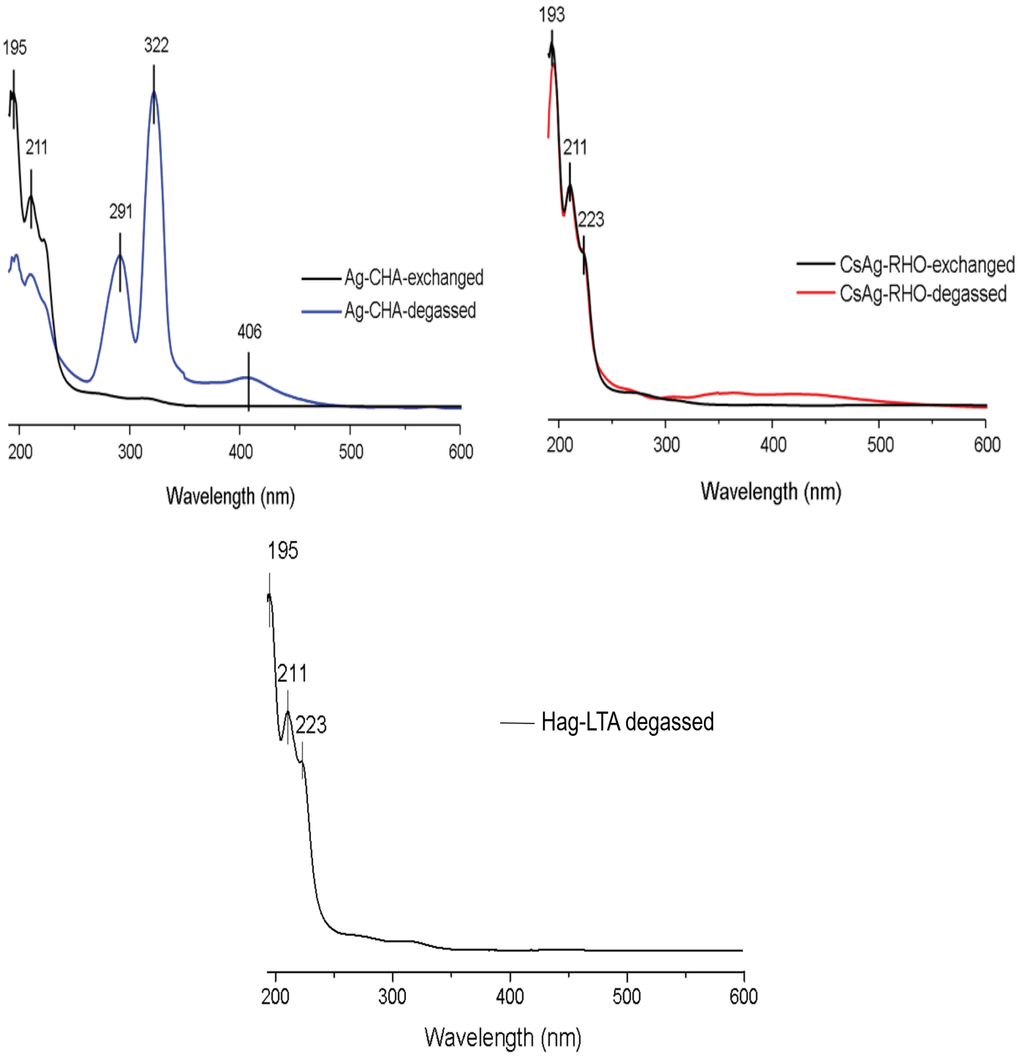

Figure A.2: UV-Visible spectra of silver exchanged and degassed (at 400 °C overnight) for Ag-CHA, CsAg-RHO and HAg-LTA (only degassed spectrum).

A Bruker Oxford-Avance spectrometer, with a 7 mm probe and spinning the sample at 5 kHz, was used to record ^{13}C NMR spectra at 400 MHz. ^{13}C NMR spectra were obtained at 25 °C by cross polarization sequence under angle spinning conditions (^{1}H-^{13}C CP-MAS), considering 4 µs $\pi/2$ pulses for ^{1}H with a contact time of 2 ms and a recycle delay of 3 s. Adamantane (δ ^{13}C = 38.3 ppm) was employed as reference.

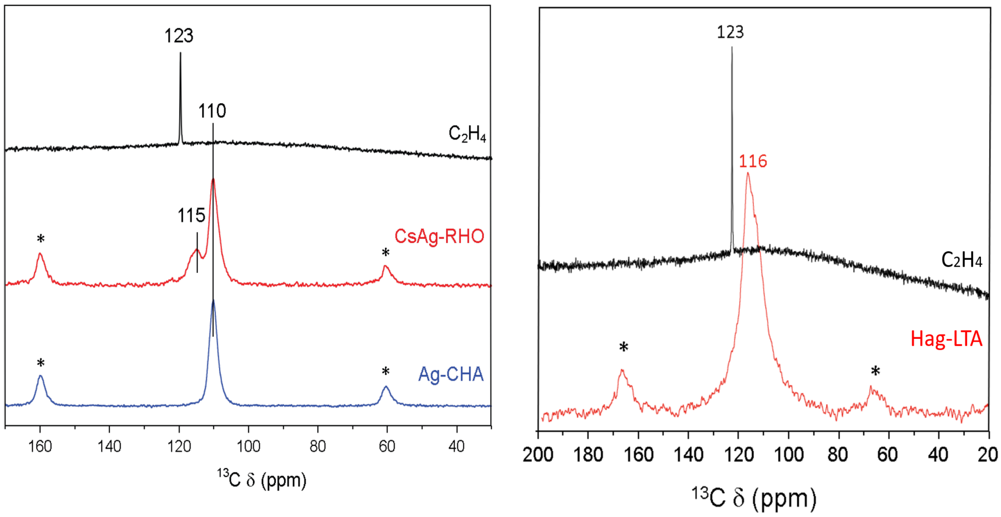

Figure A.3: ^{13}C MAS NMR spectra of free-ethylene gas compared to ethylene adsorbed on Ag-CHA, CsAg-RHO and HAg-LTA zeolites. Spinning rotation bands are indicated by asteriks (*).

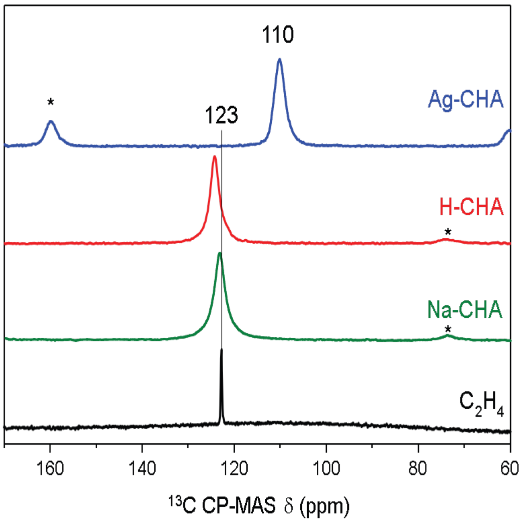

Figure A.4: ^{13}C NMR spectra of ethylene adsorbed on Ag-CHA, H-CHA and Na-CHA in comparison with C_2H_4. Spinning rotation bands are signed by asterisk.

A.3 Structural details of DFT models

A.3.1 Energy Calculation details for Ag-CHA model: framework configuration

Two different placement schemes for Ag cations in Ag-CHA model were considered. The first scheme was the energetically preferred combination (referred to as **A**), which is the one described and used in section 3.2. The other scheme is called **B**. The energy difference ΔE(**A-B**) is given by:

A = 1 Ag @ S_2, 1 Ag @ S_2, 1 Ag @ S_3

B = 1 Ag @ S_2, 1 Ag @ S_2, 1 Ag @ S_2

ΔE(**A-B**)= -10.94 kJ/mol, which is also the ΔE($\mathbf{S_2}$-$\mathbf{S_3}$) calculated with DFT, assuming 1 Ag atom would be at position S_2 OR S_3.

A.3.2 C_2H_4 $Ag_3{}^+$-CHA configuration

One Ag_3^+ cluster was introduced at S_2 site of CHA cavity with 1 ethylene/u.c.The energy values for this configuration are described in Table A.5. After geometry optimization, the cluster turned into an isosceles triangle (Fig. A.1). The distances of $Ag_{(1)}$-$O_{(1)}$, $Ag_{(1)}$-$O_{(2)}$, $Ag_{(3)}$-$C_{(1)}$, $Ag_{(3)}$-$C_{(2)}$ and the cluster dimensions are found in Table A.1. The values obtained for the optimized cluster size, with Ag-Ag separations ranging from 2.7 to 2.9 are in agreement with previous studies[122].

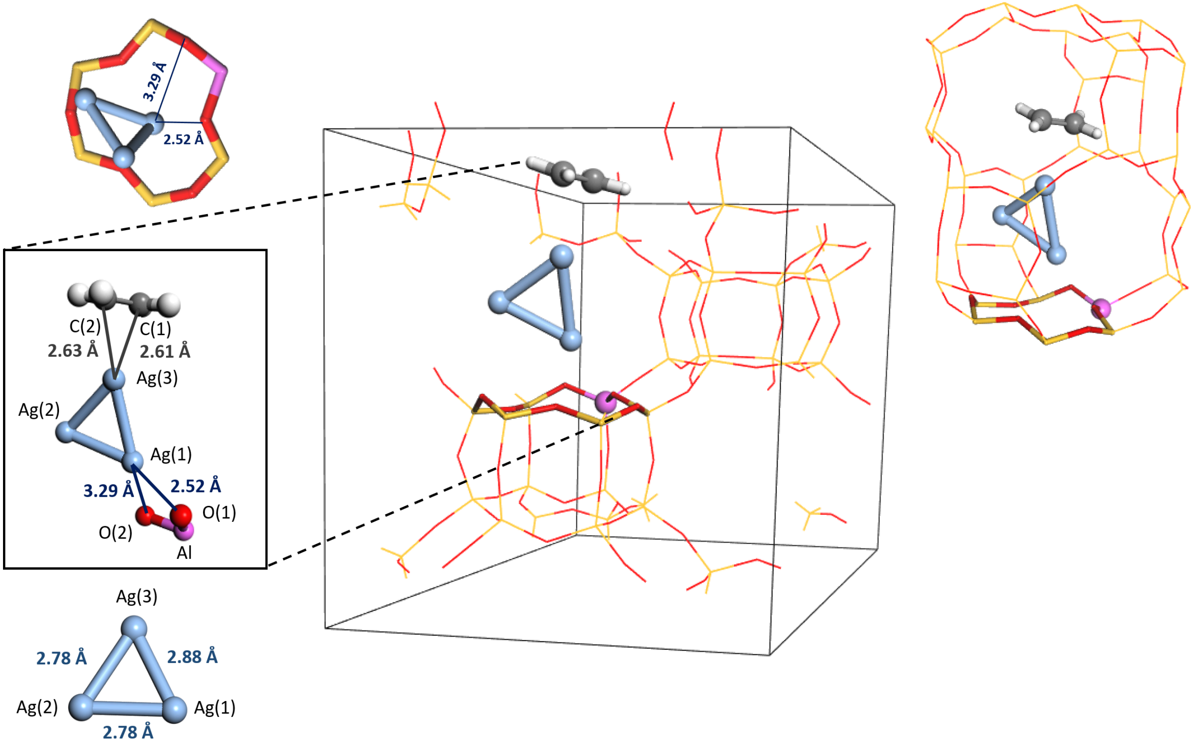

Figure A.5: C_2H_4 Ag_3^+ configuration after geometry optimization. Details of atom distances and atoms also shown.

Table A.1: DFT equilibrium distances and adsorption energy for C_2H_4 Ag_3^+ configuration.

Model	Ag-$O_{(1)}$	Ag-$O_{(2)}$	Ag-$C_{(1)}$	Ag-$C_{(2)}$	E_{ads} (kJ/mol)
C_2H_4 Ag_3^+-CHA	2.52	3.29	2.61	2.63	−64.00

A.3.3 AgRHO and NaAg-RHO: configuration details

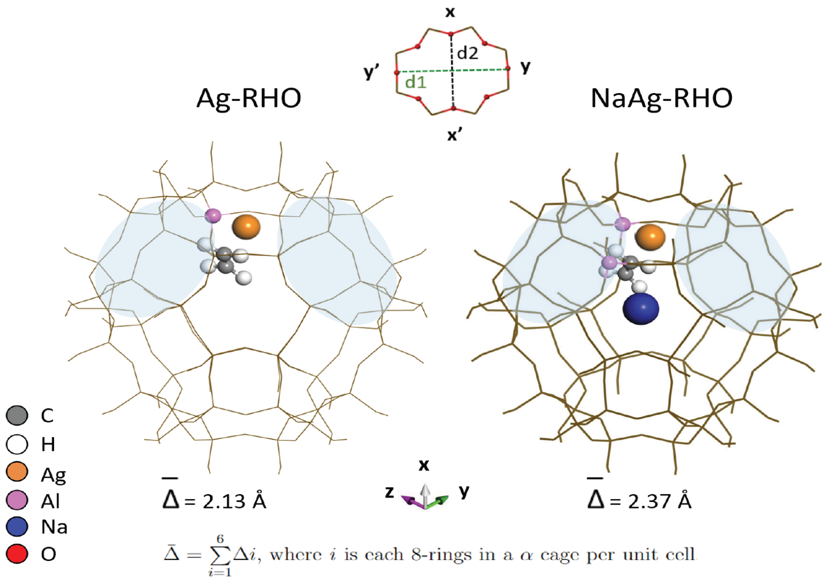
x
d2
y'
d1
y
x'
Ag-RHO
NaAg-RHO
C
H
Ag
Al
Na
O
$\bar{\Delta}$ = 2.13 Å
x
z
y
$\bar{\Delta}$ = 2.37 Å
$\bar{\Delta} = \sum_{i=1}^{6} \Delta i$, where i is each 8-rings in a α cage per unit cell

Figure A.6: Ag-RHO and NaAg-RHO are represented in the figure. For these configurations, after geometry optimization, the framework also undergoes symmetry change, as explained for CsAg-RHO. In CsAg-RHO model, the major axis (d1) of the deformed upper 8-rings are in direction x-x'. For Ag-RHO and NaAg-RHO, d1 is in the direction y-y'. As a result, in Ag-RHO and NaAg-RHO the cage narrowing occurs in the region opposite to where the Ag-C_2H_4 is located.

A.4 C=C stretching shift calculation

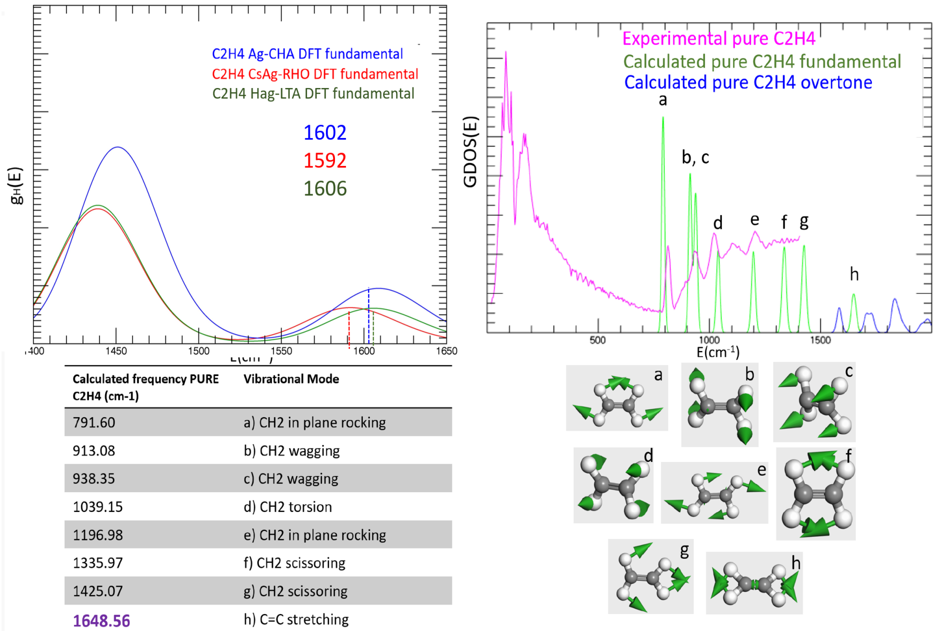

Calculated frequency PURE C2H4 (cm-1)	Vibrational Mode
791.60	a) CH2 in plane rocking
913.08	b) CH2 wagging
938.35	c) CH2 wagging
1039.15	d) CH2 torsion
1196.98	e) CH2 in plane rocking
1335.97	f) CH2 scissoring
1425.07	g) CH2 scissoring
1648.56	h) C=C stretching

Figure A.7: C=C streching calculation by comparing calculated C=C stretching frequency of C_2H_4 with the calculated C_2H_4 adsorbed on each Ag-zeolite. These values are ≈ 46 cm^{-1} for Ag-CHA, 56 cm^{-1} for CsAg-RHO and 42 to HAg-LTA.

A.5 Mulliken Charge Analysis

Total charge transfer in each system is calculated by a summation of the charges of C_2H_4 elements after adsorption [114]. Tables A.2, A.3, A.4 and figures A.8, A.9 and A.10 address the distribution of atom index and partial charges in all atoms for the systems.

Table A.2: Mulliken charges for Ag-CHA model.

Atom	System	Framework
Si1	1.766585	1.750957
Si2	1.746913	1.742517
Si3	1.757365	1.742729
Si4	1.734800	1.725956
Si5	1.759154	1.768768
Si6	1.740158	1.724813
Si7	1.732140	1.757634
Si8	1.737889	1.710807
Si9	1.758692	1.777822
Si10	1.784885	1.760466
Si11	1.762158	1.767823
Si12	1.753281	1.738466
Al13	1.271779	1.106333
Al14	1.290664	1.173184
Al15	1.303391	1.172754
Si16	1.750349	1.745853
Si17	1.746838	1.740578
Si18	1.748727	1.746208
Si19	1.737137	1.756481
Si20	1.770383	1.765670
Si21	1.730507	1.718352
Si22	1.760897	1.751337
Si23	1.766773	1.740754
Si24	1.744073	1.742595
Si25	1.783175	1.760958
Si26	1.729435	1.753838
Si27	1.724849	1.705044
Si28	1.754541	1.750105
Si29	1.747877	1.740816
Si30	1.747046	1.748776
Si31	1.761648	1.748765
Si32	1.742302	1.737951
Si33	1.768960	1.757748
Si34	1.754703	1.764200
Si35	1.743389	1.753749
Si36	1.745640	1.762576
O37	-0.842736	-0.883443
O38	-0.873322	-0.824307
O39	-0.921083	-0.875071
O40	-0.884921	-0.883443
O41	-0.895499	-0.905683
O42	-0.900944	-0.888736

Continued on next page

Table A.2 – Mulliken charges for all atoms in Ag-CHA model

Atom	System	Framework
O43	-0.882261	-0.878555
O44	-0.887264	-0.879451
O45	-0.877313	-0.883162
O46	-0.884741	-0.877486
O47	-0.895100	-0.880183
O48	-0.906933	-0.891054
O49	-0.890335	-0.881488
O50	-0.887836	-0.886734
O51	-0.884839	-0.892481
O52	-0.878855	-0.882351
O53	-0.901984	-0.884411
O54	-0.885322	-0.887250
O55	-0.836462	-0.820570
O56	-0.833989	-0.821108
O57	-0.882454	-0.834153
O58	-0.874406	-0.870272
O59	-0.865209	-0.879441
O60	-0.870499	-0.876735
O61	-0.866780	-0.871714
O62	-0.876119	-0.890277
O63	-0.863543	-0.872496
O64	-0.884683	-0.877849
O65	-0.878917	-0.886278
O66	-0.870806	-0.879662
O67	-0.861926	-0.875001
O68	-0.868474	-0.876941
O69	-0.866236	-0.871772
O70	-0.885963	-0.872991
O71	-0.881115	-0.871928
O72	-0.895874	-0.880099
O73	-0.842882	-0.837267
O74	-0.875868	-0.845068
O75	-0.846518	-0.810672
O76	-0.898010	-0.867850
O77	-0.887443	-0.873857
O78	-0.865146	-0.864885
O79	-0.876950	-0.870573
O80	-0.917891	-0.887203
O81	-0.864306	-0.864772
O82	-0.879800	-0.868597
O83	-0.875990	-0.877551
O84	-0.869700	-0.873533
O85	-0.863195	-0.862174
O86	-0.879423	-0.870549
O87	-0.873670	-0.86991
O88	-0.857476	-0.865651
O89	-0.861036	-0.866375
O90	-0.918667	-0.897803
O91	-0.893868	-0.884575
O92	-0.957627	-0.898897

Continued on next page

Table A.2 – Mulliken charges for all atoms in Ag-CHA model

Atom	System	Framework
O93	-0.955396	-0.924985
O94	-0.903753	-0.880406
O95	-0.934508	-0.890161
O96	-0.952046	-0.902306
O97	-0.861596	-0.825698
O98	-0.937575	-0.848656
O99	-0.923041	-0.884864
O100	-0.8926487	-0.885301
O101	-0.8902257	-0.891740
O102	-0.883500	-0.885585
O103	-0.888108	-0.885233
O104	-0.895366	-0.903315
O105	-0.881184	-0.884316
O106	-0.896794	-0.892600
O107	-0.905402	-0.900002
O108	-0.884334	-0.893856
Ag109	0.700000	0.587789
Ag110	0.554283	0.603281
Ag111	0.645515	0.660387
C112	-0.522312	
C113	-0.521096	
H114	0.320428	
H115	0.278777	
H116	0.342794	
H117	0.278191	

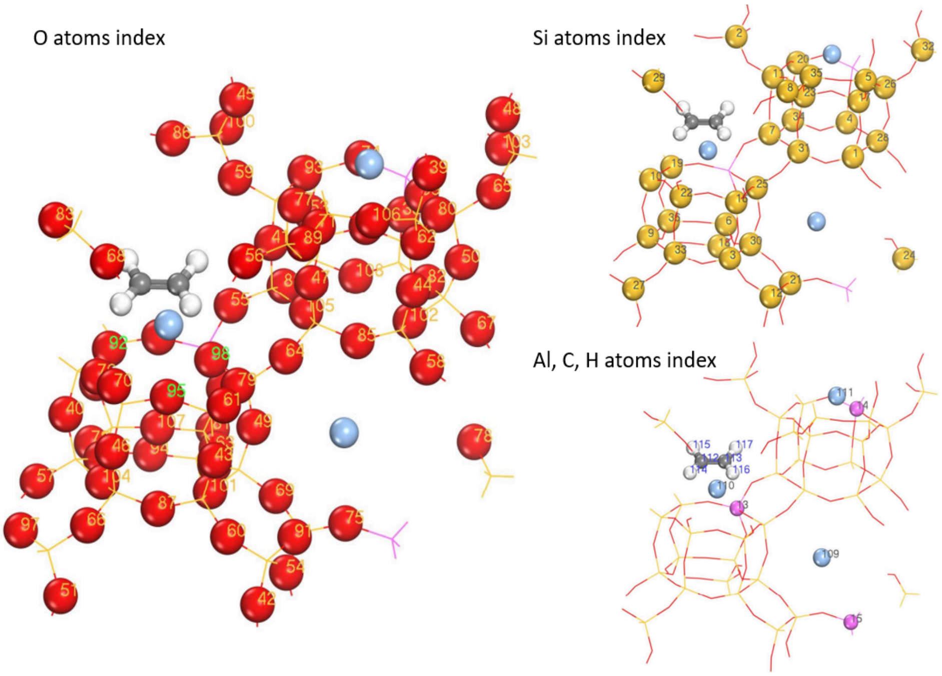

Figure A.8: Server atom index generated by Materials Studio for C_2H_4 Ag-CHA model.

Table A.3: Mulliken charges for all atoms in CsAg-RHO model.

Atom	**System**	**Framework**
O1	-0.88675	-0.886652
O2	-0.89537	-0.892104
O3	-0.89009	-0.888740
O4	-0.88021	-0.880352
O5	-0.87960	-0.878751
O6	-0.88236	-0.882487
O7	-0.89696	-0.891397
O8	-0.88201	-0.881866
O9	-0.88283	-0.882704
O10	-0.93095	-0.928334
O11	-0.89299	-0.885871
O12	-0.91502	-0.915091
O13	-0.88266	-0.881727
O14	-0.92468	-0.924872
O15	-0.88443	-0.880638
O16	-0.92863	-0.928886
O17	-0.88656	-0.886494
O18	-0.84382	-0.841377
O19	-0.88822	-0.887645
O20	-0.88516	-0.884848
O21	-0.83751	-0.836816
O22	-0.88267	-0.882802
O23	-0.89183	-0.891453
O24	-0.88117	-0.881004
O25	-0.88633	-0.886035
O26	-0.88176	-0.881388
O27	-0.94577	-0.945380
O28	-0.87940	-0.879379
O29	-0.88734	-0.887124
O30	-0.88221	-0.881863
O31	-0.88608	-0.885976
O32	-0.88946	-0.883917
O33	-0.87933	-0.879119
O34	-0.88276	-0.881400
O35	-0.88217	-0.881895
O36	-0.84431	-0.844175
O37	-0.90972	-0.910128
O38	-0.88449	-0.884451
O39	-0.88076	-0.880506
O40	-0.88286	-0.882640
O41	-0.88574	-0.885241
O42	-0.88013	-0.879875
O43	-0.88747	-0.887367
O44	-0.88355	-0.880559
O45	-0.88928	-0.889044
O46	-0.87852	-0.878271
O47	-0.94078	-0.941930
O48	-0.88304	-0.883026
O49	-0.87604	-0.875870

Continued on next page

Table A.3 – Mulliken charges for all atoms in Ag-RHO model.

Atom	System	Framework
O50	-0.89054	-0.890090
O51	-0.88174	-0.881770
O52	-0.88179	-0.882047
O53	-0.87910	-0.878576
O54	-0.87966	-0.879793
O55	-0.88325	-0.882374
O56	-0.88335	-0.881280
O57	-0.88138	-0.881229
O58	-0.87111	-0.869285
O59	-0.87042	-0.856071
O60	-0.90341	-0.903458
O61	-0.88486	-0.884135
O62	-0.90873	-0.908862
O63	-0.88033	-0.879135
O64	-0.91508	-0.914586
O65	-0.88129	-0.881180
O66	-0.88913	-0.888827
O67	-0.88734	-0.887519
O68	-0.87816	-0.878156
O69	-0.88498	-0.884511
O70	-0.87824	-0.878333
O71	-0.88121	-0.880992
O72	-0.88560	-0.881359
O73	-0.87764	-0.877500
O74	-0.84503	-0.844879
O75	-0.88915	-0.890103
O76	-0.88011	-0.880236
O77	-0.83464	-0.834170
O78	-0.88062	-0.880700
O79	-0.87788	-0.877651
O80	-0.89241	-0.889029
O81	-0.88482	-0.883556
O82	-0.90705	-0.906237
O83	-0.88318	-0.882512
O84	-0.91280	-0.912738
O85	-0.89355	-0.890033
O86	-0.91056	-0.910780
O87	-0.87873	-0.878527
O88	-0.91175	-0.910777
O89	-0.88497	-0.884317
O90	-0.87872	-0.878843
O91	-0.88254	-0.881878
O92	-0.88319	-0.882238
O93	-0.88262	-0.882500
O94	-0.88427	-0.883278
O95	-0.89851	-0.892148
O96	-0.88037	-0.880327
Si97	1.760785	1.760934
Si98	1.756905	1.756432
Si99	1.760469	1.760591

Continued on next page

Table A.3 – Mulliken charges for all atoms in Ag-RHO model.

Atom	System	Framework
Si100	1.730501	1.730231
Si101	1.762508	1.762683
Si102	1.748148	1.743858
Si103	1.743433	1.743213
Si104	1.758192	1.758685
Si105	1.769606	1.769664
Si106	1.762955	1.763110
Si107	1.755222	1.755089
Si108	1.763336	1.763866
Si109	1.768107	1.767972
Si110	1.756916	1.752310
Si111	1.738545	1.738588
Si112	1.765526	1.765580
Si113	1.756586	1.756360
Si114	1.764948	1.763396
Si115	1.776134	1.775297
Si116	1.758417	1.757992
Si117	1.773742	1.770542
Si118	1.770942	1.770838
Si119	1.773403	1.773172
Si120	1.745924	1.742800
Si121	1.782402	1.779188
Si122	1.763398	1.763599
Si123	1.763858	1.763426
Si124	1.769090	1.769079
Si125	1.770977	1.770912
Al126	1.268096	1.262900
Si127	1.763583	1.763656
Si128	1.764510	1.764142
Si129	1.761428	1.761155
Si130	1.770270	1.767504
Si131	1.774735	1.772252
Si132	1.763911	1.763971
Si133	1.768076	1.767899
Si134	1.768464	1.768326
Si135	1.770453	1.770067
Si136	1.765678	1.765873
Si137	1.756847	1.757524
Al138	1.250611	1.250797
Si139	1.770732	1.770576
Si140	1.761601	1.760293
Si141	1.758351	1.756215
Si142	1.760950	1.761712
Si143	1.772011	1.77236
Si144	1.770128	1.766739
Cs145	0.789034	0.788618
Ag146	0.516930	0.666051
C147	-0.517420	
C148	-0.513970	
H149	0.282408	

Continued on next page

Table A.3 – Mulliken charges for all atoms in Ag-RHO model.

Atom	System	Framework
H150	0.320184	
H151	0.283700	
H152	0.345235	

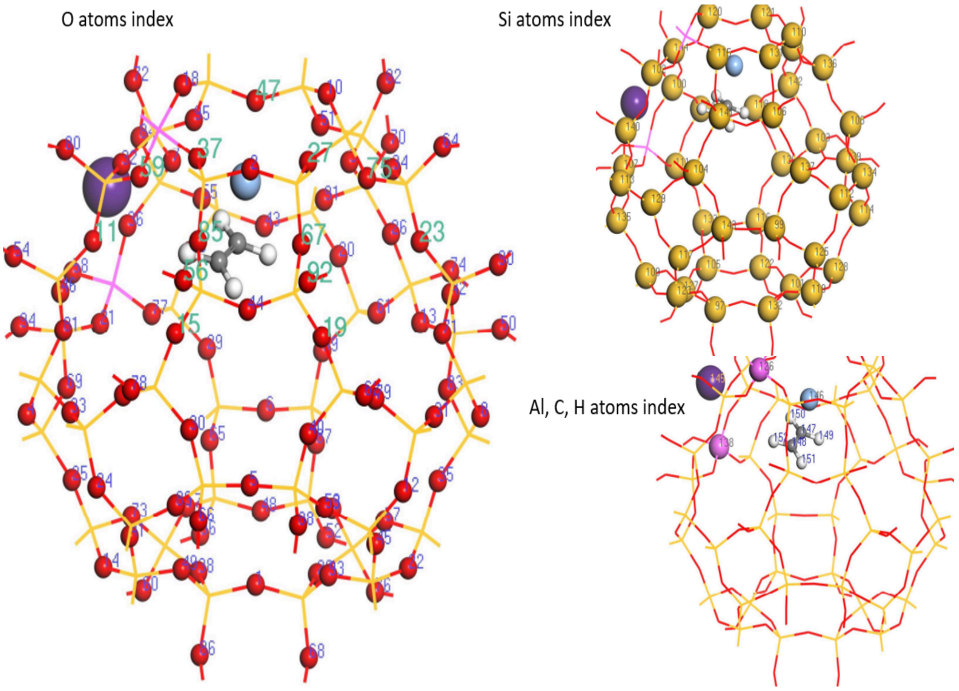

Figure A.9: Server atom index generated by Materials Studio for C_2H_4 CsAg-RHO model.

Table A.4: Mulliken charges for HAg-LTA model.

Atom	System	Framework
Atom	System	Framework
O (1)	-0.867649	-0.86957
O (2)	-0.880795	-0.8749
O (3)	-0.887598	-0.88612
O (4)	-0.894399	-0.89035
O (5)	-0.884534	-0.88105
O (6)	-0.903983	-0.89115
O (7)	-0.889583	-0.88934
O (8)	-0.896866	-0.8928
O (9)	-0.900483	-0.88709
O (10)	-0.882752	-0.87973
O (11)	-0.883607	-0.88149
O (12)	-0.852642	-0.84842
O (13)	-0.865934	-0.86677
O (14)	-0.876715	-0.88149
		Continued on next page

Table A.4 – Mulliken charges for all atoms in HAg-LTA model

Atom	System	Framework
O (15)	-0.842041	-0.84178
O (16)	-0.884072	-0.88366
O (17)	-0.880024	-0.88159
O (18)	-0.868086	-0.87131
O (19)	-0.847117	-0.84574
O (20)	-0.88457	-0.88178
O (21)	-0.87772	-0.88046
O (22)	-0.879332	-0.87687
O (23)	-0.877113	-0.87625
O (24)	-0.881693	-0.88178
O (25)	-0.946077	-0.94646
O (26)	-0.937993	-0.94512
O (27)	-0.880099	-0.87831
O (28)	-0.87261	-0.87093
O (29)	-0.913393	-0.9115
O (30)	-0.875623	-0.87227
O (31)	-0.927333	-0.95018
O (32)	-0.873086	-0.87211
O (33)	-0.91716	-0.91763
O (34)	-0.877303	-0.87682
O (35)	-0.874285	-0.87654
O (36)	-0.922036	-0.923
O (37)	-0.864858	-0.86447
O (38)	-0.870304	-0.86829
O (39)	-0.842	-0.83144
O (40)	-0.889394	-0.89128
O (41)	-0.865178	-0.86302
O (42)	-0.871476	-0.87017
O (43)	-0.868066	-0.86602
O (44)	-0.884641	-0.88467
O (45)	-0.869493	-0.86752
O (46)	-0.879493	-0.86964
O (47)	-0.86574	-0.86333
O (48)	-0.84568	-0.84493
Si(49)	1.716367	1.717612
Si(50)	1.751227	1.752796
Al(51)	1.287984	1.289594
Si(52)	1.778715	1.777468
Si(53)	1.747281	1.745263
Si(54)	1.722344	1.721528
Si(55)	1.733113	1.732705
Si(56)	1.782796	1.776098
Si(57)	1.751128	1.751228
Si(58)	1.755507	1.750101
Si(59)	1.747332	1.745722
Si(60)	1.74185	1.750334
Si(61)	1.788865	1.793524
Si(62)	1.752534	1.752525
Si(63)	1.757258	1.75662
Si(64)	1.751607	1.753004

Continued on next page

Table A.4 – Mulliken charges for all atoms in HAg-LTA model

Atom	System	Framework
Si(65)	1.724157	1.713135
Si(66)	1.746444	1.745419
Si(67)	1.761496	1.77232
Si(68)	1.754428	1.754291
Si(69)	1.752615	1.755021
Si(70)	1.706517	1.710107
Si(71)	1.751789	1.751679
Al(72)	1.285368	1.283703
Ag(73)	0.536304	0.645781
H (74)	0.567134	0.569532
C (75)	-0.50082	
C (76)	-0.522513	
H (77)	0.275281	
H (78)	0.322039	
H (79)	0.279289	
H (80)	0.317191	

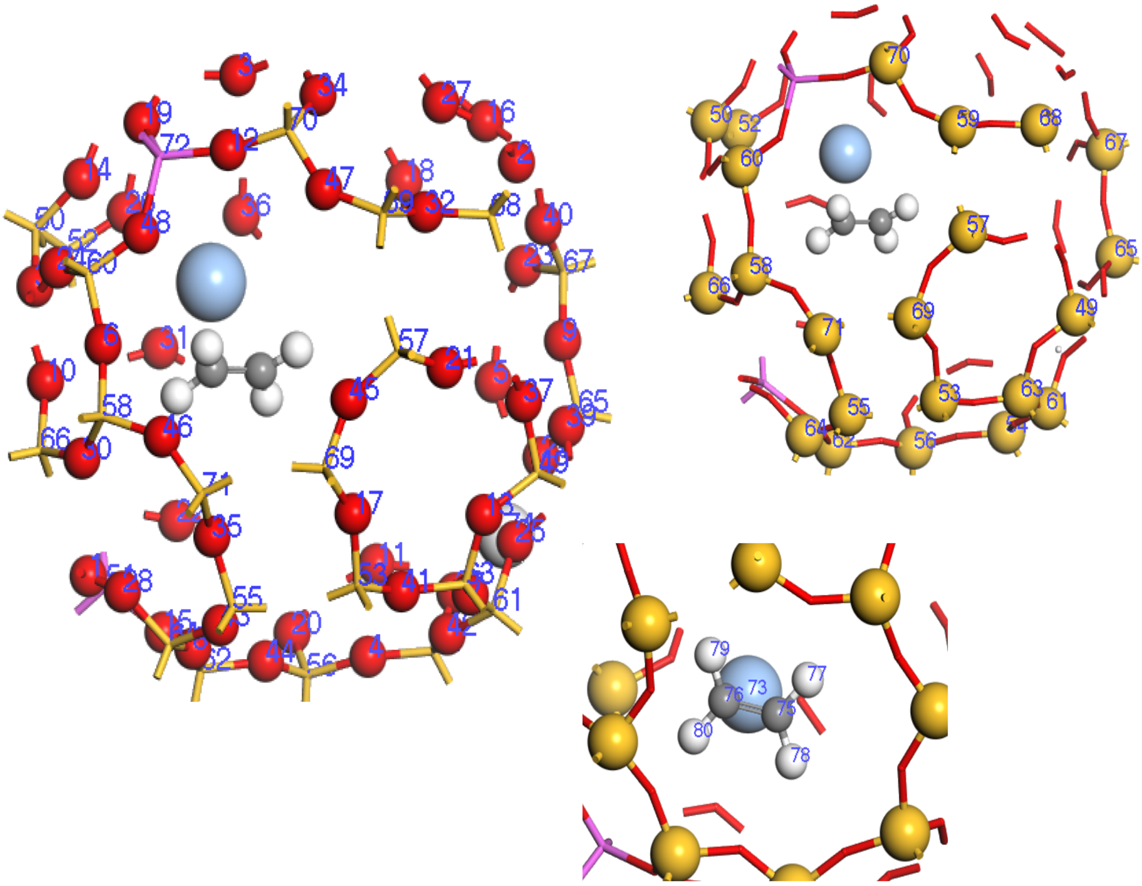
3
34
27
16
19
72
12
70
2
14
47
18
36
32
68
40
48
23
67
6
31
9
57
21
10
5
37
58
46
45
65
66
30
69
71
17
13
35
26
11
28
53
41
55
61
20
42
44
56
4
70
50
52
59
68
60
67
57
58
65
66
71
69
49
55
53
63
61
64
62
56
54
79
76
73
77
75
80
78

Figure A.10: Server atom index generated by Materials Studio for C_2H_4 HAg-LTA model.

A.6 Molecular Dynamics

In Ab-initio Molecular Dynamics (AIMD) simulations, atoms are moved making use of classical Newton's mechanics while quantum mechanics is applied to calculate the interatomic forces acting between atoms, i.e. the electronic structure of an assembly of atomic positions are solved from first-principles, which allow the calculation of resulting forces acting on each atom.

Thus, the vibrational spectra is obtained from MD trajectories based on the Time Fourier Transform of the velocity-velocity autocorrelated function, as follows:

$$g(\omega) = \sqrt{\frac{1}{2\pi}} \int_{-\infty}^{\infty} e^{i\omega t} \sum_i \frac{\langle \vec{v}_i(t)\vec{v}_i(0)\rangle}{\langle \vec{v}_i(0)\vec{v}_i(0)\rangle} dt$$

In this formula, the term $\frac{\langle \vec{v}_i(t)\vec{v}_i(0)\rangle}{\langle \vec{v}_i(0)\vec{v}_i(0)\rangle}$ is the velocity-velocity correlation function. It is calculated parting from a chosen initial time (t=0) for the MD trajectory and for each atom of the system i, along all three components of the velocity $\vec{v}_i$.

For the set of calculations in this thesis, MD simulations were run using CASTEP code implemented on Materials Studio software. All calculations used norm-conserving pseudopotentials with the Perdew-Burke-Ernzerhof (PBE) functional within the generalized-gradient approximation (GGA). Plane-wave cut-off was set as standard at 700eV. These calculations were performed in the same cells used for normal modes calculations in a set considering 250K in the NVT ensemble over 7 ps (CHA and RHO) and 3ps (LTA, due to time constrain) with 1 fs time step. The thermally calibrated structures helped to set the ethylene position in the cells used for normal modes calculation before energy optimization. The density of states (DOS) was calculated based on time-Fourier transform of the velocity autocorrelation function, considering the coordinates of each step of the trajectories. This transformation was carried out using MDANSE software [123]. The g_H(E) considered only H of ethylene molecule. Figure A.11 compare the experimental results with calculated ones.

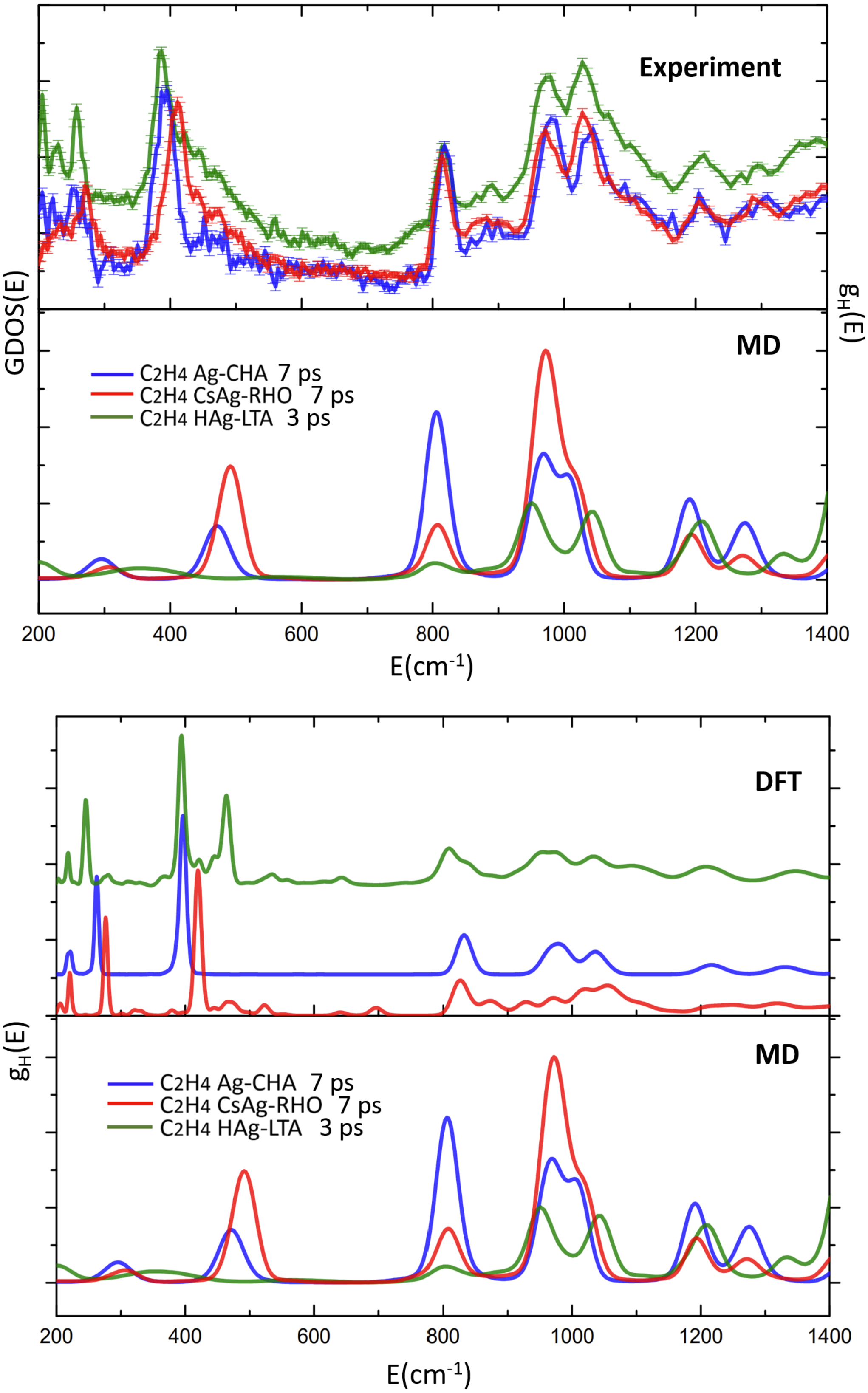

Figure A.11: Experimental, DFT and MD results.

A.7 Supporting QENS and INS data

A.7.1 QENS C_2H_4 Ag-CHA

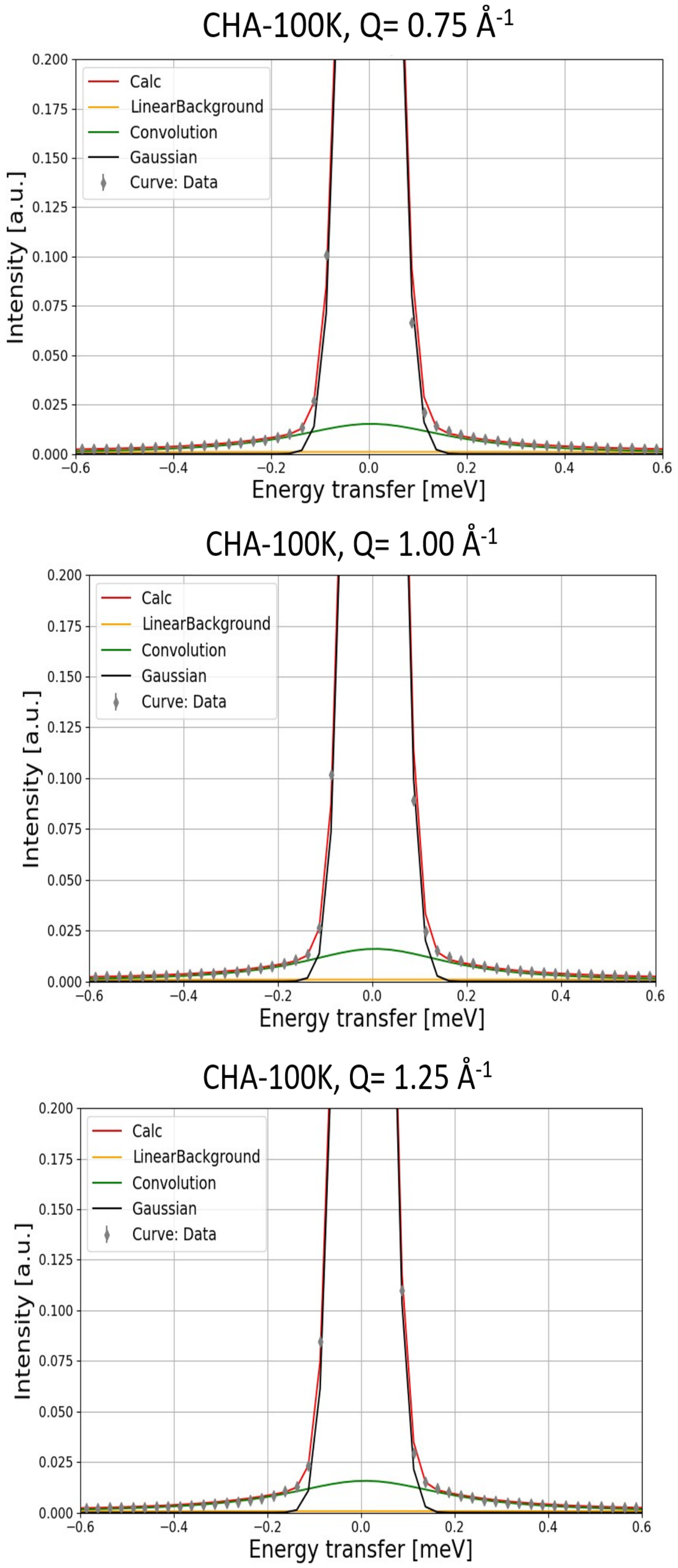

Figure A.12: QENS spectra obtained for ethylene adsorbed on Ag-CHA at 100K at different Q values. Red is the total fit while Black, Green and Yellow are used to represent the instrument resolution, Lorentzian and flat background functions.

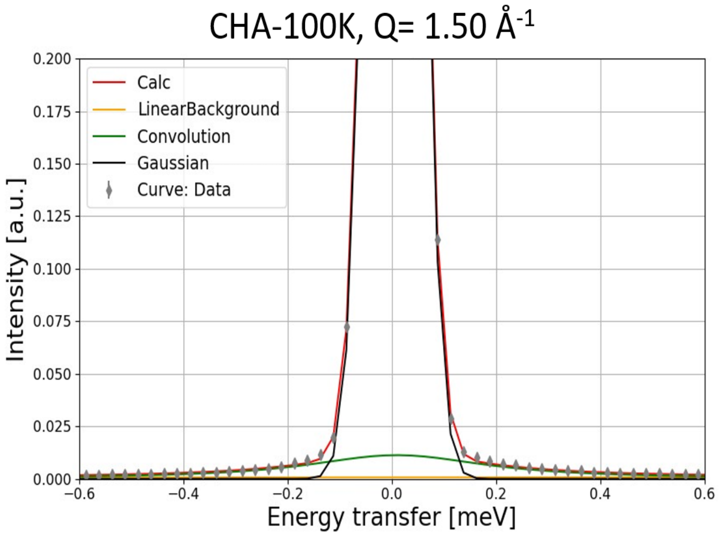
CHA-100K, Q= 1.50 Å^{-1}

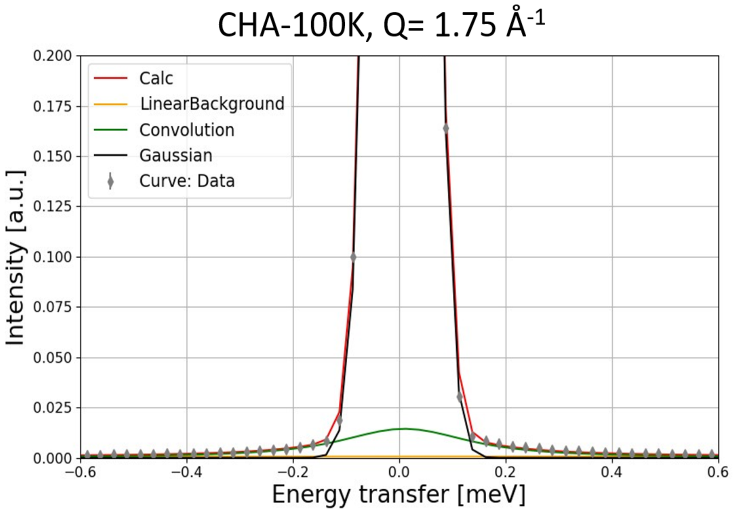
CHA-100K, Q= 1.75 Å^{-1}

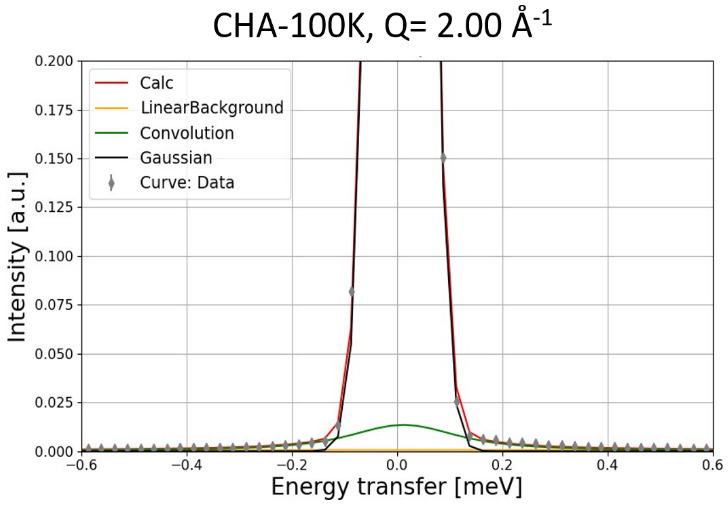
CHA-100K, Q= 2.00 Å^{-1}

Figure A.13: QENS spectra obtained for ethylene adsorbed on Ag-CHA at 100K at different Q values. Red is the total fit while Black, Green and Yellow are used to represent the instrument resolution, Lorentzian and flat background functions.

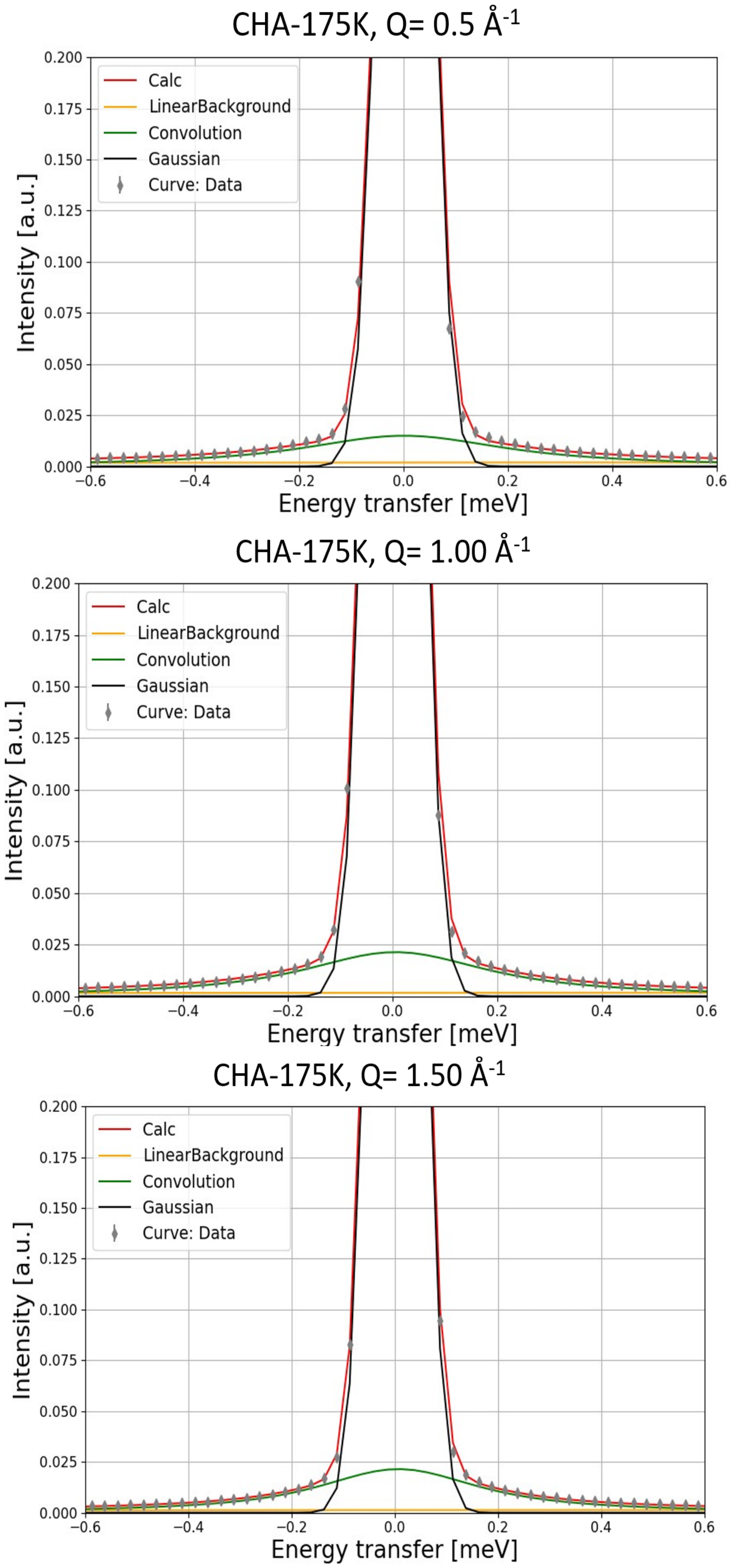

Figure A.14: QENS spectra obtained for ethylene adsorbed on Ag-CHA at 175K at different Q values. Red is the total fit while Black, Green and Yellow are used to represent the instrument resolution, Lorentzian and flat background functions.

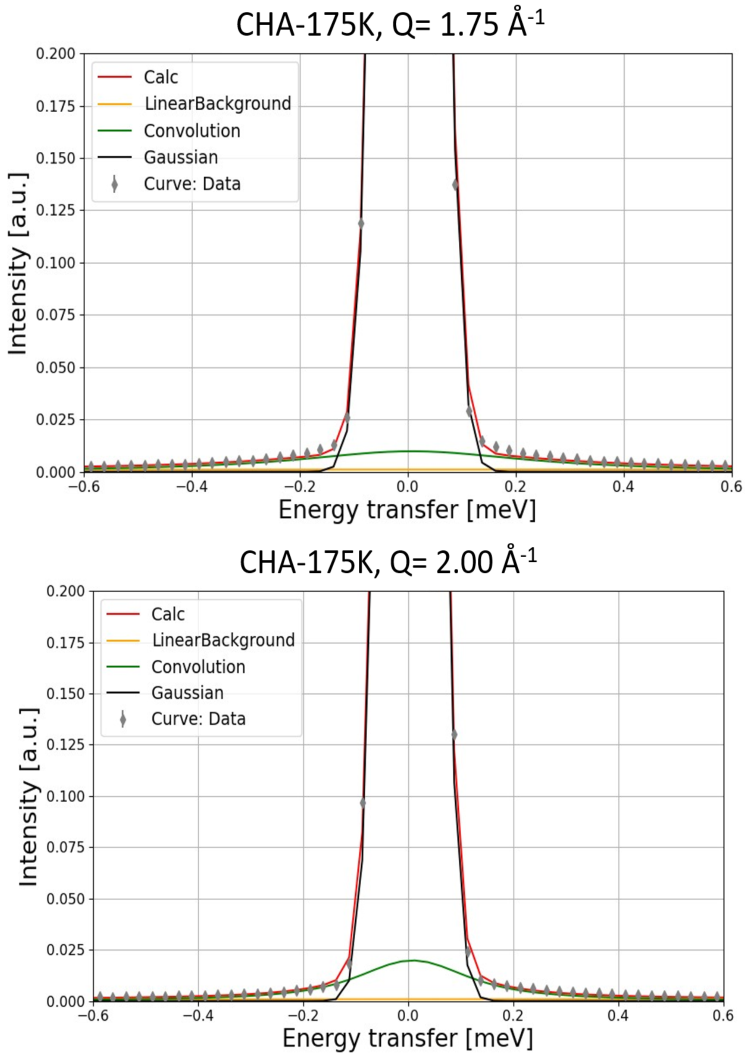

CHA-175K, Q= 1.75 Å^{-1}

CHA-175K, Q= 2.00 Å^{-1}

Figure A.15: QENS spectra obtained for ethylene adsorbed on Ag-CHA at 175K at different Q values. Red is the total fit while Black, Green and Yellow are used to represent the instrument resolution, Lorentzian and flat background functions.

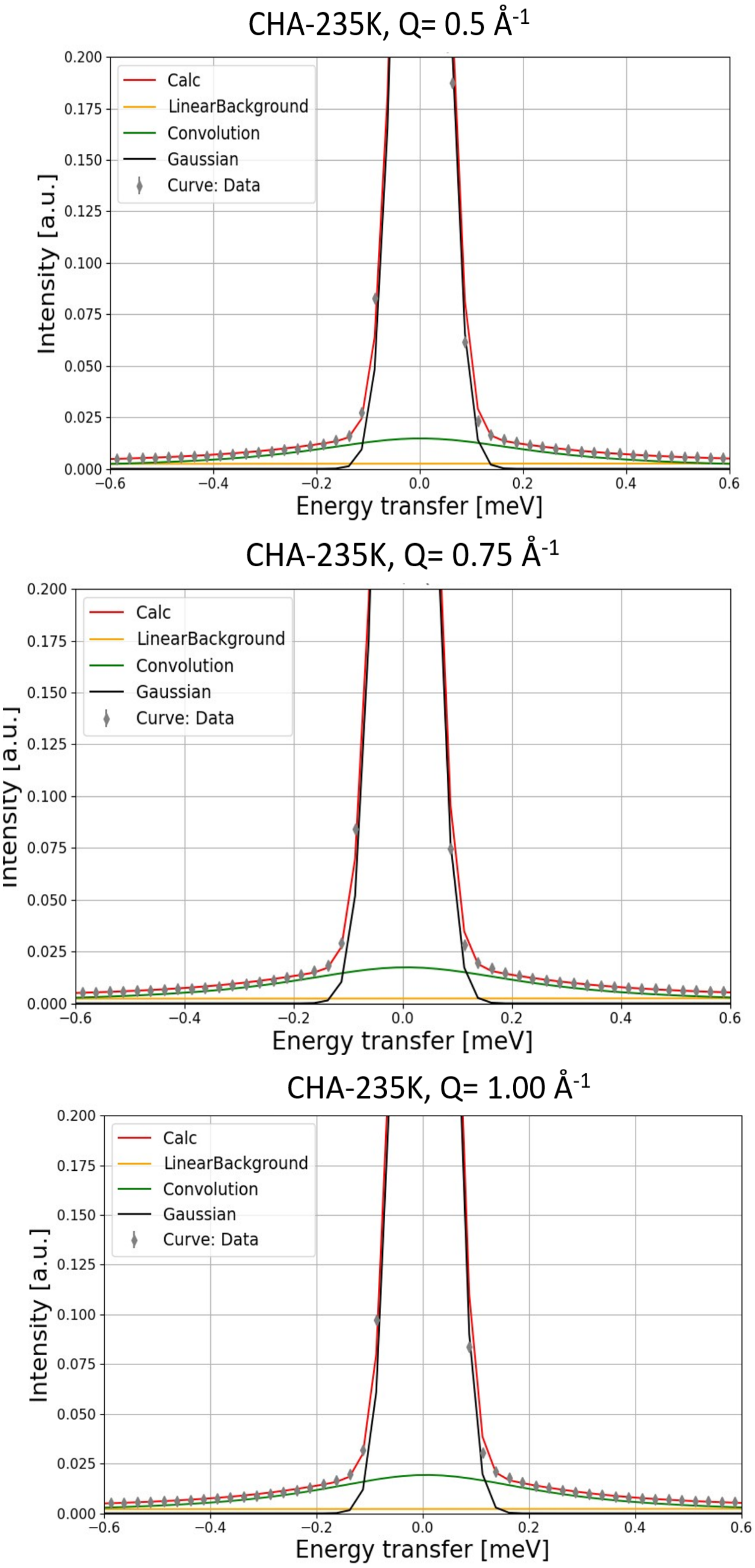

Figure A.16: QENS spectra obtained for ethylene adsorbed on Ag-CHA at 235K at different Q values. Red is the total fit while Black, Green and Yellow are used to represent the instrument resolution, Lorentzian and flat background functions.

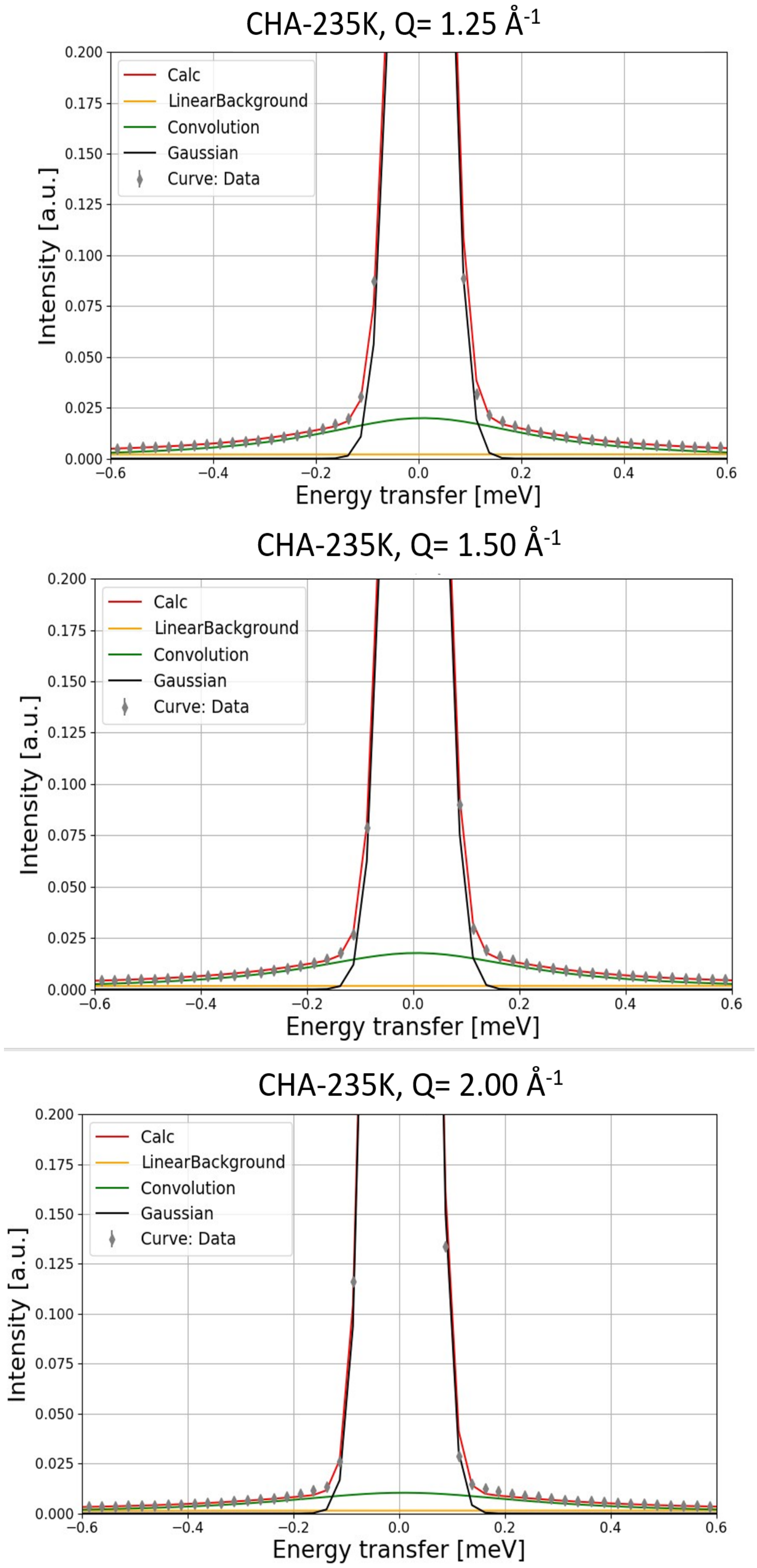

Figure A.17: QENS spectra obtained for ethylene adsorbed on Ag-CHA at 235K at different Q values. Red is the total fit while Black, Green and Yellow are used to represent the instrument resolution, Lorentzian and flat background functions.

A.7.2 QENS C_2H_4 CsAg-RHO

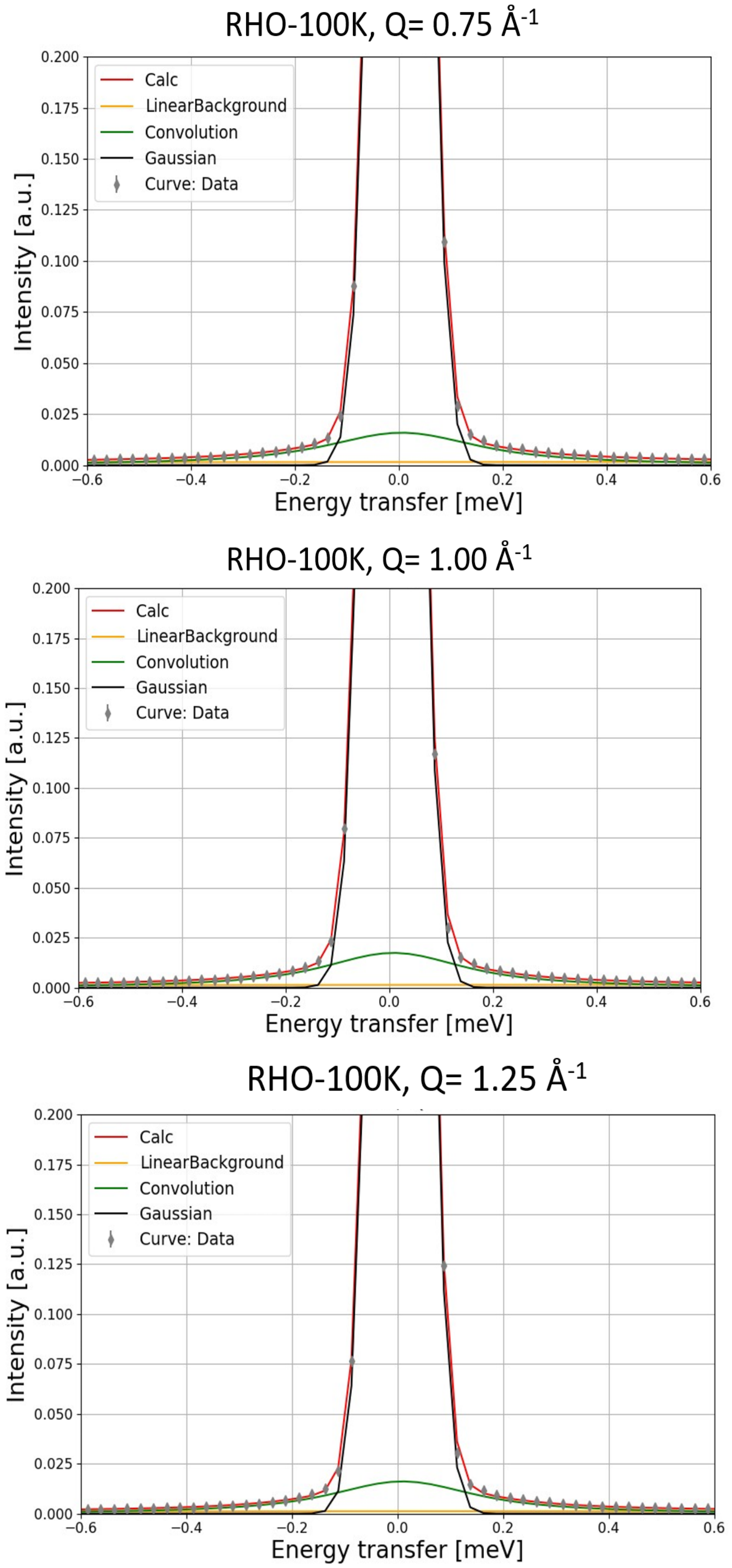

Figure A.18: QENS spectra obtained for ethylene adsorbed on CsAg-RHO at 100K, 175K and 235K at different Q values. Red is the total fit while Black, Green and Yellow are used to represent the instrument resolution, Lorentzian and flat background functions.

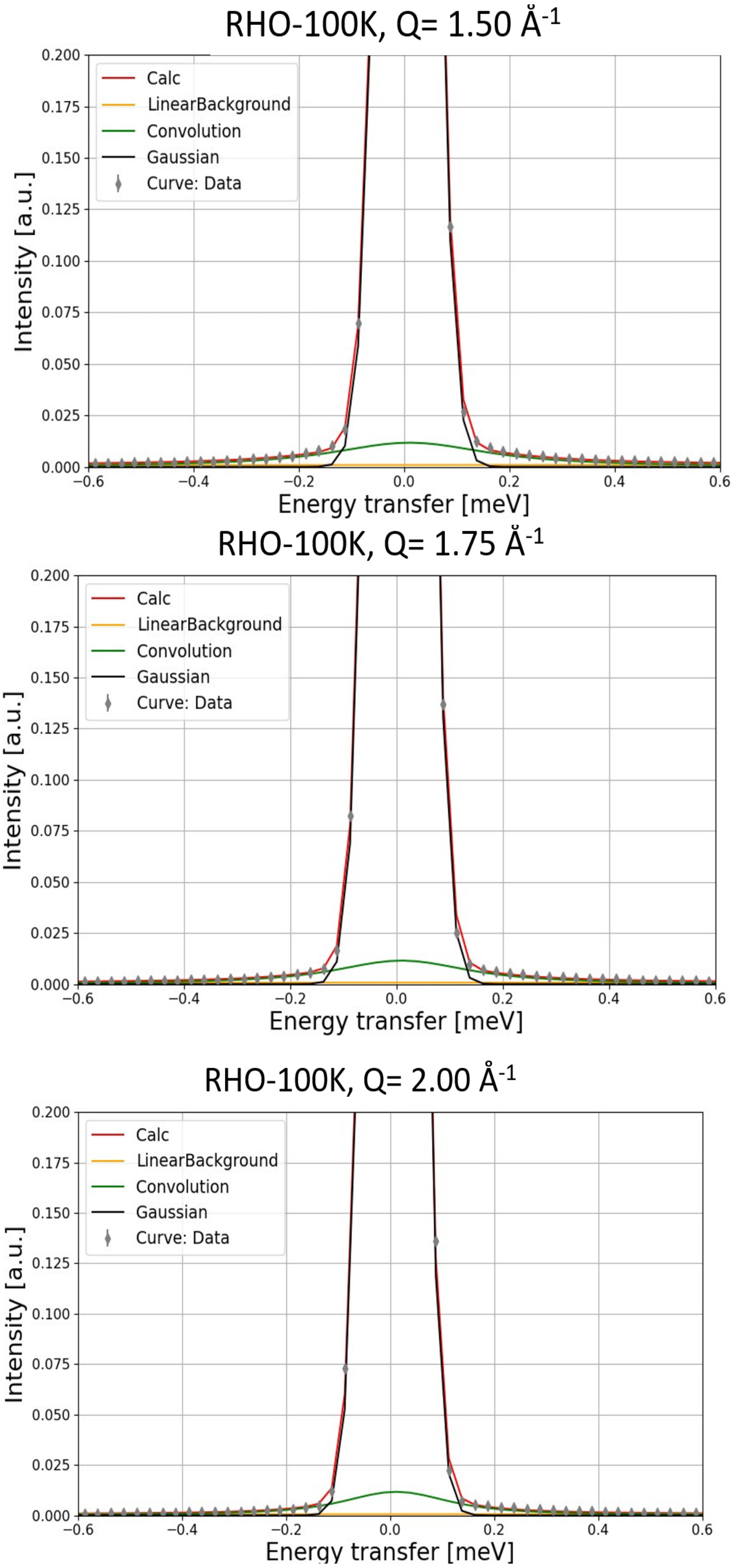

Figure A.19: QENS spectra obtained for ethylene adsorbed on CsAg-RHO at 100K, 175K and 235K at different Q values. Red is the total fit while Black, Green and Yellow are used to represent the instrument resolution, Lorentzian and flat background functions.

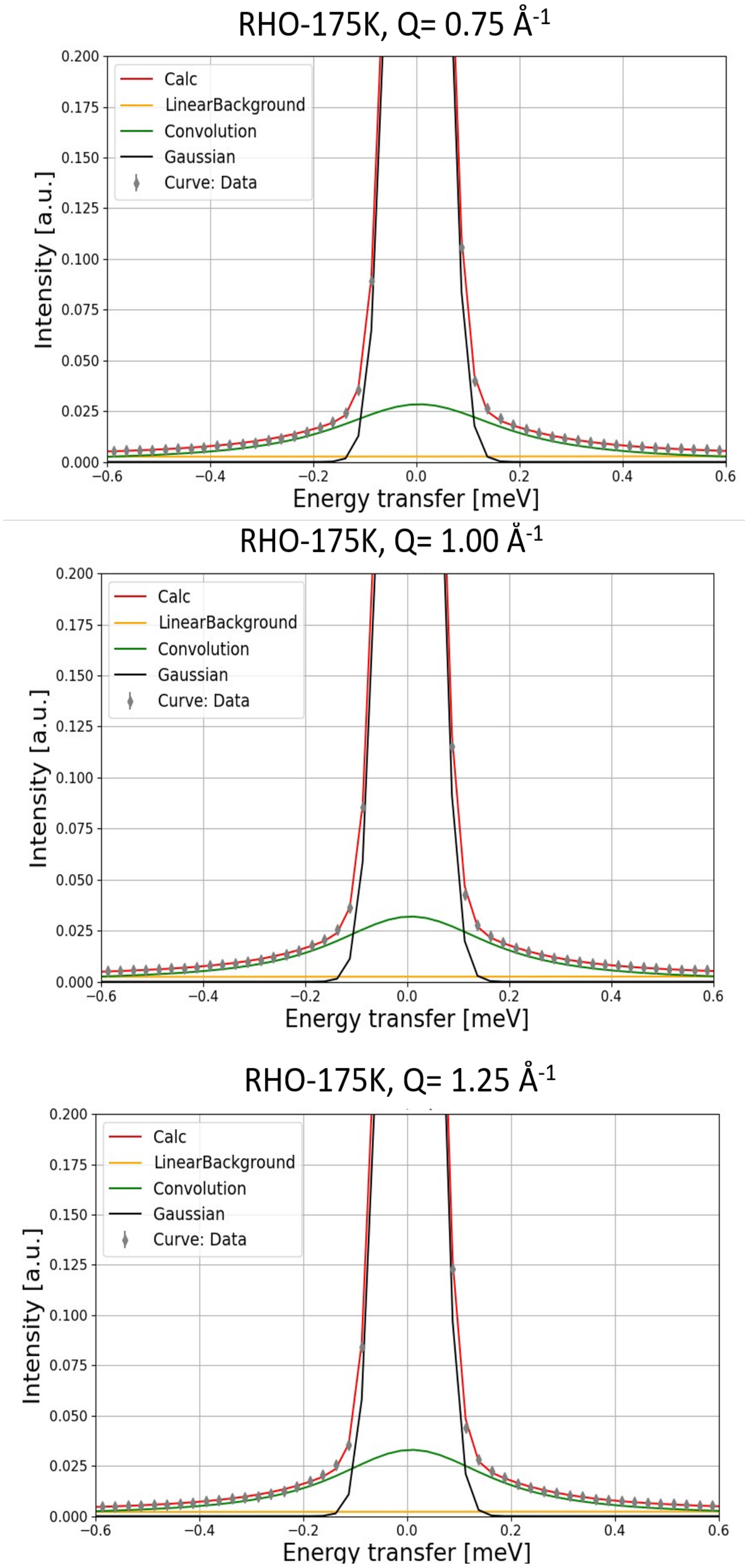

Figure A.20: QENS spectra obtained for ethylene adsorbed on CsAg-RHO at 175K, 175K and 235K at different Q values. Red is the total fit while Black, Green and Yellow are used to represent the instrument resolution, Lorentzian and flat background functions.

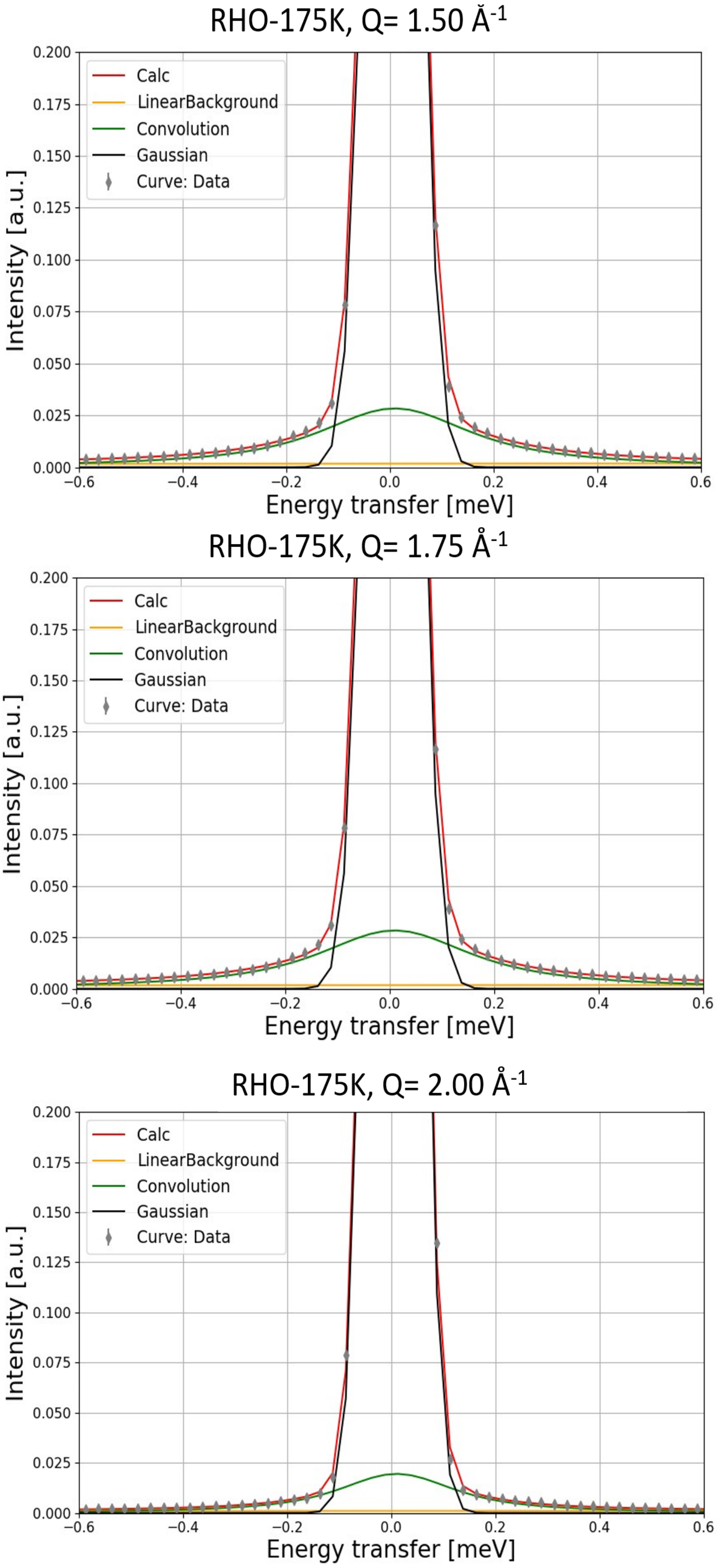

Figure A.21: QENS spectra obtained for ethylene adsorbed on CsAg-RHO at 175K, 175K and 235K at different Q values. Red is the total fit while Black, Green and Yellow are used to represent the instrument resolution, Lorentzian and flat background functions.

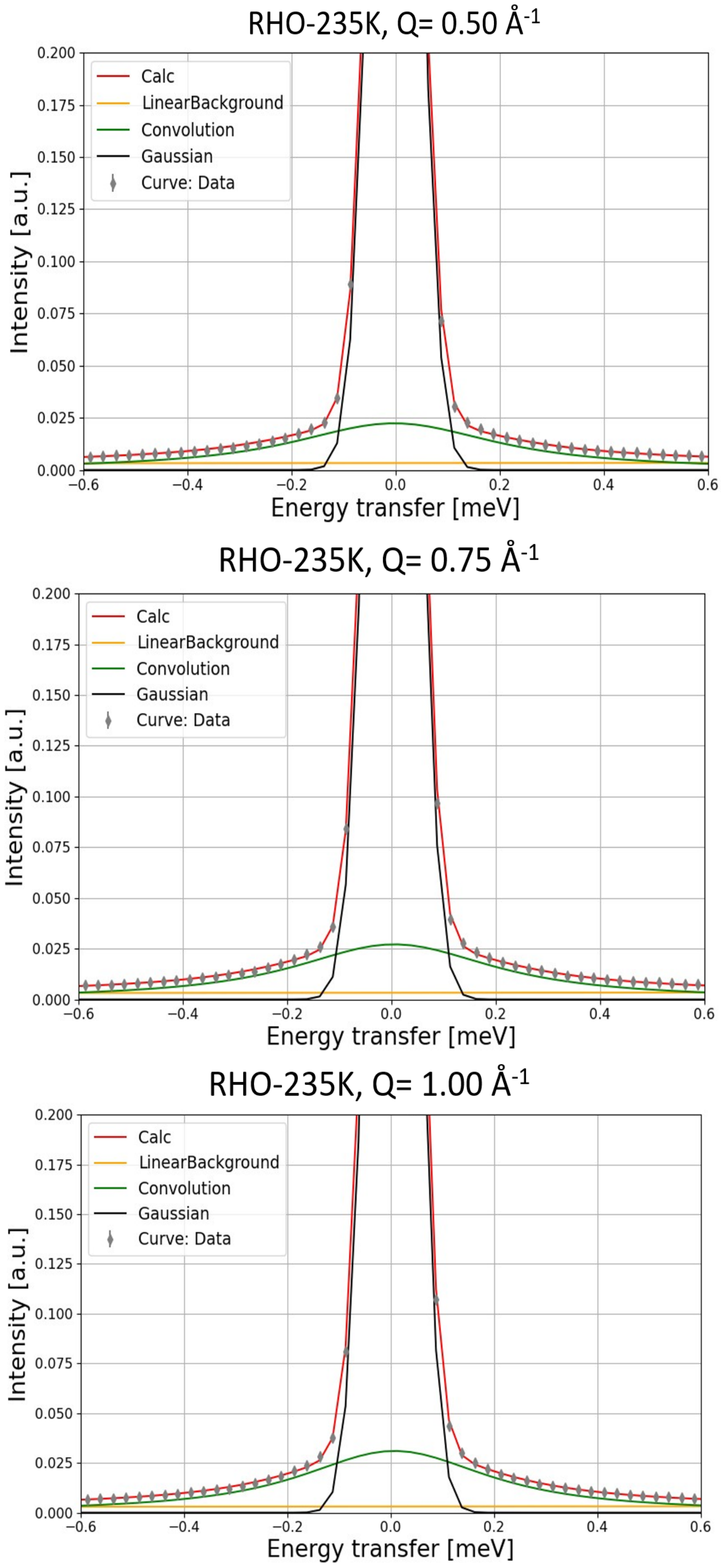

Figure A.22: QENS spectra obtained for ethylene adsorbed on CsAg-RHO at 235K, 175K and 235K at different Q values. Red is the total fit while Black, Green and Yellow are used to represent the instrument resolution, Lorentzian and flat background functions.

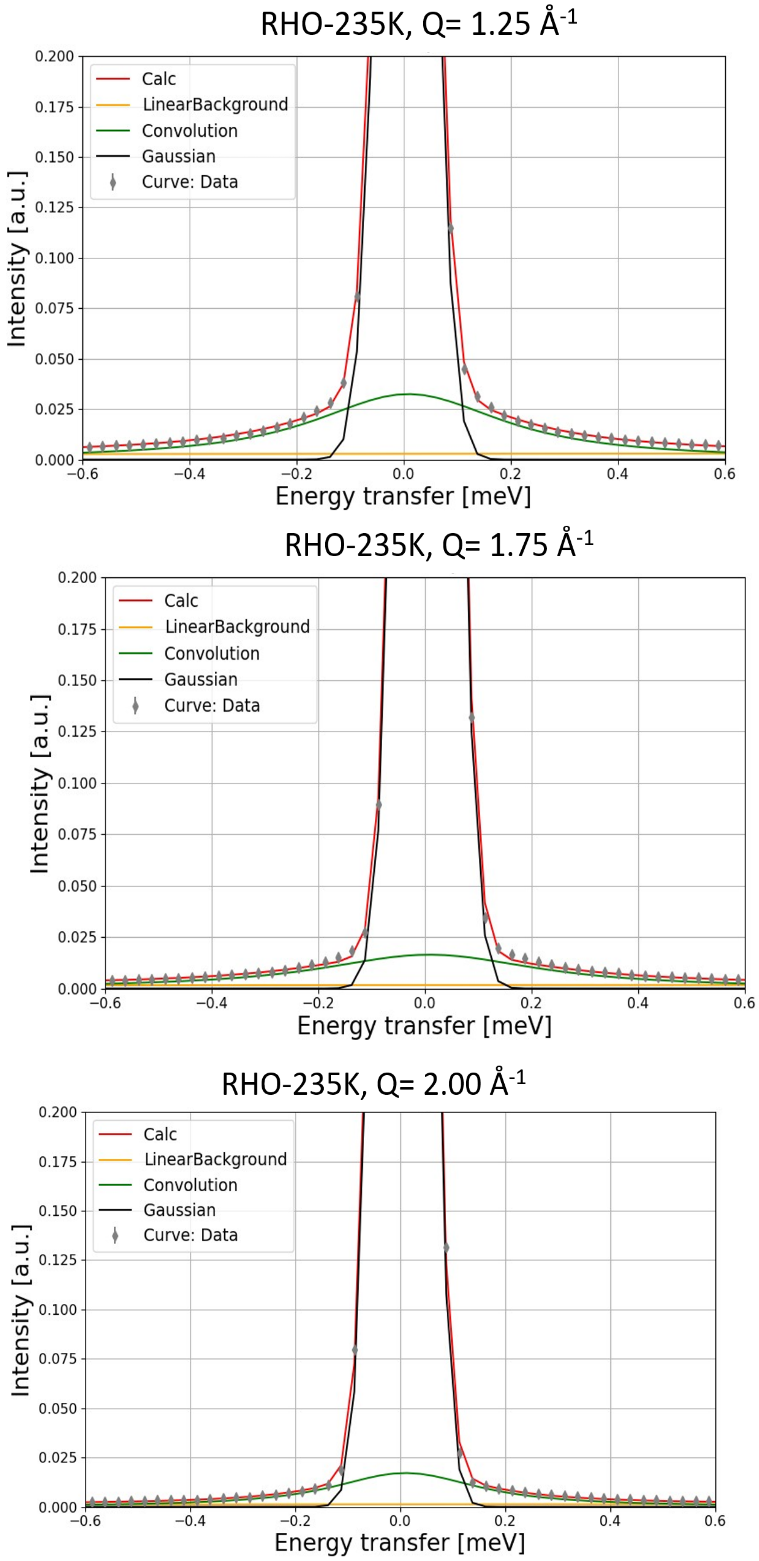

Figure A.23: QENS spectra obtained for ethylene adsorbed on CsAg-RHO at 235K, 175K and 235K at different Q values. Red is the total fit while Black, Green and Yellow are used to represent the instrument resolution, Lorentzian and flat background functions.

A.7.3 QENS C_2H_4 HAg-LTA

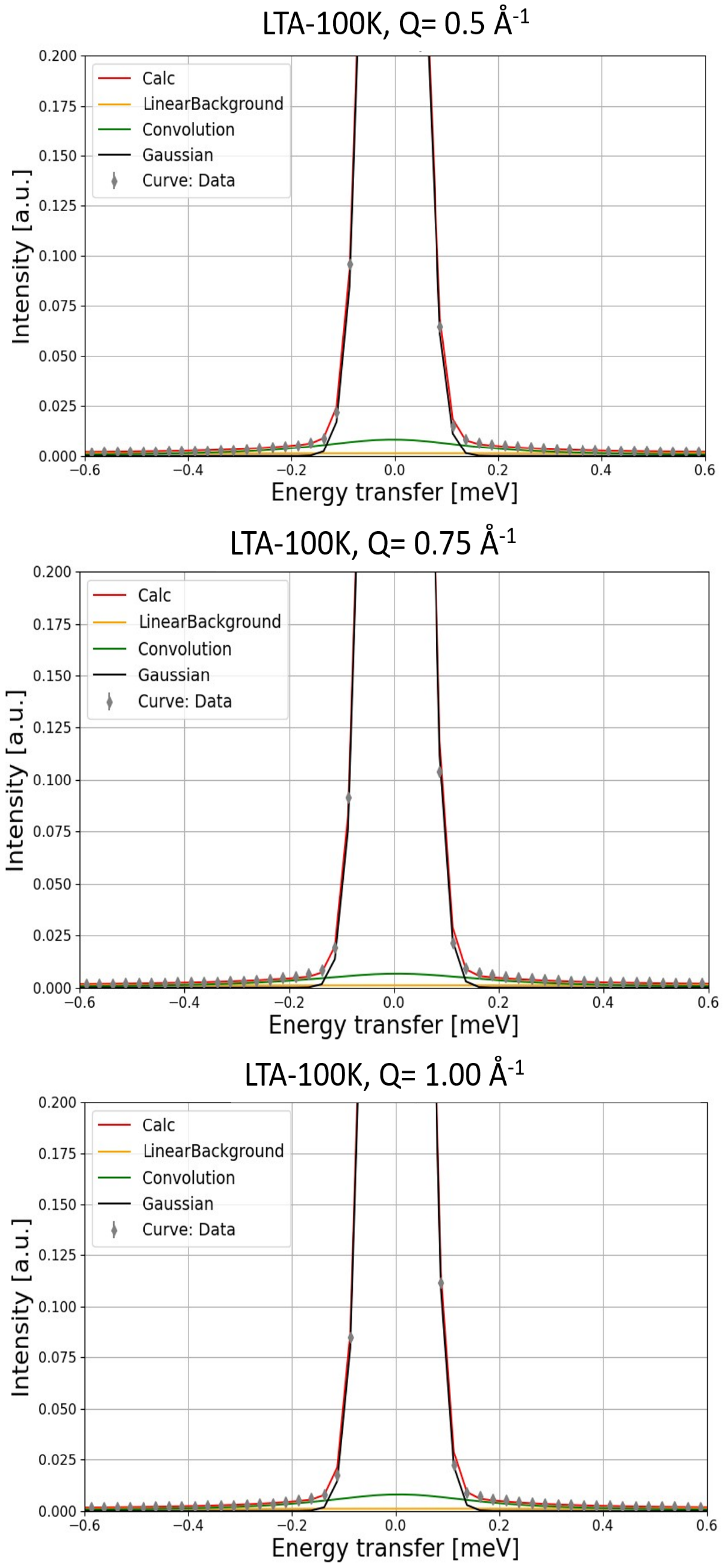

Figure A.24: QENS spectra obtained for ethylene adsorbed on HAg-LTA at 100K at different Q values. Red is the total fit while Black, Green and Yellow are used to represent the instrument resolution, Lorentzian and flat background functions.

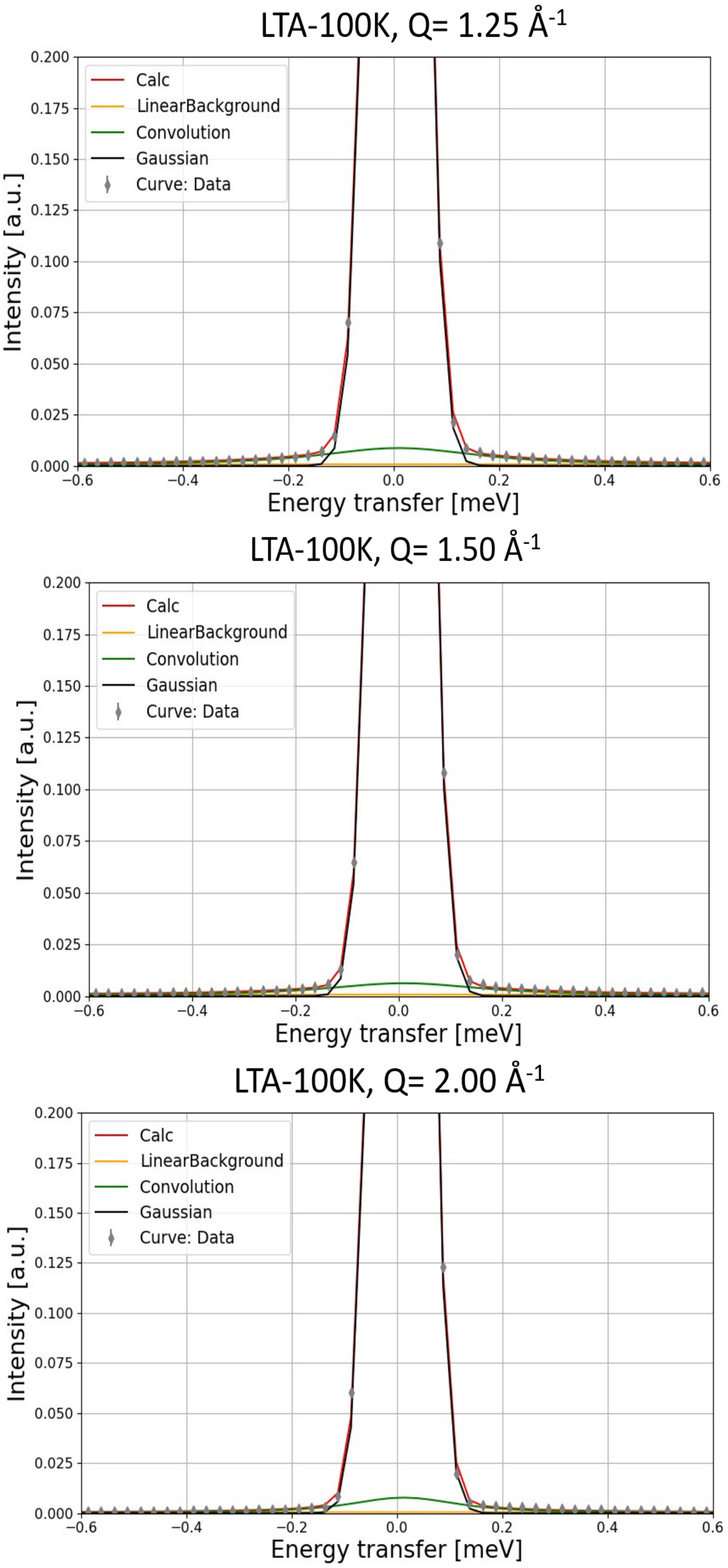
LTA-100K, Q= 1.25 Å^{-1}

LTA-100K, Q= 1.50 Å^{-1}

LTA-100K, Q= 2.00 Å^{-1}

Figure A.25: QENS spectra obtained for ethylene adsorbed on HAg-LTA at 100K at different Q values. Red is the total fit while Black, Green and Yellow are used to represent the instrument resolution, Lorentzian and flat background functions.

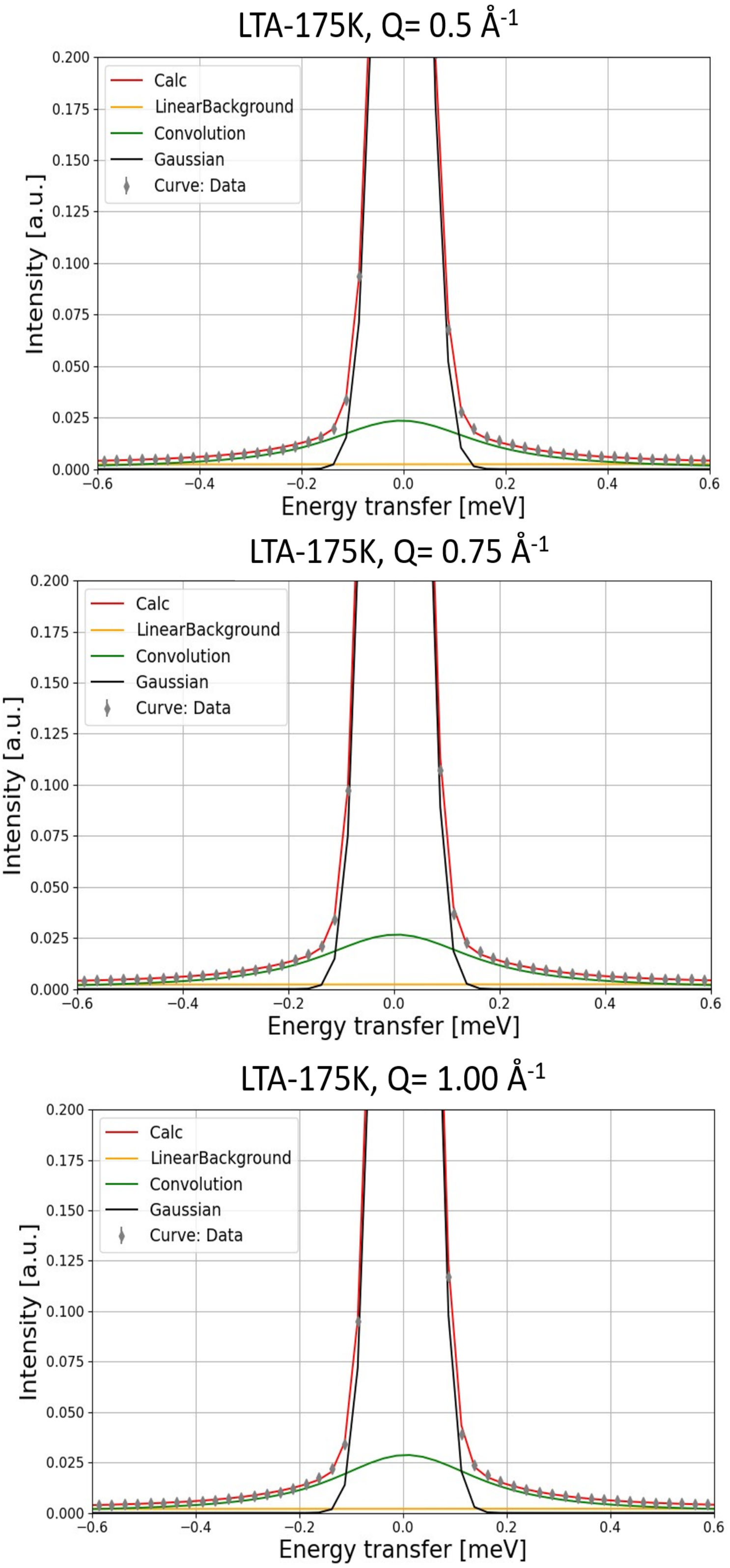

Figure A.26: QENS spectra obtained for ethylene adsorbed on HAg-LTA at 175K at different Q values. Red is the total fit while Black, Green and Yellow are used to represent the instrument resolution, Lorentzian and flat background functions.

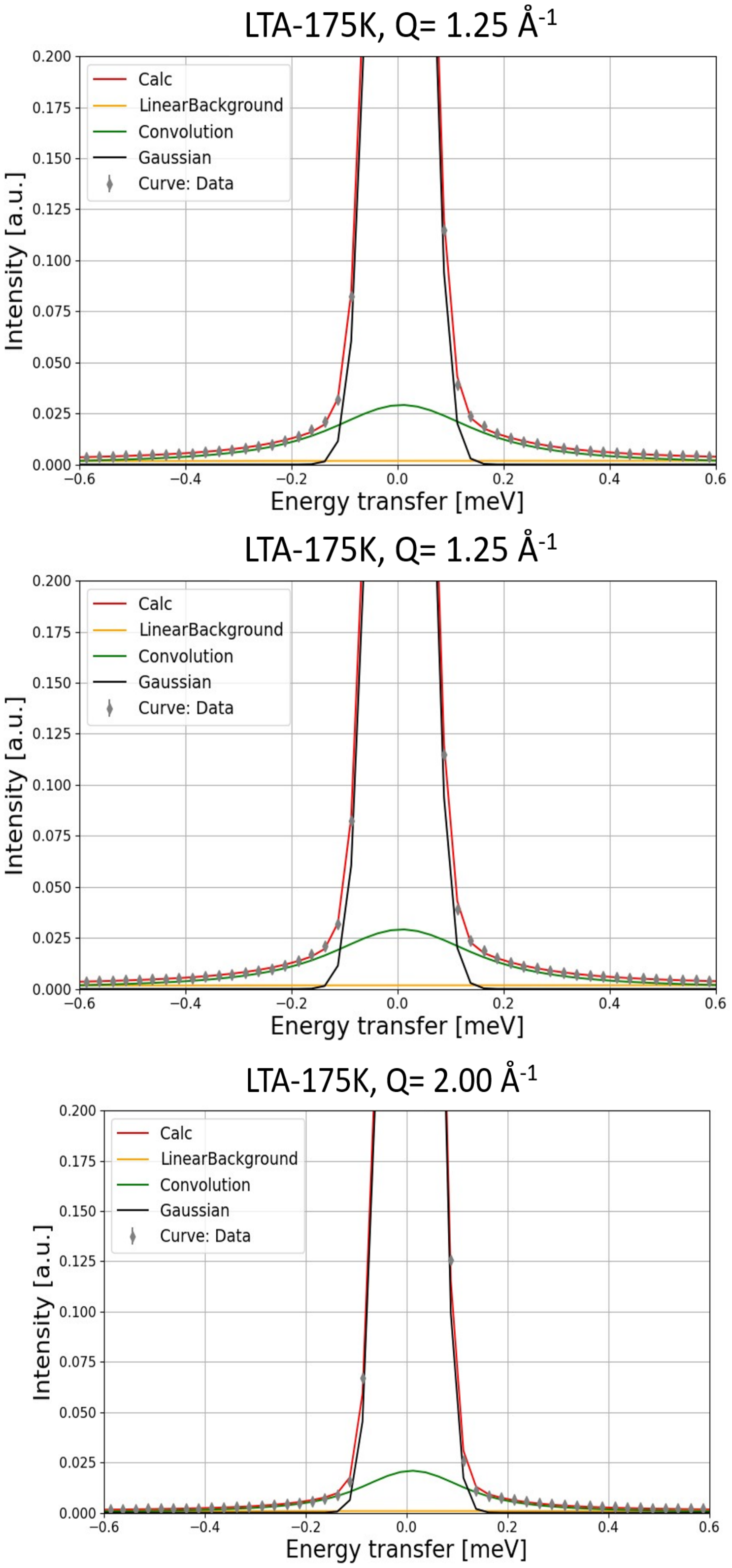

Figure A.27: QENS spectra obtained for ethylene adsorbed on HAg-LTA at 175K at different Q values. Red is the total fit while Black, Green and Yellow are used to represent the instrument resolution, Lorentzian and flat background functions.

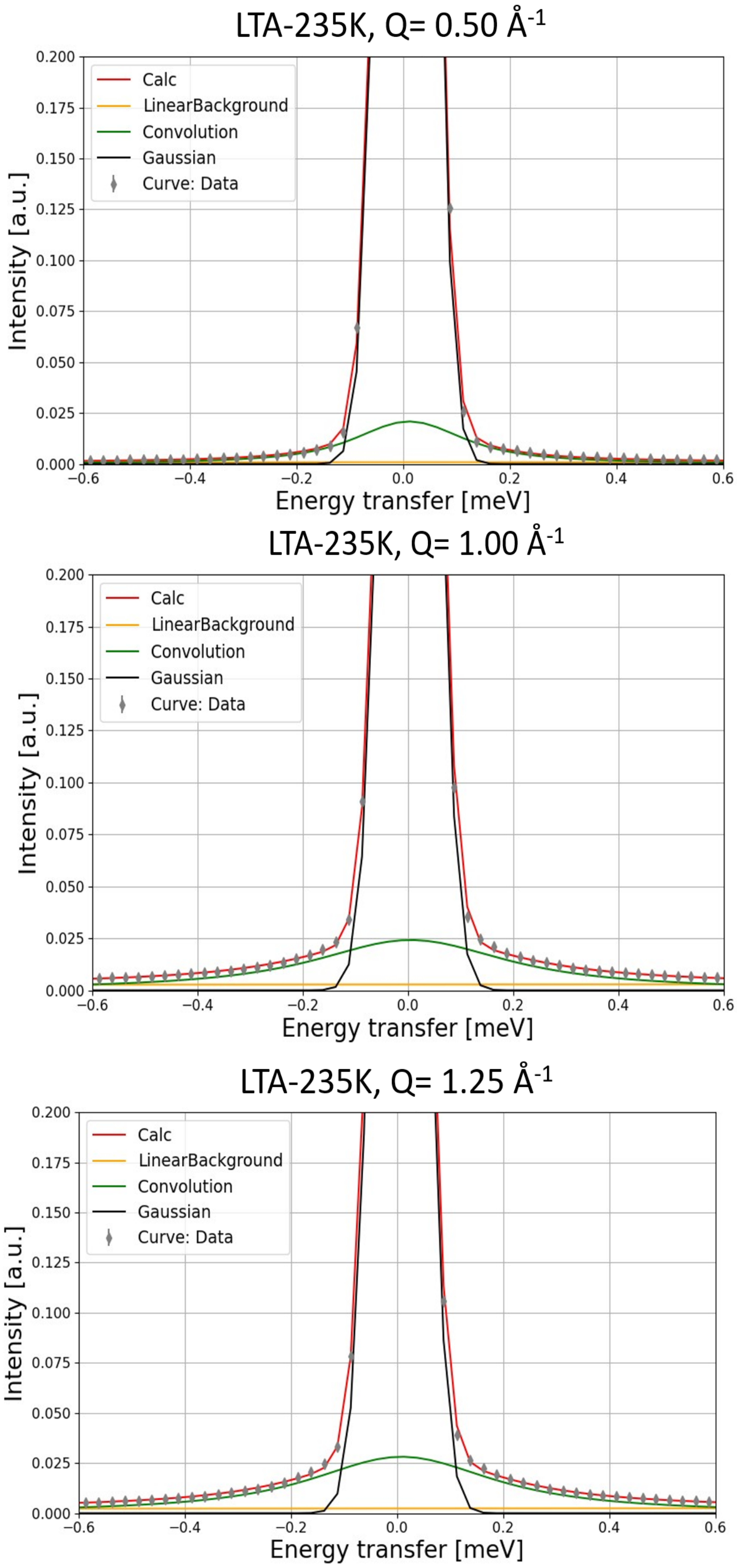

Figure A.28: QENS spectra obtained for ethylene adsorbed on HAg-LTA at 235K at different Q values. Red is the total fit while Black, Green and Yellow are used to represent the instrument resolution, Lorentzian and flat background functions.

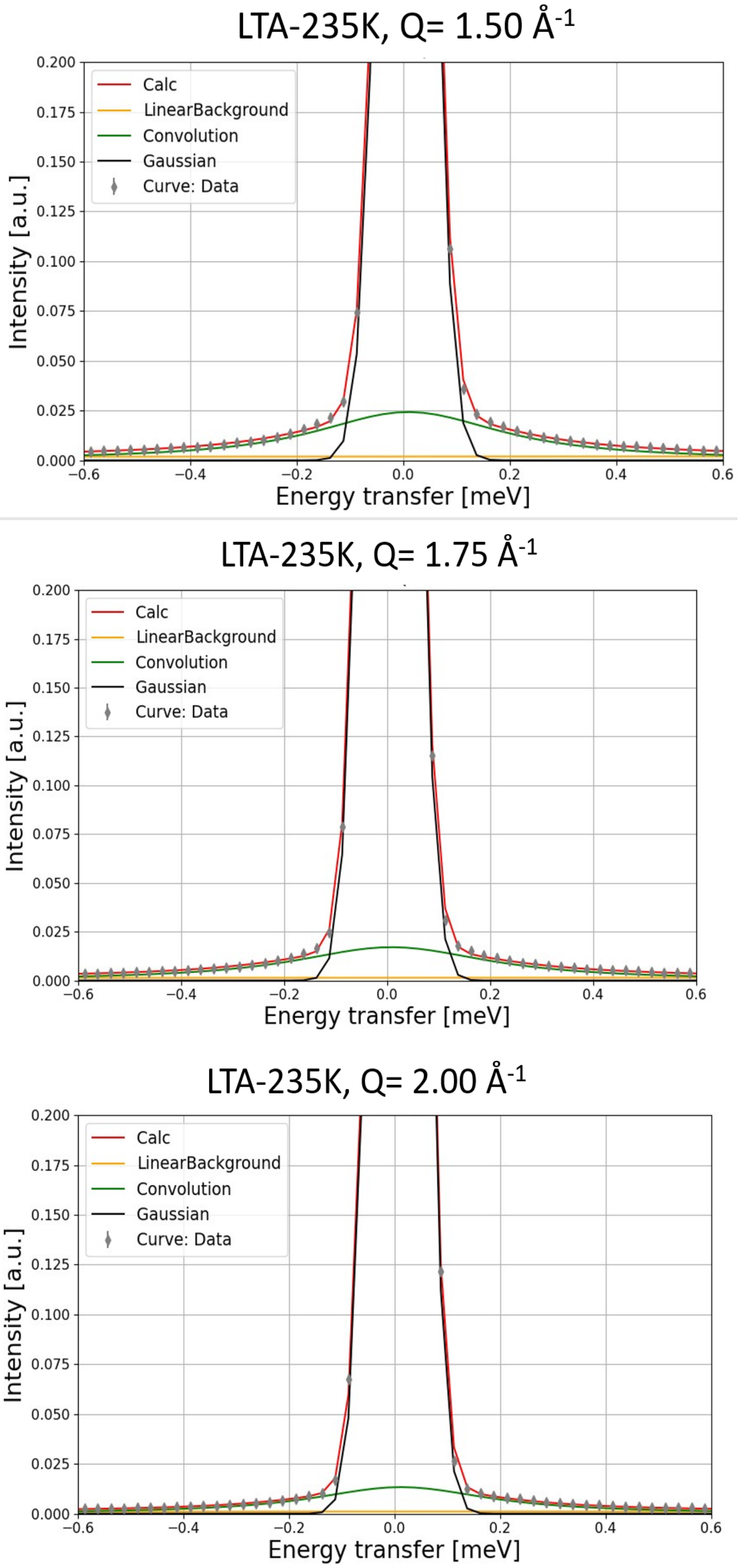

Figure A.29: QENS spectra obtained for ethylene adsorbed on HAg-LTA at 235K at different Q values. Red is the total fit while Black, Green and Yellow are used to represent the instrument resolution, Lorentzian and flat background functions.

A.7.4 S(Q) of C_2H_4 Ag-zeolites

The Q-ω space of the measured samples is represented in the Figure A.30 below.

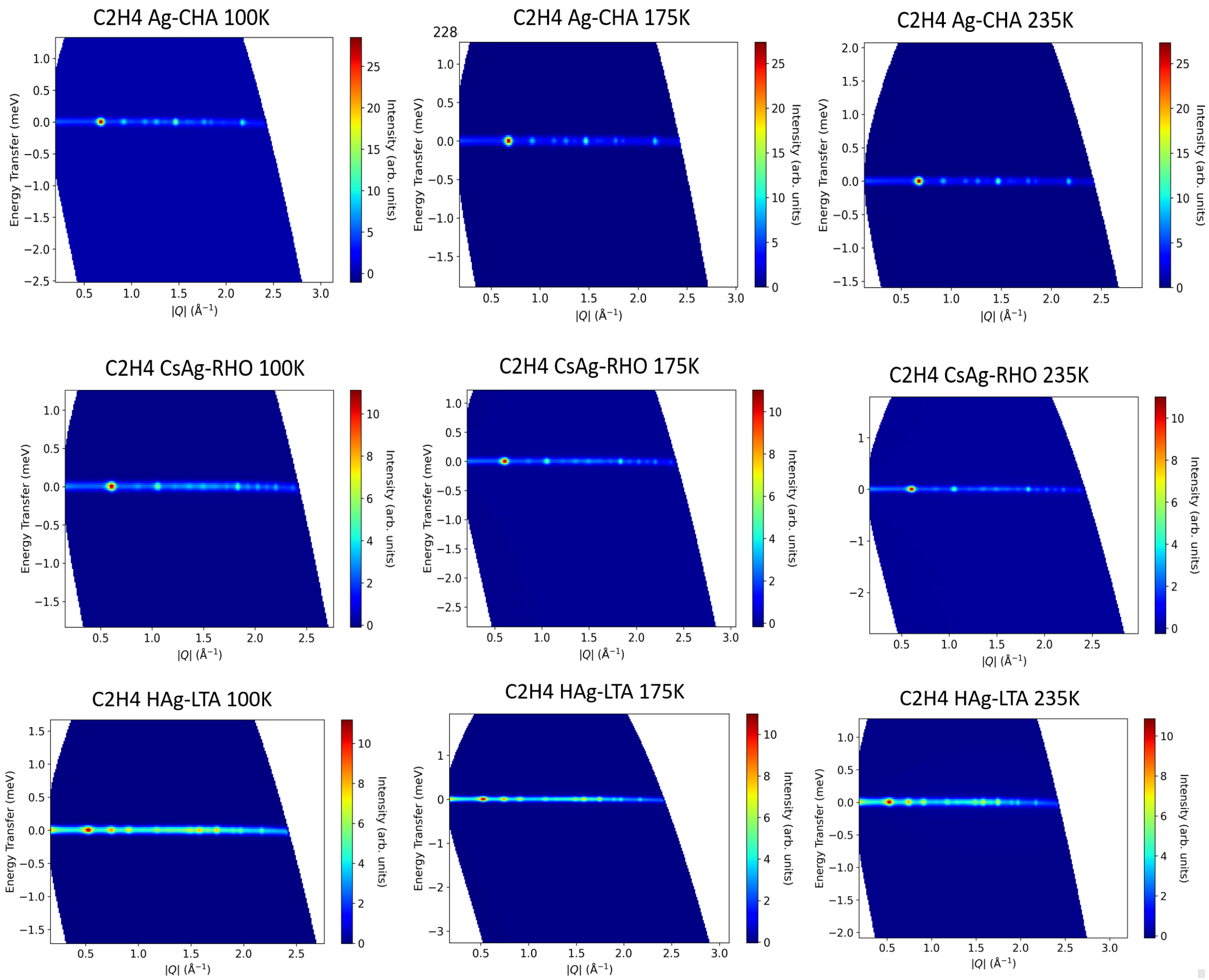

Figure A.30: The Q-ω space of C_2H_4 Ag-zeolites measured in IN5.

The cuts along |Q| from 0 to 2.5 $Å^{-1}$ over energy values from -0.2 to 0.2 meV for each system are represented in Figure A.31.

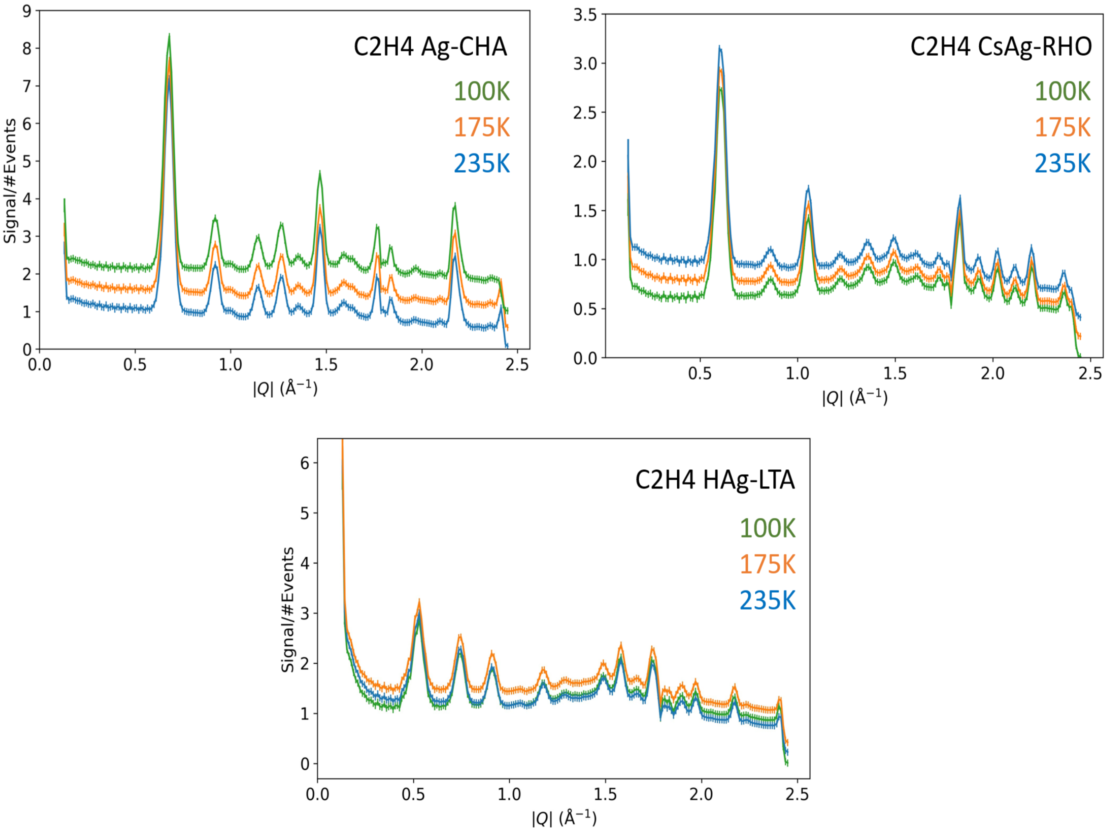

Figure A.31: Cuts of S(Q,ω) along |Q| from 0 to 2.5 Å^{-1} over energy values from -0.2 to 0.2 meV, representing S(Q).

A.7.5 INS: heated sample at 300K

C_2H_4 Ag-CHA sample was heated at 300K prior INS measurement, following the same parameters as decribed in 2.1.3.2. The aim was to verify if there were differences in the INS spectra before and after the heating. A difference in the spectrum after heating could indicate a change in the system conditions. It was verified, however, that the spectra and, therefore, the system was unchanged. In other words, after heating, ethylene is still adsorbed by π-complexation on Ag-CHA.

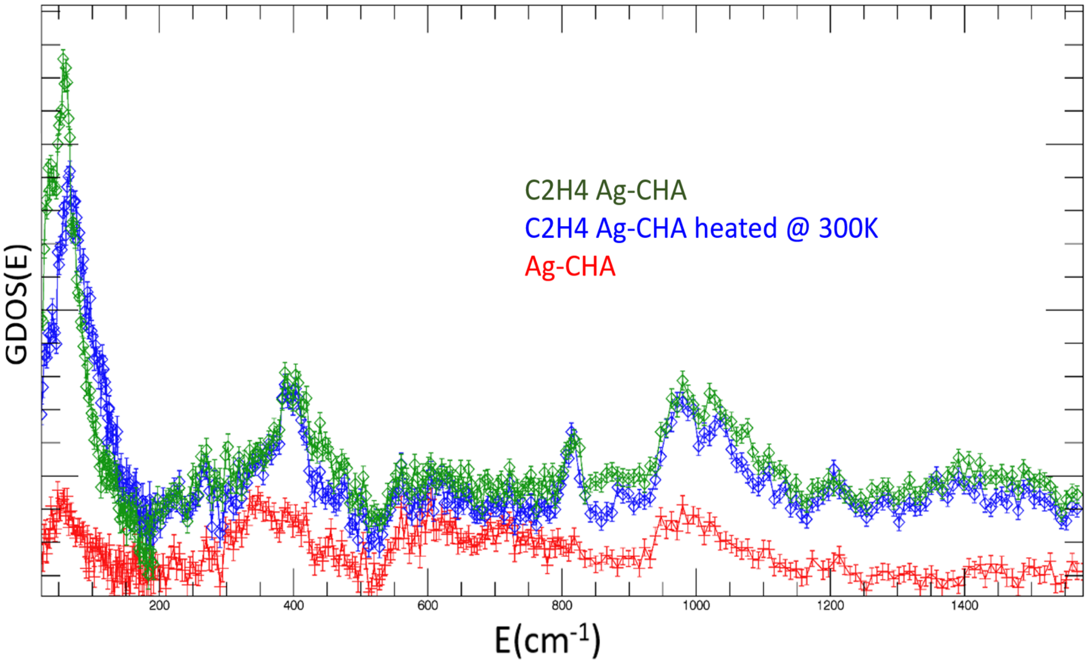

Figure A.32: INS comparison between C_2H_4 Ag-CHA sample before and after heating at 300K.

Bibliography

[1] Dipendu Saha et al. “Elucidating the mechanisms of Paraffin-Olefin separations using nanoporous adsorbents: An overview”. In: *iScience* 24.9 (2021), p. 103042. DOI: `10.1016/j.isci.2021.103042`.

[2] Yaqi Wu and Bert M Weckhuysen. “Separation and Purification of Hydrocarbons with Porous Materials”. In: *Angewandte Chemie* 63.35 (2021), pp. 18930–18949. DOI: `10.1002/anie.202104318`.

[3] Tao Ren, Martin Patel, and Kornelis Blok. “Steam cracking and methane to olefins: Energy use, CO2 emissions and production costs”. In: *Energy* 33.5 (2008), pp. 817–833. DOI: `10.1016/j.energy.2008.01.002`.

[4] Junjun Hou et al. “Olefin/paraffin separation through membranes: from mechanisms to critical materials”. In: *Journal of Materials Chemistry A* 7 (2019), 23489–23511. DOI: `10.1039/c9ta06329c`.

[5] Zahra Gholami et al. “A Review on the Production of Light Olefins Using Steam Cracking of Hydrocarbons”. In: *Energies* 14.23 (2021). DOI: `10.3390/en14238190`.

[6] Pannida Dugkhuntod and Chularat Wattanakit. “A Comprehensive Review of the Applications of Hierarchical Zeolite Nanosheets and Nanoparticle Assemblies in Light Olefin Production”. In: *Catalysts* 10.2 (2020). DOI: `10.3390/catal10020245`.

[7] Michael Bender. “An Overview of Industrial Processes for the Production of Olefins - C4 Hydrocarbons”. In: *Applied Catalysis A, General* 557 (2018), pp. 119–124. DOI: `doi.org/10.1016/j.apcata.2018.03.018`.

[8] Aaron Akah, Jesse Williams, and Musaed Ghrami. “An Overview of Light Olefins Production via Steam Enhanced Catalytic Cracking”. In: *Catalysis Surveys from Asia* 23 (Dec. 2019). DOI: `10.1007/s10563-019-09280-6`.

[9] Zhitong Zhao, Jingyang Jiang, and Feng Wang. “An economic analysis of twenty light olefin production pathways”. In: *Journal of Energy Chemistry* 56 (2021), pp. 193–202. ISSN: 2095-4956. DOI: `https://doi.org/10.1016/j.jechem.2020.04.021`.

[10] Vanessa F. D. Martins et al. "High purity ethane/ethylene separation by gas phase simulated moving bed using ZIF-8 adsorbent". In: *AIChe Journal* 65 (2019). DOI: `10.1002/aic.16619`.

[11] Yuxiang Wang, Shing Bo Peh, and Dan Zhao. "Alternatives to Cryogenic Distillation: Advanced Porous Materials in Adsorptive Light Olefin/Paraffin Separations". In: *Small* 15.25 (2019), p. 1900058. DOI: `10.1002/smll.201900058`.

[12] Chunyu Lu et al. "Energy efficient ethylene purification in a commercially viable ethane-selective MOF". In: *Separation and Purification Technology* 282 (2022), p. 120126. ISSN: 1383-5866. DOI: `https://doi.org/10.1016/j.seppur.2021.120126`.

[13] Ruobing Bai et al. "Low-energy adsorptive separation by zeolites". In: *National Science Review* 9 (2022). DOI: `10.1093/nsr/nwac064`.

[14] Nan Lu et al. "Ethane/ethylene separation in a metal-organic framework with shape-matching ethane traps". In: *Journal of Solid State Chemistry* 304 (2021), p. 122594. DOI: `10.1016/j.jssc.2021.122594`.

[15] D. Sholl and R. Lively. "Seven chemical separations to change the world". In: *Nature* 532 (2016), pp. 435–437. DOI: `doi.org/10.1038/532435a`.

[16] Baiyan Li et al. "Seven chemical separations to change the world". In: *Journal of American Chemistry Society* 136 (2014), 8654–8660. DOI: `doi.org/10.1021/ja502119z`.

[17] Fahmi Anwar et al. "Selectivity Tuning of Adsorbents for Ethane/Ethylene Separation: A Review". In: *Industrial Engineering Chemistry Research* 61.34 (2022), 12269–12293. DOI: `doi.org/10.1021/acs.iecr.2c02438`.

[18] Ingo Pinnau and Lora G. Toy. "Solid polymer electrolyte composite membranes for olefin/paraffin separation". In: *Journal of Membrane Science* 184 (2001), p. 39. DOI: `10.1016/S0376-7388(00)00603-7`.

[19] Huan Xiang et al. "Selective adsorption of ethane over ethylene on M(bdc)(ted)0.5 (M = Co, Cu, Ni, Zn) metal-organic frameworks (MOFs)". In: *Microporous and Mesoporous Materials* 292 (2020), p. 109724. DOI: `10.1016/j.micromeso.2019.109724`.

[20] Yongli Sun et al. "A Novel Copper(I)-Based Supported Ionic Liquid Membrane with High Permeability for Ethylene/Ethane Separation". In: *Industrial Engineering Chemistry Research* 56 (2017). DOI: `doi.org/10.1021/acs.iecr.6b03364`.

[21] Liliana C. Tomé et al. "Polymeric ionic liquid membranes containing IL–Ag+ for ethylene/ethane separation via olefin-facilitated transport". In: *Journal of Materials Chemistry A* 2 (16 2014), pp. 5631–5639. DOI: `10.1039/C4TA00178H`.

[22] Matthew N. Davenport et al. "Ethylene and ethane transport properties of hydrogen-stable Ag+-based facilitated transport membranes". In: *Journal of Membrane Science* 647 (2022), p. 120300. ISSN: 0376-7388. DOI: `10.1016/j.memsci.2022.120300`.

[23] Ling Zhang and Libo Li. “Boosting Ethylene/Ethane Separation within Copper(I)-Chelated Metal-Organic Frameworks through Tailor-Made Aperture and Specific pi-Complexation”. In: *Advanced Science* 7.2 (2019). DOI: `10.1002/advs.201901918`.

[24] Rami Faiz and Kang Li. “Olefin/paraffin separation using membrane based facilitated transport/chemical absorption techniques”. In: *Chemical Engineering Science* 73 (2012), pp. 261–284. DOI: `10.1016/j.ces.2012.01.037`.

[25] Rui-Biao Lin, Libo Li, and Banglin Chen. “Molecular sieving of ethylene from ethane using a rigid metal–organic framework”. In: *Nature Matter* 17.1128–1133 (2018). DOI: `10.1038/s41563-018-0206-2`.

[26] “Zeolite materials: recent discoveries and future prospects”. In: *Current Opinion in Solid State and Materials Science* 1.1 (1996), pp. 107–117. ISSN: 1359-0286. DOI: `https://doi.org/10.1016/S1359-0286(96)80018-0`.

[27] Pablo J. Bereciatuga et al. “Control of zeolite framework flexibility and pore topology for separation of ethane and ethylene”. In: *Science* 358.6366 (2017), pp. 1068–1071. DOI: `10.1126/science.aao0092`.

[28] Quang Hung Trinh, Sang Baek Lee, and Young Sun Mok. “Removal of ethylene from air stream by adsorption and plasma-catalytic oxidation using silver-based bimetallic catalysts supported on zeolite”. In: *Journal of Hazardous Materials* 285 (2015), pp. 525–534. DOI: `10.1016/j.jhazmat.2014.12.019`.

[29] Norberto J. Abreu et al. “Ethylene adsorption onto natural and transition metal modified Chilean zeolite: An operando DRIFTS approach”. In: *Microporous and Mesoporous Materials* 274 (2019), pp. 138–148. DOI: `10.1016/j.micromeso.2018.07.043`.

[30] J. Min, K. Kemp, and S. Hong. “Silver ZK-5 Zeolites for Selective Ethylene/ ethane Separation”. In: *Separation and Purification Technology* 250 (2020), p. 117146. DOI: `10.1016/j.seppur.2020.117146`.

[31] Joseph Howard, Zahrah A. Kadir, and Keith Robson. “Infrared spectroscopic studies of ethylene adsorbed on silver A zeolite”. In: *Zeolites* 3 (1982). DOI: `doi.org/10.1016/0144-2449(83)90198-7`.

[32] Joseph Howard, Thomas C. Wassingt, and Christopher J. Wright. “Ethylene Adsorbed by Silver Exchanged 13X Zeolite; an Inelastic Neutron Scattering Study”. In: *ournal of the Chemical Society Chemical Communications* (1975), pp. 775–776. DOI: `doi.org/10.1039/C39750000775`.

[33] Sonia Aguado et al. “Absolute Molecular Sieve Separation of Ethylene/Ethane Mixtures with Silver Zeolite A”. In: *Journal of the American Chemical Society* 134.36 (2012), pp. 14635–14637. DOI: `10.1021/ja305663k`.

[34] M. Fischer and R. Bell. “Cation-exchanged SAPO-34 for adsorption-based hydrocarbon separations: predictions from dispersion-corrected DFT calculations”. In: *Physical Chemistry Chemical Physics* 16 (2014), pp. 21062–21072. DOI: `10.1039/C4CP01049C`.

[35] Caitlin Horvatits et al. “Ethylene and Water Co-Adsorption on Ag/SSZ-13 Zeolites: A Theoretical Study”. In: *The Journal of Physical Chemistry C* 124 (2020), pp. 7295–7306.

[36] Richard M. Barrer. "Zeolites and their synthesis". In: *Zeolites* 1.3 (1981), pp. 130–140. ISSN: 0144-2449. DOI: `10.1016/S0144-2449(81)80001-2`.

[37] Jule A. Rabo and Michael W. Schoonover. "Early discoveries in zeolite chemistry and catalysis at Union Carbide, and follow-up in industrial catalysis". In: *Applied Catalysis A: General* 222.1 (2001). Celebration Issue, pp. 261–275. ISSN: 0926-860X. DOI: `https://doi.org/10.1016/S0926-860X(01)00840-7`.

[38] Paul A. Wright and Magdalena Lozinska. *Structural Chemistry and Properties of Zeolites.* Editorial Universitat Politècnica de València, 2011. Chap. 1, pp. 1–36.

[39] Manuel Moliner. *Basic principles of zeolite synthesis.* Editorial Universitat Politècnica de València, 2011. Chap. 2, pp. 37–66.

[40] Philip A. Barret and Neil A. Stephenson. *Adsorption Properties of Zeolites.* Editorial Universitat Politècnica de València, 2011. Chap. 6, pp. 149–180.

[41] Roberto Millini. *Zeolites in refining and petrochemistry.* Editorial Universitat Politècnica de València, 2011. Chap. 8, pp. 211–244.

[42] Svetlana Mintova Jean-Pierre Gilson Olivier Marie and Valentin Valtchev. *Emerging Applications of Zeolites.* Editorial Universitat Politècnica de València, 2011. Chap. 9, pp. 245–300.

[43] Anthony F. Masters and Thomas Maschmeyer. "Zeolites – From curiosity to cornerstone". In: *Microporous and Mesoporous Materials* 142.2 (2011), pp. 423–438. ISSN: 1387-1811. DOI: `https://doi.org/10.1016/j.micromeso.2010.12.026`.

[44] Eduardo Pérez-Botella, Susana Valencia, and Fernando Rey. "Zeolites in Adsorption Processes: state of art and future prospects". In: *Chemical Reviews* 122.24 (2022), 17647–17695. DOI: `10.1021/acs.chemrev.2c00140`.

[45] *Ch. Baerlocher and L.B. McCusker.* Database of Zeolite Structures: http://www.iza-structure.org/databases/. Accessed: 06-12-2023.

[46] D. H. Olson et al. "Crystal structure and structure-related properties of ZSM-5". In: *Journal of Physical Chemistry* 85.15 (1981), pp. 2238–2243. DOI: `doi:10.1021/j150615a020`.

[47] Miguel Palomino et al. "Zeolite Rho: a highly selective adsorbent for CO2/CH4 separation induces by a structural phase modification". In: *Chemical Communications* 48.2 (2011), pp. 231–238. DOI: `10.1039/c1cc16320e`.

[48] Julien Grand et al. "Flexible Template-Free RHO Nanosized Zeolite for Selective CO2 Adsorption". In: *Chemistry of Materials* 32 (2020), pp. 5985–5993. DOI: `doi.org/10.1021/acs.chemmater.0c01016`.

[49] Jaroslaw Sadlo, Marek Danilczukb, and Jacek Michalik. "Interaction of tetrameric silver with ammonia in AgCs-rho zeolite". In: *Physical Chemistry Chemical Physics* 3 (2001), pp. 1717–1720. DOI: `10.1039/b008246p`.

[50] Le Xu et al. "Cs-RHO Goes from Worst to Best as Water Enhances Equilibrium CO2 Adsorption via Phase Change". In: *Langmuir* 37 (2021), 1390313908. DOI: `doi.org/10.1021/acs.langmuir.1c02430`.

[51] Magdalena M. Lozinska et al. "Cation Gating and Relocation during the Highly Selective Trapdoor Adsorption of CO2 on Univalent Cation Forms of Zeolite Rho". In: *Chemistry of Materials* 26 (2014), pp. 2052–2061. DOI: `dx.doi.org/10.1021/cm404028f`.

[52] Douglas M. Ruthven and Sebastian C. Reyes. "Adsorptive separation of light olefins from paraffins". In: *Microporous and Mesoporous Materials* 104.1 (2007), pp. 59–66. DOI: `doi.org/10.1016/j.micromeso.2007.01.005`.

[53] Yaqi Wu and Bert M Weckhuysen. "Separation and Purification of Hydrocarbons with Porous Materials". In: *Angewandte Chemie* 60.35 (2021), pp. 18930–18949. DOI: `doi.org/10.1002/anie.202104318`.

[54] "Bimetallic ions regulate pore size and chemistry of zeolites for selective adsorption of ethylene from ethane". In: *Chemical Engineering Science* 220 (2020), p. 115636. DOI: `doi.org/10.1016/j.ces.2020.115636`.

[55] Vasant R. Choudhary, S. Mayadevi, and Anand Pal Singh. "Sorption isotherms of methane, ethane, ethene and carbon dioxide on NaX, NaY and Na-mordenite zeolites". In: *J. Chem. Soc.* 91 (1995), pp. 2935–2944. DOI: `10.1039/FT9959102935`.

[56] E. Costa et al. "Adsorption equilibrium of ethylene, propane, propylene, carbon dioxide, and their mixtures on 13X zeolite". In: *J. Chem. Eng.* 36.2 (1991), pp. 218–224. DOI: `10.1021/je00002a020`.

[57] F. Migliardini et al. "Adsorption of Light Hydrocarbons on LTA and FER Zeolites". In: *American Journal of Analytical Chemistry* 4.7A (2013), pp. 109–114. DOI: `10.4236/ajac.2013.47A015`.

[58] J. L. Carter and V. Kevorkian. "The Adsorption of Ethylene on a Series of Near-Faujasite Zeolites Studied by Infrared Spectroscopy and Calorimetry". In: *The journal of Physical Chemistry* 70.4 (1966), pp. 1126–1136. DOI: `10.1021/j100876a026`.

[59] Philip Mitchell et al. *Vibrational spectroscopy with Neutrons with Applications in Chemistry, Biology, Materials Science and Catalysis*. 3rd ed. United Kingdom: World Scientific, 2005.

[60] Ellie L. Uzunova and Hans Mikosch. "Adsorption and Activation of Ethene in Transition Metal Exchanged Zeolite Clinoptilolite: a Density Functional Study". In: *ACS catalysis* 3 (2013), pp. 2759–2767. DOI: `10.1021/cs4005997`.

[61] E. Kassab, K. Seiti, and M. Allavena. "Determination of structure and acidity scales in zeolite systems by ab initio and pseudopotential calculations". In: *The Journal of Physical Chemistry* 92.23 (1988), 6705–6709. DOI: `doi.org/10.1021/j100334a043`.

[62] I. L. Mudrakovskii et al. "Nature of ethylene complexes on the surface of Ag/SiO2 as evidenced by 13C NMR data". In: *Reaction Kinetics and Catalysis Letters* 34 (1987), pp. 185–190. DOI: `doi.org/10.1007/BF02069222`.

[63] Juergen K. Plischke, Alan J. Benesi, and M. Albert Vannice. “A 13C NMR study of ethylene adsorbed on reduced and oxygen-covered ag surfaces”. In: *Journal of Catalysis* 138.1 (1992), pp. 223–239. DOI: `doi.org/10.1016/0021-9517(92)90019-E`.

[64] Yu Hsing Chin and Paul D. Ellis. “Chemisorption of ethylene onto supported platinum gamma alumina and silver gamma alumina as followed by solid-state static and CP/MAS carbon-13 and static proton NMR spectroscopy”. In: *Journal of the American Chemical Society* 115.1 (1993), 204–211. DOI: `doi.org/10.1021/ja00054a029`.

[65] Anton A. Gabrienko et al. “Methane Activation and Transformation on Ag/H-ZSM-5 Zeolite Studied with Solid-State NMR”. In: *The Journal of Physical Chemistry C* 117.15 (2013), pp. 7690–7702. DOI: `10.1021/jp4006795`.

[66] H. Jobic and A. Méthivier. “Intracrystalline Diffusion in Zeolites Studied by Neutron Scattering Techniques”. In: *Oil Gas Science and Technology - Revue d’IFP Energies nouvelles* 60.5 (2005), pp. 815–830.

[67] Danny Schuring. “Diffusion in Zeolites: Towards a Microscopic Understanding”. PhD thesis. Eindhoven University of Technology, 2002.

[68] Johannes A. Lercher and Andreas Jentys. *Zeolites and ordered porous solids: fundamentals and applications*. Editorial Universitat Politècnica de València, 2011. Chap. 7, pp. 181–210.

[69] H. Jobic. “Molecular Motions in zeolites”. In: *Spectrochimica Acta Part A: Molecular Spectroscopy* 48 (1992), pp. 293–312. DOI: `10.1016/0584-8539(92)80060-A`.

[70] H. Jobic. “Diffusion studies using quasi-elastic neutron scattering”. In: *Membrane Science and Technology* 6 (2000), pp. 109–137. DOI: `doi.org/10.1016/S0927-5193(00)80007-8`.

[71] Hervé Jobic. “On the jump diffusion of molecules in zeolites measured by quasi-elastic neutron scattering”. In: *Microporous and Mesoporous Materials* 55 (2002), 159–169. DOI: `doi.org/10.1016/S1387-1811(02)00400-6`.

[72] H. Jobic and Doros N. Theodorou. “Quasi-elastic neutron scattering and molecular dynamics simulation as complementary techniques for studying diffusion in zeolites”. In: *Microporous and Mesoporous Materials* 102 (2007), pp. 21–50. DOI: `10.1016/j.micromeso.2006.12.034`.

[73] Niklas Hedin et al. “PFG NMR self-diffusion of small hydrocarbons in high silica DDR, CHA and LTA structures”. In: *Microporous and Mesoporous Materials* 109 (2008), 327–334. DOI: `10.1016/j.micromeso.2007.05.007`.

[74] Alexander J. O’Malley et al. “Ammonia mobility in chabazite: insight into the diffusion component of the NH3-SCR process”. In: *Physical Chemistry Chemical Physics* 18 (26 2016), pp. 17159–17168. DOI: `10.1039/C6CP01160H`.

[75] A. J. O’Malley et al. “Comparing ammonia diffusion in NH3-SCR zeolite catalysts: a quasielastic neutron scattering and molecular dynamics simulation study”. In: *Physical Chemistry Chemical Physics* 20 (17 2018), pp. 11976–11986. DOI: `10.1039/C8CP01022F`.

[76] Carlos Hernandez-Tamargo et al. “Molecular behaviour of phenol in zeolite Beta catalysts as a function of acid site presence: a quasielastic neutron scattering and molecular dynamics simulation study”. In: *Catalysis Science Technology* 9 (23 2019), pp. 6700–6713. DOI: `10.1039/C9CY01548E`.

[77] G. L. Squires. *Introduction to the theory of thermal neutron scattering.* Courrier Corporation, 1978.

[78] Andrew T. Boothroyd. *Principles of neutron scattering from condensed matter.* 1st ed. New York: Oxford University Press, 2020.

[79] R.Scherm and B. Fak. *Neutron and X-Ray spectroscopy.* Springer, 2006. Chap. 11, pp. 361–380.

[80] R. Eccleston. *Neutron and X-Ray spectroscopy.* Springer, 2006. Chap. 14, pp. 457–481.

[81] Tetiana Lemishko. “Inelastic Neutron Scattering study of Bronsted acidity in LTA zeolite”. PhD thesis. Universitat Politècnica de València, 2019.

[82] Thomas Lorne. “Contribution of Inelastic Neutron Scattering to the characterization of the grafting of fluorophores onto double walled carbon nanotubes”. PhD thesis. Université de Toulose.

[83] Alexander James O’Malley. “Hydrocarbon Dynamics in Microporous Catalysts”. PhD thesis. University College London, 2015.

[84] A. Rauch and W. Waschkowski. *Neutron Data Booklet.* Institut Laue Langevin, 2003. Chap. 1.

[85] Jisue Moon et al. “Neutron Scattering (NS) Spectroscopy”. In: *Springer Handbook of Advanced Catalyst Characterization.* Ed. by Israel E. Wachs and Miguel A. Bañares. Cham: Springer International Publishing, 2023, pp. 493–516.

[86] S. F. Parker, D. Lennon, and P.W. Albers. “Vibrational Spectroscopy with Neutrons: A Review of New Directions”. In: *Applied Spectroscopy* 65 (12 2011), pp. 1325–1341. DOI: `10.1366/11-06456`.

[87] *Institut Laue Langevin.* IN1-Lagrange: https://www.ill.eu/users/instruments/instruments-list/in1-lagrange/characteristics. Accessed: 15-01-2024.

[88] A. Ivanov, M. Jiménez-Ruiz, and J. Kulda. “IN1-LAGRANGE – the new ILL instrument to explore vibration dynamics of complex materials”. In: *Journal of Physics: Conference Series* 554 (2014), pp. 012001–012007. DOI: `10.1088/1742-6596/554/1/012001`.

[89] Mark T F Telling. *A Practical Guide to Quasi-elastic Neutron Scattering.* The Royal Society of Chemistry, July 2020. ISBN: 978-1-78801-262-1. DOI: `10.1039/9781839169090`. URL: `https://doi.org/10.1039/9781839169090`.

[90] C T Chudley and R J Elliott. “Neutron Scattering from a Liquid on a Jump Diffusion Model”. In: *Proceedings of the Physical Society* 77 (1961), p. 353. DOI: `10.1088/0370-1328/77/2/319`.

[91] P. L. Hall and D. K. Ross. "Incoherent neutron scattering functions for random jump diffusion in bounded and infinite media". In: *Molecular Physics* 42 (1981), pp. 673–682. DOI: doi.org/10.1080/00268978100100521.

[92] K. S. Singwi and Alf Sjölander. "Diffusive Motions in Water and Cold Neutron Scattering". In: *Phys. Rev.* 119 (1960), p. 863. DOI: doi.org/10.1103/PhysRev.119.863.

[93] S. Mitra et al. "Acetylene diffusion in Na-Y zeolite". In: *Pramana journal of physics* 63 (2004), 449–453. DOI: doi.org/10.1103/PhysRev.119.863.

[94] *Institut Laue Langevin.* IN5: https://www.ill.eu/users/instruments/instruments-list/in5/characteristics. Accessed: 20-01-2024.

[95] R. G. Parr and Y. Weitao. *Density-Functional Theory of Atoms and Molecules.* Oxford Uiversity Press, 1989.

[96] Feliciano Giustino. *Materials Modelling using Density Functional Theory: Properties and Predictions.* Oxford Uiversity Press, 2014.

[97] D.S. Scholl and J. A. Steckel. *Density functional theory: a practical introduction.* Wiley, 2009.

[98] M. T. Dove. *Introduction to lattice dynamics.* Wiley, 1993.

[99] R. S. Mulliken. "Electronic Population Analysis on LCAO–MO Molecular Wave Functions. I". In: *The Journal of Chemical Physics* 23.10 (1955), pp. 1833–1840. DOI: 10.1063/1.1740588.

[100] P. Hunt. *Molecular Orbital and Population Analysis.* https://www.huntresearchgroup.org.uk/teaching/teaching_comp_chem_year4/L7_bonding.pdf. Accessed on 19-06-2023.

[101] S. Huzinaga and S. Narita. "Mulliken Population Analysis and Point Charge Model of Molecules". In: *Israel Journal of Chemistry* 19.1-4 (1980), pp. 242–254. DOI: 10.1002/ijch.198000027.

[102] J.P. Perdew, K. Burke, and M. Ernzerhof. "Generalized Gradient Approximation Made Simple". In: *Physical Review Letters* 77 (1996), pp. 3865–3868. DOI: https://doi.org/10.1103/PhysRevLett.77.3865.

[103] Alexandre Tkatchenko and Matthias Scheffler. "Accurate Molecular Van Der Waals Interactions from Ground-State Electron Density and Free-Atom Reference Data". In: *Phys. Rev. Lett.* 102 (7 2009), p. 073005. DOI: 10.1103/PhysRevLett.102.073005.

[104] K. Dymkowski et al. "AbINS: The modern software for INS interpretation". In: *Physica B* 443-448 (2018). DOI: 10.1016/j.physb.2018.02.034.

[105] O. Arnold. "Mantid—Data analysis and visualization package for neutron scattering and microSR experiments, Nuclear Instruments and Methods". In: *Physics Research Section A* 764 (2014), pp. 156–166. DOI: 10.1016/j.nima.2014.07.029.

[106] BIOVIA. *Materials Studio*. 2021.

[107] M. Matsuoka et al. “The photocatalytic decomposition of nitric oxide on Ag^+/ZSM-5 catalyst prepared by ion-exchange”. In: *Journal of Molecular Catalysis A: Chemical* 107.1 (1996). Proceedings of the 8th International Symposium on the Relations between Homogeneous and Heterogeneous Catalysis, pp. 399–403. ISSN: 1381-1169. DOI: `https://doi.org/10.1016/1381-1169(95)00239-1`.

[108] Jung Gi Min et al. “Silver-exchanged CHA zeolite as a CO_2-resistant adsorbent for N_2/O_2 separation”. In: *Microporous and Mesoporous Materials* 323 (2021), p. 111239.

[109] Takashi Yumura et al. “Combined Experimental and Computational Approaches To Elucidate the Structures of Silver Clusters inside the ZSM 5 Cavity”. In: *The Journal of Physical Chemistry C* 118 (2014), pp. 23874–23887. DOI: `10.1021/jp508150w`.

[110] L.S. Dent and J. V. Smith. “Crystal Structure of chabazite, a molecular sieve”. In: *Nature* 181 (1958), pp. 1794–1796.

[111] M. Calligaris et al. “Cation sites and framework deformations in dehydrated chabazites. Crystal structure of a fully silver-exchanged chabazite”. In: *Zeolites* 4 (1984), pp. 323–328. DOI: `10.1016/0144-2449(84)90007-1`.

[112] B. Civalleri et al. “Cation Selectivity in Alkali-Exchanged Chabazite:An ab Initio Periodic Study”. In: *Chemistry of Materials* 15.21 (2003), pp. 3996–4004. DOI: `10.1021/cm0342804`.

[113] Joseph Howard et al. “Inelastic Neutron Scattering Study of Ethylene Adsorbed on silver - A zeolite”. In: *Zeolites* 2 (1982), pp. 2–12. DOI: `doi.org/10.1016/S0144-2449(82)80033-X`.

[114] Zhimin Ao et al. “Density functional theory calculations on graphene/a-SiO2(0001) interface”. In: *Nanoscale Research Letters* 158.7 (2012). DOI: `10.1186/1556-276X-7-158`.

[115] Lloyd Abrams and David R. Corbin. “Sorption properties of zeolite rho”. In: *Journal of Catalysis* 127.1 (1991), pp. 9–21. DOI: `doi.org/10.1016/0021-9517(91)90204-H`.

[116] S. R. G. Balestra et al. “Simulation Study of Structural Changes in Zeolite RHO”. In: *The Journal of Physical Chemistry C* 117 (2013), pp. 11592–11599. DOI: `doi.org/10.1021/jp4026283`.

[117] Ramin Ekhteiari Salmas et al. “SilverSodium Ion Exchange Dynamics in LTA Zeolite Membranes”. In: *The Journal of Physical Chemistry C* 117 (2013), 16631671. DOI: `/10.1021/jp311534e`.

[118] Marcin Sterniczuk et al. “Density Functional Theory Study of nonframework cations in zeolite lattice”. In: *Radiation Chemistry and Physics, Radiation Technologies* 67 (2007).

[119] Tetiana Lemishko et al. “Inelastic Neutron Scattering Study on the Location of Brønsted Acid Sites in High Silica LTA Zeolite”. In: *The Journal of Physical Chemistry C* 120 (2016), 2490424909. DOI: `10.1021/acs.jpcc.6b09012`.

[120] Marco Grimaldo et al. “Hierarchical molecular dynamics of bovine serum albumin in concentrated aqueous solution below and above thermal denaturation”. In: *Physical Chemistry Chemical Physics* 17 (2015), pp. 4645–4655. DOI: `10.1039/C4CP04944F`.

[121] Shushu Gao et al. “Cavity-controlled diffusion in 8-membered ring molecular sieve catalysts for shape selective strategy”. In: *Journal of Catalysis* 377 (2019), pp. 51–62. DOI: `doi.org/10.1016/j.jcat.2019.07.010`.

[122] Zhixin Tian and Zichao Tang. “Experimental and theoretical studies of the interaction of silver cluster cations Agn+ (n = 1-4) with ethylene”. In: *Rapid Communications in Mass Spectrometry* 19 (2005), pp. 2893–2904. DOI: `10.1002/rcm.2139`.

[123] G. Goret, B. Aoun, and E. Pellegrini. “MDANSE: An Interactive Analysis Environment for Molecular Dynamics Simulations”. In: *Journal of Chemical Information and Modeling* 57.1 (2017), pp. 1–5. DOI: `10.1021/acs.jcim.6b00571`.